Fermions and Bosons on an Atom Chip

by

Marcius H. T. Extavour

A thesis submitted in conformity with the requirements
for the degree of Doctor of Philosophy
Graduate Department of Physics
University of Toronto

Copyright © 2009 by Marcius H. T. Extavour

Abstract

FERMIONS AND BOSONS ON AN ATOM CHIP
Marcius H.T. Extavour, Doctor of Philosophy, 2009
Graduate Department of Physics, University of Toronto

Ultra-cold dilute gases of neutral atoms are attractive candidates for creating controlled mesoscopic quantum systems. In particular, quantum degenerate gases of bosonic and fermionic atoms can be used to model the correlated many-body behaviour of Bose and Fermi condensed matter systems, and to study matter wave interference and coherence.

This thesis describes the experimental realization and manipulation of Bose-Einstein condensates (BECs) of $^{87}\mathrm{Rb}$ and degenerate Fermi gases (DFGs) of $^{40}\mathrm{K}$ using static and dynamic magnetic atom chip traps. Atom chips are versatile modern tools used to manipulate atomic gases. The chips consist of micrometre-scale conductors supported by a planar insulating substrate, and can be used to create confining potentials for neutral atoms tens or hundreds of micrometres from the chip surface. We demonstrate for the first time that a DFG can be produced via sympathetic cooling with a BEC using a simple single-vacuum-chamber apparatus. The large $^{40}\mathrm{K}$-$^{87}\mathrm{Rb}$ collision rate afforded by the strongly confining atom chip potential permits rapid cooling of $^{40}\mathrm{K}$ to quantum degeneracy via sympathetic cooling with $^{87}\mathrm{Rb}$. By studying $^{40}\mathrm{K}$-$^{87}\mathrm{Rb}$ cross-thermalization as a function of temperature, we observe the Ramsauer-Townsend reduction in the $^{40}\mathrm{K}$-$^{87}\mathrm{Rb}$ elastic scattering cross-section. We achieve DFG temperatures as low as $T \approx 0.1T_F$, and observe Fermi pressure in the time-of-flight expansion of the gas.

This thesis also describes the radio-frequency (RF) manipulation of trapped atoms to create dressed state double-well potentials for BEC and DFG. We demonstrate for the first time that RF-dressed potentials are species-selective, permitting the formation of simultaneous $^{87}\mathrm{Rb}$ double-well and $^{40}\mathrm{K}$ single-well potentials using a $^{40}\mathrm{K}$-$^{87}\mathrm{Rb}$ mixture. We also develop tools to measure fluctuations of the relative atom number and relative phase of a dynamically split $^{87}\mathrm{Rb}$ BEC. In particular, we observe atom number fluctuations at the shot-noise level using time-of-flight absorption imaging. These measurement tools lay the foundation for future investigations of number squeezing and matter wave coherence in BEC and DFG systems.

Acknowledgements

This thesis is the product of many years of hard work, and I have many people to thank. The work really would not have been possible were it not for the professional and personal support of physics faculty, my fellow graduate students and lab mates, friends, and family.

My thesis supervisor Professor Joseph Thywissen has been a supportive and responsive thesis adviser. Joseph was always generous with his time, making himself available to discuss physics, technical issues and experiment strategy one-on-one and in groups. I particularly appreciated his focus on the broader field and his optimism for the future during the early days of bare optics tables and freshly painted lab walls. He sold me on ultra-cold atoms on my first visit to his office, where he told me about fermionization of bosons in a one-dimensional trap. I mention this detail as a testament to his enthusiasm for the research, which I value greatly. I would also like to thank Prof. Aephraim Steinberg for his feedback on my research throughout my Ph.D, and Prof. Allan Griffin for his valuable advice during the writing of my thesis.

Dr. Seth Aubin taught me most of what I know about atomic spectroscopy and general cold-atoms laboratory technique. My first lesson from Seth was that a Ph.D in experimental atomic physics would require tightening no fewer than ten-thousand vacuum bolts. He led the build-up phase of our experiment, and was the driving force behind our achievements of BEC and DFG. Dr. Stefan Myrskog and Lindsay LeBlanc were also instrumental in the early years in bringing the cold atoms machine online, as were the first summer students Phil Scrutton, Swati Singh and Hyun Youk. Alan Stummer's skills and support on so many technical projects have also been an invaluable resource for this work.

Dr. Thorsten Schumm's 2006 visit to our group was very productive time. Thorsten brought his expertise in radio-frequency double-well potentials to our group, along with his considerable atom chip experience. We observed matter wave interference for the first time during his stay, which was the starting point of my subsequent work on relative number and phase measurements in a split Bose-Einstein condensate.

My fellow lab mates Lindsay LeBlanc, David McKay, Alma Bardon, Dylan Jervis and Dr. Jason McKeever have kept life interesting in the lab over the years. Lindsay's ice cream, McKay's chatter, Alma's cheer, Dylan's tunes and McKeever's edge made the good times great and the bad times bearable. Outside of the lab, I was lucky to have many friends to talk physics and commiserate with, especially Elham, Shabnaz, Lisa, Reza, Patrick P., Patrick M., Chris E., John V. and Krister. I am also grateful to the Torontula ultimate, especially the On Point Kings, and to many musical masters to name, with whom I also shared all of the ups and downs.

Special thanks are due to my sisters Cassandra, Ericka and Mariea for their support and laughter, and to my parents Hughgo and Doris for never asking when I would graduate. Finally, my deepest thanks are for my wife Janine – for her love, her faith in me, and her tremendous patience. Janine always knew when to cheer me on, when to shut me up, and how to help me see the forest for the trees.

Preface

My first experience at an international atomic physics meeting came at the 2005 International Conference on Laser Spectroscopy (ICOLS) in Aviemore, Scotland. The name initially struck me as an odd choice for a conference dedicated to ultra-cold atoms research, which my thesis supervisor and the list of invited speakers assured me it was. I followed their lead and prepared a poster entitled *Cold Bose-Fermi Mixtures in a Microchip Trap*, describing our recent achievement of Bose-Einstein condensation in an atom chip trap, and ongoing efforts to achieve a degenerate Fermi gas.

At the conference's opening reception, Professor Norman Ramsey greeted the attendees and regaled us with tales of the early days of the laser, and of atomic spectroscopy. As he recalled the origins of ICOLS at a 1971 laser physics symposium in Esfahan, I couldn't help but overhear the quiet grumbling of two nearby physicists: here was one of the great spectroscopists presiding over a conference which had been hijacked by the quantum gas people, they said. "Hijacked" is surely an overstatement, but their sentiment did highlight a theme of that conference, and of contemporary atomic physics research in general: namely, the gradual and ongoing shift toward the physics of interacting many-body quantum systems.

This thesis presents my graduate research in quantum degenerate gases of neutral alkali atoms in Professor Joseph H. Thywissen's group at the University of Toronto in Toronto, Canada. The experimental work was carried out between September 2003 and the present in the McLennan Physical Labs, room MP023.

Publications arising from this thesis are:

- M. H. T. Extavour, L. J. LeBlanc J. McKeever A. B. Bardon, S. Aubin, S. Myrskog, T. Schumm and J. H. Thywissen, *Fermions on atom chips*, A chapter in the forthcoming volume *Atom Chips* ed. V. Vuletic and J. Reichel, Wiley-VCH, 30 pages, in press 2009. arXiv:0811.1401.

- M. H. T. Extavour, L.J. LeBlanc, T. Schumm, B. Cieslak, S. Myrskog, A. Stummer, S. Aubin and J. H. Thywissen, *Dual-species quantum degeneracy of* ^{40}K *and* ^{87}Rb *on an atom chip*, Atomic Physics **20**, p.241 - 249 (2006).

- S. Aubin, S. Myrskog, M. H. T. Extavour, L. J. LeBlanc, D. McKay, A. Stummer, J. H. Thywissen, *Rapid sympathetic cooling to Fermi degeneracy on a chip*, Nature Physics **2** 384 - 387 (2006).

- S. Aubin, M. H. T. Extavour, S. Myrskog, L. J. LeBlanc, J. Estève, S. Singh, P. Scrutton, D. McKay, R. McKenzie, I. D. Leroux, A. Stummer and J. H. Thywissen, *Trapping fermionic* ^{40}K *and bosonic* ^{87}Rb *in a chip*, J. Low Temp. Phys. **140** 377 - 396 (2005).

The methods and results of Chapters 7 are unpublished, but will be incorporated into future publications.

In preparing this thesis I have benefited from the specific contributions of several lab-mates. Seth Aubin led the analysis of cross-species thermalization presented in Section 5.5.2. Lindsay LeBlanc supplied up-to-date loading rate, atom number and temperature data for the $^{87}\mathrm{Rb}$ and $^{40}\mathrm{K}$ MOTs and magnetic traps presented in Section 5.1. Jason McKeever performed the analysis of optical shot noise in blanks data presented in Section B.2.2.1.

This thesis was edited using VIM 7.2, and typeset using pdfTEXversion 1.40.3.

Marcius H. T. Extavour
June 2009

Contents

List of Tables

List of Figures

List of Acronyms

AC alternating current
ADC analog-to-digital counts
AOM acousto-optic modulator
BEC Bose-Einstein condensate (condensation)
BJJ bosonic Josephson junction
CCD charge-coupled device
DC direct current
DDS direct digital synthesizer
DFG degenerate Fermi gas
HF high frequency
LD laser diode
LIAD light-induced atomic desorption
MOT magneto-optical trap
OD optical density
OSN optical shot noise
QMT quadrupole magnetic trap
RF radio frequency
RGA residual gas analyzer
RWA rotating-wave approximation
TA tapered amplifier
TOF time of flight
TSP titanium sublimation pump
UHV ultra-high vacuum

Something interesting will happen soon at work.

Wing's fortune cookie

1 Introduction

The experimental work of this thesis was carried out in a laboratory formerly occupied by the atomic and molecular spectroscopist Boris P. Stoicheff [1]. It seems fitting that our cold atoms research group should have inherited Professor Stoicheff's space, since the modern field of ultra-cold atoms grew out of the laser physics and atomic spectroscopy communities. Many of the research directions driving the ultra-cold atoms community today, however, address questions traditionally associated with condensed matter physics and quantum optics. These include quantum simulation of magnetic ordering using neutral atoms in optical lattice potentials (see for instance [2, 3]), vortex dynamics in superfluid quantum gases (e.g. [4, 5]), and matter wave coherence and squeezed states for matter wave interferometers (e.g. [6]).

The use of ultra-cold atoms to pursue these research directions reflects a broader theme in the field, which is also a central theme of this thesis: the tools used to prepare, manipulate and measure ultra-cold gases depend critically on internal atomic degrees of freedom, but the behaviour of the resulting quantum systems is dictated by quantum statistics, which apply to any gas of particles obeying Bose-Einstein or Fermi-Dirac statistics. Thus, degenerate quantum gases of neutral atoms are excellent systems for studying a broad range of physical phenomena beyond the bounds of traditional atomic physics.

Quantum degeneracy in atomic gases

The first major achievement of this thesis is the realization of degenerate Fermi gases of ^{40}K and Bose-Einstein condensates of ^{87}Rb in a simple, single-vacuum-chamber apparatus. The Bose-Einstein condensate (BEC) is one of the most unique and fascinating many-body states in physics. Unlike a conventional gas, in which particles are distributed among the available energy states, a BEC is characterized by the multiple, " macroscopic" occupation of **one** single-particle quantum state of the system. BEC in dilute alkali gases was first achieved in 1995 [7, 8, 9], following advances in the phase-space-reducing techniques used to coax the atomic gas through a phase transition and into the condensed state. The main techniques are laser cooling and evaporative cooling, which typically involve coupling external laser and radio-frequency (RF) magnetic fields to internal atomic states. Since all the particles in a BEC occupy the same single-particle quantum state, the BEC is a source of coherent matter waves analogous to a laser for light. The first observation of matter wave interference between two BECs in 1997 [10] was an immediate and

striking demonstration of the analogy between the BEC and coherent optical waves.

In 1999, the first degenerate Fermi gas (DFG) was achieved by similar means [11]. However, the Pauli exclusion principle states that two identical fermions cannot occupy the same quantum state. Thus, quantum degeneracy in fermions has a very different meaning than in boson systems. At zero-temperature, n particles in a Fermi gas fill the n lowest energy states of the system. This "filled Fermi sea" description of the single-component atomic DFG is directly analogous to elementary textbook descriptions of electrons in a metal [12], or neutrons in a neutron star [13].

Atom chips: an enabling technology

This thesis describes the preparation of atomic DFG and BEC using atom chip magnetic traps. Atom chip magnetic microtraps ("chip traps") are small-volume magnetic traps for neutral atoms formed using magnetic fields generated by an atom chip. An atom chip consists of a planar substrate patterned with lithographic, planar conductors, which generate trapping magnetic fields when DC and/or AC currents are passed through the conductors [14, 15]. Not long after the first DFG was produced, efficient loading of cold atoms into atom chip microtraps enabled the first demonstration of Bose-Einstein condensation on an atom chip [16, 17]. In subsequent years, research efforts in DFGs and atom chips progressed independently. Though the 1999 demonstration of DFG was a promising step toward observing many-body fermion dynamics in atomic systems, as of 2003, when the work of this thesis began, DFGs continued to be a challenge to produce, and had been realized in only a handful of laboratories [11, 18, 19, 20, 21, 22, 23, 24, 25, 26]. A major achievement of this thesis is the first demonstration of a DFG on an atom chip [27], which represents a significant reduction in the experimental complexity required to prepare an atomic DFG.

The use of lithographic conductor patterns for magnetic atom trapping was first proposed in [28] in 1995. A major impediment to realizing chip traps for neutral atoms was their small trap volume ($\lesssim 1\ \mu m^3$), which limits the number of atoms which can "fit" in the trap, and their proximity (hundreds of micrometres or less) from the atom chip surface. An efficient loading scheme based on laser cooling and magneto-optical trapping near the chip surface made atom chip microtraps experimentally accessible for ultra-cold atoms for the first time in 1999. In 2001 the first atom chip Bose-Einstein condensates were produced in harmonic magnetic traps based on "Z"-shaped wires [16, 17]. Since their introduction into the field of cold atoms, atom chips have been used to offer a wide array of techniques for trapping and manipulating ultra-cold atoms using a single, integrated device, including magnetostatic, electrostatic [15] and dynamic RF and microwave dressed potentials [29, 30, 31, 32, 33], and integrated optical potentials [34, 35]. The experiments described in this thesis capitalize on the versatility of atom chips by using the various conductors to generate static magnetic traps, adiabatic double-well traps, and as near-field RF antennae for forced RF evaporative cooling and RF spectroscopy.

Coherence with quantum gases in double-well potentials

The second major achievement of this thesis is the implementation of double-well potentials for BEC and DFG, and the development of tools to measure the relative atom number and relative phase of a BEC confined to a double well.

The double-well potential for atoms is analogous to a beam splitter in optics – a basic building block of optical coherence and quantum optics experiments. A key difference between matter waves and light waves is the presence of interparticle (atom-atom) interactions, which are absent in coherent optics experiments. As a coherent, interacting object, a BEC confined to a double-well potential is a versatile canonical system for studying interference and coherence effects in matter waves.

These systems have both fundamental and applied importance. Consider matter wave interference. As Kasevich points out [6], although particle-wave duality is a fundamental and well-tested aspect of quantum mechanics, demonstrations of interference with a collection of atoms – massive, composite "meta-particles" – is truly remarkable. Matter wave interference experiments also raise important questions about the meaning of the global phase of a BEC, and the relative phase between two BECs. For example: Will two independently prepared BECs, each consisting of a definite measurable number of atoms, and which have never "seen" each other, produce an interference pattern? [36, 37, 38] This question was answered in the affirmative in 1997, with the first observation of matter wave interference between two ^{23}Na BECs, which were created independently, released from their trap, and allowed to overlap [10].

In more applied terms, careful measurement and control of BECs in double well atom chip potentials are important steps toward creating compact atom interferometers for precision measurement. Trapped BECs are promising candidates for atom interferometry since they possess narrower momentum distributions than do non-condensed ultra-cold atoms [39]. The double well can act as matter wave beam-splitter, and can in principle be integrated with other atom optical elements such as waveguides, slits, diffraction gratings, and mirrors on an atom chip [6]. Along these lines, Schumm et al. have demonstrated the coherent splitting of a BEC on an atom chip [29], and Jo et al. have reported coherence times as long as 200 ms between the two halves of a split BEC [31].

One drawback of BECs for atom interferometry is the decrease of coherence time due to mean-field interactions; atom number fluctuations between the two wells can cause rapid dephasing [39]. This effect can be mitigated with atom number squeezed states, i.e. states with sub-shot-noise relative atom number fluctuations. These states are analogous to squeezed photon states, which are known to yield increased phase sensitivity in optical interferometers [40].

It is convenient to describe the split BEC as a boson Josephson junction (BJJ) for the purpose of discussing the relative number and relative phase: both the split BEC and a conventional Josephson junction consist of two superfluids connected by a tunnelling link [41, 42]. The BJJ model predicts the emergence of number squeezed states if a single-well potential is adiabatically deformed into a double-well potential to split the BEC. This has led to the recent observation of number squeezed states achieved by adiabatic splitting of a BEC [31, 43].

This thesis describes the splitting of a $^{87}\mathrm{Rb}$ BEC using RF dressed state potentials. The resulting double-well potential barrier height and well separation are tunable over a wide range, allowing access to both the strong tunnelling and weak tunnelling regimes. We develop tools to characterize fluctuations in the relative atom number and relative phase, and observe relative atom number fluctuations at the shot noise level.

Thesis outline

The thesis is divided into eight chapters and two appendices, and is organized as follows. In short, Chapters 2, 3 and 4 provide theoretical and technical material which support the experimental work of the thesis; Chapters 5 discusses the creation of BECs and DFGs; Chapters 6 and 7 describe the implementation of RF double-well potentials; the main results of the thesis are contained in Chapters 5, 6 and 7.

Chapter 2 presents a brief review of the theory of quantum gases relevant to the main results of the thesis. We review the theory of ideal BECs and DFGs at zero-temperature in harmonic traps, focusing on thermodynamics and the observable signatures of quantum degeneracy. This review is most relevant to the measurements of a DFG/BEC mixture on an atom chip presented in Chapter 5. We also discuss the relative atom number and relative phase of a BEC in a double-well potential using the Bose Josephson junction model, which supports the measurements of number and phase discussed in Chapter 7.

Chapter 3 describes the characterization of micromagnetic atom chip traps used for confining the atoms. The chapter reviews the basic theory of magnetic trapping in neutral atoms, and gives a detailed description of our anisotropic magnetic chip traps. **Appendix A** provides supporting theoretical material related to magnetic fields generated by chip wires of finite width and length.

Chapter 4 provides a detailed technical account of the design, construction and characterization of the experimental apparatus: the diode laser system, ultra-high vacuum chamber, magnetic coils, atom chips, RF sources, imaging systems and control hardware and software used in our experiment. Updates as of June 2009 to the original 2003 and 2004 designs, published in [44], are noted where appropriate.

Chapter 5 describes the laser cooling, magnetic trapping and sympathetic evaporative cooling steps used to create $^{87}\mathrm{Rb}$ BECs, $^{40}\mathrm{K}$ DFGs, and BEC-DFG mixtures on an atom chip. We discuss the experimental signatures of Bose and Fermi degeneracy. We also present data showing the Ramsauer-Townsend reduction of the $^{40}\mathrm{K}$-$^{87}\mathrm{Rb}$ elastic scattering cross-section at high temperatures. These topics are published in [33, 45, 27]. This chapter also includes a discussion of the roles of trap volume and temperature in loading atom chip microtraps from external magnetic traps.

Chapter 6 describes the formation of double-well potentials for neutral atoms on atom chips using RF dressed adiabatic potentials. We describe the application of this RF technique to the

dynamic splitting of a BEC or DFG in a chip trap. We demonstrate the species-selectivity of RF-dressed potentials by creating a simultaneous double well for bosons and a single well for fermions. The chapter also presents the results of weak-field RF spectroscopic measurements on RF-dressed potentials, and their role in the characterization of double-well potentials in our experiments.

Chapter 7 describes the development of measurement and analysis tools for studying the relative atom number and relative phase in a dynamically split BEC. We focus on the characterization of number and phase fluctuations over successive realizations of the experiment. The main results are the demonstration of non-random phases after splitting, and relative number fluctuations at the shot noise level. We estimate our number counting sensitivity to be well below shot noise, and discuss the prospects for observing number squeezing via adiabatic splitting in future work. **Appendix B** gives further detail of the analysis procedures used to quantify and distinguish atomic fluctuations and optical shot noise from technical noise in our measurements.

Chapter 8 concludes the thesis by summarizing the major achievements and briefly outlining promising new research directions arising from this work.

Summary of scientific contributions

This thesis describes the experimental realization and manipulation of $^{87}\mathrm{Rb}$ BECs and $^{40}\mathrm{K}$ DFGs on an atom chip. We demonstrate for the first time that a DFG can be produced via sympathetic cooling with a BEC using a single-vacuum-chamber atom-chip-based apparatus. We achieve DFG temperatures as low as $T \approx 0.1T_F$, and observe Fermi pressure in the time-of-flight expansion of the gas. We also observe the Ramsauer-Townsend reduction in the $^{40}\mathrm{K}$-$^{87}\mathrm{Rb}$ elastic scattering cross-section at high temperatures, and show that this is an important aspect of sympathetic cooling in this system.

The thesis also describes the application of RF double-well to BEC and DFG. We demonstrate for the first time that the RF-dressed potentials are species-selective, permitting the formation of simultaneous $^{87}\mathrm{Rb}$ double-well and $^{40}\mathrm{K}$ single-well potentials for $^{40}\mathrm{K}$-$^{87}\mathrm{Rb}$ mixture. We also develop tools to measure fluctuations of the relative atom number and relative phase of a dynamically split $^{87}\mathrm{Rb}$ BEC, and observe atom number fluctuations at the shot-noise level using time-of-flight absorption imaging. These measurement tools lay the foundation for future investigations of matter wave coherence in BEC and DFG systems.

It is proper to speak the truth.

Wing's fortune cookie

2 Theoretical basics

This thesis presents experimental work with quantum degenerate atomic gases of fermionic ^{40}K and bosonic ^{87}Rb. The tools used to prepare, manipulate and measure the atoms – laser cooling, magnetic trapping, radio-frequency manipulation, and absorption imaging – all involve external coupling to internal atomic degrees of freedom. However, the physics describing quantum degenerate Bose and Fermi gases is based on quantum statistical occupation functions, which apply equally well to any gas of particles obeying Bose-Einstein or Fermi-Dirac statistics.

The internal atomic structure and external many-body behaviour in these systems are linked through two aspects of modern ultra-cold atom experiments: interparticle interactions, and external confining potentials. Trapped, interacting Bose and Fermi gases require theoretical descriptions which go beyond the textbook statistical mechanics treatment of uniform ideal Bose and Fermi gases. These descriptions are well-established in the ultra-cold atoms literature for Bose gases and Bose-Einstein condensates [46, 47, 48, 49], and for Fermi gases [50, 51].

In this chapter, we review key aspects of the theory of Fermi and Bose gases in harmonic traps. The chapter begins with a discussion of the Bose gas and BEC. We review the Thomas-Fermi solution of the Gross-Pitaevskii equation, which gives a mean-field description of a weakly interacting condensate at zero-temperature. Next, we discuss ideal Fermi gases, with a focus on signatures of quantum degeneracy. Both the Bose and Fermi discussions include descriptions of the time-of-flight density distributions, which we observe using absorption imaging and use to measure the bulk properties of the DFG and BEC. These descriptions support the experimental work of Ch. 5. The present chapter closes with a discussion of a BEC in a double-well potential, which is pertinent to the radio-frequency double well implementation discussed in Chs. 6 and 7. We review the two-mode, bosonic Josephson junction description of this system [41, 42], which provides a useful framework for discussing the interplay of the relative atom number and relative phase of the split BEC.

2.1 Bose gases

One of the most striking features of quantum statistics is the phenomenon of Bose-Einstein condensation – the macroscopic occupation of the single-particle energy state of the system. Atomic Bose-Einstein condensation (BEC) is typically achieved in the lowest energy state of an external

magnetic or optical potential, and coexists with a non-condensed phase – the "thermal cloud". In this section, we review the thermodynamic functions which describe the non-condensed Bose gas. We then discuss the Thomas-Fermi solution of the Gross-Pitaevskii equation, which describes the weakly interacting BEC at zero temperature. The section closes by summarizing expressions for the time-of-flight density distributions of the thermal cloud and BEC.

2.1.1 Thermodynamics and Bose-Einstein condensation

In the grand canonical ensemble description of an ideal Bose gas, the mean occupation number of the single-particle energy state ϵ is

$$\langle n_\epsilon \rangle = \frac{1}{e^{\beta(\epsilon-\mu)}-1} = \frac{1}{\mathcal{Z}^{-1}e^{\beta\epsilon}-1}, \tag{2.1}$$

where $\beta \equiv 1/k_B T$, k_B is the Boltzmann constant, μ is the chemical potential of the gas, and $\mathcal{Z} \equiv e^{\beta\mu}$ is the fugacity. The mean occupation number is bounded only from below, $\langle n_\epsilon \rangle \geq 0$; any number of bosons can occupy a given single-particle energy level. We consider a non-interacting Bose gas in the external harmonic potential

$$U(\mathbf{r}) = \tfrac{1}{2}M(\omega_x^2 x^2 + \omega_y^2 y^2 + \omega_z^2 z^2), \tag{2.2}$$

which has associated single-particle energy states

$$\epsilon_{n_x,n_y,n_z} = (n_x + \tfrac{1}{2})\hbar\omega_x + (n_y + \tfrac{1}{2})\hbar\omega_y + (n_z + \tfrac{1}{2})\hbar\omega_z \tag{2.3}$$

and single-particle wavefunctions $\varphi_{n_x,n_y,n_z}(\mathbf{r})$.

At high temperatures μ is large and negative, and $\langle n_\epsilon \rangle \ll 1$. As T decreases, μ approaches the ground state energy $\epsilon_0 \equiv \epsilon_{000}$, and the occupation of the lowest energy levels increases until eventually the single-particle ground state ϵ_0 becomes macroscopically occupied. The ideal BEC transition temperature T_c^0 is the highest temperature at which this macroscopic occupation appears. $\mu = \epsilon_0$ at T_c^0. As $T \to 0$ all atoms populate the single-particle ground state. This is the phenomenon of Bose-Einstein condensation.

Critical temperature For $T < T_c^0$ we can think of the system as being composed of a mixture of two "phases": a normal phase, consisting of N_{th} atoms distributed over the excited states $\epsilon > \epsilon_0$ (the "thermal cloud"); and a condensed BEC phase consisting of N_0 particles accumulated in the ground state [13, Ch.7].

For non-interacting bosons the condensate density distribution is

$$n_c(\mathbf{r}) = N_0|\varphi_0(\mathbf{r})|^2 \tag{2.4}$$

where

$$\varphi_0(\mathbf{r}) = \frac{1}{\pi^{3/4}\sqrt{a_x a_y a_z}} \exp\left(-\frac{x^2}{2a_x^2} - \frac{y^2}{2a_y^2} - \frac{z^2}{2a_z^2}\right) \tag{2.5}$$

is the single-particle ground state wavefunction in the harmonic potential $U(\mathbf{r})$; $a_i \equiv \sqrt{\hbar/M\omega_i}$ are the harmonic oscillator lengths.

For large N and small energy level spacing with respect to the temperature $k_B T \gg \hbar\overline{\omega}$, the density distribution of the thermal cloud can be calculated using a semi-classical integration of the occupation function n_ϵ over momentum degrees of freedom, as in Eq. 2.37:

$$n_{\rm th}(\mathbf{r}) = \Lambda_T^{-3} g_{3/2}\left(\mathcal{Z}\exp\left[-\frac{\beta M}{2}(\omega_x^2 x^2 + \omega_y^2 y^2 + \omega_z^2 z^2)\right]\right) \tag{2.6}$$

$$= \frac{N_{\rm th}}{g_3(\mathcal{Z})\,\pi^{3/2}\,r_x r_y r_z} g_{3/2}\left(\mathcal{Z}\exp\left[-\frac{x^2}{2r_x^2} - \frac{y^2}{2r_y^2} - \frac{y^2}{2r_z^2}\right]\right). \tag{2.7}$$

The thermal cloud atom number below the transition temperature (for which $\mathcal{Z} = 1$) is obtained by the normalization condition

$$N_{\rm th} = N - N_0 = \int d\mathbf{r}\; n_{\rm th}(\mathbf{r}) = \zeta(3)\left(\frac{k_B T}{\hbar\overline{\omega}}\right)^3 \tag{2.8}$$

where $\zeta(3) = g_3(1) \simeq 1.202$ and $\zeta(\alpha) = \sum_{n=1}^{\infty} n^{-\alpha}$ is the Riemann zeta function. The ideal BEC transition temperature is obtained by setting $N_0 = 0$ at $T = T_c^0$ in Eq. 2.8

$$T_c^0 = \frac{\hbar\overline{\omega}}{k_B}\left(\frac{N}{\zeta(3)}\right)^{1/3} \simeq 0.94\frac{\hbar\overline{\omega}}{k_B}N^{1/3}. \tag{2.9}$$

Inserting the expression for T_c^0 from Eq. 2.9 into Eq. 2.8 results in the following expression for the temperature dependence of the condensate fraction

$$\frac{N_0(T)}{N} = 1 - \left(\frac{T}{T_c^0}\right)^3. \tag{2.10}$$

Finite-size correction to Tc The result of Eq. 2.9 is accurate in the thermodynamic limit $N \to \infty$ and $V \to \infty$ where V is the volume of the condensate. The approximation $\epsilon_0 \approx 0$ in the integrals over energy states ϵ used to arrive at Eqs. 2.30 and 2.6 is justified in this limit. In real BEC experiments, N is finite and the effect of the non-zero single-particle ground state energy $\epsilon_0 = \hbar(\omega_x + \omega_y + \omega_z)/2$ introduces an appreciable shift in the transition temperature [46, 47]. The effect is particularly important for atom chip experiments, in which the small atom number (typically 10^5 and below) and large anisotropy of micromagnetic wire traps can easily lead to corrections to T_c^0 of around -10% or -20%.

The finite-size correction to T_c^0 can be calculated by considering the effect of the zero-point energy on μ at the transition point [46]. In a cylindrically symmetric harmonic trap with $\omega_{x,z} \equiv \omega_\perp$ and $\omega_y \equiv \omega_\parallel$, the transition temperature $T_c^{\rm fs}$ that includes finite-size corrections is given by

[52, 53]

$$k_B T_c^{\text{fs}} \approx k_B T_c^0 - \frac{\zeta(2)}{6\zeta(3)}\hbar(2\omega_\perp + \omega_\parallel). \tag{2.11}$$

The correction to T_c^0 (second term on the right of Eq. 2.11) is independent of N, but the fractional change $(T_c^{\text{fs}} - T_c^0)/T_c^0$ is proportional to $N^{-1/3}$. With parameters typical of our ^{87}Rb experiments $\omega_\perp = 2\pi \times 1$ kHz, $\omega_\parallel = 2\pi \times 15$ Hz and $N = 10^4$, $(T_c^{\text{fs}} - T_c^0)/T_c^0 \simeq -9\%$. With $N = 10^3$, $(T_c^{\text{fs}} - T_c^0)/T_c^0 \simeq -20\%$.

Interaction correction to Tc The effect of interparticle interactions, ignored here thus far but discussed in Sec. 2.1.2, also introduces a shift in the transition temperature [47]. Repulsive attractions reduce the peak density at the centre of the trap, which in turn reduces T_c. The magnitude of this reduction is given by [52, 53]

$$\frac{T_c - T_c^{\text{fs}}}{T_c^0} \approx -1.326\, a\sqrt{\frac{M\overline{\omega}}{\hbar}}\, N^{1/6} \tag{2.12}$$

where a is the ^{87}Rb s-wave scattering length. Using the same representative trap frequencies as in the previous paragraph, this shift is roughly -3% for $N = 10^4$, and -5% for $N = 10^3$ in our experiment. The expression for T_c given in Eq. 2.12 is used to calibrate the total atom number measured in absorption imaging (see Sec. 5.4.3.1).

2.1.2 Interacting Bose gases at zero temperature

Elastic atom-atom interactions modify the BEC wavefunction, leading to deviations from the Gaussian density profile presented in Eq. 2.4 for the non-interacting case. In dilute ultra-cold atomic gases the effect of interactions is well-described by a mean-field approach which assumes only binary s-wave scattering [47, 46].

Since elastic scattering in ultra-cold bosons only occurs in the symmetric s-wave channel[1], atom-atom interactions can be described by a delta-function contact interaction pseudopotential

$$V(\mathbf{r} - \mathbf{r}') = g\delta(\mathbf{r} - \mathbf{r}') \tag{2.13}$$

where

$$g = \frac{4\pi\hbar^2 a}{M} \tag{2.14}$$

is the interaction parameter derived from the s-wave scattering length a [46]. The dilute-gas approximation used to derive Eq. 2.14 is justified so long as $|a| \ll d$ where $d = n^{-1/3}$ is the average interparticle separation in a gas of average density n, i.e. $n|a|^3 \ll 1$ [47]. ^{87}Rb-^{87}Rb

[1] Even-symmetry higher-order partial waves are "frozen out" by centrifugal barriers in the two-body scattering potential [54].

interactions are repulsive, with $a \approx 99\ a_0 \simeq 5.2$ nm [55], where a_0 is the Bohr radius. In our experiments, $n_c(0) \sim 10^{13}$ cm^{-3} so that $n|a|^3 \sim 10^{-6}$.

Gross-Pitaevskii equation In the dilute, "weakly interacting" regime $n|a|^3 \ll 1$ the zero-temperature properties of the non-uniform condensate can be described using the pseudopotential of Eq. 2.13 and a mean-field treatment which ignores quantum fluctuations in the condensed state [47]. The result is the Gross-Pitaevskii equation (GPE)

$$\left(-\frac{\hbar^2}{2M}\nabla^2 + U(\mathbf{r}) + g|\psi(\mathbf{r})|^2\right)\psi(\mathbf{r}) = \mu\psi(\mathbf{r}), \tag{2.15}$$

where $\psi(\mathbf{r}) = \sqrt{N_0}\,\varphi(\mathbf{r})$ is the single-particle wavefunction of the condensed state, and $n_c(\mathbf{r}) = |\psi(\mathbf{r})|^2$ the condensate density, which is subject to the normalization condition

$$N_0 = \int d\mathbf{r}\ n_c(\mathbf{r}). \tag{2.16}$$

The time-independent GPE is obtained from the time-dependent version by assuming a time-dependent condensate "wavefunction"[2] of the form $\Phi(\mathbf{r}, t) = \psi(\mathbf{r})\exp(-i\mu t/\hbar)$ [47]. The GPE has the form of a non-linear Schrödinger equation, in which the effective potential acting on each boson is a sum of the external potential U and the mean-field $g|\psi(\mathbf{r})|^2$ produced by the other bosons. The mean-field approximation used in deriving Eq. 2.15 is valid so long as $N_0 \gg 1$ [46].

Thomas-Fermi approximation Though the system is said to be "weakly interacting" when $n|a|^3 \ll 1$, interaction effects are actually large compared with the kinetic energy of atoms in the trap in most atomic BEC experiments.[3] The quantity $N_0 a/\overline{a}$ is a dimensionless measure of the strength of the interaction, where $\overline{a} \equiv (a_x a_y a_z)^{1/3} = \sqrt{\hbar/M\overline{\omega}}$ [47]. For $N_0 a/\overline{a} \ll 1$ interactions are a small perturbation, while for $N_0 a/\overline{a} \gg 1$ equilibrium is determined by the competition between potential energy and interaction energy [46]. Most atomic BEC experiments are in this interaction-dominated "Thomas-Fermi" regime, with $N_0 \sim 10^5$ to 10^7. This is also the case for atom chip traps, which have smaller N_0 but larger $n_c(0)$ due to large trapping frequencies. With typical ^{87}Rb parameters in our experiment $N_0 = 10^4$, $\omega_\perp = 2\pi \times 1$ kHz, $\omega_\parallel = 2\pi \times 15$ Hz, $a = 5.2$ nm for ^{87}Rb [55], $N_0 a/\overline{a} \simeq 77$.

The Thomas-Fermi approximation amounts to neglecting the kinetic energy term $(-\hbar^2/2M)\nabla^2$ in the GPE of Eq. 2.15. In this approximation the equilibrium condensate density for repulsive interactions is given by

$$n_c(\mathbf{r}) = |\psi(\mathbf{r})|^2 = \frac{1}{g}\left(\mu - U(\mathbf{r})\right) \tag{2.17}$$

for $\mu > U(\mathbf{r})$, and $n_c = 0$ otherwise. Thus, $U(\mathbf{r}) = \mu$ defines the edge of the condensate. The

[2] $\Phi(\mathbf{r})$ is the expectation value of a bosonic field operator and is the order parameter of the condensate. It is not equal to the many-body condensate wavefunction $\Psi_N(\mathbf{r}_1 \ldots \mathbf{r}_N : t)$ [48].

[3] The gas is considered weakly interacting because the interaction energy is small compared to the single-particle energy, which includes potential energy.

spatial half-widths ("Thomas-Fermi radii") of the condensate are

$$R_i = \sqrt{\frac{2\mu}{M\omega_i^2}}. \tag{2.18}$$

The relationship between N and μ is established by the normalization condition for the Thomas-Fermi wavefunction (see Eq. 2.16). Integrating $n_c(\mathbf{r})$ over the volume defined by the Thomas-Fermi radii gives

$$N_0 = \frac{8\pi\mu}{15g}\overline{R}^3. \tag{2.19}$$

where $\overline{R} \equiv (R_x R_y R_z)^{1/3}$ is the geometric mean Thomas-Fermi radius of the condensate. Eqs. 2.18 and 2.19 can be used to express the condensate density profile as [56]

$$n_c(\mathbf{r}) = \frac{15}{8\pi}\frac{N_0}{R_x R_y R_z}\left(1 - \frac{x^2}{R_x^2} - \frac{y^2}{R_y^2} - \frac{z^2}{R_z^2}\right) \tag{2.20}$$

for $\mu > U(\mathbf{r})$, and $n_c(\mathbf{r}) = 0$ otherwise. Eq. 2.20 describes a parabolic cloud in three dimensions with peak density $n_c(0) = \mu/g$. From Eq. 2.19, the chemical potential is given by

$$\mu = \frac{\hbar\overline{\omega}}{2}\left(\frac{15N_0 a}{\overline{a}}\right)^{2/5}. \tag{2.21}$$

Combining Eqs. 2.18 and 2.21 gives

$$\overline{R} = \left(\frac{15N_0 a}{\overline{a}}\right)^{1/5}\overline{a}. \tag{2.22}$$

Eq. 2.22 can be used to demonstrate that, as a result of repulsive interactions, the zero-temperature size of the condensate $\overline{R}$ is much larger than that predicted by the non-interacting treatment $\overline{a}$. For ^{87}Rb parameters typical of our experiment, $N_0 = 10^4$, $\omega_\perp = 2\pi \times 1$ kHz and $\omega_\parallel = 2\pi \times 15$ Hz, $\mu \simeq h \times 1.4$ kHz $\approx 53\hbar\overline{\omega}$, and $\overline{R} \simeq 2.8$ µm, whereas $\overline{a} \simeq 0.7$ µm. Considering the transverse and longitudinal axes of the trap separately, $R_\perp \simeq 2\ a_\perp$ and $R_\parallel \simeq 17\ a_\parallel$. The peak density of the condensate is also much lower in the Thomas-Fermi approximation than in the non-interacting case: $n_c(0)^{TF} \approx 0.074\ n_c(0)^{non-int}$ for the same experimental parameters [47].

The Thomas-Fermi approximation is excellent for $\mu = gn(\mathbf{r}) \gg \hbar\overline{\omega}/2$, i.e. near the centre of the cloud, but not at the edges, where the density vanishes. Numerical solutions of the full GPE (Eq. 2.15) presented in [47] show that the slight Thomas-Fermi underestimate of $n_c(\mathbf{r} \approx R)$ is even less severe in column density distributions observed in time-of-flight absorption imaging. Finally, we note that in strongly anisotropic atom chip traps the transverse kinetic energy may be too large to ignore for sufficiently large $\omega_\perp$. In this case the condensate may deviate from the parabolic shape of the Thomas-Fermi solution in the transverse direction. For the experimental parameters presented above, $\mu \simeq 2\hbar\omega_\perp$.

2.1.3 Time-of-flight density distributions

We measure the atom number and temperature of $^{87}\mathrm{Rb}$ Bose gases using time-of-flight absorption imaging after abruptly switching off the trapping potential and allowing the cloud to expand for a time t. Assuming the thermal cloud density is sufficiently low that interactions during expansion may be neglected, the time-of-flight density may be written

$$n_{\mathrm{th}}(\mathbf{r},t) = \frac{N_{\mathrm{th}}}{(2\pi)^{3/2}\, r_x(t)\, r_y(t)\, r_z(t)\, g_3(\mathcal{Z})} g_{3/2}\left(\mathcal{Z}\, \exp\left[-\frac{x^2}{2r_x^2(t)} - \frac{y^2}{2r_y^2(t)} - \frac{z^2}{2r_z^2(t)}\right]\right), \tag{2.23}$$

where $r_i^2(t) = k_B T(1+\omega_i^2 t^2)/M\omega_i^2$ is the cloud size in the $i \in \{x,y,z\}$ direction after a time t of free expansion [56]. The column density along x is obtained by integrating Eq. 2.23 along x:

$$\tilde{n}_{\mathrm{th}}(y,z,t) = \frac{N_{\mathrm{th}}}{2\pi\, r_y(t)\, r_z(t)\, g_3(\mathcal{Z})} g_{3/2}\left(\mathcal{Z}\, \exp\left[-\frac{y^2}{2r_y^2(t)} - \frac{z^2}{2r_z^2(t)}\right]\right). \tag{2.24}$$

At long times of flight the expansion of the thermal cloud becomes isotropic, similar to that of the ideal Fermi gas (see Eq. 2.2.3). When analyzing thermal clouds below the transition temperature, one must use $\mathcal{Z} = 1$ in Eqs. 2.23 and 2.24.

For the condensate, interparticle interactions play an important role during time-of-flight expansion. Approximate analytic solutions of the time-dependent Gross-Pitaevskii equation reveal that, remarkably, the parabolic shape of the condensate is preserved during time-of-flight expansion, though the aspect ratio is not [47]. In particular, for a BEC from a cylindrically symmetric anisotropic trap with $\omega_\parallel = \lambda\omega_\perp$, the condensate Thomas-Fermi radii evolve according to [47]

$$R_\perp(t) = R_\perp(0)\sqrt{1+\tau^2} \tag{2.25}$$

$$R_\parallel(t) = R_\parallel(0)\left(1 + \lambda^2[\tau \arctan\tau - \ln\sqrt{1+\tau^2}]\right) \tag{2.26}$$

where $\tau \equiv \omega_\perp t$. Thus the Thomas-Fermi condensate density in time-of-flight is given by Eq. 2.20 with the Thomas-Fermi radii re-scaled according to Eqs. 2.25 and 2.26. The BEC column density in the yz plane is obtained by integrating the result along x in the region bounded by $x \in [-R_x(t), R_x(t)]$

$$\tilde{n}_c(y,z,t) = \frac{5N_0}{2\pi R_y(t) R_z(t)}\left(1 - \frac{y^2}{R_y^2(t)} - \frac{z^2}{R_z^2(t)}\right)^{3/2}. \tag{2.27}$$

Throughout this thesis x and z are the transverse directions, and y the longitudinal direction.

2.2 Ideal Fermi gases

Ultra-cold Fermi gases differ from ultra-cold Bose gases in their simplest theoretical description in two important ways: first, there is no macroscopic occupation of the single-particle ground state; second, spin-polarized Fermi gases are completely non-interacting at ultra-cold temperatures [51, 57]. Ideal thermodynamic functions are thus excellent descriptors of cold spin-

polarized fermions, even as $T \to 0$. In this section, we review fermion thermodynamics, calculate trapped density distributions, and discuss observable signatures of Fermi degeneracy.

2.2.1 Thermodynamics

In the grand canonical ensemble description of an ideal Fermi gas, the mean occupation number of the single-particle energy state ϵ is

$$\langle n_\epsilon \rangle = \frac{1}{e^{\beta(\epsilon-\mu)}+1} = \frac{1}{\mathcal{Z}^{-1}e^{\beta\epsilon}+1}. \tag{2.28}$$

The mean occupation number is bounded $0 \leq \langle n_\epsilon \rangle \leq 1$ as a result of the Pauli exclusion principle. The $T = 0$ ideal Fermi gas is characterized by a filled "Fermi sea": each energy level ϵ for which $\epsilon \leq E_F$ is occupied ($n_\epsilon = 1$), while all those for which $\epsilon > E_F$ are empty ($n_\epsilon = 0$). The Fermi energy E_F is equal to the chemical potential μ at $T = 0$. At high temperatures the gas is described by a Boltzmann-like distribution [13].

Since a trapped gas is not in contact with number or energy reservoirs in experiments, we ignore fluctuations in the total number and energy predicted by the grand canonical ensemble description, taking N and E to be the *average* total number and total energy, respectively. These can be calculated using the discrete sums

$$N = \sum_\epsilon \langle n_\epsilon \rangle \qquad \text{and} \qquad E = \sum_\epsilon \epsilon \langle n_\epsilon \rangle, \tag{2.29}$$

where the sums run over all discrete states. In the limit of a large number of occupied states we can take the continuum limit, writing

$$N = \int_{\epsilon=0}^{\infty} g(\epsilon)\langle n_\epsilon \rangle \, d\epsilon \qquad \text{and} \qquad E = \int_{\epsilon=0}^{\infty} g(\epsilon)\epsilon \langle n_\epsilon \rangle \, d\epsilon, \tag{2.30}$$

where $g(\epsilon) = \epsilon^2/2(\hbar\overline{\omega})^3$ is the energy density of states of a harmonically trapped gas in three dimensions [58], and $\overline{\omega} \equiv (\omega_x\omega_y\omega_z)^{1/3}$ is the geometric mean harmonic trap frequency.

Integrals of this type can be evaluated using the Fermi-Dirac integrals [13]

$$f_n(C) \equiv \frac{1}{\Gamma(C)} \int_0^\infty \frac{a^{\,n-1} da}{C^{-1}e^{\,a}+1} = -\mathrm{Li}_n(-C) \quad (0 \leq C < \infty, n > 0), \tag{2.31}$$

where $\mathrm{Li}_n(C) = \sum_{j=1}^{\infty} C^j/j^n$ is a polylogarithmic function and $\Gamma(C)$ is the gamma function. For $n = 1$, $f_1 = \ln(1 + C)$. Using 2.31 we find that the average total number and energy are

$$N = (\beta\hbar\overline{\omega})^{-3} f_3(\mathcal{Z}) \qquad \text{and} \qquad E = 3k_B T(\beta\hbar\overline{\omega})^{-3} f_4(\mathcal{Z}). \tag{2.32}$$

The number and energy at zero temperature can be found using the zero-temperature limit

of the Fermi-Dirac integral [13]

$$\lim_{T\to 0} f_n(\mathcal{Z}) = \frac{(\beta\mu)^n}{\Gamma(n+1)}. \tag{2.33}$$

As mentioned above, the Fermi energy E_F is defined as the zero temperature limit of μ. For convenience, we will also refer to the "Fermi temperature" $T_F \equiv E_F/k_B$, even though this temperature does not correspond to a phase transition, as is the case for T_c of Bose gases. Re-writing Eq. 2.32 in terms of E_F and taking the $T \to 0$ limit, we find

$$N = \frac{1}{6}\left(\frac{E_F}{\hbar\overline{\omega}}\right)^3 \qquad \text{and} \qquad E = \frac{3}{4} N\, E_F. \tag{2.34}$$

The chemical potential and fugacity at finite temperature can be found numerically by solving

$$6 f_3(\mathcal{Z}) = (\beta E_F)^3. \tag{2.35}$$

Using the Sommerfeld expansion of the polylogarithms, one obtains low- and high-temperature approximations to the chemical potential in a three-dimensional harmonic trap [59]:

$$\mu \approx \begin{cases} E_F\left[1 - \frac{\pi^2}{3}\left(\frac{k_B T}{E_F}\right)^2\right] & \text{for } k_B T \ll E_F, \text{ and} \\ -k_B T \ln\left[6\left(\frac{k_B T}{E_F}\right)^3\right] & \text{for } k_B T \gg E_F. \end{cases} \tag{2.36}$$

Low dimensionality Under certain conditions, a $T = 0$ Fermi gas in an anisotropic magnetic trap having $\omega_\perp \gg \omega_\parallel$ may become effectively one-dimensional. If the atom number and temperature are such that $E_F < \hbar\omega_\perp$, the transverse degrees of freedom are "frozen out" and fermions occupy only the longitudinal energy levels of the trap. The maximum number of fermions N_{1D} that can populate such a one-dimensional configuration at $T = 0$ is equal to the aspect ratio of the trap: $N_{1D} = \omega_\perp/\omega_\parallel$. This scenario is especially relevant to atom chip micromagnetic traps, whose aspect ratios can be on the order of 10^2 to 10^4 [60].

2.2.2 Density distribution

Apart from the choice of $g(\epsilon)$, many of the expressions derived in Sec. 2.2.1 resemble the textbook treatment of a uniform Fermi gas. In this section, we calculate the non-uniform position and momentum distributions of *trapped* fermions. The position distribution is observable *in situ* (with sufficient spatial resolution), while the momentum distribution is observable in time-of-flight expansion. We calculate these distributions by two different conceptual starting points: first, using semi-classical integrals; and second, using the local density approximation.

Semi-classical approximation Taking the energies $\epsilon \equiv \epsilon(\mathbf{r}, \mathbf{p}) = p^2/2M + U(\mathbf{r})$ to be those of a classical free particle at position $\mathbf{r}$, where $U(\mathbf{r})$ is the trapping potential and M is the atomic mass,

we can integrate the occupation function of Eq. 2.28 over the momentum degrees of freedom to find the semi-classical position distribution:

$$n(\mathbf{r}) = \int \frac{d^3p}{(2\pi\hbar)^3}[\mathcal{Z}^{-1}e^{\beta\epsilon(\mathbf{r},\mathbf{p})} + 1]^{-1}, \tag{2.37}$$

in which we have used the semi-classical phase-space volume of one quantum state, $(2\pi\hbar)^3$. Integration using Eq. 2.31 yields

$$n(\mathbf{r}) = \Lambda_T^{-3} f_{3/2}(\mathcal{Z}e^{-\beta U(\mathbf{r})}), \tag{2.38}$$

where $\Lambda_T = \sqrt{2\pi\hbar^2\beta/M}$ is the thermal de Broglie wavelength. Unlike the corresponding expression for ideal bosons, Eq. 2.38 is valid *at all temperatures*. The difference lies in the fact that we have ignored the occupation of the single-particle ground state in taking the continuum limit (see Eq. 2.30), evidenced by the vanishing density of states $g(\epsilon)$ for $\epsilon = 0$. This does not pose a problem for fermions, for which the occupation of the ground state $\mathcal{Z}/(1+\mathcal{Z}) \leq 1$. For bosons, however, the corresponding expression $\mathcal{Z}/(1-\mathcal{Z})$ diverges; the continuum limit completely ignores the condensed fraction, whose contribution to the thermodynamics must be accounted for separately [13].

Local density approximation An alternate conceptual approach to the calculation of inhomogeneous distributions is the local density approximation. We start with the expression for the density of a *uniform* Fermi gas $n_{\text{uniform}} = \Lambda_T^{-3} f_{3/2}(\mathcal{Z})$ [13] and assume that local properties can be described by a local chemical potential $\mu - U(\mathbf{r})$ and hence a local fugacity $\mathcal{Z}e^{-\beta U(\mathbf{r})}$. We immediately recover Eq. 2.38, and obtain its zero-temperature using Eq. 2.33

$$n_{\text{uniform}} \xrightarrow{T=0} \frac{1}{6\pi^2}\left[\frac{2M}{\hbar^2}E_F\right]^{3/2}. \tag{2.39}$$

This implies that long-range properties of the Fermi gas may be ignored, unlike in a BEC, which exhibits long-range phase coherence. In fact, the local density approximation and the semi-classical approach generally yield identical results for non-interacting fermions [51].

Specializing to the case of a three-dimensional harmonic oscillator potential (see Eq. 2.2), we obtain

$$n(\mathbf{r}) = \Lambda_T^{-3} f_{3/2}\left(\mathcal{Z}\exp\left[-\frac{\beta M}{2}(\omega_x^2x^2 + \omega_y^2y^2 + \omega_z^2z^2)\right]\right). \tag{2.40}$$

At zero temperature,

$$n(\mathbf{r}) = \frac{8N}{\pi^2\overline{R}_{TF}^3}\left[1 - \frac{x^2}{X_{TF}^2} - \frac{y^2}{Y_{TF}^2} - \frac{z^2}{Z_{TF}^2}\right]^{3/2}\Theta\left(1 - \frac{x^2}{X_{TF}^2} - \frac{y^2}{Y_{TF}^2} - \frac{z^2}{Z_{TF}^2}\right) \tag{2.41}$$

where $\overline{R}_{TF} = \sqrt{2E_F/M\overline{\omega}^2}$ is the mean Thomas-Fermi radius of the cloud, $X_{TF} = \sqrt{2E_F/M\omega_x^2}$

etc. are the Thomas-Fermi lengths along each trapping axis, and $\Theta(\cdots)$ is the Heaviside step function.

The momentum distribution can also be calculated using either the local density or semi-classical approach. Experimentally, we observe the momentum distribution in a time-of-flight density image, for which the distribution is obtained by rescaling all spatial coordinates $x_i \to x_i/\sqrt{1+\omega_i^2 t^2}$ in Eq. 2.40 along the direction $i \in \{x, y, z\}$, and renormalizing to conserve particle number [57].

2.2.3 Crossover to Fermi degeneracy

The $T = 0$ filled Fermi sea is quantum degenerate in the sense that it represents the absolute many-particle ground state of this non-interacting system. The meaning of the term "degenerate" here should not be confused with its more conventional meaning for a gas of bosons, for which degeneracy implies multiple or macroscopic occupation of the single-particle ground state. Multiple occupancy is forbidden for fermions.

What, then, is the nature of the transition to quantum degeneracy in fermions? In contrast to the boson case, there is no phase transition into or out of the filled Fermi sea. As is the case with bosons, however, high-temperature expansions for thermodynamic quantities fail around $\mathcal{Z} = 1$. At lower temperatures the behaviour differs dramatically from the predictions of classical, Boltzmann statistics. As $T \to 0$, $\mathcal{Z} \to 1^-$ for ideal bosons, whereas $\mathcal{Z} \to \infty$ for ideal fermions with the scaling $\mathcal{Z} \approx e^{\beta E_F}$, as implied by Eq. 2.36. It is interesting to note the quantitative relationship between fugacity and degeneracy for fermions:

$$n_0 \Lambda_T^3 = f_{3/2}(\mathcal{Z}), \tag{2.42}$$

where $n_0 \equiv n(0)$ is the central density of the cloud. Thus $n_0\Lambda_T^3 \simeq 0.77$ when $\mathcal{Z} = 1$ for fermions, which occurs at $T \simeq 0.57 T_F$. By comparison, $n_0\Lambda_T^3 \simeq 2.61$ when $\mathcal{Z} \approx 1$ for bosons, at $T = T_c$. (In the thermodynamic limit, $\mathcal{Z} = 1$ at $T = T_c^0$ [61].)

The lack of a marked phase transition raises the question of what an experimental signature of Fermi degeneracy might be. Unlike a BEC, the non-interacting DFG has an isotropic momentum distribution in time-of-flight, even when released from an anisotropic trap [59]. Thus the aspect ratio of the cold cloud cannot be a signature of degeneracy. Instead, observations of Fermi degeneracy rely on two signatures: the average energy per particle, and the shape of the time-of-flight density distribution.

Using Eq. 2.32 we may write the average energy per particle as

$$\frac{E}{N} = 3 k_B T \frac{f_4(\mathcal{Z})}{f_3(\mathcal{Z})}. \tag{2.43}$$

The finite zero-temperature limit of Eq. 2.43 is $3E_F/4$, corresponding to the Fermi pressure [13]. By comparison, the corresponding expression for the Boltzmann gas is $E/N = 3k_BT$, which tends toward zero at zero temperature.

The second signature of Fermi degeneracy is evident when the observed fermion time-of-flight distribution is compared to the predictions of the Boltzmann and Fermi-Dirac models. The latter is obtained by integration of Eq. 2.40 along the imaging line of sight.[4]

Taking x as the imaging direction we obtain the column density distribution of the expanding gas

$$\tilde{n}(y,z,t) = \frac{N}{2\pi\, r_y(t)\, r_z(t)\, f_3(\mathcal{Z})} f_2\left(\mathcal{Z}\, \exp\left[-\frac{y^2}{2r_y^2(t)} - \frac{z^2}{2r_z^2(t)}\right]\right), \tag{2.44}$$

where $r_i^2(t) = k_B T(1+\omega_i^2 t^2)/M\omega_i^2$ is the cloud size in the $i \in \{x,y,z\}$ direction after a time t of free expansion. By comparison, the column density distribution for an expanding cloud of classical particles is

$$\tilde{n}_{\rm cl}(y,z,t) = \frac{N}{2\pi\, r_y(t)\, r_z(t)} \exp\left[-\frac{y^2}{2r_y^2(t)} - \frac{z^2}{2r_z^2(t)}\right], \tag{2.45}$$

using the same definitions for $r_i(t)$.

2.3 A Bose-Einstein condensate in a double-well potential

The behaviour of a BEC confined in a double-well potential is analogous to a Josephson junction of two superconductors separated by an insulating barrier. For low temperatures and low-energy excitations, the bosonic Josephson junction (BJJ) can be described by a model which considers only the two lowest BEC eigenstates of the double well. The atoms in the two modes are coupled between wells by tunnelling, and to each other by repulsive atom-atom interactions. In a basis of Fock states of well-defined atom numbers N_L and N_R in the left and right wells, the BJJ behaviour can be fully characterized by the mean value and fluctuations of the relative atom number and relative phase ϕ between the two wells. In our experiments we probe the relative atom number N_r with direct measurements of N_R and N_L after short times-of-flight, and ϕ via matter wave interference patterns formed after long times-of-flight.

Many theoretical efforts have been devoted to exploring the interplay of relative number and relative phase in split BEC systems [62, 63, 64, 65, 66, 37, 67, 68, 69, 70, 71, 72, 73, 38, 74]. Several double well BEC experiments in recent years have also reported observations well described by BJJ theory [75, 76, 77, 78]. In this section, we review the BJJ description of a BEC in a double-well potential within a two-mode approximation. The discussion is meant to introduce the roles of mean value and fluctuations in N_r and ϕ within the two-mode BJJ model, which motivate the N_r and ϕ measurement apparatus and techniques described Ch. 7. We refer the reader to [42] and references therein for a thorough and up-to-date review of the subject.

[4] When integrating Fermi functions over Gaussian degrees of freedom, it is useful to note that $\int_{-\infty}^{\infty} dx\, f_n(Ce^{-x^2}) = \sqrt{\pi} f_{n+1/2}(C)$.

2.3.1 Two-mode model of the double well

We imagine a BEC trapped in a symmetric double-well potential formed by erecting a central potential barrier in an initial harmonic potential. In the case of a large potential barrier height, the symmetric ground state ψ_s and antisymmetric first excited state ψ_a are nearly degenerate, and are well separated from the higher energy states. This is true when the barrier height exceeds the chemical potentials of these two modes, denoted by μ_a and μ_s. The wavefunctions $\psi_{s,a}(\mathbf{r})$ and chemical potentials $\mu_{s,a}$ can be determined by solving the time-dependent Gross-Pitaevskii equation. The two-mode approximation consists of ignoring all higher energy modes, and writing the many-body bosonic field operator as

$$\hat{\Psi} = \psi_s \hat{a}_s + \psi_a \hat{a}_a \tag{2.46}$$

where $\hat{a}_s^\dagger$ and $\hat{a}_a^\dagger$ ($\hat{a}_s$ and $\hat{a}_a$) are the single-particle creation (annihilation) operators for the symmetric and antisymmetric states [76]. For a large barrier we can imagine each atom lying predominantly (but not exclusively) in one of the "left" or "right" wells. The left and right well modes can be constructed using superpositions of the symmetric and antisymmetric wavefunctions and creation/annihilation operators [42]

$$\phi_L = \frac{1}{\sqrt{2}}(\psi_s + \psi_a) \quad \text{and} \quad \phi_R = \frac{1}{\sqrt{2}}(\psi_s - \psi_a), \tag{2.47}$$

$$\hat{a}_L = \frac{1}{\sqrt{2}}(\hat{a}_s + \hat{a}_a) \quad \text{and} \quad \hat{a}_R = \frac{1}{\sqrt{2}}(\hat{a}_s - \hat{a}_a), \tag{2.48}$$

in terms of which

$$\hat{\Psi} = \psi_L \hat{a}_L + \psi_R \hat{a}_R. \tag{2.49}$$

The two-mode Hamiltonian for this system [62] is obtained by inserting Eq. 2.47 into the Hamiltonian describing N weakly interacting bosons with s-wave contact interactions confined to an external potential (see [65]). The result is [42]

$$\hat{H}_{2\mathrm{M}} = \frac{E_c}{2}\hat{n}^2 - E_j\hat{\alpha} \tag{2.50}$$

where

$$\hat{n} = \frac{\hat{a}_R^\dagger \hat{a}_R^\dagger - \hat{a}_L^\dagger \hat{a}_L^\dagger}{2} \tag{2.51}$$

is half the relative atom number $(N_R - N_L)/2 \equiv N_r/2$, and

$$\hat{\alpha} = \frac{\hat{a}_R^\dagger \hat{a}_L + \hat{a}_L^\dagger \hat{a}_R}{N} = \frac{\hat{a}_s^\dagger \hat{a}_s - \hat{a}_a^\dagger \hat{a}_a}{N} \tag{2.52}$$

is the tunnelling operator and is related to the relative phase of the two condensates. Eq. 2.50 is

known as the "canonical Josephson Hamiltonian" [48, 62]. The term proportional to E_j describes tunnelling of atoms between the two wells. E_j is known as the "Josephson coupling energy" and depends linearly on the chemical potential difference as $N(\mu_a - \mu_s)$ where N is the total atom number, as well as the wavefunction overlap between ψ_L and ψ_R. As the barrier height becomes infinite E_j vanishes since μ_s and μ_a become equal, and the wavefunction overlap vanishes. The term proportional to E_c corresponds to intra-well atom-atom interactions. E_c is known as the "on-site energy" or "charging energy" and is proportional to the intra-well "left-left" and "right-right" wavefunction overlap, as well as the inter-well "left-right" wavefunction overlap [42]. Eq. 2.50 ignores two-particle tunnelling effects ("correlated hopping"), which in any case vanish in the high-barrier limit [62, 48].

The two-mode model has been discussed extensively in the literature [62, 63, 65, 66, 67, 71, 72, 73, 74, 79]. It should be fairly realistic in the large barrier case described so far, but is known to have limited validity (a) in the case of low barrier, when the symmetric-antisymmetric energy separation becomes comparable to the energy gap between ϕ_a and the next highest excited state, and (b) for strong atom-atom interactions [63, 73].

2.3.2 Simplified mean-field Hamiltonian

Eq. 2.50 can be rewritten in terms of classical fields satisfying the time-dependent GPE using substitutions of the form $\hat{a}_L \rightarrow \sqrt{N_L(t)}e^{i\phi_L(t)}$ etc. in Eqs. 2.50, 2.51 and 2.52 [42, 62]. This results in a mean-field description of the BJJ Hamiltonian [42]

$$H = \frac{E_c}{2}n^2 - E_j\sqrt{1 - \frac{4n^2}{N^2}}\cos\phi \tag{2.53}$$

where

$$\hat{n} = \frac{N_R - N_L}{2} \equiv \frac{N_r}{2} \quad \text{and} \quad \phi = \phi_R - \phi_L \tag{2.54}$$

are the relative atom number (occupation) and relative phase between the left and right well wavefunctions.

Observables: relative number and relative phase Eq. 2.53 is a mean-field description of a quantum system whose character depends on the ratio E_c/E_j. The mean values $\langle n\rangle$ and $\langle\phi\rangle$ and their rms fluctuations Δn and $\Delta\phi$ can be probed experimentally over many realizations of the experiment, i.e. successive preparations and measurements of the BEC trapped in the external double-well potential. In a single realization of the experiment the relative atom number can be deduced by measuring and subtracting the left and right well populations. Atom numbers can be measured in-situ, as in [43], or after turning off the double-well potential and allowing a short free expansion time, as we do in our experiments (see Ch. 7).

The single-shot relative phase can be deduced by allowing an expansion time long enough that the expanding BECs overlap and interfere. The resulting matter wave interference pattern

is a measure of the in-trap momentum distribution

$$n(\mathbf{p}) = G(\mathbf{p})\left[1 + \cos(pd/\hbar + \phi)\right] \tag{2.55}$$

where d is the initial double well separation along the x direction, ϕ is the relative phase, and $G(\mathbf{p})$ is a Gaussian envelope function. After long times-of-flight t the mean interference pattern, averaged over many experimental realizations, is [74, 76]

$$\langle n(\mathbf{r})\rangle = G(\mathbf{r})\left[1 + \alpha\cos(mdx/\hbar t)\right] = G(\mathbf{r})\left[1 + \frac{N_s - N_a}{N}\cos(mdx/\hbar t)\right] \tag{2.56}$$

where

$$\alpha = \langle\cos\phi\rangle = \langle\hat{\alpha}\rangle = \frac{\langle N_s - N_a\rangle}{N} \tag{2.57}$$

is the visibility of the mean interference pattern. α is also known as the coherence factor [74] since it provides the degree of first order coherence in the system [80, 76]. Eq. 2.57 shows that, in the two-mode model, α is given by the mean atom number difference of the symmetric and antisymmetric modes [76]. $\alpha = 1$ corresponds to prefect coherence and a fixed relative phase $\phi = 0$ in each experimental realization; $\alpha = 0$ corresponds to completely random phases. It is important to note that the fringe visibility in any single interference pattern (single experimental realization) is expected to be very high, **even if the initial state is not coherent**.[5] This point is of key importance in interpreting BEC interference experiments, and has been widely discussed in the literature; see for instance [36, 48, 37] and references therein. The spatial fringe spacing is $\Delta x = ht/md$, if we assume that atom-atom interactions do not significantly alter the velocity distribution during expansion [46, 47].

2.3.3 Number and phase fluctuations at zero temperature

The BJJ Hamiltonian in Eq. 2.53 corresponds to motion of a particle in a one-dimensional sinusoidal potential. The relative atom number n plays the role of the momentum p, and the relative phase $\phi \in [-\pi, \pi]$ plays the role of position x [42]. E_j defines the height of the sinusoidal potential, and $1/E_c$ is the particle mass. At low energies, the quantum mechanical level spacing is approximately given by

$$\hbar\omega_p = \sqrt{E_j\left(E_c + \frac{4E_j}{N^2}\right)}; \tag{2.58}$$

[5] For instance, two independently prepared BECs which have never "seen" one another will nevertheless interfere with high contrast, but with a completely unpredictable relative phase [36, 38].

ω_p is known as the "plasma frequency" or "Josephson frequency" [48, 76]. Expanding Eq. 2.53 up to second order in n and ϕ gives

$$H = \left(E_c + \frac{4E_j}{N^2}\right)\frac{n^2}{2} + \frac{E_j}{2}\phi^2. \tag{2.59}$$

This system exhibits quantum mechanical fluctuations

$$\Delta p^2 \leftrightarrow \Delta n^2 = \frac{1}{2}\sqrt{\frac{E_j}{E_c + 4E_j/N^2}} \quad \text{and} \quad \Delta x^2 \leftrightarrow \Delta\phi^2 = \frac{1}{2}\sqrt{\frac{E_c + 4E_j/N^2}{E_j}} \tag{2.60}$$

at zero temperature, which satisfy the uncertainty relation

$$\Delta n^2\, \Delta\phi^2 \geq \frac{1}{4}, \quad \text{or} \quad \Delta N_r^2\, \Delta\phi^2 \geq 1. \tag{2.61}$$

The tunnelling strength is parametrized by E_c/E_j, and defines three dynamical regimes of the BJJ: the "Rabi", "Josephson" and "Fock" regimes [48]. The "Rabi" regime $E_c/E_j \ll N^{-2}$ is the non-interacting limit. The state is dominated by tunnelling and is delocalized between the two wells. The system approaches the ideal "phase state" or "coherent state" [37], with Poissonian relative atom number fluctuations, vanishing phase fluctuations $\Delta\phi \to 0$, a well-defined relative phase and maximal coherence [42]. The "Josephson" regime is a strong-tunnelling regime defined by $N^{-2} \ll E_c/E_j \ll 1$. The system exhibits small oscillations in time about the equilibrium values $n = 0$, $\phi = 0$ at the plasma frequency $\omega_p = \sqrt{E_c E_j}/\hbar$, described by the simplified Hamiltonian

$$H \approx \frac{E_c}{2}n^2 + \frac{E_j}{2}\phi^2. \tag{2.62}$$

The state is delocalized between the two wells, and the relative phase fluctuations $\Delta\phi^2 = \sqrt{E_c/E_j}/2 \ll 1$ are small [74, 42]. In the "Fock" regime $E_c/E_j \gg 1$; interactions dominate and tunnelling is negligible. The system corresponds essentially to two independent condensates with well-defined atom numbers and vanishing relative number fluctuations $\Delta n^2 = \sqrt{E_j/E_c} \to 0$. Coherence vanishes and ϕ becomes random and unpredictable [36].

In addition to the requirements for the Josephson regime stated above, Stringari and Pitaevskii [74] point out that the two-mode model assumes a decoupling of the BJJ dynamics from the other modes of the BEC. This assumption should be valid if the plasma frequency is much smaller than the harmonic oscillation frequencies of the BEC in the external potential: $\omega_p \ll \omega_{x,y,z}$.

Attaining the Josephson and Fock regimes in experiments In the two-mode approximation, the "charging energy" E_c and the chemical potential $\mu_{s,a}$ remain approximately constant over a wide range of barrier heights $V_0 \ll \mu_{s,a}$ to $V_0 \gg \mu_{s,a}$ [79]. We confirm this for our experimental parameters by numerically solving the GPE. Our experimental control parameter is the "Josephson coupling energy" E_j, which can be varied by changing the barrier height and well separation. In experimental configurations which produce visible matter wave interference patterns (V_0 close

to $\mu_{s,a}$), numerical solutions of the GPE yield parameters on the order of $E_c/h < 1$ Hz, $E_j/h \sim 1$ to 5 kHz and $\omega_p/2\pi \sim 1$ to 2 Hz for $N \sim 10^4$ ^{87}Rb atoms, $\mu/h \sim 1$ kHz and $V_0/h \sim 1$ to 3 kHz. With $Ec/E_j \sim 10^{-3}$ and $N = 10^4$, we expect to be well beyond the Rabi regime and well into the Josephson regime. Because V_0 can be made made arbitrarily high with our radio-frequency splitting technique, we also expect to be able to access the Fock regime with large barriers $V_0 \gg \mu$ and well separations of tens or hundreds of micrometres (see Ch. 7).

According to [48], the Rabi regime is never attainable with conventional superfluids (e.g. ^{4}He), and very unlikely in atomic gases. A simple scaling argument supports this claim in our experiment. One might imagine reducing the repulsive ^{87}Rb interactions, and hence E_c, using a Feshbach resonance. We rule this out in our experiments since we confine atoms to chip-based micromagnetic traps having magnetic field minima on the order of 1 G, far too small to access any ^{87}Rb Feshbach resonances. A second option is to reduce N, thereby reducing E_c. In the Thomas-Fermi approximation ($\mu \propto N^{2/5}$), assuming the N atoms to be divided equally between the two wells, $E_c = 2(\mathrm{d}\mu_{L,R}/\mathrm{d}N_{L,R}) = 8\mu/5N$ where $\mu \approx \mu_{L,R} \approx \mu_{a,s}$ is the chemical potential [74]. Thus $E_c \propto N^{-3/5}$. E_j is proportional to $N(\mu_s - \mu_a)$ [42], so $E_j \propto N^{7/5}$ in the Thomas-Fermi approximation. Thus E_c/E_j varies as N^{-2} as N is reduced. But since our goal for accessing the Rabi regime is $E_c/E_j \ll N^{-2}$, the right hand side of which also varies as N^{-2} (exactly), it would be difficult to reach the Rabi regime in our setup.

2.3.4 Number and phase fluctuations at finite temperature

In addition to zero-temperature quantum fluctuations, thermal fluctuations are present in any experimental implementation of the BJJ. Thermal fluctuations at finite temperatures might arise, for example, from interactions between the BEC and the thermal cloud of non-condensed atoms. Thermal fluctuations of Δn^2_{th} and $\Delta\phi^2_{\mathrm{th}}$ are expected to be larger than quantum fluctuations [74].

For small phase fluctuations $\Delta\phi \ll \pi$ we can estimate the randomizing effects of temperature on the relative number and relative phase by assigning an energy $k_BT/2$ to each degree of freedom in the harmonic oscillator BJJ Hamiltonian of Eq. 2.59 [74]. This leads to [42]

$$\Delta n^2_{\mathrm{th}} = \frac{k_BT}{E_C + 4E_j/N^2} \quad \text{and} \quad \Delta\phi^2_{\mathrm{th}} = \frac{k_BT}{E_j}. \tag{2.63}$$

This assumes that the BJJ interaction with the thermal environment is via energy transfer only, and ignores the effects of particle exchange and other dynamics between the condensate and thermal cloud. This estimate lead to a thermal version of the number-phase uncertainty relation [42]

$$\Delta n^2_{\mathrm{th}}\Delta\phi^2_{\mathrm{th}} \geq \left(\frac{k_BT}{\hbar\omega_p}\right)^2. \tag{2.64}$$

A more careful analysis of thermal fluctuations is presented in [74], in which the thermal average of the coherence factor is calculated as a function of E_j and T. Their work points out that the thermal decoherence of ϕ becomes important for $k_BT \sim E_j$. Thermal fluctuations in the BJJ have

been studied experimentally and shown to be useful as a direct measurement of the temperature of the system [78, 76, 81]. We use Eq. 2.63 to estimate the role of thermal fluctuations on the measured phase fluctuations in our splitting experiment (see Ch. 7).

You have an unusually magnetic personality.

Wing's fortune cookie

3

Characterization of atom chip magnetic microtraps

Atom chip magnetic microtraps are small-volume magnetic traps formed using magnetic fields generated by wires on a planar substrate known as an "atom chip". This chapter focuses on the characterization of the magnetic atom chip potentials used for confining $^{87}\mathrm{Rb}$ and $^{40}\mathrm{K}$ in this thesis. The chapter begins with a review of magnetic trapping of neutral atoms. These ideas are then applied to archetypal wire-based atom chip traps: the single-wire "atom-guide" quadrupole trap, and the Z-wire Ioffe-Pritchard-type harmonic trap [16, 17]. Focusing on the Z-trap, we present three simple models of current flow in the Z-wire, and compare the analytic calculations of the total Z-trap magnetic field from each of these models. The most realistic model is based on current flow in three wire segments of finite length and width, which together approximate the Z-wire. The chapter closes with notes on the calibration of analytic Z-trap magnetic field calculations using experimental Z-trap parameters such as the magnetic field minimum and the harmonic oscillation frequencies, which are measured using ultracold $^{87}\mathrm{Rb}$.

3.1 Magnetic trapping of neutral atoms

Magnetic trapping of neutral atoms is based on the Zeeman effect – the interaction of an atom's magnetic dipole moment $\boldsymbol{\mu}$ with a static magnetic vector field $\mathbf{B}$. The interaction Hamiltonian for a neutral atom with magnetic moment $\boldsymbol{\mu}$ in a magnetic field $\mathbf{B}$ is [82]

$$\mathrm{H_{int}} = -\boldsymbol{\mu} \cdot \mathbf{B}. \tag{3.1}$$

The magnetic moment of a neutral atom in an internal state with total angular momentum $\mathbf{F}$ is

$$\boldsymbol{\mu} = -\frac{g_F \mu_B}{\hbar}\mathbf{F}, \tag{3.2}$$

where μ_B is the Bohr magneton, g_F is the Landé factor, and $\hbar = h/2\pi$ where h is Planck's constant [82]. Using Eq. 3.2, we can evaluate the dot product in Eq. 3.1 to obtain

$$\mathrm{H_{int}} = \frac{g_F \mu_B}{\hbar} B\mathrm{F}, \tag{3.3}$$

where $B \equiv |\mathbf{B}|$ is the magnetic field amplitude, and F is the component of the $\mathbf{F}$ vector operator along the quantization axis defined by the direction of $\mathbf{B}$. The spin angular momentum states $|F, m_F\rangle$ are eigenvalues of F with eigenvalues $\hbar m_F$:

$$\mathrm{F}|F, m_F\rangle = \hbar m_F |F, m_F\rangle, \tag{3.4}$$

where $m_F \in \{-F, -F+1, \ldots, F\}$ as usual [82]. Using Eq. 3.4 and 3.3, we can easily calculate the potential energy of an atom in the atomic spin state $|F, m_F\rangle$ in the presence of a static magnetic field:

$$U = \langle F, m_F|\mathrm{H_{int}}|F, m_F\rangle = m_F g_F \mu_B B, \tag{3.5}$$

or, more generally

$$U(\mathbf{r}) = m_F g_F \mu_B B(\mathbf{r}) \tag{3.6}$$

for a spatially varying static magnetic field $\mathbf{B}(\mathbf{r})$.

Trappable spin states The magnetic potential of Eq. 3.6 must have a three-dimensional minimum to allow magnetic confinement. Since $B(\mathbf{r})$ and μ_B are positive quantities, it follows that $g_F m_F > 0$ and the existence of a magnetic field minimum are requirements for magnetic trapping.[1] The sign of $g_F m_F$ depends on the particular hyperfine state occupied by the atom. In particular, g_F is a function of the atomic angular momentum quantum numbers F, J, I, L and S [82]:

$$g_F = \left[1 + \frac{J(J+1) + S(S+1) - L(L+1)}{2J(J+1)}\right]\left[\frac{F(F+1) + J(J+1) - I(I+1)}{2F(F+1)}\right]. \tag{3.7}$$

S, L and I are the electron spin angular momentum, orbital angular momentum and nuclear spin angular momentum quantum numbers respectively. $g_F = 1/2$ for $^{87}\mathrm{Rb}$ in $|F = 2, m_F = 2\rangle$, and $g_F = 2/9$ for $^{40}\mathrm{K}$ in $|F = 9/2, m_F = 9/2\rangle$.

Those states having $g_F m_F > 0$ are referred to as *weak-field seekers* and are magnetically trappable in static traps. On the other hand, atomic states having $g_F m_F < 0$ are termed *strong-field seekers* and are repelled from magnetic field minima. An efficient magnetic trap therefore relies on the atoms being in trappable weak-field-seeking states.

Finally, we note that $m_F = 0$ states may be magnetically trapped owing the quadratic Zeeman effect [84]. An expression for the magnetic potential due to the linear and quadratic Zeeman effects is expressed by the Breit-Rabi formula [85]. We have only considered the linear Zeeman effect in this section, since stretched states $|F, F\rangle$ were used in the work of this thesis, and since the quadratic Zeeman effect is absent for "pure spin states" $|F, \pm F\rangle$ [84].

[1] The existence of free-space magnetic field maxima are ruled out by Maxwell's equations and Wing's theorem [83].

Adiabatic following Classically, the response of an atomic spin $\boldsymbol{\mu}$ to an applied magnetic field $\mathbf{B}$ is to precess about the local direction of the magnetic field at the Larmor precession frequency ω_L where

$$\hbar\omega_L = m_F g_F \mu_B B. \tag{3.8}$$

To remain trapped in a weak-field-seeking state, the atomic spin must be able to adiabatically follow the local direction of $\mathbf{B}$. In magnetic trap, this requires that the rate of change of the magnetic field's direction θ (in the reference frame of the moving atom) be much slower than the precession frequency [14]

$$\frac{\mathrm{d}\theta}{\mathrm{d}t} \ll \omega_L. \tag{3.9}$$

This inequality shows that magnetic traps are susceptible to "Majorana loss" via transitions to untrapped spin states whenever B is small enough or $\mathrm{d}\mathbf{B}/\mathrm{d}t$ is large enough that Eq. 3.9 is violated [86, 87].

3.2 Static magnetic waveguides and the "Z-trap"

Static magnetic microtraps use currents in atom chip conductors to produce confining magnetic field minima for neutral atoms. There are several popular chip trap geometries in use in the cold atoms community, their differences being mainly in conductor arrangements and layout, and in the resulting magnetic potential shapes and characteristics. Some microtraps, including the linear "U-trap" [88] and quadratic "Z-trap" [14], combine chip wire fields with external uniform bias fields, typically using auxiliary magnetic field coils. Others, including ring traps and three-wire traps [28], and parallel-wire guides [89] use chip wire fields *alone* to generate three-dimensional trapping or lower-dimensional "atom-guiding" potentials.

Although we have dabbled briefly with U-traps and three-wire traps, the work in this thesis was carried out exclusively with a Z-trap as the central atom chip trapping element. First used to create a BEC on an atom chip in 2001 [17, 16], the Z-trap combines the static magnetic field generated by DC current flowing in a "Z"-shaped atom chip wire with a uniform external magnetic field to create a non-zero magnetic minimum at some finite distance from the atom chip surface. In the vicinity of the minimum the total magnetic field grows quadratically with distance, creating to very good approximation a harmonic trap near the trap centre [14, 15]. This section is devoted to a brief theoretical review of the Z-trap, including the basis of its formation, analytic approximations of the total magnetic trapping field, and descriptions of the Z-trap's anisotropy and position as functions of the Z-wire current and the external magnetic bias field amplitudes.

3.2.1 First step: a magnetic waveguide

The formation of the Z-trap's magnetic minimum is best understood by first considering a simplified system: a single, infinitesimally thin and long wire segment bearing DC current I_z, and a

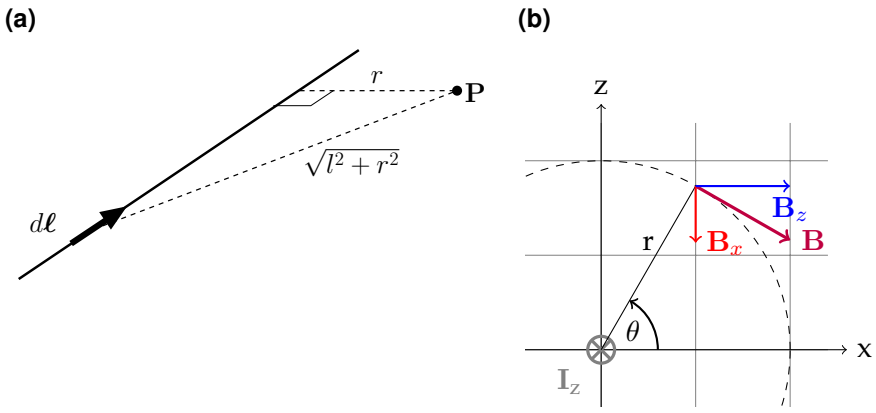

Fig. 3.1: (a): Magnetic field at point $\mathbf{P}$ due to an infinitely long and thin wire segment may be calculated using the Biot-Savart formula. **(b)**: xz plane B-field components generated by current I_z flowing along $+y$ in the wire.

second externally applied uniform magnetic bias field $\mathbf{B}_{\text{bias}} = -B_{\text{bias}}\mathbf{x}$ in a direction perpendicular to the wire.

The magnetic field of the wire alone is calculated using the Biot-Savart formula

$$\mathrm{d}\mathbf{B} = \frac{\mu_0}{4\pi} I_z \frac{\mathrm{d}\boldsymbol{\ell} \times \mathbf{r}}{|\mathbf{r}|^3}, \tag{3.10}$$

which specifies the differential flux density ("differential magnetic field") $\mathrm{d}\mathbf{B}$ arising at the observation point $\mathbf{P}$ from a constant current I_z flowing in the length element $\mathrm{d}\boldsymbol{\ell}$ (and in the direction of $\mathrm{d}\boldsymbol{\ell}$) [90, Ch.6]. The observation point is connected to the length element $\mathrm{d}\boldsymbol{\ell}$ by the vector $\mathbf{r}$, as shown in Fig. 3.1a.

For a straight wire the magnetic field direction follows the right hand rule, circulating symmetrically around the wire all along its length, and perpendicular to the direction of current flow everywhere. The total magnetic field magnitude at some distance r from the wire is calculated by integrating Eq. 3.10 over a coordinate $l \in (-\infty, \infty)$, which defines the position of an element $\mathrm{d}\boldsymbol{\ell}$ on the wire, and noting that the distance from the observation point P to the wire position l is $\sqrt{r^2+l^2}$. The magnitude of the total field as a function of the perpendicular wire-to-observation-point distance r is then

$$B(r) = |\mathbf{B}| = \frac{\mu_0}{4\pi} I_z \int_{-\infty}^{\infty} dl \frac{r}{(r^2+l^2)^{3/2}} = \frac{\mu_0 I_z}{2\pi r}. \tag{3.11}$$

Using this expression for the magnetic field magnitude in the plane perpendicular to $\mathrm{d}\boldsymbol{\ell}$, and knowing the field direction in this plane, we can construct a vector expression for the magnetic field generated by current I in the wire. The in-plane field components are shown in Fig. 3.1b, in

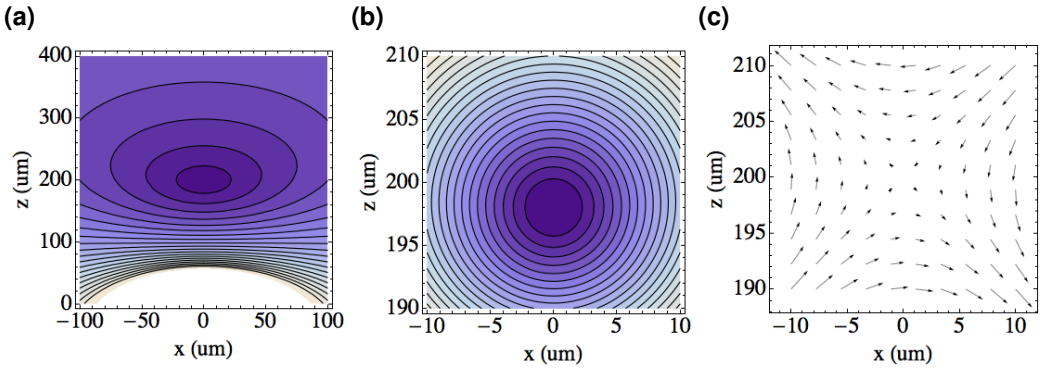

Fig. 3.2: Quadrupole magnetic field in the xz plane produced by $I = 2$ A in an infinitely long and thin wire, plus an external field $\mathbf{B}_{\text{bias}}$ = -20 G $\mathbf{x}$. **(a,b)**: Contour plots of B_{quad}; darker shades indicate smaller field amplitude. **(c)**: Vector field plot of $\mathbf{B}_{\text{quad}}$ (see Eq. 3.14) near the trap centre located at z_0 = 200 µm.

which the wire is defined to lie along the y axis, bearing current in the $+\mathbf{y}$ direction:

$$\mathbf{B}_{\text{wire}}(r,\theta) = \frac{\mu_0 I_{\text{z}}}{2\pi r}(\sin\theta\mathbf{x} - \cos\theta\mathbf{z}) \tag{3.12}$$

$$\mathbf{B}_{\text{wire}}(x,z) = \frac{\mu_0 I_{\text{z}}}{2\pi(x^2+z^2)}(z\mathbf{x} - x\mathbf{z}) \tag{3.13}$$

in polar and Cartesian coordinates. Note that the y-component of the field is zero everywhere along the length of this infinitesimally thin, infinitely long wire.

Adding a bias field $\mathbf{B}_{\text{bias}} = -B_{\text{bias}}\mathbf{x}$ creates the magnetic minimum at $(x = 0, z = z_0)$. The expression for the full quadrupole magnetic field

$$\mathbf{B}_{\text{quad}}(x,y,z) = \mathbf{B}_{\text{wire}} + \mathbf{B}_{\text{bias}} = \left[\frac{\mu_0 I_{\text{z}}}{2\pi}\frac{z}{x^2+z^2} - B_{\text{bias}}\right]\mathbf{x} - \left[\frac{\mu_0 I_{\text{z}}}{2\pi}\frac{x}{x^2+z^2}\right]\mathbf{z} \tag{3.14}$$

Eq. 3.14 describes a quadrupole field pattern in which the magnitude of the total field vanishes along the line $(x = 0, y, z = z_0)$, along which $\mathbf{B}_{\text{wire}}$ and $\mathbf{B}_{\text{bias}}$ exactly cancel. The magnitude of the total field increases linearly in all directions in the xz plane from the trap centre point $(x = 0, z = z_0)$. The distance from the wire to the trap centre is easily determined by setting the quadrupole magnetic field of Eq. 3.14 to zero at the trap centre:

$$z_0 = \frac{\mu_0 I_{\text{z}}}{2\pi B_{\text{bias}}}. \tag{3.15}$$

Eq. 3.15 may be rewritten in a convenient form so that B is in units of gauss, I_{z} in amperes, and z_0 in micrometres:

$$B_{\text{bias}}[G] \simeq 2000\frac{I_{\text{z}}[A]}{z_0[\mu\text{m}]}. \tag{3.16}$$

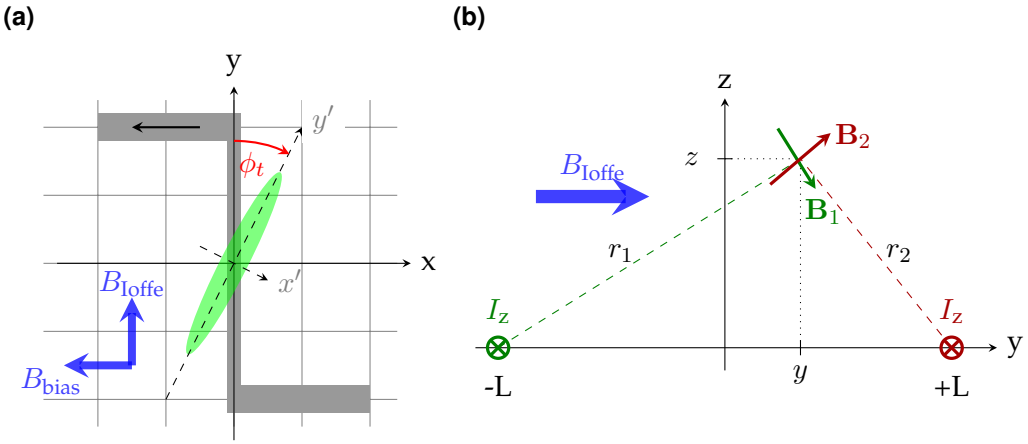

Fig. 3.3: (a): Schematic diagram of the Z-wire (grey), as well as the direction of DC current flow (black arrow) and the two external bias fields (thick arrows). The position of the trapped atom cloud (green ellipse) shows the twist angle ϕ_t, discussed in Sec. 3.3.2. x', y' denote the local directions along which magnetic field curvatures should be computed to accurately calculate estimate the harmonic oscillation frequencies (see Sec. 3.3.2). **(b)**: Magnetic field components in the xz plane due to the "end-cap" segments of the Z-wire, which ensure magnetic confinement along y, and provide the "natural Ioffe" field (see text). The external, applied Ioffe field is also indicated.

3.2.2 Adding longitudinal confinement: a 3-D harmonic trap

It is clear from the lack of y-dependence in Eq. 3.14 that the quadrupole "waveguide" structure does not provide three-dimensional confinement of atoms; the magnetic field is zero everywhere along the line $(x = 0, y, z = z_0)$. Also, a non-zero magnetic potential minimum is necessary to avoid Majorana spin-flip losses at the temperatures required to reach quantum degeneracy [91]. This makes quadrupole magnetic traps inherently unsuitable for BEC and DFG experiments. Longitudinal (y direction) confinement with a finite B-field minimum is provided by adding a spatially-dependent magnetic field along the y direction. In a Z-trap this is achieved using the "end cap" wires which bear current along the $-x$ direction. We can think of this conceptually as a truncation of the infinitely long wire considered in Sec. 3.2.1 to some finite length along y, and the addition of two end cap wire segments parallel to the x axis (see Fig. 3.3). This wire pattern has the shape of the letter "Z", hence "Z-trap" and "Z-wire". The end cap wire segments add the required y-direction field so that, taken together, the total magnetic field due to DC current flowing through the Z-wire plus the external bias field produce a three-dimensional non-zero magnetic minimum.

We can write down expressions for the end-cap wire contribution by considering current flowing wires running along x, bearing current I_z in the $-x$ direction at $y = \pm L$, as shown in Fig. 3.3a. Using the geometric relations $r_1^2 = z^2 + (L + y)^2$ and $r_2^2 = z^2 + (L - y)^2$ from Fig. 3.3b,

the y and z-component contribution of the end-cap wires to the total Z-trap field is

$$B^{y}_{Z,\text{end-cap}}(y,z) = \frac{\mu_0 I_z}{2\pi}\left[\frac{z}{z^2+(L+y)^2} + \frac{z}{z^2+(L-y)^2}\right] \tag{3.17}$$

$$B^{z}_{Z,\text{end-cap}}(y,z) = \frac{\mu_0 I_z}{2\pi}\left[-\frac{L+y}{z^2+(L+y)^2} + \frac{L-y}{z^2+(L-y)^2}\right], \tag{3.18}$$

where we have used the infinitesimally thin, infinitely long wire approximations of the magnetic field.

To summarize this subsection, the magnetic minimum of the Z-trap has three key features:

1. a *non-zero magnetic minimum* at the trap centre $(x=0, y=0, z_0)$
2. a parabolic shape in all three dimensions *in the vicinity of the centre*
3. an ellipsoidal "cigar shape"; the "radial" x and z directions are roughly symmetric, while the "axial" y direction exhibits much weaker confinement (see Fig. 3.3a)

Because of the first two features, the Z-trap is often referred to as a *Ioffe-Pritchard-type* magnetic trap [14] in analogy to the Ioffe-Pritchard magnetic trapping configuration use widely in conventional quantum gas experiments [56].

Adding versatility with an external "Ioffe field" Since the all x and z-components of the Z-trap magnetic field vanish at the trap centre, the value of the y-components dictate the magnitude of the total field at trap centre. Although any DC current in the Z-wire will produce a small non-zero B-field minimum, it is customary to apply an external uniform field to the Z-trap along y. This external "Ioffe field" B_{Ioffe} allows B_0 (and hence the absolute minimum trap energy or "trap bottom") to be tuned arbitrarily, and most importantly, to be controlled *without changing the position of the trap minimum* located at $(0,0,z_0)$. Including the two external uniform fields B_{bias} and B_{Ioffe}, the expressions for the vector field and scalar amplitude of the Z-trap magnetic field may be written

$$\begin{aligned}\mathbf{B}_Z(x,y,z) = &\left[\frac{\mu_0 I_z}{2\pi}\frac{z}{x^2+z^2} - B_{\text{bias}}\right]\mathbf{x} + \left[B^{y}_{Z,\text{end-cap}}(y,z) + B_{\text{Ioffe}}\right]\mathbf{y} \\ &+ \left[B^{z}_{Z,\text{end-cap}}(y,z) - \frac{\mu_0 I_z}{2\pi}\frac{x}{x^2+z^2}\right]\mathbf{z}\end{aligned} \tag{3.19}$$

$$\begin{aligned}B^{xz}_{Z}(x,y,z) \approx &\left[\left(\frac{\mu_0 I_z}{2\pi}\frac{z}{x^2+z^2} - B_{\text{bias}}\right)^2 + \left(B^{y}_{Z,\text{end-cap}}(y,z) + B_{\text{Ioffe}}\right)^2\right. \\ &\left. + \left(B^{z}_{Z,\text{end-cap}}(y,z) - \frac{\mu_0 I_z}{2\pi}\frac{x}{x^2+z^2}\right)^2\right]^{1/2}.\end{aligned} \tag{3.20}$$

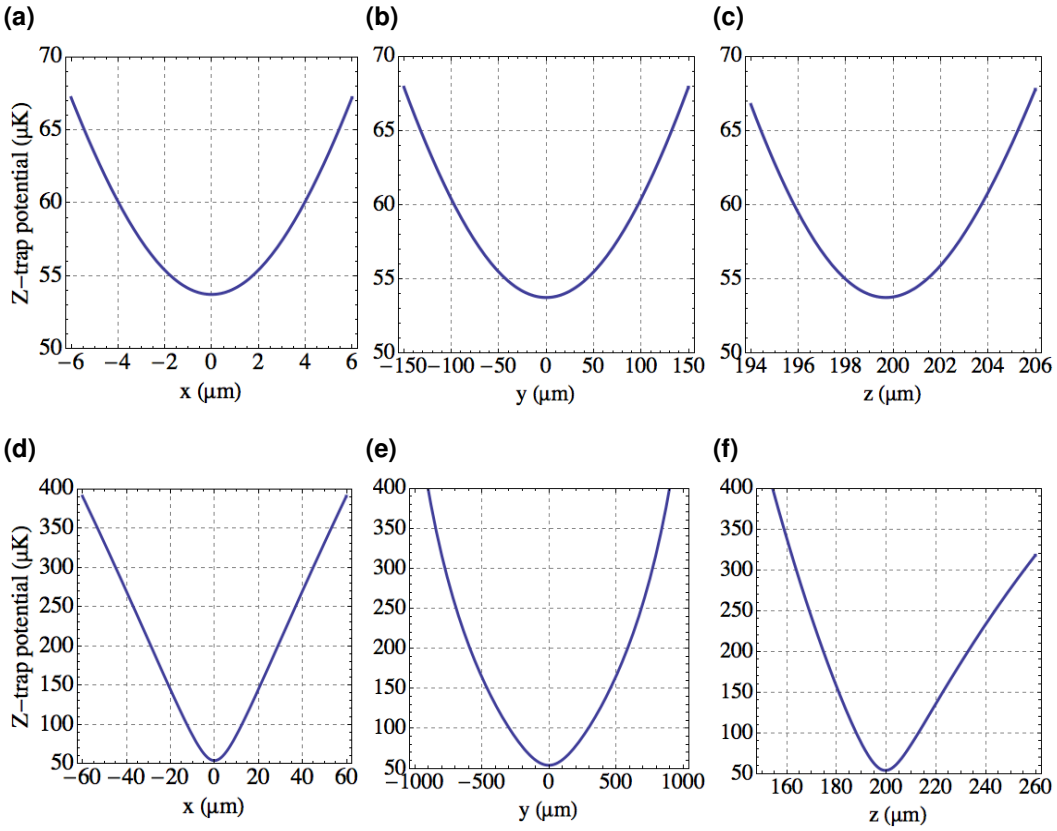

Fig. 3.4: Z-trap magnetic potential sections through the trap minimum $(0, 0, z_0)$, along x, y, z. The vertical axes correspond to $\mu_B B_Z / k_B$ in units of microkelvin, where B_Z is calculated according to the infinitesimally thin, infinitely long wire formula Eq. 3.20. The magnetic potentials are harmonic in all directions near the trap minimum **(a-c)**, but are roughly linear at higher energies along the radial directions x and z, further from the trap centre **(d-f)**. The curves were calculated assuming $I = 2$ A, $B_{\text{Ioffe}} = 0$, and $B_{\text{bias}} = -20$ G along $-x$, which gives $z_0 = 200$ μm.

The z-direction contribution of the end-cap wires vanishes at the trap centre $(x = 0, y = 0, z_0 = 0)$, while the y-direction contribution vanishes as $z_0 \to 0$. In our experiments $B_{\text{Ioffe}} \gg B^y_{Z,\text{end-cap}}(0, z_0)$ typically (see Tab. 3.1).

3.2.3 High-temperature behaviour: trap depth and anharmonicity

Although the Z-trap provides an excellent approximation to a three-dimensional harmonic potential near the trap centre, the potential becomes more linear in character further out, particularly in the transverse x and z directions as shown in Fig. 3.4. As a result the character of the Z-trap potential experienced by trapped atoms depends strongly on the temperature of the atomic ensemble; cold atoms sample the lower-energy part of the potential and experience harmonic confinement, while hot atoms sample the higher-energy, linear portions of the potential along x and z. Note that there are no pseudo-linear sections in the potential along y.

At high temperatures, the Z-trap has the character of a quadrupole trap transversely, combined with a harmonic trap longitudinally. The high-temperature scenario is relevant to the

intermediate stages of our experimental sequence, just prior to the forced RF evaporative cooling step, when atoms are loaded into the Z-trap at temperatures of roughly 300 µK (see Sec. 5.2).

3.3 Analytic models of the Z-trap

This section is devoted to quantitative characterization the Z-traps used in the work of this thesis, with an emphasis on calculations of the trap oscillation frequencies, magnetic potential minima, and distance from the chip surface. Re-characterizing the Z-trap potential after slight parameter changes is time-consuming in the lab, so it is useful to have accurate analytic expressions for the trap for quick estimates of trap parameters, and to guide experimental choices for wire currents and external bias fields. More importantly, accurate models of our potentials have proven invaluable in evaluating new atom chip potentials or trap configurations, diagnosing anomalous behaviours, and understanding nuances and fine detail in static and dynamic magnetic traps relevant to our experiments (see also Ch. 6) on length and energy scales too small to easily probe experimentally.

3.3.1 Beyond idealized long thin wire models

The Z-wire magnetic field expressions of Sec. 3.2, based on infinitesimally thin and infinitely long expressions for wire fields, are clearly only an approximation to the actual field generated by DC current flowing in a real Z-shaped conductor of finite width, length and height. Though they do capture the essential qualitative behaviour of Z-traps, accurate calculations of trap frequencies, distances from the chip surface, and especially harmonic oscillation frequencies require more realistic models.

Three models of the Z-wire field are compared here. The three models suppose the Z-wire to be composed of

1. three infinitesimally thin, infinitely long wires ("**thin-inf.**"),
2. three infinitesimally thin, finite length wire segments, ("**thin-fin.**"), or
3. three finite thickness, finite length wire segments ("**thick-fin.**"),

carrying DC current I_z. For the "thin-inf." model, the end-cap wires are assigned a current $I_z/2$ to better account for their magnetic field contribution along y. These models are depicted schematically in Fig. 3.5, along with the actual dimensions of the central part of the Z-wire used in our atom chips. The Z-wires on our atom chips might be better called *strips* or *ribbons*, since they are 3 µm to 6 µm tall, 50 µm wide, and have segment lengths 2 mm to 5 mm (see Sec. 4.6). With typical working distances z_0 of 80 µm to 200 µm, the effects of finite wire height are negligible, and are ignored here. Z-trap characteristics calculated using these three models are compared in the following subsections.

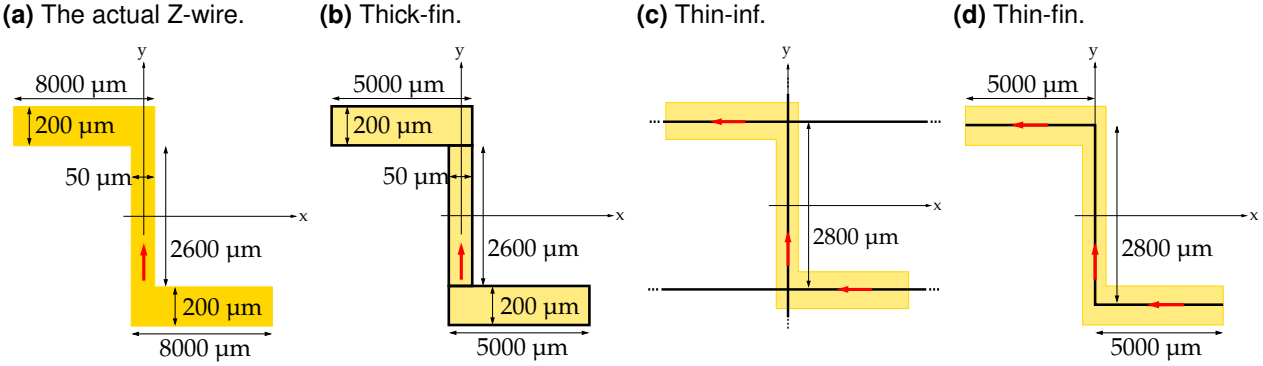

Fig. 3.5: Three models for calculating the Z-wire magnetic field. **(a)**: Actual central dimensions of the Orsay an Toronto chip Z-wires. **(b)-(d)**: Three calculation models with outlines of the actual Z-wire included for reference: **(b)** "thick wire" model, consisting of three separate wire segments; **(c)** infinitesimally thin, infinitely long wires; the end-cap wires running parallel to x bear one half the current; **(d)** infinitely thin, finite-length wire segments. Red arrows indicate the direction of current flow.

3.3.2 Calculating harmonic oscillation frequencies

The centre-of-mass oscillation frequency $\omega_i/2\pi$ of a particle of mass M in a harmonic magnetic trap $U(x,y,z) = \frac{1}{2}M(\omega_x^2 x^2 + \omega_y^2 y^2 + \omega_z^2 z^2)$ is a function of the local magnetic field curvature (see Eq. 3.6):

$$\omega_i = \sqrt{\frac{1}{M}\frac{\mathrm{d}^2 U}{\mathrm{d}^2 x_i}} \propto \sqrt{\frac{1}{M}\frac{\mathrm{d}^2 B}{\mathrm{d}^2 x_i}}, \tag{3.21}$$

where $x_i \in \{x, y, z\}$.

Thin-inf model The simplest calculations of magnetic field curvatures are based on direct differentiation of the "thin-inf." magnetic field amplitude given in Eq. 3.20 along x,y and z. Although the Z-trap potential is asymmetric along z (see Fig. 3.4), the curvatures in the x and z directions are equal in the limits $x \to 0$ and $z \to z_0$, and are given by the following expression:

$$B''_{x,z}(0) \equiv \left.\frac{\mathrm{d}^2 B_Z^{xz}}{\mathrm{d}z^2}\right|_{\substack{x\to 0\\ z\to z_0}} = \left.\frac{\mathrm{d}^2 B_Z^{xz}}{\mathrm{d}x^2}\right|_{\substack{x\to 0\\ z\to z_0}} = \left(\frac{2\pi}{\mu_0 I_z}\right)^2 \frac{B_{\text{bias}}^4}{B_{\text{Ioffe}}} = \frac{B_{\text{bias}}^2}{z_0^2 B_{\text{Ioffe}}}. \tag{3.22}$$

The radial oscillation frequencies are then $\omega_\perp = \omega_{x,z} = \sqrt{m_F g_F \mu_B B''_{x,z}(0)/M}$.

The corresponding expression for the longitudinal field curvature along y requires the explicit consideration of the end cap wire fields (see Fig. 3.3b). The total magnetic field amplitude at the trap centre, B_0, and the curvature along y at the trap centre are both obtained from the Eq. 3.17 expression for the total y-component field, accounting for the end-cap contributions and the

applied Ioffe field B_{Ioffe}:

$$B_0 = B_Z^y(y=0, z=z_0) = \frac{\mu_0 I_z}{\pi}\frac{z_0}{z_0^2+L^2} + B_{\text{Ioffe}} \tag{3.23}$$

$$B_y''(0) = \left.\frac{\mathrm{d}^2 B_Z^y}{\mathrm{d}y^2}\right|_{\substack{y\to 0\\ z\to z_0}} = \frac{6\mu_0 I_z z_0}{\pi L^4}\frac{1-z_0^2/3L^2}{(1+z_0^2/L^2)^3}\,. \tag{3.24}$$

The first term in the expression for B_0 is the contribution from the "natural Ioffe" y-direction field due to end-cap wires, while the second term is the externally applied Ioffe field B_{Ioffe}. From Eqs. 3.23 and 3.21, the longitudinal oscillation frequency is then $\omega_\parallel = \omega_y = \sqrt{m_F g_F \mu_B B_y''(0)/M}$.

Wait: Z-trap twist! Before comparing the trap frequencies predicted by the three models, we stop to recognize an error in the thin-inf. trap frequency calculation in the previous section. **The magnetic potential minimum of the Z-trap is an ellipsoid which is *twisted* with respect to the coordinate axes** x, y, z. As depicted in Fig. 3.3a, the proper axes of the trap x', y' are at some finite angle ϕ_t with respect to x, y. Though the effect is small, with ϕ_t typically on the order of a few degrees, an accurate calculation of the oscillation frequencies – particularly the *longitudinal* oscillation frequency – requires that the magnetic field curvatures be evaluated along twisted axes x' and y'.

We can gain some intuition about the cause of the twist by considering the z-component of the Z-trap magnetic field. The twist may be thought of as a y-dependent displacement along x of the trap centre (keeping the vertical trap centre fixed at $z = z_0$). Both the central Z-wire segment fields and the external bias fields are completely uniform along y.[2] Therefore, the *end-cap wires* must be the source of the twist; they are the only source of non-uniform and z field components along the y direction (see Eq. 3.17).

Consider two geometric properties of the Z-trap: (1) According to Eq. 3.18, the z component of the end-cap wire field varies linearly with y for $|y| \ll L$, and changes sign at $y = 0$, where it is also equal to zero. (2) A z-direction magnetic field has the effect of translating the trap centre horizontally along the x-direction. Taken together, these two ideas explain the twist angle: it is a y-dependent, x-direction translation of the potential minimum, and is due to the z-component field of the end-cap wires.

The twist angle ϕ_t can be expressed very generally as

$$\phi_t = \tan^{-1}\left(\frac{\Delta x}{\Delta y}\right) \approx \frac{\Delta x}{\Delta y} \tag{3.25}$$

where Δx and Δy are the small displacements of the trap centre along x and y due to the end-cap wires. ($\Delta y \gg \Delta x$ due to the large ($\gg 1$) aspect ratio typical of Z-traps.) For any model of the Z-trap magnetic field, this expression may be written in terms of derivatives of the Z-trap

[2] This is certainly true in the thin-inf. model, but even for a centre segment of finite length, the y and z field components are nearly uniform along y near the trap centre.

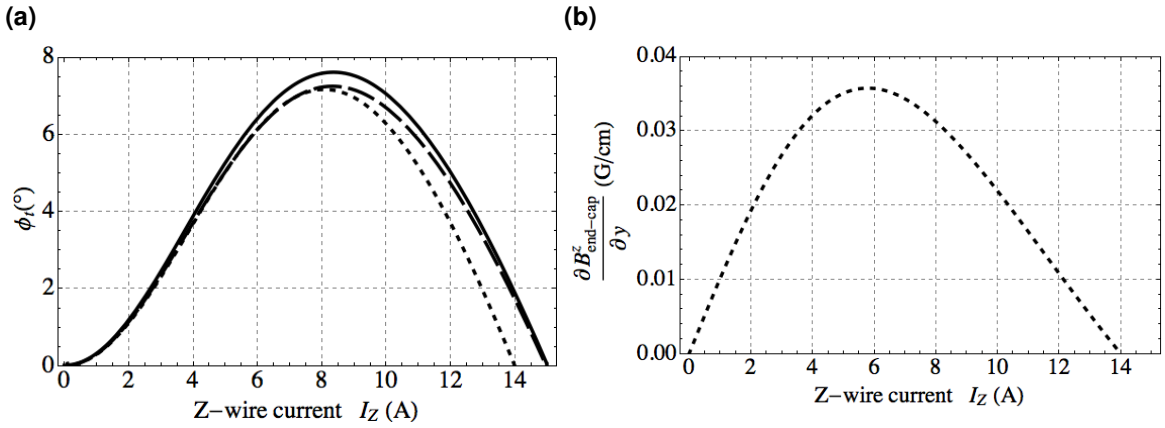

Fig. 3.6: **(a)** Twist angle ϕ_t vs. Z-wire current I_z for $B_{\text{bias}} = -20$ G along $-x$, and $B_{\text{Ioffe}} = 1$ G along $+y$ calculated using the thin-inf. (dotted), thin-fin. (dashed) and thick-fin. (solid) models. With these parameters, $z_0[\mu\text{m}] \approx 100 I_z[\text{A}]$. The three models agree very well for small I_z, but diverge slightly at large I_z. **(b)** y-direction gradient of the z component of the end-cap wire magnetic field which gives rise to the twist (thin-inf. model).

z-component field B^z_Z at the trap centre r_0:

$$\phi_t = -\frac{\mathrm{d}B^z_Z}{\mathrm{d}y}\left[\frac{\mathrm{d}B^z_Z}{\mathrm{d}x}\right]^{-1}\Bigg|_{r\to r_0} \tag{3.26}$$

where $r_0 \equiv (x = 0, y = 0, z = z_0)$. In the thin-inf. model, for instance, the twist angle may be written

$$\phi_t = \frac{z_0^2}{L^2}\left(\frac{1 - z_0^2/L^2}{1 + z_0^2/L^2}\right). \tag{3.27}$$

If we imagine fixing the bias fields and increasing I_z from zero to increase z_0 from zero, then $\phi_t = 0$ when $z_0 = 0$, increases to its maximum positive value when $z_0 = \sqrt{\sqrt{2} - 1}L$, decreases again to zero when $z_0 = L$, and continues to decrease from there as z_0 continues to increase. This behaviour is demonstrated for all three models in Fig. 3.6.

Two more points regarding the role of end-cap wire fields are worth mentioning here. First, there is no yz plane twist of the Z-trap. In other words, the proper axis for trap frequency calculation z' is just equal to z. Such a twist would require a y-dependent x-component of the magnetic field (to cause vertical translations), but no such dependence exists: the end-cap wires do not contribute to B^x_Z, the external field B_{bias} is assumed to be uniform in space, and the central Z-wire segment contributes a nearly uniform x-component along y, especially near the trap centre. Second, the uniform x-direction shift of the trap centre in a U-wire trap [14] is also explained by the z-component field of the end-cap wires. In the U-trap case, the end-cap wires bear currents in *opposite* directions. The end-cap z-component fields do not vanish at $y = 0$ (as they do for the Z-trap), resulting in a uniform translation along x rather than a twist in the xy plane.

3.3.3 Thin-fin. and thick-fin. models

Expressions for the magnetic field of a straight wire segment of finite width w and length $2L$ are derived in Appendix A. The basic procedure is to use the Biot-Savart formula of Eq. 3.10 to build up expressions for a straight wire segment by integrating over a finite width and/or length. The full three-dimensional magnetic field of the Z-wire is then modelled by summing the contributions of individual straight, finite-length and finite-width wire segments as shown in Fig. 3.5. This method amounts to a crude finite-element analysis, and can be used to compute the field pattern of any rectilinear wire arrangement.

One known flaw of this method is that it assumes the DC current to be spread uniformly across the width w of a wire for its entire length, which is not generally true of real conductors. This approach also fails to account for proper current flow around right-angle corners at which the individual wire segments of the model overlap [92]. Not surprisingly, this model is at is worst when computing magnetic fields in and around right-angle wire bends. On the other hand, the model is an excellent approximation to the actual magnetic field far from any wire bends. Despite the known flaws mentioned here, calculations of this type accurately reproduce the measured oscillation frequencies and trap minima to within our measurement error. The effects of finite length and width, in that order, are the dominant corrections to the idealized conductor expressions of Sec. 3.2.

The magnetic field curvatures required to estimate the harmonic oscillation frequencies are obtained by differentiating the full Z-wire expressions along the directions x' and y', following [93]. To carry out the differentiation, one constructs a 3x3 matrix of spatial second derivatives; each entry corresponds to one of the 9 possible Cartesian coordinate second derivatives of the total magnetic field. The diagonal elements of this matrix are the second derivatives with respect to x, y and z. Diagonalizing this matrix yields eigenvectors which correspond to the trap oscillation axes x', y' and z', and eigenvalues corresponding to the magnetic field curvatures along those directions [93]:

$$\begin{pmatrix} \frac{d^2B}{dx^2} & \frac{d^2B}{dxdy} & \frac{d^2B}{dxdz} \\ \frac{d^2B}{dydx} & \frac{d^2B}{dy^2} & \frac{d^2B}{dydz} \\ \frac{d^2B}{dzdx} & \frac{d^2B}{dzdy} & \frac{d^2B}{dz^2} \end{pmatrix} \xrightarrow{\text{diag.}} \begin{pmatrix} \frac{d^2B}{dx'^2} & 0 & 0 \\ 0 & \frac{d^2B}{dy'^2} & 0 \\ 0 & 0 & \frac{d^2B}{dz'^2} \end{pmatrix} \quad \text{in the } \{x', y', z'\} \text{ basis.} \tag{3.28}$$

3.3.4 Comparing models

The predicted trap twist ϕ_t, trap centre height z_0, magnetic field minima B_0, and harmonic oscillation frequencies ω_i calculated using the three models are compared in Figs. 3.6a, 3.7, and 3.8, respectively. These figures show trap parameters plotted as a function of the Z-wire current I_z for fixed values of the external bias fields ("bias" and "Ioffe"). The inputs to each model are the fixed Z-wire geometry, the Z-wire current, and the three external bias fields. The models could be compared over a vast array of input parameters; to highlight the essential differences in the models, I have chosen a fixed set of bias fields which roughly corresponds to actual labo-

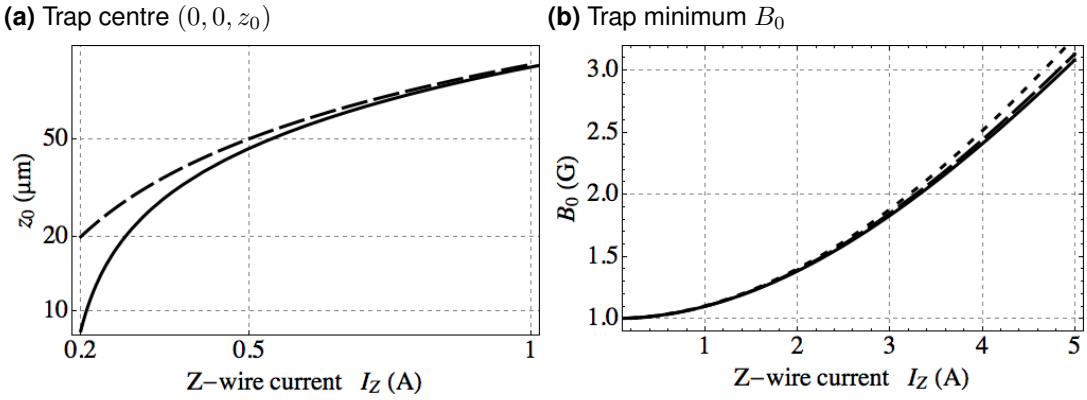

Fig. 3.7: Trap centre z_0 and field minimum B_0 as functions of the Z-wire current I_z for fixed $B_{\text{bias}} = -20$ G along $-x$, and $B_{\text{Ioffe}} = 1$ G along $+y$, predicted by the thin-inf. (dotted), thin-fin. (dashed) and thick-fin. (solid) Z-wire models. For these parameters, $z_0 \approx 100 I_z$ **(a)**: The thin-inf. model results are not shown since they overlap almost exactly with the thin-fin. results (dashed). Both thin-wire models provide excellent approximations to z_0 over a wide range, but fail for traps very near to the chip surface ($z_0 \lesssim 50$ μm). **(b)** All three models agree very closely for small I_z, and diverge only slightly for large I_z.

ratory conditions in the work of this thesis. Table 3.1 presents trap parameters computed by the three models, as an alternative the aforementioned figures, and to highlight the slight differences where they exist.

The winner is: thick-fin. These comparisons clearly demonstrate that the finite-length models thin-fin. and thick-fin. give very similar results over a wide range of Z-wire currents. They also predict the measured values of B_0 and $\omega_{x,y,z}$ to within our measurement error of these quantities (see Sec. 3.3.5), which also demonstrates the inaccuracy of the simple thin-inf. model. Of the two, the thick-fin. model has the slight advantage in accuracy when $z_0 \lesssim w$, where w is the width of the chip wire. For this reason, the thick-fin. model is our primary model for calculating chip trap potentials. Though this model's full analytic expression for the Z-trap is *much* more cumbersome the that of the thin-fin. model (see Appendix A), calculations of $\mathbf{B}_Z(x, y, z)$ and $B_Z(x, y, z)$ are easily carried out using analytic software packages such as Mathematica.

3.3.5 Calibrating calculations with laboratory measurements

The calculations presented in this chapter are only useful if well calibrated using input from experimental measurements. Of the "input" variables to each Z-wire model – Z-wire current I_z and the bias fields B_x, B_y, B_z – only I_z is well known. We can easily measure I_z using a sense resistor in series with the atom chip connection to an accuracy of ± 1 mA ($\sim \pm 0.1\%$), but absolute values of the bias fields produced by external coils (see Ch. 4) are only known to an accuracy of roughly 10%. However, these poor bias field calibrations are compensated for by accurate measurements of the minimum magnetic field $B(\mathbf{r} = 0) \equiv B_0$ and the harmonic oscillation frequencies $\omega_{x,y,z}$ in the Z-trap.

The calibration procedure is as follows:

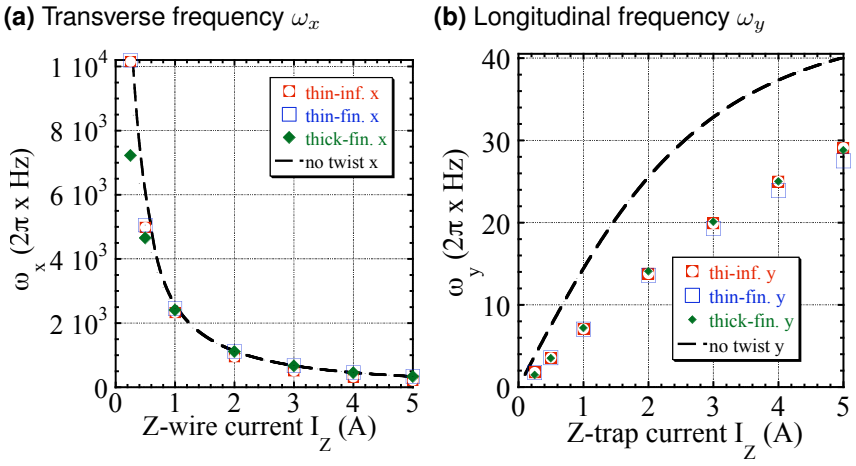

Fig. 3.8: Transverse (x) and longitudinal (y) oscillation frequencies vs. Z-wire current I_z for fixed $B_{\text{bias}} = -20$ G along $-x$, and $B_{\text{Ioffe}} = 1$ G along $+y$, calculated using the thin-inf. (red dots), thin-fin. (blue squares) and thick-fin. (green diamonds) Z-wire models. Frequencies are computed at the trap centre along the appropriate twisted axes x' and y' (see Fig. 3.3a). The black dashed line indicates the trap frequencies in the thin-fin. model computed along the "no twist" coordinate axes x, y. Accounting for the twist is a significant correction for the longitudinal frequency ω_y, but makes almost no difference for the transverse directions $\omega_{x,z}$. Calculations of ω_z are not shown since they overlap almost exactly with the ω_x results (see Tab. 3.1).

1. Since the minimum Z-trap magnetic field $B_0 = B_{\text{Ioffe}} \propto I_z + B_y$ at the trap centre (see Eq. 3.23), direct measurements of I_z and B_0 together specify the total applied y direction bias field B_y.

2. With B_y, I_z and B_0 known, a measurement of the transverse oscillation frequency $\omega_\perp$ is sufficient to specify the total xz-plane bias field $\sqrt{B_x^2 + B_z^2}$. We typically isolate B_x by working in a Z-trap with zero applied z-direction field.

3. In analytic Z-trap calculations, the input parameters B_x, B_y, B_z are tuned until the calculated values of B_0 and $\omega_\perp$ match the measured values for a given I_z.

Once the bias field model values are calibrated in this way, other trap parameters such as the axial oscillation frequency, magnetic field gradients, trap position (x_0, y_0, z_0) etc. can be accurately calculated. Trap parameters for other Z-trap configurations can also be easily calculated by scaling the values of I_z, B_x, B_y, B_z according to calibrations applied in the lab.

One systematic flaw in this calibration method is that is does not account for gradients and curvatures in the real bias magnetic fields. Spatial gradients and curvatures in B_x, B_y, B_z can easily be added to analytic calculations, but calibrating these terms against experimental values is difficult. We try to minimize the gradients and curvatures by aligning the three pairs of bias coils (see Ch. 4) as closely to the x, y, z experimental coordinate axes as possible. Nevertheless, cross-coupling between the bias fields due to spatial non-uniformities persists.

Measuring $\mathbf{B_0}$ We deduce B_0 by performing radio-frequency (RF) spectroscopy on the Zeeman states in a trapped gas. At the trap minimum the Zeeman energy splitting between adjacent m_F

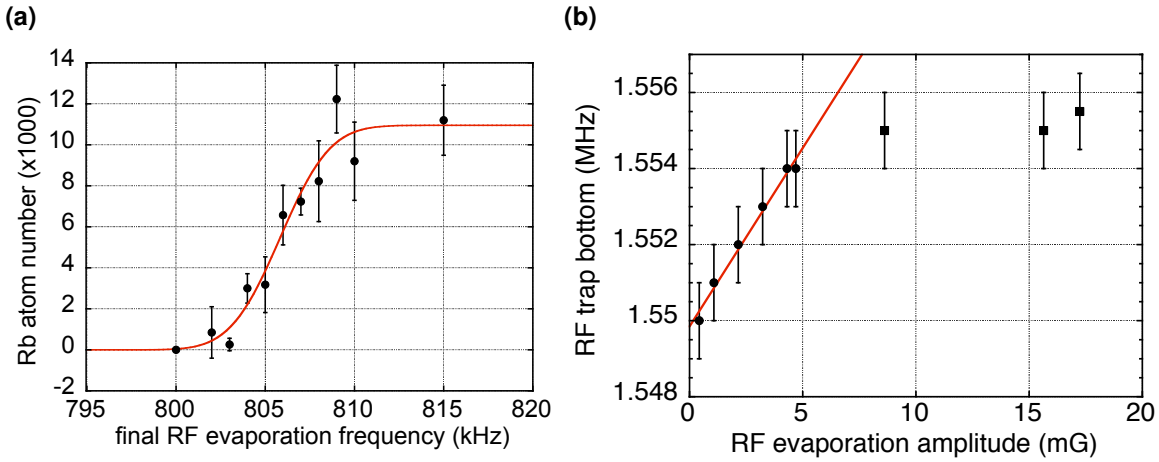

Fig. 3.9: Measuring the RF trap bottom $\Omega_0(0) \equiv g_F \mu_B B_0(0)/\hbar$ in ^{87}Rb. **(a)** Evaporating to lower and lower final frequencies at a fixed RF amplitude probes Ω_0. This data gives $\Omega_0 = 2\pi \times 800 \pm 1$ kHz, using a fit to an error function (solid line). Error bars represent standard deviations over repeated measurements. **(b)** RF trap bottom values measured as in **(a)** as a function of RF amplitude $B_{\rm rf}$. We use the extrapolated $B_{\rm rf} \to 0$ value of Ω_0 as the best estimate of the Zeeman level separation in a bare (i.e. no RF) magnetic trap. The solid line is a linear fit to the lowest $B_{\rm rf}$ points (circles). Error bars are ± 1 kHz from measurements of the type in **(a)**.

states is $g_F \mu_B B_0$ according to Eq. 3.6. The associated Larmor frequency Ω_0 – the "RF trap bottom" – is defined as

$$\hbar\Omega_0 \equiv g_F \mu_B B_0. \tag{3.29}$$

During RF evaporation, sweeping the RF frequency down to lower and lower final frequencies results in more and more atom loss into untrapped states [91]. The RF frequency at which all the atoms are ejected from the trap corresponds to Ω_0. Fig. 3.10a shows the ^{87}Rb atom number remaining in the Z-trap in after RF frequency sweeps to various final values.

Measuring Ω_0 in this way is subject to a systematic overestimate since any non-zero RF magnitude $B_{\rm rf}$ perturbs the "bare" (i.e. no RF) Zeeman states [91, 94]. (See also Ch. 6 of this thesis.) To correct for this, we measure the apparent RF trap bottom at decreasing RF amplitudes, and take Ω_0 to be the value extrapolated down to $B_{\rm rf} = 0$ (see Fig. 3.10b). We have used this method to measure Ω_0 with an uncertainty of $\sim \pm 1$ kHz for Ω_0 between 300 kHz and 4 MHz. These values correspond to measurements of $B_0 = 429 \pm 2$ mG ($\pm 0.3\%$) and $B_0 = 5714 \pm 2$ mG ($\pm 0.03\%$), respectively.

Measuring $\omega_{x,y,z}$ The harmonic oscillation frequencies are measured by directly observing centre-of-mass motion of trapped, ultra-cold gases in the Z-trap. Oscillations are excited by perturbing the trap centre using atom chip wire currents and/or external bias fields. For example, to measure ω_z, the trap centre z_0 is slowly[3] shifted by several µm by smoothly increasing $B_{\rm bias}$ at a fixed I_z, then quickly resetting $B_{\rm bias}$ to its original value. The sudden shift in the trap position induces

[3] "Slowly" on a timescale much larger than the expected centre-of-mass oscillation period.

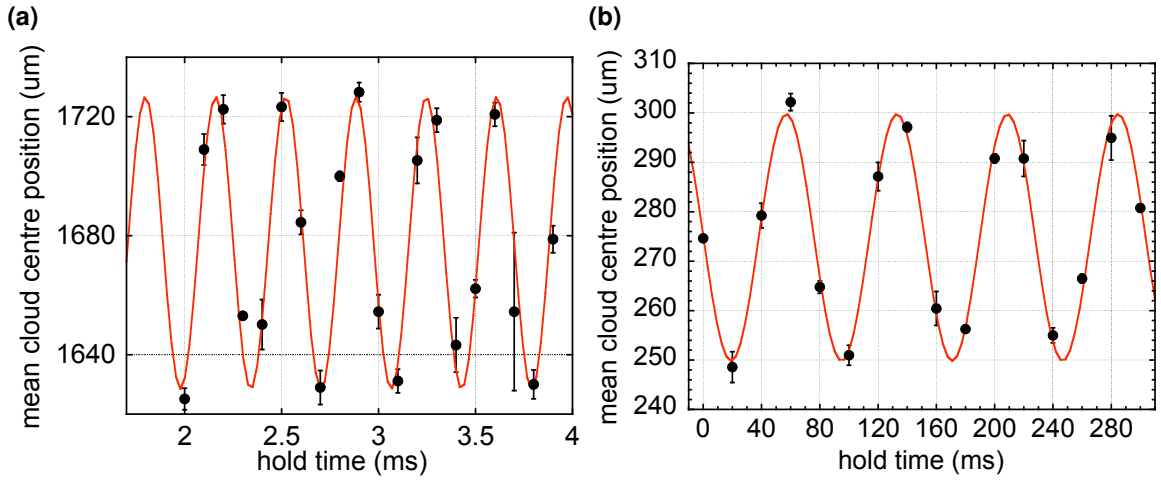

Fig. 3.10: Harmonic centre-of-mass oscillations for trapped $^{87}\mathrm{Rb}$. **(a)** Measured radial oscillations; the sinusoidal fit gives $\omega_x/2\pi = 2.76$ kHz.**(b)** Measured axial oscillations; the sinusoidal fit gives $\omega_z/2\pi = 13.2$ Hz. Error bars represent standard deviations over repeated measurements.

harmonic oscillations which we observe as oscillations in the cloud centre position in time-of-flight after a variable hold time in the trap and a fixed time-of-flight. Fig. 3.10 shows example measurements of x and y $^{87}\mathrm{Rb}$ oscillations as a function of in-trap hold times in two different Z-traps. We use sinusoidal fits to extract the oscillation frequency.

3.4 Summary

This chapter describes the characterization of Z-trap magnetic trapping potentials used for confining ultra-cold $^{87}\mathrm{Rb}$ and $^{40}\mathrm{K}$ in this thesis. We show how DC current in a Z-shaped wire and an external uniform magnetic bias field together produce an anisotropic three-dimensional magnetic minimum suitable for trapping neutral atoms. We derive analytic expressions for the total Z-trap magnetic field, using three separate models of current flow in the Z-wire. The most realistic of these models approximates current flow in the Z-wire using uniform DC currents in three wire segments of finite length and width. We identify the Z-trap "twist" – the misalignment of the Z-trap axes with respect to the Z-wire – and point out that the twist angle must be accounted for in order to accurately calculate the oscillation frequencies in the Z-trap, particularly the longitudinal oscillation frequency. Analytic calculations of the Z-wire magnetic fields are calibrated using laboratory measurements of the magnetic field minimum at trap centre, as well as the centre-of-mass oscillation frequency of ultra-cold $^{87}\mathrm{Rb}$ in the Z-trap.

model	**input**	**outputs**						
	I_z	z_0	B_0	$B^{\text{nat.}}_{\text{Ioffe}}$	ω_x	ω_y	ω_z	ϕ_t
	A	µm	G		$2\pi\times$ Hz			◦
thin-inf.	.25	25	1.006	.006	10153	1.8	10186	.02
thin-fin.		25	1.006	.006	10192	1.8	10192	.02
thick-fin.		16	1.004	.004	7223	1.5	7223	.03
thin-inf.	.5	50	1.025	.025	4984	3.6	5045	.07
thin-fin.		50	1.025	.025	5057	3.6	5057	.08
thick-fin.		46	1.023	.023	4652	3.5	4652	.09
thin-inf.	1	100	1.102	.102	2329	7.1	2434	.29
thin-fin.		100	1.098	.098	2457	7.1	2457	.30
thick-fin.		98	1.098	.098	2405	7.2	2405	.31
thin-inf.	2	200	1.400	0.400	952	13.8	1080	1.1
thin-fin.		198	1.381	0.381	1119	13.6	1119	1.1
thick-fin.		197	1.390	0.390	1109	14.1	1110	1.2
thin-inf.	5	500	3.262	2.262	213	29.1	284	5.1
thin-fin.		474	3.079	2.079	338	27.5	339	4.9
thick-fin.		473	3.127	2.127	332	28.8	337	5.1

Tab. 3.1: Comparison of the thin-inf. thin-fin., and thick-fin. Z-trap models with bias fields $B_x \equiv B_{\text{bias}} = 20$ G along $-x$, $B_y \equiv B_{\text{Ioffe}} = 1$ G along y, and $B_z = 0$. Much of this data is plotted in Figs. 3.6a, 3.7, and 3.8.

You tend to look at the practical side of things.

Wing's fortune cookie

4 Experimental apparatus

This chapter provides detailed technical descriptions of the trapping, cooling, manipulation and measurement apparatus for atomic ^{40}K an ^{87}Rb used in the work of this thesis. Most of the subsystems described here were first designed and implemented in my first two years at a graduate student, but nearly all have been continually refined or upgraded. The descriptions in this chapter are current as of the submission of this thesis (May 2009).

The apparatus was designed to produce a ^{40}K DFG via sympathetic cooling with ^{87}Rb on an atom chip in a simplified, single-chamber ultra-high vacuum (UHV) system. Key features of the apparatus resulting from this specific goal, and which distinguish our setup from other ultra-cold atoms apparatus in the field are:

- Rather than a chip-based reflected surface-MOT [88], we use a traditional six-beam MOT consisting of 4 cm-diameter beams to capture ^{40}K as efficiently as possible. ^{40}K has a natural isotopic abundance of only 0.012% [95].
- The large MOT beams set the scale of the required optical vacuum cell and MOT-to-atom-chip distance, as well as the radii of MOT and magnetic trapping coils.
- The large collision rates made possible by the strong confinement of atom chip traps permits rapid evaporation to degeneracy, eliminating the need for vacuum minutes-long lifetime, a multi-chamber vacuum system and a Zeeman slower. The MOT is loaded directly from atomic vapour produced using conventional atom dispensers and light-induced atomic desorption (LIAD, see Sec. 4.1.3).

The following subsections give technical detail of the laser system for MOT, probe and optical pumping beams, the UHV chamber and atom sources, magnetic field coils, radio-frequency (RF) sources, imaging systems, and atom chips used in this work.

4.1 Vacuum chamber and atom sources

The UHV chamber has three main component groups: the main Pyrex cell, the atom chip and its support stack, and the vacuum pumps. The single-chamber system is centred around a 6" Conflat (CF) stainless steel cube. The six faces of the cube are attached to the following components (see Fig. 4.1):

1. 74 mm $\times$ 74 mm $\times$ 170 mm rectangular Pyrex cell, which houses the atom chip, and in which all atom trapping and cooling takes place;
2. multi-port top flange and electrical feedthrough, which also supports the atom chip stack;
3. residual gas analyzer (RGA) (Stanford Research Systems RGA 100);
4. titanium sublimation pump (TSP) (Varian 8" cryopanel and titanium filament), cooled with liquid nitrogen (LN_2);
5. ion pump (Varian VacIon Plus 75 Starcell)
6. pneumatic vacuum valve (VAT Mini UHV 2.75"), behind which are attached a turbo-molecular pump and a roughing pump for pumping down from atmospheric pressure

In steady state operation, the ion pump runs continuously and the TSP cryopanel is cooled with LN_2. The TSP is an excellent getter of H_2, which is the dominant background gas in our baked vacuum chamber (see Fig. 4.2). According to the manufacturer, -195°C LN_2 cooling increases the pumping speed of H_2 by roughly a factor of three compared to 20°C water cooling.[1] We measure a factor of three increase in the chip trap lifetime with LN_2 cooling vs. un-cooled room temperature operation of the cryopanel. The titanium filament is not used during each experimental cycle, but approximately once per week, after the atom dispensers are used.

Fig. 4.3 demonstrates the effect of LN_2 TSP cooling on the background gases in our UHV chamber. RGA measurements of the partial pressure of hydrogen, water and other trace gases are plotted against time in two scenarios: first, in the system starting at room temperature as LN_2 is added to the TSP; second, as the system is left to naturally warm up to room temperature as the LN_2 boils off.

4.1.1 Bakeout and vacuum pressure

The stainless steel vacuum components (flanges, TSP shell) were all air-baked at 400°C for 3 - 5 hours to outgas hydrogen, and to create an oxide layer on the bare steel to reduce the hydrogen outgassing rate of the steel [96, Ch.16]). After assembling and mounting the entire system, the chamber was baked at 150°C under vacuum (turbo pump, then later ion pump) for three weeks using ohmic heater tapes and layers of aluminum foil wrapping.

The full system maximum bake temperature was always limited by materials on the atom chip and stack. In particular, peeling of the electroplated wires from the silicon substrate was our biggest concern when baking the Orsay chip. When baking the Toronto chip and stack, the electrically conductive epoxy and Kapton wire insulation were the bake temperature bottlenecks. The epoxy manufacturer advised that cured epoxy bonds would weaken and even break if reheated above 150°C; Kapton was rated UHV-safe up to 260°C. A fear of destroying chip electrical connections during the bake ultimately limited the final bake temperature. Chip wires, dispensers and the TSP filament were all degassed during the bake.

[1] Source: Varian, Inc. ion pump technical documentation.

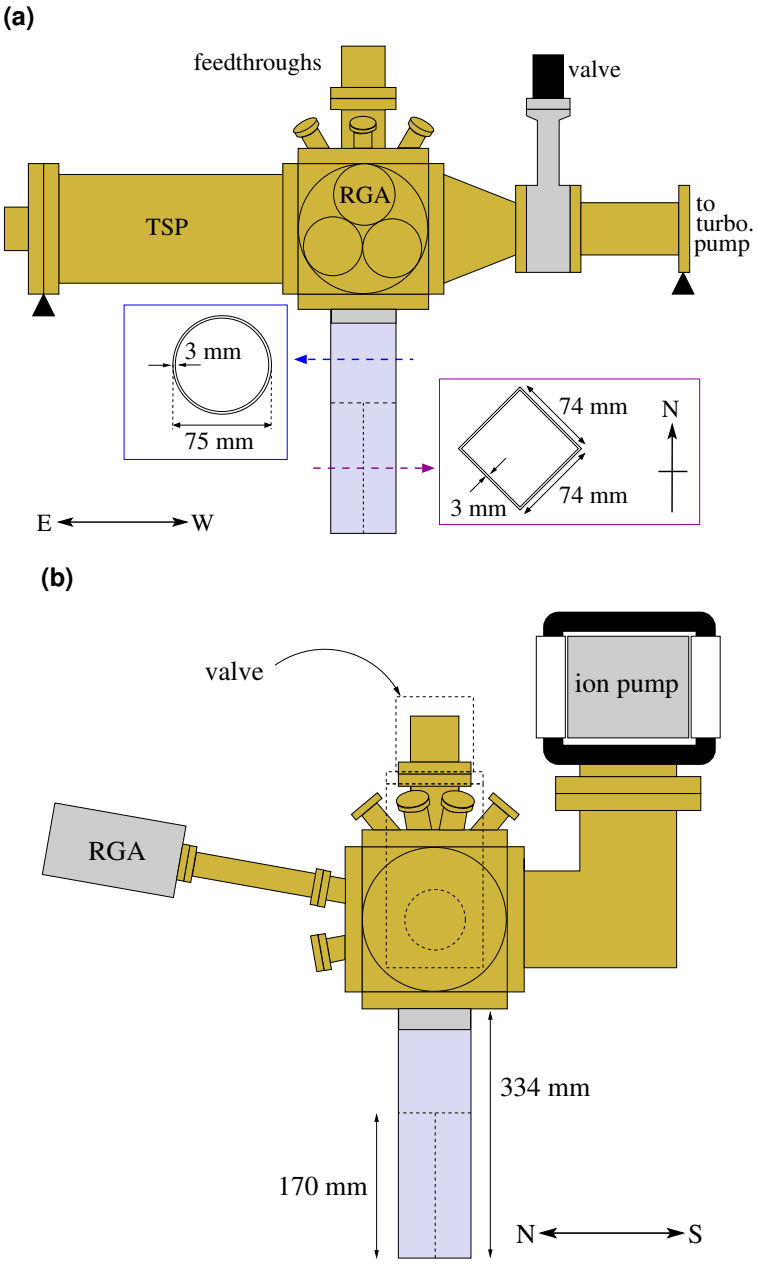

Fig. 4.1: (a) Side view of the vacuum system looking at the RGA showing cross-sections of the Pyrex cell, titanium sublimation pump (TSP), and top multi-port flange and electrical feedthrough. The cell's faces are at roughly 45 degrees to the plane of the diagram. The vacuum system is supported at the points shown by black triangles using aluminum stands bolted to the optical table. Ion pump not shown. **(b)** Side view of vacuum system looking directly at the TSP showing the RGA and ion pump.

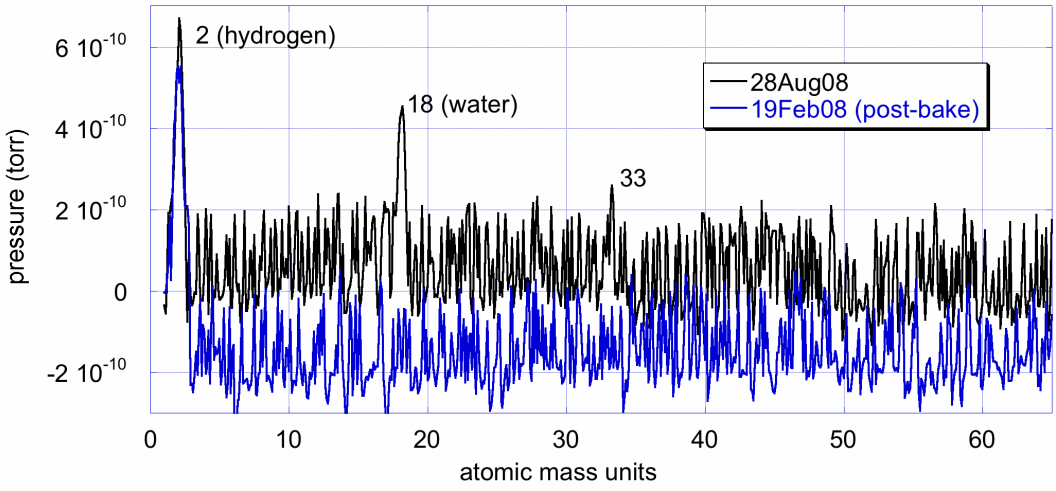

Fig. 4.2: RGA scan of UHV environment immediately after a bakeout (19Feb08, blue), and after running the experiment for several months (28Aug08, black). Water vapour was successfully removed from the system during the bake, but returned during normal use of the system, likely due to regular use of unbaked Alvatec K and Rb dispensers.

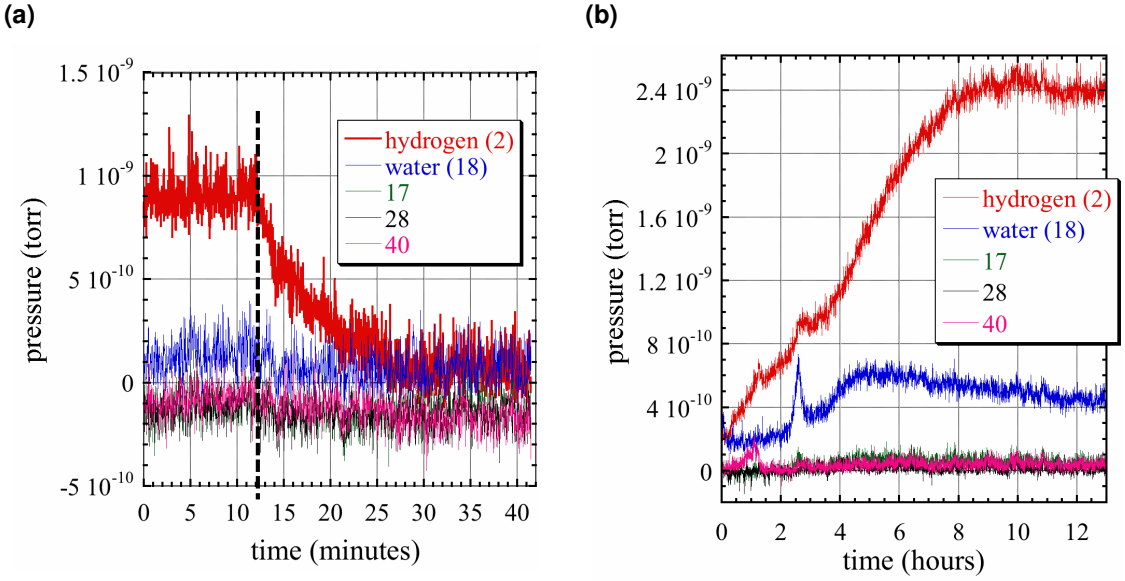

Fig. 4.3: Effect of LN_2 cooling on TSP pumping of UHV background gases, listed according to their mass numbers in atomic mass units (e.g. 2 = H_2). **(a)** The hydrogen partial pressure drops dramatically after the LN_2 is added (dashed black vertical line) to the TSP cryopanel. **(b)** Partial pressures of H_2 and H_2O slowly increase as the LN_2 is allowed to boil off, returning the TSP and UHV chamber to room temperature. The spike in the water signal likely corresponds to the vaporisation and subsequent pumping of ice and/or liquid water from the cold cryopanel.

By this method, we achieved magnetic chip trap lifetimes of 20 to 25 s, with the system cooled to room temperature, the valve shut, and only the ion pump running (with ion currents below the sensitivity of the ion pump controller ion gauge, i.e. less than 1 nA). After running dispensers for the first time after the bake, and running the experiment daily, the lifetimes stabilized at around 10 s over the course of several weeks.

4.1.2 Dispensers

We use a combination of homemade and commercial dispersers for $^{87}\mathrm{Rb}$ and $^{40}\mathrm{K}$. The rubidium dispensers are getters from SAES (model RB/NF/3.4/12), and Alvatec (Alvasource AS-Rb-20-S). These dispensers work well for generating $^{87}\mathrm{Rb}$ vapour since the natural isotopic abundance of $^{87}\mathrm{Rb}$ is 28% [95]. By contrast, the 0.012% natural isotopic abundance of $^{40}\mathrm{K}$ [95] makes the use of commercial potassium getters (e.g. from SAES) impractical. Instead, we constructed our own homemade dispensers following DeMarco [97, 98], using with KCl powder isotopically enriched to 7% (purchased from Trace Sciences).

In 2008 we also began using commercial $^{40}\mathrm{K}$ dispensers from Alvatec (Alvasource AS-K40(4+%)-10-S), which have $^{40}\mathrm{K}$ enriched to 4%. Initial tests have shown that these dispensers pollute the UHV chamber much less than do our homemade $^{40}\mathrm{K}$ dispensers. We achieve comparable MOT lifetimes and loading efficiencies with the SAES, homemade and Alvatec dispensers, but the Alvatec versions pollute the chamber the least, registering a much lower vacuum pressure during operation than the homemade or SAES designs: 0.9 µA (Alvatec) vs. 4 µA (SAES) for $^{87}\mathrm{Rb}$, and 0.5 - 2 µA (Alvatec) vs. 8 µA (homemade) for $^{40}\mathrm{K}$, measured with the ion pump's ion gauge. The baseline pressure in the chamber corresponds to roughly 0.5 µA at room temperature with the experiment off. (0.51 µA corresponds roughly to a pressure of 4×10^{-9} torr; 1 µA corresponds roughly to 7×10^{-9} torr.)

4.1.3 Atomic vapour and LIAD

The $^{87}\mathrm{Rb}$ and $^{40}\mathrm{K}$ MOTs are loaded directly from atomic vapour created using light-induced atom desorption (LIAD). The Pyrex vacuum cell is irradiated during MOT loading using ten Marubeni L405 series illuminators positioned around the cell. Each illuminator package consists of 60 integrated 405 nm LEDs and a spherical collimating lens. The illuminators are powered by 300 mA each, sourced from a constant-current supply circuit, and each produce roughly 16 mW at $\lambda = 405$ nm. Rather than turning on the dispensers during every MOT loading cycle, we rely on LIAD to load the MOT; dispensers are only run to replenish the $^{87}\mathrm{Rb}$ and $^{40}\mathrm{K}$ on the interior walls of the vacuum chamber by running them as required, typically every few days or weeks.

LIAD permits rapid and repeatable modulation of the vapour pressure in our single vacuum chamber. LIAD satisfies the competing requirements of high and low vapour pressure in our single chamber experiment; higher vapour pressures are required for MOT loading, but lower pressures are necessary to minimize background gas collisions which limit magnetic trap lifetimes (see Sec. 5.1). We observe a 100-fold increase in the $^{87}\mathrm{Rb}$ MOT number compared to loading from the background vapour alone (see Fig. 5.1). The increase in $^{40}\mathrm{K}$ MOT atom number is

unknown since we cannot observe a ^{40}K MOT with the LEDS off.

4.2 Lasers and optical frequency control

The laser system is based on locked external-cavity grating-stabilized diode lasers, free-running injected mulitimode slave diode lasers, acousto-optic modulators (AOMs) and tapered optical amplifiers (TA). Four master diode lasers (New Focus Vortex 6013) supply all the light for the experiment; two at $\lambda \approx 766.700$ nm for ^{40}K, and two at $\lambda \approx 780.250$ nm, outputting 8 - 10 mW each with laser diode currents of 50 mA and 90 mA, respectively.[2]

4.2.1 Laser locking

We refer to the master lasers for each species as "trap" and "repump" – one pair for each species – since they are tuned to the common cycling ($5^2S_{1/2}\,F = 2 \rightarrow 5^2P_{3/2}\,F = 3$ for ^{87}Rb and $4^2S_{1/2}F = 9/2 \rightarrow 4^2P_{3/2}\,F = 11/2$ for ^{40}K) and repumping transitions ($5S_{1/2}\,F = 1 \rightarrow 5P_{3/2}\,F = 2$ for ^{87}Rb and $4S_{1/2}F = 7/2 \rightarrow 4P_{3/2}\,F = 9/2$ for ^{40}K). The ground state hyperfine splittings of ^{87}Rb and ^{40}K (approximately 6.8 GHz and 1.3 GHz, respectively, see Fig. 4.5) are large enough that separate trap and repump masters are convenient. All light for the MOT, optical pumping, imaging probes and depumping beams are split off from these four lasers (see Tab. 4.1).

All four Vortex masters are locked to peaks in Doppler-free saturated absorption spectra produced with Rb and K vapour cells and balanced photodiodes (New Focus Nirvana Autobalanced Photoreceivers, Model 2007). To probe the atomic resonances, two weak "probe" and "reference" beams ($\sim$ 20 µW each) are directed through a vapour cell; the probe beam is overlapped with a stronger, counterpropagating $\sim$ 70 µW pump beam to saturate the absorption signal. The broad Doppler absorption profile and saturated peaks (hyperfine transitions and crossover peaks) are probed by scanning the master frequency using the piezo voltage at 20 Hz. Locking is carried out by the modulation transfer method [99, 100]. The pump frequency is modulated at 110 kHz using an AOM in double-pass configuration (see Fig. 4.4a). The resulting amplitude modulation of the probe beam on the photodetector is used to lock to a peak maximum [101, 102]. The output of a lock circuit is sent to both piezo voltage and current of the master laser via the laser diode controller to complete the feedback loop. By this method we a lock bandwidth of over 5 kHz, and observe a short-term stability of 300 kHz with a 30 ms integration time.

4.2.2 Slave diodes for higher power

Roughly 1 mW of the locked output of each saturated-spectroscopy setup is used to injection lock free-running mulitimode laser diodes for the Rb trap, K trap and K repump lasers. Frequency tuning of the injected light is accomplished with an AOM in double-pass configuration (see Fig. 4.4b). This combination of locked low-power master diodes and injected free-running

[2]The lasers are controlled using New Focus Vortex 6000 series controllers, and have been extremely stable and reliable parts of the experiment. We turn the diode current completely off at the end of each day. All four lasers had been running trouble-free for 6 years as of June 2009.

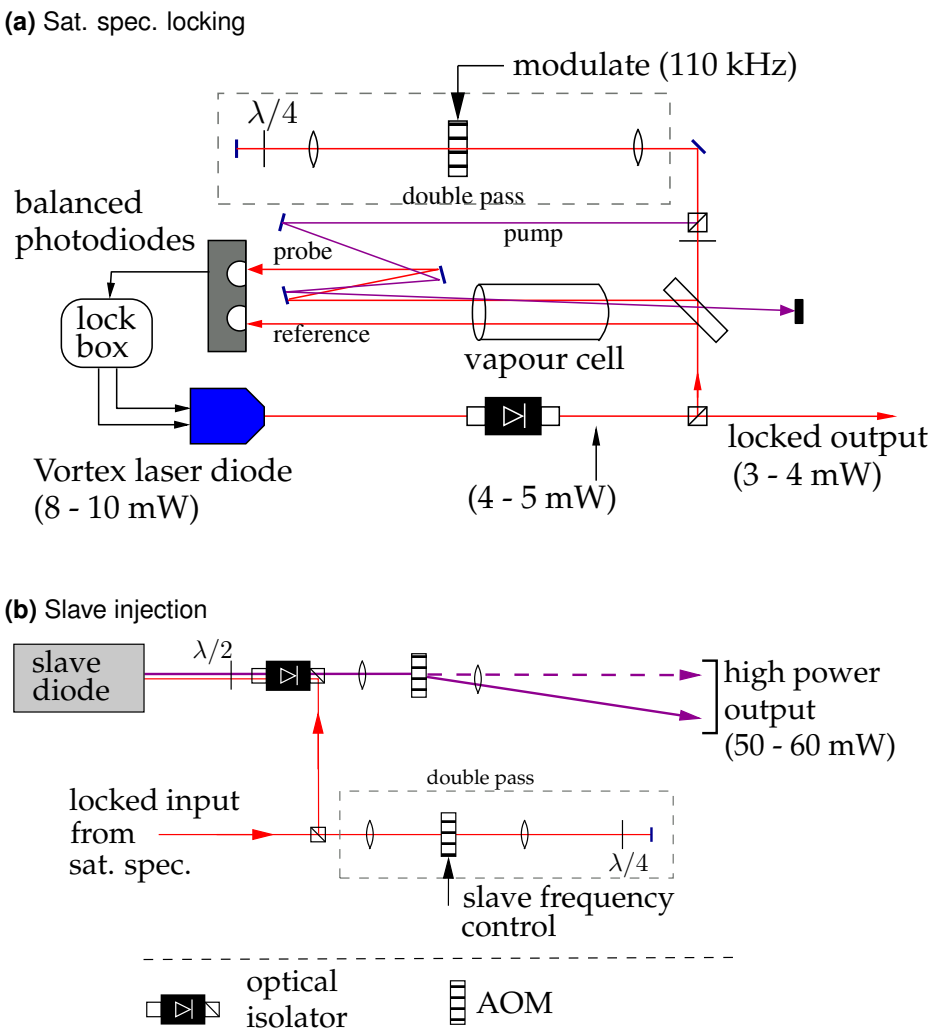

Fig. 4.4: **(a)** Frequency locking of the master Vortex diode laser to peaks in the Doppler-free saturated absorption spectrum using the modulation transfer scheme (see text). The "lock box" electronics feed back to the Vortex laser's piezo voltage and current inputs via the laser diode controller. **(b)** Injection of a multi-mode slave laser diode with locked light from the master laser diode.

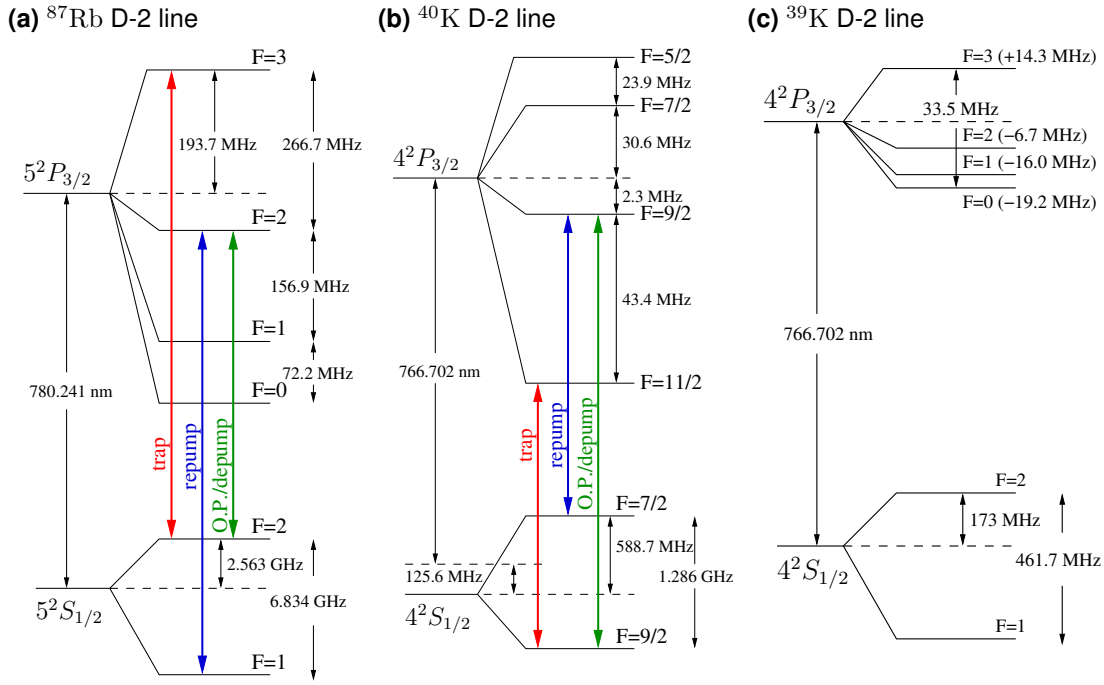

Fig. 4.5: D-2 line hyperfine structure of ^{87}Rb and ^{40}K with the relevant optical transitions indicated. The ^{39}K level structure is also included since the ^{40}K lasers are locked to ^{39}K peaks (see text). The Rb diagrams are reproduced from [103, p.25] and the K diagrams from [104, p.78] and references therein: [105, 106, 107].

slave diodes (Sanyo DL-7140-210W at 782 ± 2 nm and Sacher GmbH FP-0765-30 at 771 nm in Thorlabs TCLDL9-TEC laser diode mounts) provides 60 - 70 mW of locked light. The double-pass AOM geometry allows frequency tuning over 40 MHz range without affecting the slave injection or the optical alignment downstream.

4.2.3 MOT, optical pumping and imaging beams

A schematic diagram of the lasers system, optical frequency control and generation of beams for trapping, repumping, optical pumping, and imaging is show in Fig. 4.6. The AOM frequency control of each beam is summarized in Tab. 4.1. The trapping, repump and optical pumping transitions are depicted in Rb and K hyperfine level diagrams in Fig. 4.5.

MOT beams The ^{87}Rb trap light is generated from the injection-locked output of the "Rb-trap" laser system using a combination of single and double-pass AOMs (see Fig. 4.6). The double-passed AOM2 frequency is computer-controlled, and is used to tune the frequency of this beam near to the ^{87}Rb hyperfine cycling transition of the D-2 line ($F = 2 \rightarrow F' = 3$). The "+1"-order diffracted output of single-passed AOM3 is coupled into the MOT fibre. ^{87}Rb repump light is taken directly from the locked output of the master diode laser without an injection locked slave diode. The frequency is manually tuned to the $F = 1 \rightarrow F' = 2$ ^{87}Rb D-2 transition using AOM3 in single-pass configuration.

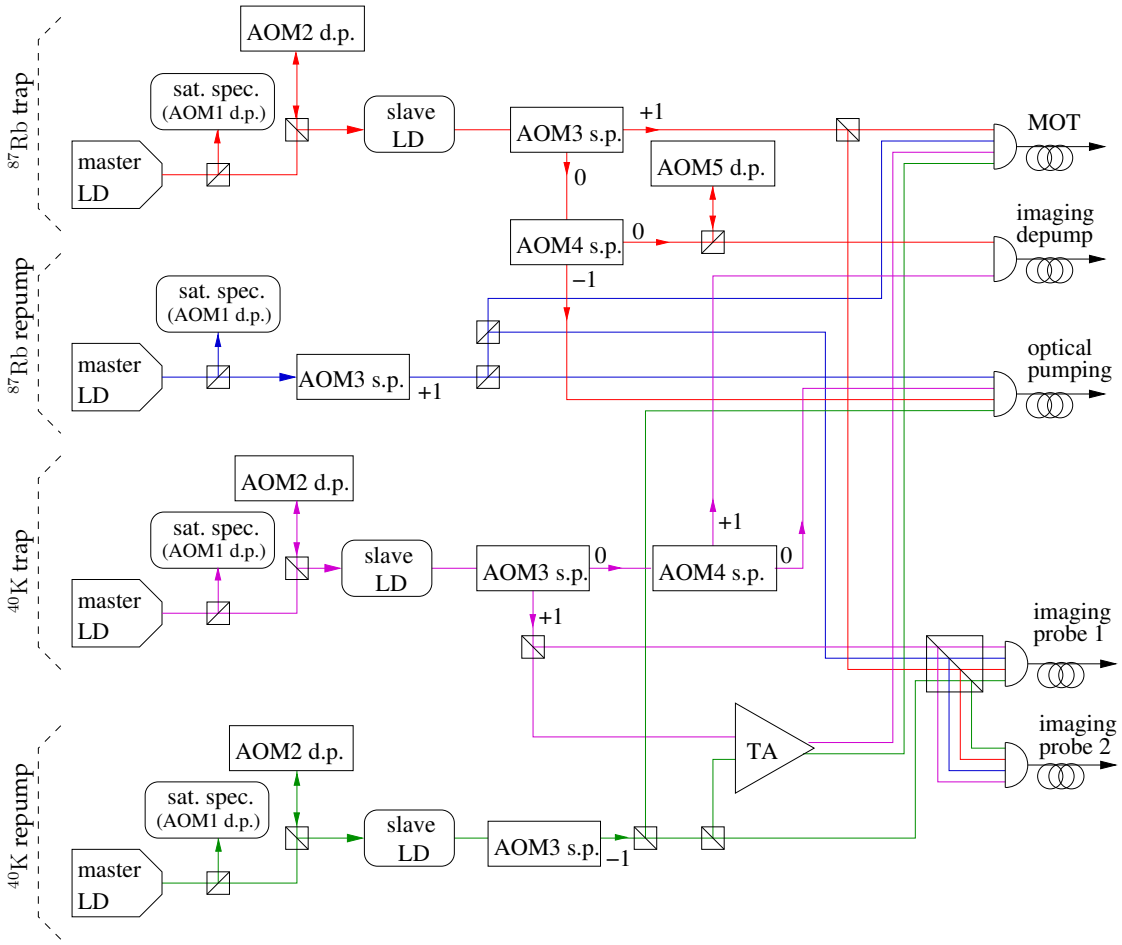

Fig. 4.6: Rb and K laser schematic (colour helps). Laser light is sourced from low-power master laser diodes (LD) and amplified using injection-locked slave laser diodes and a TA. Frequency tuning is accomplished using AOMs in single-pass (s.p.) and double-pass (d.p.) configurations. The fibre-coupled MOT light is directed through a second tapered optical amplifier, whose output is divided into the six MOT beams for $^{87}\mathrm{Rb}$ and $^{40}\mathrm{K}$ (see Fig. 4.7). The fibre-coupled depump, optical pumping and probe beams are sent directly to the UHV chamber.

The ^{40}K trap setup is nearly identical to the ^{87}Rb trap setup. The main exceptions are (1) that a second stage of optical amplification is added after the "-1"-order diffraction output of AOM3, and (2) the repump laser power is boosted using an injected slave diode. The TA is of the Orsay design [108]. It uses an Eagleyard EYP-TPA-0780 775 nm TA chip, and steps the optical power up from 1.6 mW to 41 mW (767 nm, trap + repump). After some spatial shaping of the TA output beam, the trap and repump beams are directed toward the MOT fibre.

The output of the MOT fibre is fed into a Toptica TA100 1 W tapered amplifier to step up the power for the MOT beams. The bandwidth of the TA100 is 20 nm – wide enough to amplify light near 780 nm and 767 nm simultaneously when cooled to 11°C. The output of the TA100 amplifier divided into six 4 cm diameter MOT beams, detailed schematically in Fig. 4.7. The amplifier output is spatially filtered by focusing through a 20 µm pinhole; this improves the beam's spatial profile, but also results in a 30% power loss.

Polarizing beamsplitters and dichroic waveplates are used to divide the 4-colour amplifier output into six MOT beams, with **independent control of the beam powers for ^{87}Rb and ^{40}K**. The six 4-cm diameter beams are directed toward $\lambda/4$ waveplates to generate the required σ^+ and σ^- polarizations, and from there into the Pyrex UHV cell along the directions shown in Fig. 4.9. AOM3s are used to switch the MOT beams on and off. Optical shutters are also included before the MOT fibre input and after the TA100 output to block any AOM leakage and/or spontaneous emission from the TA100.

Rb & K beam control Amplifying MOT light for both species with the same amplifier means that the ^{87}Rb and ^{40}K MOT beam k-vectors are *not* independent. In 2006 we separated the ^{87}Rb and ^{40}K MOT light amplification by adding a Orsay-style TA for ^{40}K and leaving the TA100 for ^{87}Rb only. This swap made only a modest improvement in the dual-species MOT loading efficiency, however, and so the setup was returned to the original, simpler form described here.

Optical pumping and depumping beams Optical pumping beams on the transitions shown in Fig. 4.5 and listed in Tab. 4.1 are produced from weak beams picked off of the output of the injected slave diodes. Their frequencies are set using AOMs 2, 3 and 4. Repumper light for ^{87}Rb and ^{40}K is also coupled into the optical pumping fibre for efficient pumping. The output of the optical pumping fibre is collimated, polarized σ^+, and sent directly into the UHV cell. Depumping light – used in rapid absorption imaging of atoms released from the chip trap (see Ch. 7) – is generated separately and coupled into its own fibre. This beam does not include repump light; its purpose is to pump atoms into the states $F = 1$ for ^{87}Rb and $F = 7/2$ for ^{40}K, which are dark with respect to the imaging probe beams tuned to the cycling transitions. The optical frequencies of these beams are tuned manually with AOM4 in the ^{40}K trap system and AOM5 in the ^{87}Rb trap system. AOM3s are used to pulse the pumping/depumping beams on and off. Optical shutters block any AOM leakage.

Imaging probe beams The absorption imaging probe beams are produce from picked off output of injected slave lasers. Imaging is typically carried out on resonance (i.e. resonant with the

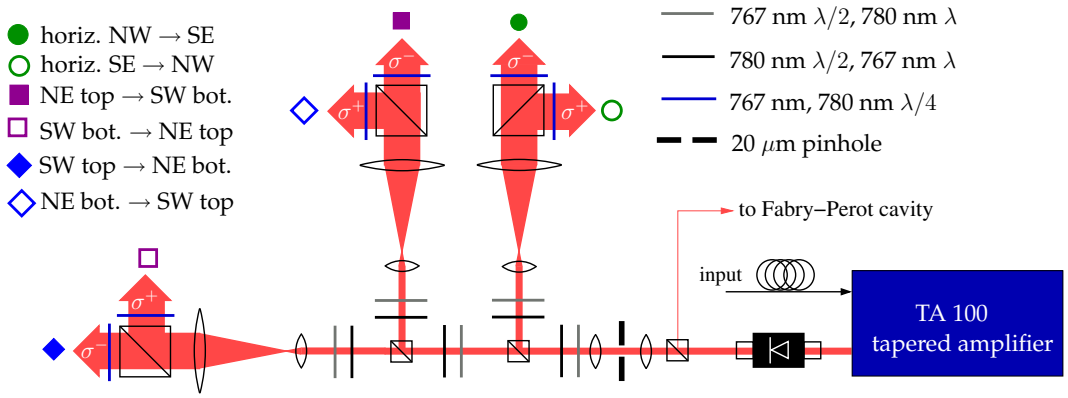

Fig. 4.7: Rb and K MOT optics, showing the second TA and telescopes used to create the six 4 cm diameter beams. Dichroic waveplates (grey and black) allow independent power balance of the ^{87}Rb and ^{40}K MOT beams. The beams are labelled according to their propagation directions in the lab. The coloured shapes indicated pairs of counterpropagating MOT beams – see also Fig. 4.9.

^{87}Rb and ^{40}K cycling transitions), or detuned by one linewidth ($\Gamma \approx 6$ MHz) or less. The laser system is set up to accommodate both trap and repump light for both species in the imaging probes, but we find that repump light is not usually required. Each atom scatters roughly 190 photons during a typical 100 µs pulse from a resonant probe beam at intensity $I = I_{sat}/10$. We expect that atoms are fully optically pumped into the $|F = 2, m_F = 2\rangle$ and $|F = 9/2, m_F = 9/2\rangle$ Zeeman states after scattering at most the first five (ten) photons in ^{87}Rb (^{40}K), eliminating the need for optical (re)pumping. The probe light is divided between the two probe fibres, whose output is collimated, polarized σ^+, and directed into the UHV cell horizontally, skimming just below the atom chip surface along the directions y and x, respectively (see Figs. 4.9 and 4.16). AOM3s switch the probe beams on and off. Optical shutters block any AOM leakage.

4.3 Coils: MOT, magnetic trap and transfer

The magnetic field coils in our apparatus are of two functional types: (1) bias coils, which provide weak, uniform magnetic fields to counteract environmental DC magnetic fields; and (2) trapping coils, which provide strong quadrupole magnetic fields for the MOT, and for magnetic trapping and transport to the atom chip. The design and construction of the trapping coils is described in detail in [109]. This section provides a review of the key elements of the coil system design and implementation, including slight modifications to the original 2004 setup.

4.3.1 Coil design considerations

The MOT uses a three-dimensional quadrupole magnetic field and six counterpropagating laser cooling beams. The quadrupole magnetic trap (QMT) requires a similar magnetic field configuration, but with a field gradient roughly one order of magnitude larger than that required for the MOT. These two field constraints needed to be satisfied in the system design in such a way that the appropriate magnetic fields and magnetic field gradients could be generated in the region of

	target D-2 line transition †	D-2 line locking transition ‡	optical frequency shifts (MHz)					
			AOM1 (d.p.)	AOM2 (d.p.)	AOM3 (s.p.)	AOM4 (s.p.)	AOM5 (s.p.)	total
^{87}Rb trap	$F = 2 \rightarrow F' = 3$	$F = 2 \rightarrow F' = 3$	65	-172	80	-	-	-27
^{87}Rb repump	$F = 1 \rightarrow F' = 2$	$F = 1 \rightarrow F' = 2$	-80	-	80	-	-	0
^{87}Rb O.P.	$F = 2 \rightarrow F' = 2$	$F = 2 \rightarrow F' = 3$	65	-160	0	-172	-	-267
^{87}Rb depump	$F = 2 \rightarrow F' = 2$	$F = 2 \rightarrow F' = 3$	65	-160	0	0	-172	-267
^{40}K trap	$F = 9/2 \rightarrow F' = 11/2$	$F = 1 \rightarrow P_{3/2}$	91	146	110	-	-	347
^{40}K repump	$F = 7/2 \rightarrow F' = 9/2$	$F = 2 \rightarrow P_{3/2}$	-116	-204	-110	-	-	-430
^{40}K O.P.	$F = 9/2 \rightarrow F' = 9/2$	$F = 1 \rightarrow P_{3/2}$	91	146	0	169.2	-	237
^{40}K depump	$F = 9/2 \rightarrow F' = 9/2$	$F = 1 \rightarrow P_{3/2}$	91	146	0	0		-267

† ^{87}Rb: $5^2S_{1/2} \rightarrow 5^2P_{3/2}$ of ^{87}Rb, ^{40}K: $4^2S_{1/2} \rightarrow 4^2P_{3/2}$ of ^{40}K

‡ ^{87}Rb: $5^2S_{1/2} \rightarrow 5^2P_{3/2}$ of ^{87}Rb, ^{40}K: $4^2S_{1/2} \rightarrow 4^2P_{3/2}$ of ^{39}K

Tab. 4.1: Summary of beams and their optical frequency control.

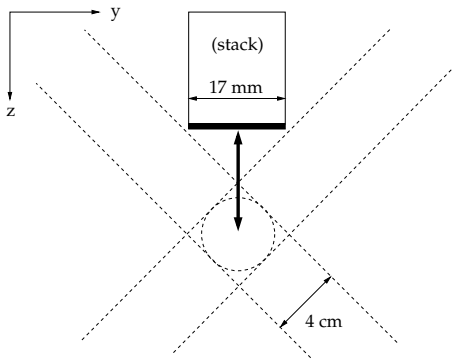

Fig. 4.8: Schematic diagram (not to scale) showing the minimum transfer distance from the MOT to the atom chip surface. The minimum transfer distance (vertical black arrow) is established by aligning the MOT beams (dashed lines) as close to the atom chip as possible without clipping the edge of the chip (horizontal black line). The 4 cm beam diameter and 17 mm chip width constrain the distance to be at least 3.7 cm. Our working distance is roughly 5 cm.

the glass vacuum cell without overly restricting optical access to the cell (i.e. lines of sight for MOT and molasses cooling beams, imaging systems, and probe beams).

Having settled on the idea of trapping atoms in a quadrupole field configuration, the next step was to identify physical and technical constraints, as well as performance criteria for the coils before choosing a final design.

Overcoming gravity in magnetic trapping Levitation of a neutral atom of mass M against gravity requires that the force of gravity $F_g = Mg$ be balanced by an upward force $F = -\nabla U$ from the gradient of the conservative magnetic potential. Using the magnetic potential expression from Eq. 3.5, the magnetic levitation force may be written $F = -\nabla U = g_F m_F \mu_B \frac{dB}{dz}$. Setting this force magnitude equal to $F_g$to results in an estimate of the trapping magnetic field gradient needed to overcome the downward pull of gravity. Using the fact that $g_F m_F = \frac{2}{9} \times \frac{9}{2} = 1$ for the $|F = 9/2, m_F = 9/2\rangle$ state of ^{40}K, and setting the two forces equal yields $\frac{dB}{dz} \doteq 7\,\mathrm{G/cm}$. This result means that any usable magnetic trap for ^{40}K atoms must have a magnetic field gradient of at least 7 G/cm in the vertical direction. The corresponding value for $^{87}\mathrm{Rb}$ atoms in the $|F = 2, m_F = 2\rangle$ level of the ground state is 15 G/cm.

Magnetic transfer distance We transport magnetically trapped atoms from the site of the MOT up to the atom chip. The widths of the atom chip and stack, along with the MOT beam diameter, set the lower bound of this transfer distance at roughly 4 cm (see Fig. 4.8). The MOT beams are aligned at right angles for optimal capture efficiency. In the interest of keeping scattered light to a minimum the atom chip needed to be positioned outside of the MOT beams.

UHV cell diameter and MOT coil separation The 74 mm-wide UHV cell sets a lower bound on the separation of exterior magnetic field coils. The minimum separation affects the final coil

radius since it is desirable to keep the MOT coil geometry close to the anti-Helmholtz geometry[3] to maximize the quadrupole field gradient.

Fast magnetic field switching Loading atoms from one magnetic trapping potential to another requires fine control over the turn-on and turn-off of the individual traps. A rapid and clean turn-off is crucial for time-of-flight absorption imaging. Fast switching of magnetic field coils presents a particular challenge because of the high inductance of large coils. As such, it is important to minimize inductance in the final coil system to allow the large currents eventually required to be switched well within a single atomic oscillation period in the magnetic trap.

4.3.2 Final design: off-coil-centre MOT and magnetic trap

Magnetic fields for the MOT, quadrupole magnetic trap (QMT) and magnetic transfer are generated using three circular coils: a pair of "MOT coils" arranged in anti-Helmholtz configuration, and a single "transfer coil". The MOT coils generate magnetic quadrupole fields suitable for the MOT and the quadrupole magnetic trap. The transfer coil is used to displace the quadrupole field minimum along the z-axis. The MOT and QMT are formed 2.5 cm below the MOT coils' geometric centre. The transfer coil current is then reversed to transfer the magnetically trapped atoms 5 cm vertically (the "transfer distance" of Sec. 4.3.1) to just below the surface of the atom chip. The off-centre MOT, QMT and transport scheme is more than one order of magnitude more power-efficient than a scheme based on a MOT located at the centre of the MOT coils. This point is further explained in Sec. 4.3.2.

Why only one transfer coil? The original design and setup described in [109] used a pair of transfer coils powered in Helmholtz configuration to generate as spatially homogeneous a field as possible. The lower coil of the pair was removed in 2005 after we discovered that it was periodically magnetizing the optical table. This resulted in unacceptable hour-to-hour and day-to-day fluctuations in the radio-frequency trap bottom of the atom chip Z-trap. Removing the lower coil, which had been mounted 120 mm from the optical table and generated fields of up to $\sim$40 G at the table surface, improved our trap bottom stability dramatically.

The MOT coils consist of 100 turns of square, insulated, hollow-core copper wire. The coil inner diameters of 10 cm and outer diameters of 18.4 cm. Their cross-sectional profiles are square. Their inner separation is 8.4 cm. In this configuration the MOT coils generate quadrupole magnetic field gradients of 1.56 G/cm per ampere of DC current, near the trap centre. The transfer coil also has a square cross-section and is made of the same hollow-core copper wire. It has 49 turns, an inner diameter of 28 cm and an outer diameter of 36.4 cm. The transfer coil generates a quasi-uniform magnetic field of 1.6 G/A at the MOT position, and 1.8 G/A at the atom chip surface. The mounting geometry of all three coils is depicted in Fig. 4.9. Their physical and electrical characteristics are summarized in Tab. 4.2.

[3] Coil radius $\approx$ coil separation

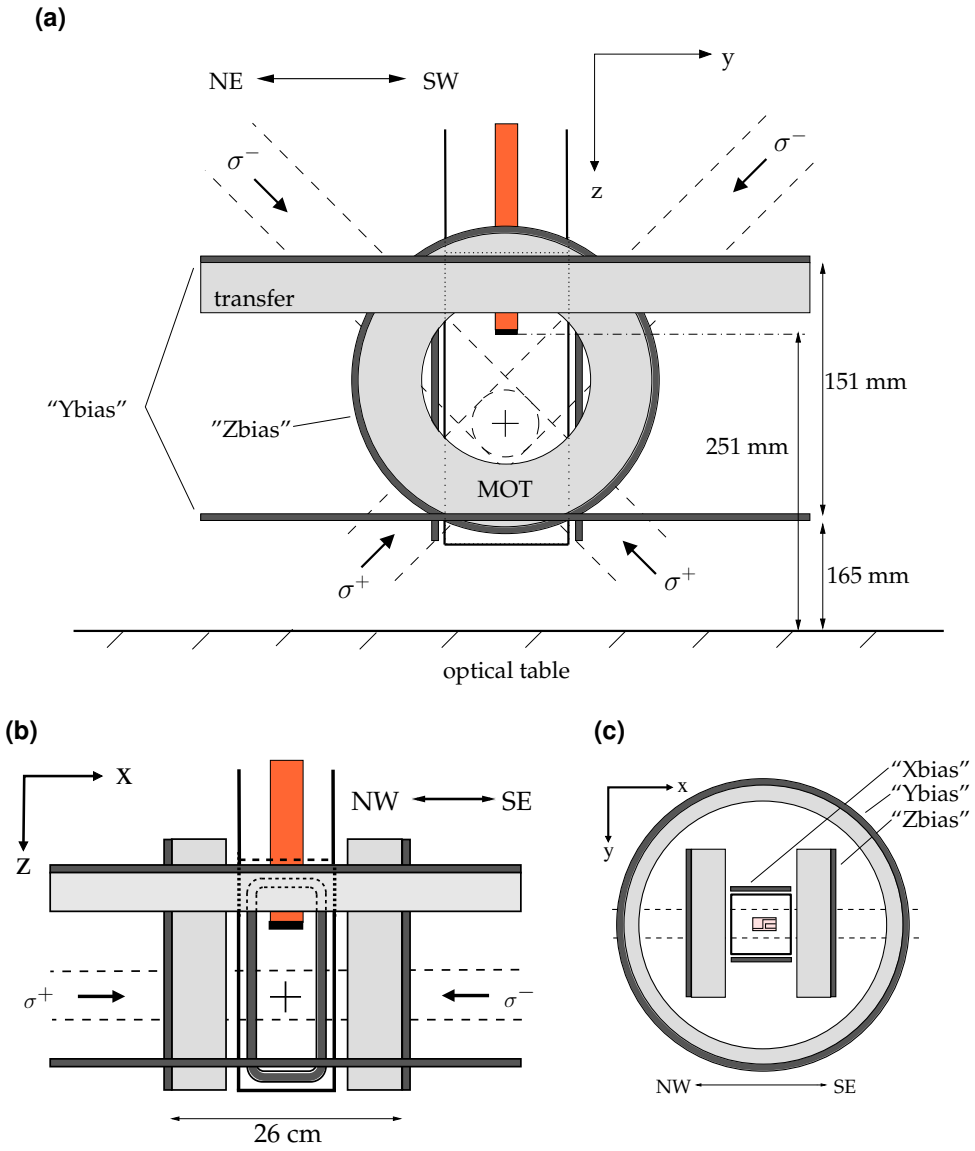

Fig. 4.9: Two side views **(a,b)** and one top view **(c)** of the MOT and coil geometry, showing the Pyrex UHV cell, MOT and transfer coils (light grey), bias coils (dark grey), MOT beams and their polarizations (dashed lines), and the copper stack (copper colour). The "+" indicates the MOT position. See Tab. 4.3 for bias coil name convention.

	MOT	transfer	"Zbias"	"Xbias" (Ioffe)	"Ybias" (up/dn.)
Cu wire type	hollow	hollow	14 AWG	14 AWG	14 AWG
wire length	44 m	47 m	12 m	11 m	21 m
shape	circular	circular	circular	rectangular	circular
inner diam.	10 cm	28 cm	19 cm	7.5 cm×19.5 cm	33 cm
outer diam.	18.4 cm	36.4 cm	20 cm	8.5 cm×20.5 cm	34 cm
inner sep'n.	8.5 cm	n/a	8.5 cm	8.5 cm	13 cm
# turns	100	49	20	20	20
resistance	0.16 Ω (pair)	0.11 Ω	100 Ω	95 Ω	190 Ω
inductance	2.3 mH (pair)	2.8 mH	0.63 mH		1.2 mH
MOT current	7 A	6.1 A	60 mA	10 mA	0.45 A
QMT current	45 A	48 A	60 mA	10 mA	0.45 A
Z-trap current	n/a	n/a	0	0.5 - 4 A	10 A
QMT dB/dx	1.56 G/cm.A †	n/a	n/a	n/a	n/a
field at MOT	7.5 G/A †	1.60 G/A †	2.2 G/A	∼ 1.1 G/A	∼ 1.8 G/A
field at chip	7.0 G/A †	1.83 G/A †	2.2 G/A	∼ 1.1 G/A	∼ 1.8 G/A
power supply	2 × Kepco ATE-25-40M	2 × Kepco ATE-15-50M	FuG NLN 140M-6,5‡	HighFinesse BCS-5/5	HighFinesse BCS-5/5

† Results of analytic calculations that are considered accurate to within ±5% [109].
‡ Modified for fast-switching and reduced current noise by Stefan Myrskog. See text.

Tab. 4.2: Summary of MOT, transfer, and bias coil characteristics.

Construction All three coils were wrapped by hand. The square, hollow-core wire was purchased as bare wire from Wolverine Fabricated Products, Inc.; the double polyester glass insulation[4] (similar to fibreglass) was applied by S&W Wire Co. The square wire was chosen to facilitate the wrapping of large, matched coil pairs. The coil was wrapped around a homemade jig, which we turned by hand in the jaws of a lathe in neutral gear. The stiff wire (see wire cross-section in Fig.4.10a) was bent and tensioned by hand. "20-minute" epoxy was used during wrapping as well as after the coils were complete to stabilize the turns and to maintain the coil's square shape.

Water cooling The maximum operating current and power in the MOT and transfer coils are 100 A at 16 W, and 50 A at 6 W, respectively. The heat load is dissipated by water plumbed through the hollow wire centre. Vinyl water hoses were attached to the square wire using Swagelok hardware and homemade wire-to-Swagelok adaptors (see Figs. 4.10a and 4.10b). Cooling water is sourced from laboratory process cooling water at a pressure of roughly 80 psi (5.4 ATM). The MOT coils are water cooled in parallel, with a net flow rate of ∼9 mL/s through both coils. This scheme easily provides adequate water cooling for our purposes: in steady state operation[5] the exit water temperature is only 2 – 3°C warmer than the input temperature. During normal operation, the coil temperature is thus stabilized at roughly 9°C in winter and 13°C in summer (the cooling water input temperature varies slightly with the seasons).

[4]The insulation is can withstand temperatures up to 155°C and has a dielectric breakdown voltage of roughly 500 V.

[5]In a typical cycle, the coils bear low currents for the MOT for 5 - 30 s, followed by high currents for the QMT for 400 ms in a total cycle of anywhere between 8s and 40 s. See Tab.4.2.

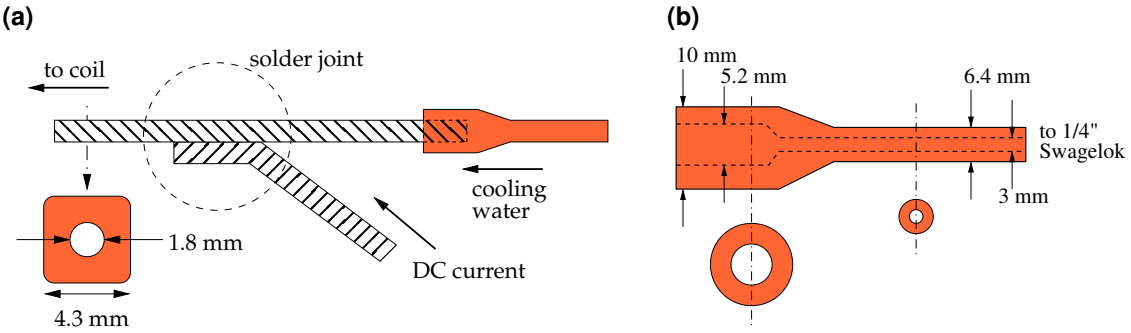

Fig. 4.10: (a) Electrical and water cooling connections for MOT and transfer coils. Downstream of the water cooling adaptor, a second length of square hollow-core wire is used for the electrical connection to maximize surface contact between the two wires, which are connected by direct soldering. The diagram also shows a cross-section of the hollow-core wire (not to scale). **(b)** Schematic diagram showing the dimensions of the copper adaptor between water cooling plumbing and the square hollow-core wire. The wide end of the adaptor accepts the stripped end of the wire, which is attached (and water sealed) using solder. The water cooling plumbing is connected using 1/4" Swagelok fittings on the small end of the adaptor.

Advantage: power efficiency The most significant advantage of this off-centre MOT setup is its power efficiency. The off-centre MOT saves over an order of magnitude of power as compared to a setup based on a conventional centred MOT.

Analytic calculations of the quadrupole field showed that the magnetic trap formed in the centre could by shifted by applying a uniform bias field, but only to a certain distance. Using a coordinate system with $z = 0$ defined at the geometric centre of the MOT coils, the trap centre can be shifted up to $z = \pm R/2$, where R is the coil radius, without a significant reduction in the trap depth or quadrupole field gradient. Shifting beyond $|z| > R/2$ resulted in a decreasing trap depth and magnetic field non-linearity.

Given the constraints on the maximum safe magnetic transfer distance $R/2$ and the minimum required transfer distance d, we might have tried setting the coil MOT radius equal to twice the desired transfer distance: $R/2 = d$. In such an arrangement the MOT and magnetic trap would be located at the centre of two quadrupole coils ($z = 0$) and could be safely transferred vertically to $z = R/2$. The coil size and power dissipated is considerably reduced, however, if the MOT and magnetic trap are positioned *off-centre* with respect to the MOT coils - specifically at $z = -R'/2$ and $R' = d$. Under this scheme, which is the one adopted in our experiment, atoms move from below to above centre of the MOT coils – $z = -R'/2 \rightarrow z = +R'/2$. This allows the coils themselves to be *one half the radius* for a given transfer distance d, and thus to dissipate *one sixteenth* the power compared with coils having $R/2 = d$.[6] As an additional advantage, the net inductance of the MOT coils is greatly reduced by reducing their size and current, which enables much easier and faster switching of large DC currents.

[6]For a circular coil, $P \sim I^2$, $I \sim r^2$ and $B \sim I/r^2$, where P, I, R, r and B represent electrical power, current, resistance, coil radius and magnetic field amplitude. For a fixed magnetic field B, halving the coil radius means the current must be decreased by a factor of four. A factor of four decrease in current in turn implies a factor of 16 decrease in the dissipated power.

Circuit and switching The MOT and transfer coils are powered by Kepco, Inc. linear DC power supplies. The MOT coils use two model ATE-25-40M supplies connected in a parallel master-slave configuration to deliver up to 80 A to the MOT coils. The transfer coil is powered by a similar arrangement of two ATE-15-50M supplies for a maximum achievable DC current of 100 A. The supplies are computer-controlled by the ADwin sequencer and switched the custom-built Mag-O-Matic switch, designed and built by our research technologist Alan Stummer.[7]

Several phases of the experiment require fast switching of the magnetic trap coils. In order to load atoms from the MOT into the magnetic trap, the coils must be turned off quickly to create a zero-field condition for optical molasses, and then turned on quickly to high current for efficient loading of the magnetic trap. Fast turn-off is also necessary when imaging the atoms in order to avoid heating, distortion of the cloud, and Zeeman shifts of the atomic energy levels.

Mag-O-Matic operation The necessary time scale for coil switching is determined by the motion of atoms in the trap: magnetic fields should be switched in less time than a single classical oscillation period to avoid excessive heating. At 3 mH inductance and 60 A of current, voltages up to 1 kV are required to achieve sub-millisecond switching times.

Fig. 4.11 shows a schematic of one of the Mag-O-Matic switches designed for switching large DC currents. The full Mag-O-Matic consists of two nearly identical switches, one for the MOT coils and the other for the transfer coil. The difference is the role of the relay: the MOT relay can be used to toggle the current directions between Helmholtz and anti-Helmholtz configurations; the transfer relay toggles the current direction in the single transfer coil. When the coils are operating in steady state, the IGBT (insulated gate bipolar junction transistor) stack is on and the coil supplies are running in constant current mode. The current flows through the blocking diode, the coils, the IGBT stack, and a giant magneto-resistive (GMR) current sensor. The sensor is used for quantitative monitoring only.

The coils are turned off by turning the IGBT stack off. The counter- EMF ("flyback") caused by the inductance of the coils produces a high voltage spike which is clamped by the transient voltage suppressors (TVS) at about 940 V. The coil current is dissipated at 0.4 A/µs, as shown in Fig. 4.11.

There are two ways to turn on the coil current. If the IGBT stack alone is turned on, the current will rise asymptotically to the steady-state value in roughly 20 ms. The other turn-on method – the "fast on" – works as follows. At any time before the fast turn-on is needed, the high voltage (HV) supply is used to charge up the HV capacitor. Fast turn-on is triggered by first turning on the IGBT stack, and then triggering the HV silicon controlled rectifier (SCR). In the few microseconds between these two events, no significant current flows due to the coil inductance. Triggering the SCR creates an LC parallel resonant circuit with the coil inductance and the HV capacitor. During the *first quarter-cycle* of the resonance, roughly 350 µs, the capacitor transfers its charge to the coil (see Fig. 4.11). The charge on the capacitor is chosen such that after this quarter-cycle the coil is at its steady state voltage, and the blocking diode of the supplies will

[7] See www.physics.utoronto.ca/∼astummer for Alan's wonderful documentation of this and many other projects.

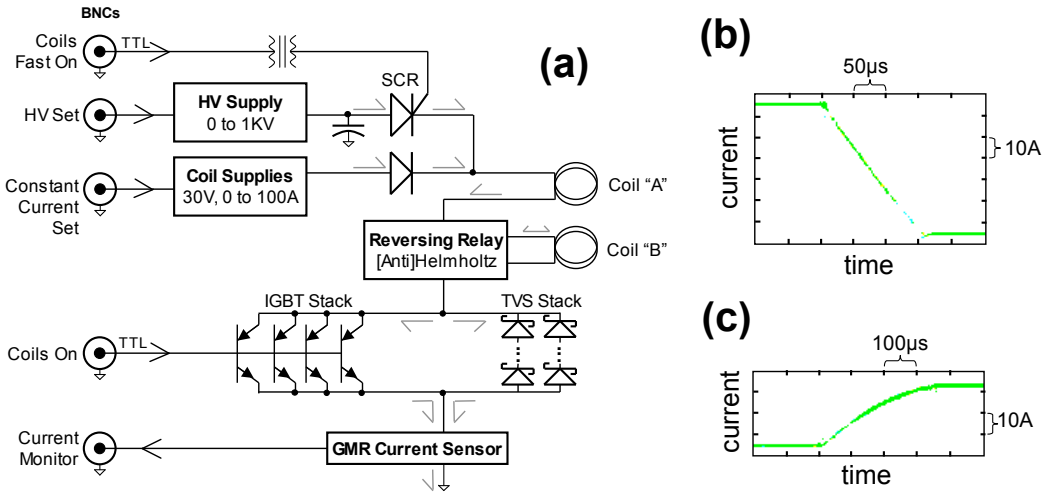

Fig. 4.11: **(a)** Schematic circuit diagram of the Mag-O-Matic switch for the MOT coils. The primary switch is a stack of insulated gate bipolar junction transistors (IGBT's). Turn-on is accelerated with a high voltage (HV) charge in a capacitor, whose discharge is triggered using a silicon controlled rectifier (SCR). Turn-off is accelerated with transient voltage suppressors (TVS's). Current is sensed using a giant magneto-resistive (GMR) current sensor. Arrows indicate the direction of controls and monitors; half arrows indicate coil currents. **(b)** Turn-off performance: current falls from 60 A to zero in 150 µs. **(c)** Turn-on performance: rise of current from 0 to 26.5 A in 350 µs.

conduct to provide the steady state current. The SCR turns off when the current flowing through it falls to zero.

4.3.3 Bias coils

In addition to the MOT and transfer coils, three pairs of much smaller coils are used to control the background magnetic field environment at the site of the MOT and chip magnetic trap. In particular, the coils are used to null the environmental field during optical molasses cooling, and to provide the uniform "bias" and "Ioffe" fields for the atom chip microtrap (see Ch. 3).

Each pair of coils is wired in series and produces a uniform magnetic field along one of the three experiment axes x, y or z. For historical reasons[8], we refer to the three pairs as"Xbias", "Ybias" and "Zbias", respectively. This thesis uses coordinate axes based around the atom chip, with the z-axis corresponding to the direction of gravity, but keeps the historical bias coil names (which are still de rigueur in the lab). See Tab. 4.3 for name clarification.

All bias coils were wrapped by hand using insulated 14 AWG copper wire. Fig. 4.9 shows the shape and placement of the bias coils. Their physical and electrical specifications are summarized in Tab. 4.2. The Xbias and Ybias coils are powered by HighFinesse GmbH model BCS-5/5 low-noise, bipolar constant current linear supplies. Current ripple in the BCS-5/5 output is rated as 10^{-4} of the output current, maximum. The Zbias coils are powered by a FuG GmbH model

[8]The bias coils were originally named according to MOT-centric experimental coordinate axis definitions, in which the strong axis of the MOT coils is Z, the vertical direction Y, and the longitudinal (Ioffe field) axis of the Z-trap X.

lab/coil name	axis (thesis coordinates)	function/direction
"Zbias"	x	Z-trap holding field
"Xbias"	y	Z-trap Ioffe field
"Ybias"	z	vertical bias field

Tab. 4.3: Bias coil/field name conventions.

NLN 140M-6,5 linear power supply. This supply was modified by Stefan Myrskog to allow for sub-millisecond switching while maintaining a low output voltage ripple.

4.4 Radio-frequency sources

After loading atoms into the Z-trap, we achieve quantum degeneracy in $^{87}\mathrm{Rb}$ and $^{40}\mathrm{K}$ using forced radio-frequency (RF) evaporative cooling. RF radiation is also used as a tool to manipulate and spatially form the Z-trap magnetic potential – in particular, to create double well potentials (see Ch. 6). In both cases, one or more atom chip wires serve as near-field RF antennae, to which RF electronics are connected on the air side of the experiment. This section describes our direct digital synthesizer (DDS) -based RF sources and their accompanying amplification and switching circuits.

4.4.1 DDS basics

While many quantum gas experiments use standard commercial function generators as RF sources, such devices typically have dwell times and switching times of 10 ms or greater, rendering them unable to sweep quickly enough for an on-chip evaporation that may last only one second. Instead we generate RF fields using DDSs, which have sufficient frequency sweep speed and precision for our applications, at a fraction of the cost of a complete high-frequency function generator. A DDS creates a sinusoidal waveform digitally (point-by-point), which is then sent through a digital to analog converter. Using dividers implemented in digital logic, any frequency from μHz up to the Nyquist frequency (150 MHz in our case) can be generated with 48-bit resolution. Linear sweeps can be produced by specifying the start and stop frequencies, the number of frequency steps, and the step time. Since no phase-locked loop is involved, the sweep speed is effectively unlimited.

4.4.2 RF for evaporative cooling

A schematic diagram of our RF evaporation source is depicted in Fig. 4.12. A listing of parts and functions is given in Tab. 4.4. All components from the DDS up to the load are connected via coaxial BNC and/or SMA shielded cables.

Fig. 4.12 also gives circuit detail of the load, which consists of the atom chip antenna wire ($R \approx 1\,\Omega$), contact resistance and other small losses (net $\approx 2\,\Omega$) and a $47\,\Omega$ resistor added in series

part	function	device†
DDS	RF source	AD9854 evaluation board (AD)
VCA	voltage-controlled attenuator, RF amplitude control	ZAS-3 (M)
transformer	block DDS DC bias	FTB-1-1 (M)
switch	RF on/off	ZASWA-2-50DR (M)
amp.	amplification	ZHL-3A (M)
cpl.	directional coupler, signal monitor	ZDC-20-3 (M)
DC blk.	block amp. DC bias	BLK-89+ (M)
lo-pass	low-pass filter	BLP-15 (M)
combiner	for other RF manipulation	ZA3CS-300-3W (M)

† AD = Analog Devices, Inc., M = Mini-Circuits

Tab. 4.4: RF evaporation chain hardware.

for impedance matching. The capacitors in the signal and ground lines serve as additional high-pass filters. The 47 Ω resistor and capacitors are bundled together in an impedance-matching package called "Lindsay's box" (an updated version of "Ian's box") outside of the UHV chamber.

The DDS frequency and amplitude are controlled via digital programming on five serial control lines from the control software and sequencer. All frequency sweeps are programmed in the experimental control software GUI. A voltage-controlled attenuator on the DDS output is used for fine and/or dynamic amplitude control. A more coarse, stepwise amplitude control is also possible by directly programming the DDS. Forced RF evaporation is carried out with a series of linear frequency sweeps, which together approximate an exponential frequency sweep.

The Analog Devices AD9854 DDS evaluation board supplies signals with amplitudes up to -12.5 dBm (54 mV rms) at frequencies from several mHz to 150 MHz. Adding the linear RF amplifier allows the full RF circuit to source amplitudes up to 9 dBm (640 mV rms). This maximum corresponds to a RF current amplitude of roughly 20 mA in the chip wire antenna, a magnetic field amplitude of roughly 160 mG and a Rabi frequency $\Omega_R = \frac{1}{2}\mu_B B \approx 110$ MHz for atoms trapped 200 µm from the chip surface. (The distance from the RF antenna wire the an atom cloud trapped 200 µm below the centre of the Z-wire is 247 µm (see Sec. 4.6.1). We typically use RF amplitudes of 430 mV rms or less during evaporation.

At some point upstream of the antenna wire, a coaxial cable was cut and opened up so that the tip and shield could be connected to the antenna wire directly. In the Orsay stack, this was done at a multi-pin electrical feedthrough. RF is piped into the UHV system via a DC feedthrough pin, down to the atom chip via insulated copper wire, through the chip wire, and back up to the air side in the same way. In the Toronto stack (in anticipation piping microwave radiation onto the chip for future work) SMA vacuum feedthroughs are used to bring RF into the UHV chamber. UHV-compatible coaxial cable (Kapton and Teflon-insulated, from Allectra Inc.) bring the RF signal right to the atom chip. This vacuum coax is cut and split just a few centimetres from the chip surface to allow connections to the antenna wire (see Sec. 4.6.2).

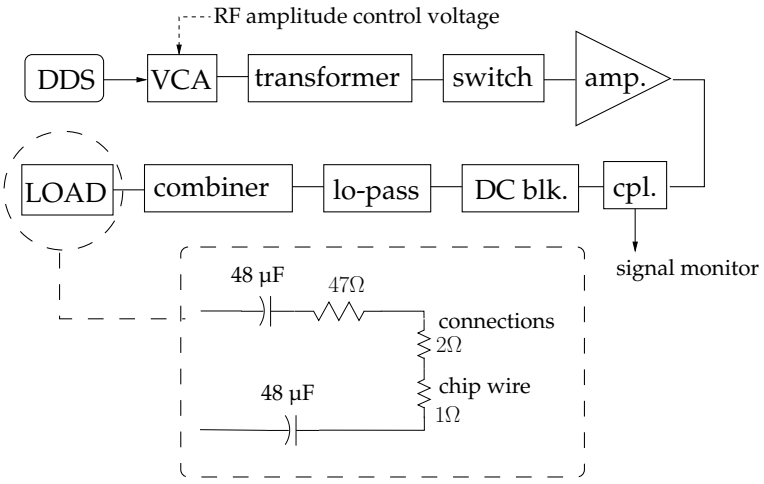

Fig. 4.12: RF evaporation chain. The load consists of the impedence-matching Lindsay's box (see text) and the chip antenna wire.

4.4.3 RF for double well potentials

Our first attempts at creating RF dressed adiabatic potentials (see Ch. 6) used the RF evaporation circuit described in Sec. 4.4.2, including the RF evaporation wire on the Orsay chip. After changing to the Toronto chip, we began using *two* RF antennae to produce RF double-well potentials, and supplied RF using a new RF circuit based on a two-channel RF source.

2-channel RF source: PhaseOMatic The PhaseOMatic is a RF source designed for the double-well relative atom number and relative phase experiments described in Ch. 7.[9] It supplies two adjustable RF signals with independent amplitude control, tunable relative phase from 0 to 2π, and control of the RF phase at turn-off.

The idea of monitoring and controlling the phase of the RF dressing field at turn-off was suggested to us by the Ketterle group as a way of stabilizing interference experiments (see [31], for example). The amplitudes of the bare $|m_F\rangle$ components in an RF-dressed state $|m'_F\rangle$ depend on the RF phase. Fixing the phase at the moment of turn off should ensure that the atoms are in the same superposition at the beginning of each time-of-flight. The effect of the PhaseOMatic-locked phase versus the random phase has thus far been small, likely because the experiment is dominated by other sources of noise such at temperature and atom number fluctuations from cycle to cycle.

The PhaseOMatic is based on an Analog Devices AD9854 300 MHz DDS evaluation board, identical to the one described in Sec. 4.4.2. The AD9854 board supplies two RF outputs exactly $\pi/2$ out of phase, which are mixed and amplified to generate the phase-tunable PhaseOMatic outputs. Referring to the AD9854 outputs as $\sin\omega t$ and $\cos\omega t$, Fig. 4.13 illustrates schematically how the two signals are combined to form the PhaseOMatic output. The inputs α, β, γ represent amplifier gains (in practice, voltage inputs to voltage-controlled amplifiers) and also the resulting

[9] See www.physics.utoronto.ca/∼astummer for more technical detail.

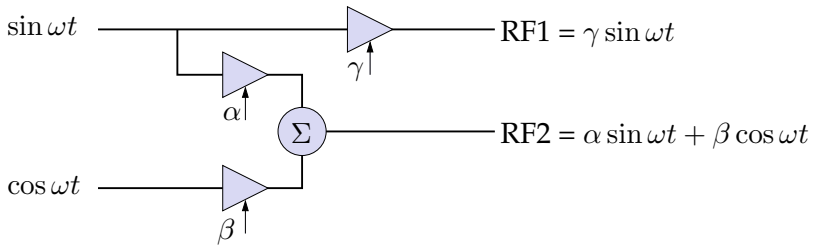

Fig. 4.13: Conceptual schematic of PhaseOMatic dual RF source with tunable amplitudes and relative phase.

signal amplitudes.

If α and β can be tuned from -1 to 1, then the relative phase between outputs RF1 and RF2 ranges from 0 to 2π. Though α and β also control the total RF2 amplitude, they may be carefully chosen so that the relative phase ϕ between RF2 and RF1 may be tuned while keeping the amplitude of RF2 fixed. Choosing $\alpha \propto \cos\phi$ and $\beta \propto \sin\phi$ makes this so. γ is completely independent of α and β, so that the amplitudes of RF1 and RF2 can be tuned independently over their full range of 0 to 200 mV rms per channel.

Another feature of the PhaseOMatic is a delayed trigger signal for switching off RF signals at a well-defined phase of the radiation. RF signals are switched off by TTL control voltages sent to the PhaseOMatic, which relays them on to RF switches downstream. The PhaseOMatic monitors the RF phase in real time, and delays the turn-off TTL signal until the RF reaches a user-defined phase in its cycle. Buffering the TTL control signal in this way ensures that the turn-off of RF radiation experienced by the atoms is constant from experiment to experiment. Though this results in a variable cycle time, the variation is negligible since the TTL signals are delayed by at most one RF period, e.g. 1 µs for a 1 MHz RF frequency. Fig. 4.14 demonstrates the stability of the TTL-turn off-signal with respect to input signals arriving at random times from the ADwin.

Frequency and amplitude programming of the PhaseOMatic's DDS are carried out using a microprocessor core module (RCM3200 RabbitCore from Rabbit Semiconductor) built into the PhaseOMatic and connected to the experimental control PC via Ethernet (rather than using serial programming through the ADwin, as in the RF source of 4.4.2). "Rabbit" control of the DDS is much faster than serial ADwin programming, which allows faster and more accurate frequency sweeps.

The RF for dressed potentials is delivered to the Toronto chip via two independent amplifier chains, as depicted in Fig. 4.15. As with the RF evaporation chain, RF splitting circuit is interconnected using coaxial BNC and/or SMA cables and connectors. Tab. 4.5 lists the components of the RF splitting circuits. RF is delivered into the chip wires through DC electrical feedthroughs on the stack multi-port flange, and down into the chip in Kapton-insulated copper wires.

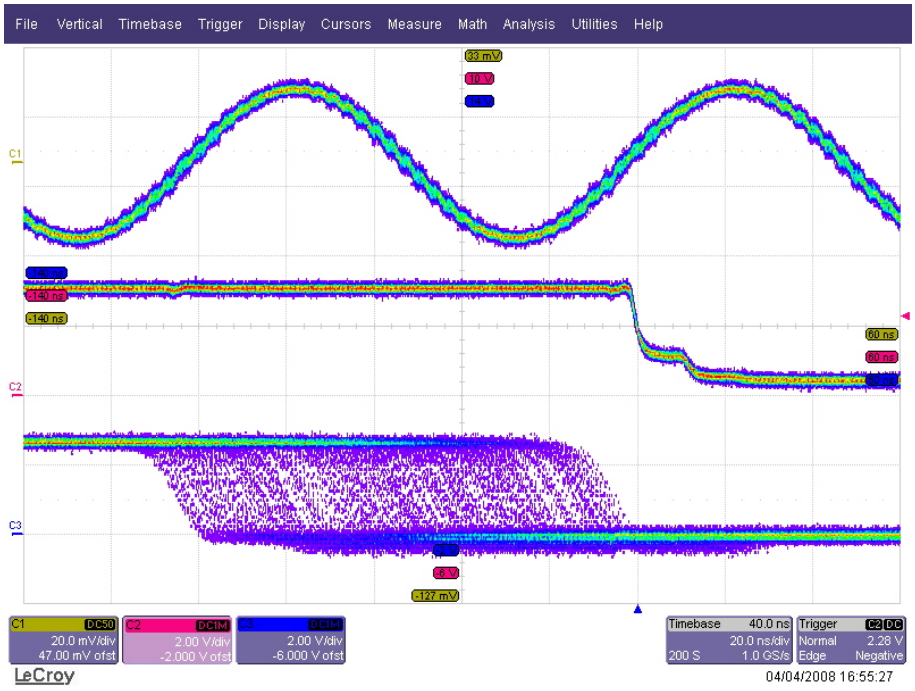

Fig. 4.14: Characterizing controlled RF phase turn-off with the PhaseOMatic, from an oscilloscope screen capture. The timebase (horizontal axis) is 20 ns/div. The upper trace is the RF signal monitor at 10 MHz. The lower trace shows TTL falling-edge "off" signals arriving at random times over 100 ns. The middle trace shows the delayed TTL output signals, which are all overlapped and fall onto a single trace at a fixed point in the RF waveform. In this example, the falling-edge of the "off" signal occurs when the RF signal rises through its point of maximum slope.

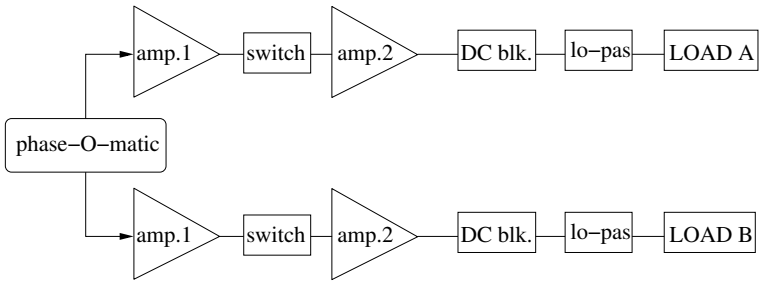

Fig. 4.15: RF splitting chain. LOADA and LOADB each consist of a 47 Ω impedence-matching resistor, stack electrical connections, and a chip wire – typically the matched "U" or "bar" wires (see Fig. 4.20).

part	function	device†
phase-O-Matic	dual RF source	homemade using AD9854 DDS, see text
amp.1	amplifier	ZHL-32A (M)
switch	RF on/off	ZASWA-2-50DR (M)
amp.2	10 W amplifier	HF10-0130 (R)
DC blk.	block amp. DC bias	BLK-89+ (M)
lo-pas	low-pass filter	BLP-70 (M)

† R = Richardson Electronics Ltd., M = Mini-Circuits

Tab. 4.5: RF splitting chain hardware.

4.5 Imaging systems

Time-of-flight absorption imaging is the primary method of detecting cold atomic clouds in this thesis. The basic elements of this type of imaging are a probe laser beam, an imaging system which collects and focuses the transmitted and scattered probe light, and a CCD camera which records the resulting image. This section describes two generations of imaging systems. The first, based on simple 1:1 telescopes and MicroPix M640 CCD cameras, was in place from 2004 to 2007, and was used to produce the BEC and DFG data presented in Ch. 5. The second generation uses additional 4X microscope objective lenses and faster, more versatile, low-read-noise Princeton Instruments Pixis 1024BR CCD cameras. This upgraded imaging system was used to collect the RF double well data presented in Ch. 7.

In both generations, two separate imaging systems are used to observe atomic clouds along the x and y axes (see Fig. 4.16a) below the chip. These imaging directions are referred to as "axial" and "radial" throughout. The "axial" imaging system uses a probe beam directed along x, and produces absorption images in the yz plane. The "radial" imaging system uses a probe beam directed along y, and produces absorption images in the xz plane. Probe beams are directed into the UHV cell, through the atom cloud, and into the imaging systems along a horizontal path skimming just below the chip surface.

4.5.1 1st generation: BEC and DFG data

Our first imaging systems were simple 1:1 telescopes. Both lenses in each imaging system were identical 1" achromatic doublets designed for near infrared optical wavelengths. The radial imaging system uses Thorlabs AC254-100-B lenses, while the axial uses Thorlabs AC254-075-B lenses (labelled "L1" and "L2" respectively in Fig. 4.16a). We estimate the optical resolution to be between 10 µm and 20 µm for both systems. A ray-tracing simulation[10] predicts best-case (on-axis, perfect focusing) diffraction-limited optical resolutions of 6 µm and 8 µm for our axial and radial systems, respectively. The discrepancy between the theoretical minimum resolutions and our larger working resolutions is attributed to imperfect probe beam and imaging system alignment (i.e. not using the system exactly on-axis), and to a lesser extent, imperfect focusing.

The numerical apertures (NA) of the radial and axial imaging systems are approximately 0.13 and 0.17. The NAs are limited by our inability to position the 1:1 imaging system closer to the atoms due to (a) the 74 mm width of the UHV cell, and (b) the need to keep imaging optics out of the path of the 4 cm-diameter diagonal MOT beams (see Fig. 4.9).

Alignment and focusing The imaging systems were built using 1" lens tubes and optomechanics. Before mounting the imaging systems in the experiment, the intra-lens distances are set using a collimated test beam (a perfect 1:1 imaging system produces collimated output with collimated input). The imaging system is focussed by fixing the CCD-to-lens distance and scanning the

[10]The analysis was performed by Vincent Kan using ZEMAX software. His report on imaging system performance is available from our research group webpage www.physics.utoronto.ca/∼jhtgroup.

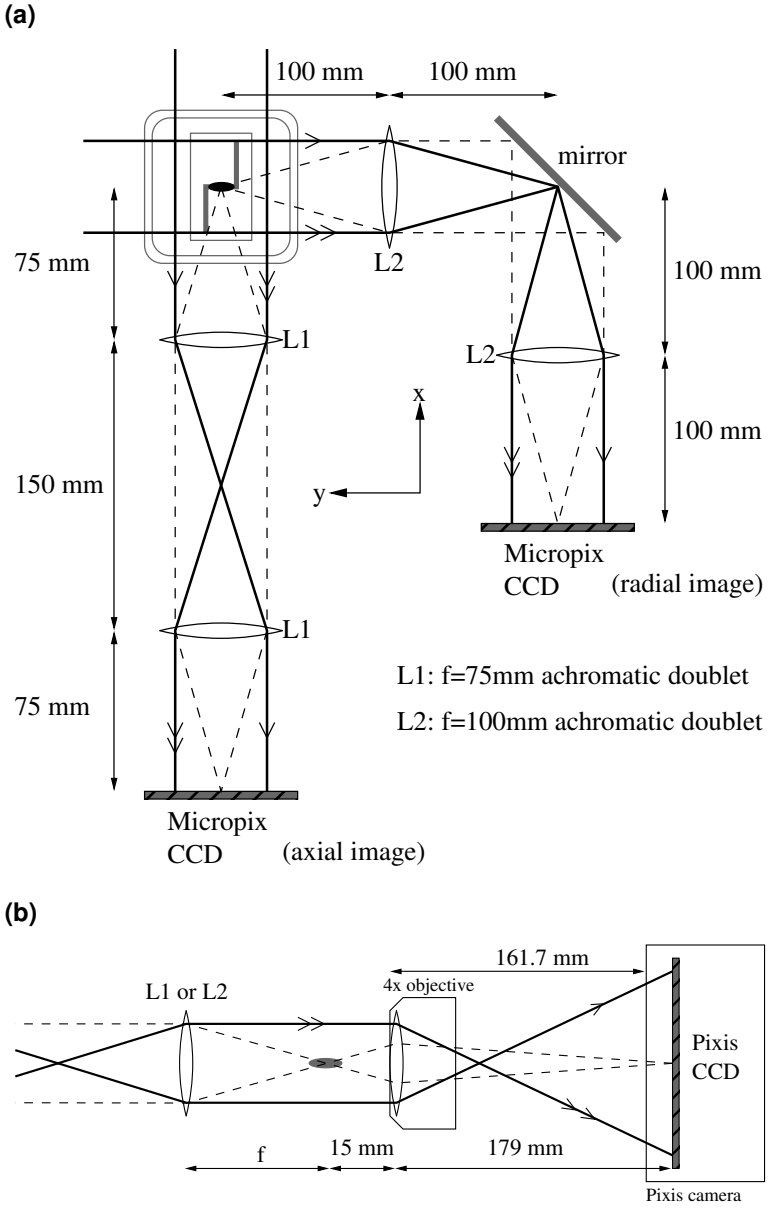

Fig. 4.16: **(a)** Radial and axial imaging systems with MicroPix M640 CCD cameras, schematically drawn looking up at the chip surface along the $-z$ direction. The "object" of the imaging system is a cold cloud of atoms (black ellipse) trapped beneath the chip surface, which is shown along with an outline of the UHV cell. **(b)** 2nd generation imaging system (see text). Same as in **(a)**, but with added 4x microscope objective and Pixis CCD camera. The objective is placed at a working distance of 15 mm from the image (grey ellipse) formed after the second lens ("L1" or "L2") of the 1:1 imaging systems in **(a)**.

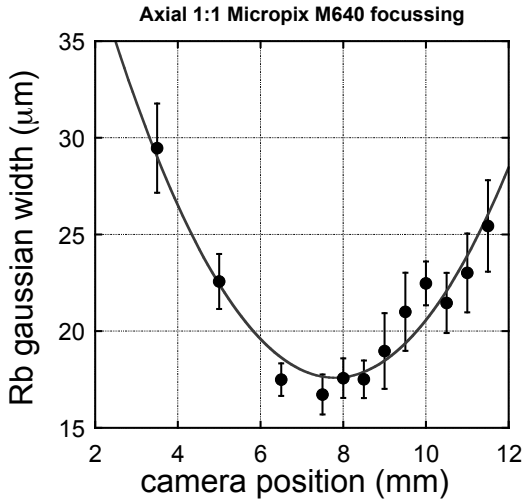

Fig. 4.17: Axial imaging system focusing with MicroPix M640. The $^{87}\mathrm{Rb}$ cloud size measured with a gaussian fits of absorption images taken after 3 ms time-of-flight. The focussed camera position is taken to the be point of minimum observed cloud size. Error bars correspond to the standard deviation of repeated measurements.

lens-to-atom distance manually while recording the apparent size of a cold $^{87}\mathrm{Rb}$ cloud in the resulting images (see Fig. 4.17). The focussed position is taken as that which produced the smallest apparent cloud size.

CCD camera and image acquisition The CCD cameras were MicroPix M640 12-bit 480×640 pixel models with 7.4 µm ×7.4 µm pixels. The M640 has a maximum image rate (full-frame readout and reset) 30 Hz, which limited the time between successive exposures of the CCD to at least 33 ms. The camera exposure is triggered by the experiment's ADwin sequencer. Images were retrieved via a FireWire connection, and analyzed on a Windows PC using homemade software written by Dr. Seth Aubin.

4.5.2 2nd generation: double well data

The change to the second generation imaging system was precipitated by an upgrade in CCD camera technology to a Pixis 1024BR from Princeton Instruments. The goal was to reduce imaging noise in double well data (see Ch. 7). To compensate for the Pixis's larger 13µm × 13µm pixels, a 4x microscope objective was introduced to decrease the effective pixel size to 3.25µm × 3.25µm . The objective is positioned between the second lens of the 1:1 telescope and the CCD camera (see Fig. 4.16b), extending the path length of the imaging system significantly. Since the 1:1 telescope portion of the imaging system are identical to of the 1st generation system described in Sec. 4.5.1, the numerical aperture and optical resolution are unchanged.

Alignment and focusing The objective lens is rigidly fixed to the 1:1 telescope using optomechanics. Focusing is carried out using the same procedure described in Sec. 4.5.1, but with the added complication that the the Pixis camera is not attached to the lens assembly. (Unlike the

MicroPix camera, which is lightweight enough to be attached directly to its imaging system, the ~ 1 kg Pixis is supported independently.) As a result, the Pixis position along the imaging system axis needed to be manually adjusted to keep the CCD-to-objective distance fixed as the lens-to-atom distance was scanned for focusing.

CCD camera and image acquisition The Princeton Instruments Pixis 1024BR is a 16-bit, back-illuminated CCD camera with an 87% quantum efficiency at 780 nm. The CCD is an 1024×1024 array of 13 µm square pixels. The read noise is quoted by the manufacturer to be as low as 4 photoelectrons (with the CCD cooled to -70° with a thermoelectric cooler) out of a single-pixel well depth of 9×10^4 photoelectrons.

The most beneficial feature of the Pixis for this work is its ability to rapidly expose multiple frames. Though the actual CCD readout is slow (between 0.5 s and 2 s for the full frame, to ensure low read noise), the camera allows multiple rapid sub-exposures of the CCD array in "Kinetics mode" – i.e. to collection of multiple images – which are then read-out slowly and all together after all imaging is complete. The sub-images are exposed one at a time on an $n \times 1024$ pixel strip of the CCD, where $n = 1024 \div$ number-of-sub-images; $n = 1$ corresponds to a full frame exposure. The time between successive sub-image exposures can be anywhere from 3.2 µs for 1024 $n \times 1024$ pixel sub-images (far too narrow a strip to capture our atomic signals) to 1.6 ms for two $n \times 1024$ sub-images. We typically use four or eight sub-images, allowing us to take successive images every 820 or 410 µs. This rapid exposure dramatically decreases background fringes in image data due to vibrations in the imaging system as compared to the 1st generation imaging system (see Sec. 4.5.1).

The Pixis image exposures are triggered using the experiment's control sequencer. CCD image data is acquired using a USB 2.0 connection and homemade control and analysis software on a Windows PC written by myself and Gaël Varoquaux [110] during his 2006 visit.

4.6 A tale of two atom chips: Orsay and Toronto

The experiments described in this thesis were carried out at the University of Toronto with two different atom chips. The first chip - the "Orsay chip" - was installed in the UHV system in August 2004. The chip was designed and fabricated at the Laboratoire Charles Fabry de l'Institut d'Optique[11] [111, 93]. It was used to trap ^{87}Rb and evaporate to BEC, and to trap ^{40}K and sympathetically cool ^{40}K to DFG for the first time on an atom chip [27]. The Orsay chip also was used to create adiabatic RF-dressed potentials for ^{87}Rb and ^{40}K for the first time in our lab. The second atom chip - the "Toronto chip" - was designed over the summer of 2006, fabricated at the University of Toronto's Bahen Centre clean-room facility throughout 2007 by Barbara Cieslak and Dylan Jervis [112], and was installed in the system in January 2008. Using the Toronto chip, we re-established BEC and DFGs, as well as RF-dressed double-well potentials. The Toronto chip was used for the bulk of the double-well BEC atom number and phase measurements presented

[11] Though the group has relocated from Orsay to Palaiseau, France, we still refer to the "Orsay chip".

in Ch. 7. This section describes the conductor layout, material composition, and supporting electrical and mechanical infrastructure of the two atom chips.

4.6.1 Orsay chip

Construction and wire pattern The Orsay chip consists of gold wires electroplated onto a cleaved 16 mm × 28 mm ×600 µm silicon substrate. The chip was patterned using photolithography, with the metal wires deposited by evaporation and electroplating. A 20 nm titanium adhesion layer and 200 nm gold seed layer were evaporated onto the SiO_2 surface oxide, followed by solution electroplating of gold to a final wire height of 6 µm. The final result is a mostly bare silicon substrate hosting eight gold electrical contact pads connecting five separate conductors on its surface [111]. Advice from l'Institut d'Optique suggested a 5 A maximum continuous DC current as a safe upper bound for the thick U and Z-wires. We took this as a guide and used voltage dividers to limit the wire currents to 5 A in the U-wire and 2 A in the Z-wire.

We use two of the five chip wires in the work presented here, highlighted in dark grey in Fig. 4.18a. The central Z-wire forms the basis of our static micromagnetic trap. An adjacent, thinner wire is used as a near-field antenna for delivering RF and microwave fields to the trapped atoms.

Electrical and mechanical connections The Orsay chip was fastened to a copper support "stack" without glues or screws, but by mechanical pressure only. Ceramic C-clamps pressed flat trips of beryllium-copper (BeCu) foil onto the gold contact pads to make the electrical connections, while at the same time pressing the chip onto a polished copper surface (see Fig. 4.18b). The C-clamps, machined in the Toronto chemistry department's machine shop out of the machinable ceramic MACOR, pressed the chip onto the stack end at three corners of the chip.

The BeCu foil strips are connected to ceramic-insulated copper wires[12] which carried currents from the air-side electrical feedthrough into the UHV chamber and onto the chip. **Note** Although ceramic-insulated wires can be baked much hotter than Kapton-insulated wires, we switched to Kapton insulation for the Toronto stack because of a magnetic nickel coating beneath the ceramic, which made the Orsay stack and chip connections susceptible to magnetic field pickup.

Orsay chip stack The copper support "stack" provided rigid support for the atom chip in vacuum, and also supported the electrical connections to the chip. The atom chip was pressed onto one end of the stack, and the other end was bolted into the vacuum side of a 6" Conflat vacuum flange. (see Fig. 4.19). The stack was designed to meet three objectives: first, be mechanically rigid to avoid Z-trap heating due to mechanical vibrations of the atom chip; second, be a good thermal conductor to heatsink the chip during operation; and third, to support electrical connections for the atom chip and atom dispensers.

[12] 18 AWG "Kulgrid" from Ceramawire.

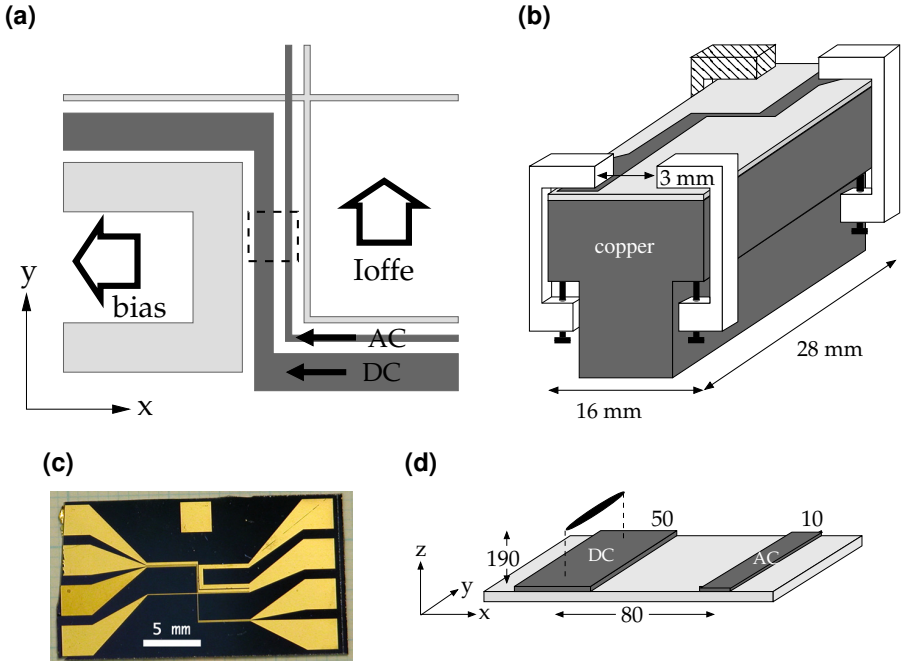

Fig. 4.18: Orsay chip conductor pattern and mounting schematic diagram. **(a)** Central atom chip conductor pattern, highlighting the Z-wire ("DC") and adjacent, thinner antenna wire ("AC") in dark grey. Thick arrows indicate the directions of external, uniform magnetic fields. **(b)** The atom chip is pressed onto a fly-cut copper block using ceramic MACOR C-clamps (white). The shaded clamp was part of the original design, but broke during mounting and was not used. **(c)** Photograph of the full Orsay chip, showing full conductor pattern and electrical contact pads. **(d)** Close-up view of dashed region in **(a)**, showing wire widths, centre-to-centre separation, and location of the trapped atomic cloud (black ellipsoid). All dimensions are in micrometres. Electrical connections are not shown.

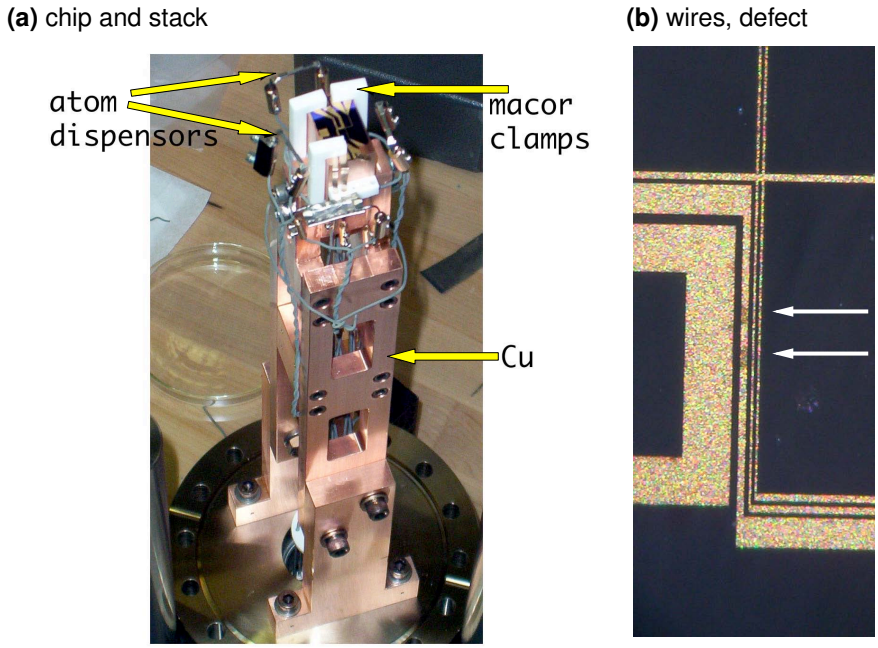

Fig. 4.19: (a) The copper Orsay stack bolted to a 6" steel Conflat electrical feedthrough UHV flange, showing electrical connections to the chip and to rubidium and potassium dispensers. The stack is mounted chip-side-down in the UHV system. **(b)** Microscope image of the Orsay chip wires. Speckle from the rough wire surface is visible, along with two apparent defects in the central segment of the thick Z-wire (darkened regions pointed to by white arrows).

	thermal conductivity (W/m.K)	electrical resistivity (μΩ-cm)
Si (bulk, undoped)	1.5	3×10^{6}
SiO_2	1†	10^{18}
AlN	140 - 180	2×10^{17} - 10^{19}
stainless steel (304)	0.15	72
Cu (OFHC)	401	1.68
Ag	429	1.59
Au	318	2.24
Al	237	2.65

† See [113].
‡ All values at 25°C.

Tab. 4.6: Electrical and thermal characteristics of atom chip and stack materials, from [95, 114] unless otherwise noted.

Heatsinking the atom chip Although the chip wires carry relatively small currents, the atom chip substrate and stack must be well heat-sunk in order to prevent wire failure due to melting. A DC current of 2 A in the Z-wire corresponds to a current density of 6.7×10^{5} A/cm^2 at the wire's narrowest point. Assuming that all electrical power is dissipated as heat in the 1 Ω, 2.8 mm×6 μm×50 μm central segment of the Z-wire (the narrowest section of the wire), this current density would heat a room temperature gold or silver Z-wire to its melting point in roughly 2 ms.[13]

Since there is no convective heat conduction in vacuum, effective heatsinking of the conductors becomes especially important. We addressed this issue first by building the stack out of oxygen-free-high-conductivity (OFHC) copper for its relatively large thermal conductivity (see Tab. 4.6), and second by fly cutting the chip-side of the stack in an attempt to maximize thermal contact to the silicon substrate.

Orsay Z-wire "defect" Fig. 4.19b shows two apparent defects in the central segment of the Z-wire. These defects are responsible for local minima in the longitudinal Z-wire potential, which were observed during our first attempts at creating a ^{87}Rb BEC. We evaporate to BEC in the deepest of these potential minima, leveraging the increased longitudinal magnetic confinement and accompanying increased elastic collision rate to achieve BEC rapidly and efficiently (see Ch. 5).

4.6.2 Toronto chip

The Orsay chip was replaced with the Toronto chip in early 2008 to add functionality and flexibility to the magnetic microtraps, while maintaining the key features of the Orsay Z-trap. The chip includes a replica of the Orsay Z-wire in addition to other wires for other types of magnetic

[13] Estimate based on the specific heats (0.031 cal/g.K, 0.057 cal/g.K), densities (19.3 g/cm^3, 10.5 g/cm^3), and melting points (1064°C, 962°C) of elemental gold and silver respectively [95].

trapping and manipulation. The Toronto chip and stack chip was also designed to with the goals of improving the current capacity of the wires via better construction and heatsinking of the chip and stack, and to improve optical access below the chip surface.

The Toronto chip and stack were designed and built entirely at the University of Toronto. The chip conductor pattern was designed by Thorsten Schumm and myself in the summer of 2006. David McKay designed the copper stack, which was machined in the Toronto chemistry department's shop. Barbara Cieslak initiated early efforts in fabricating the chip in the University of Toronto's Bahen Centre cleanroom. Dylan Jervis continues this work, finalizing the fabrication process and producing the chip [112].

Design, construction and wire pattern A complete account of the fabrication process is available in Dylan Jervis's MSc thesis [112]. This section presents only a brief summary.

The chip was designed to be compatible with the possibility of surface mirrorizing [115]. To create as smooth a chip surface as possible, all unused areas were plated to the same thickness as the wires, and wire gaps in the central chip region were kept to 10 µm . The gaps widen to 100 µm and more toward the edges of the chip. The chip is based on a polished aluminium nitride (AlN) substrate measuring 20 mm $\times$ 32 mm $\times$0.6 mm. AlN was chosen for its superior thermal conductivity (see Tab. 4.6), which we hoped would increase the current capacity of the chip wires and permit more atoms to be loaded into the chip trap (see the discussion of the role of wire current on maximum loaded atom number in Sec. 5.2.2.) The AlN chip is glued to the top of an OFHC copper stack using a thermally conductive UHV-compatible epoxy (Epotek H77).

The conductor pattern was established using photolithography, and the silver wires were evaporatively deposited to their full 3 µm thickness on top of an initial titanium adhesion layer. Despite being slow and an inefficient use of metal, evaporative deposition was used to to minimize wire rugosity; evaporative deposition produces smoother and more uniform conductors than does electroplating [111, 116], which reduces current noise [117] and the resulting magnetic field noise that famously plagued early atom chip traps [118, 119, 120]. Silver was chosen for its superior electrical conductivity (see Tab. 4.6) and relatively low cost. Evaporative deposition wastes so much metal that using gold alone would have been too expensive. A final thin gold layer was evaporated to prevent a buildup of silver oxide on the chip surface.

The wire pattern of the Toronto chip contains a Z-wire of the same dimensions as that of the Orsay chip (shaded blue in Fig. 4.20). Surrounding this Z-wire are symmetric pairs of 50 µm thick "U-wires" (red in Fig. 4.20), 200 µm thick straight "bar wires" (dark green), and thin Z-shaped "dimple wires" (yellow). The U-wires were designed to be used with the Z-wire to form a 3-wire trap without external bias fields [28]. They were also intended for use as RF antennae, operating in concert to generate RF fields of varying polarization for creating RF-dressed potentials (see [121] and Ch. 6).

The dimple wires are designed to loosely mimic the defect dimple of the Orsay Z-wire – which greatly benefited the rapid evaporation to BEC and DFG in the Orsay Z-trap (see Sec. 4.6.1) – by increasing the longitudinal confinement of the Z-trap. Parallel DC currents in the bar wires

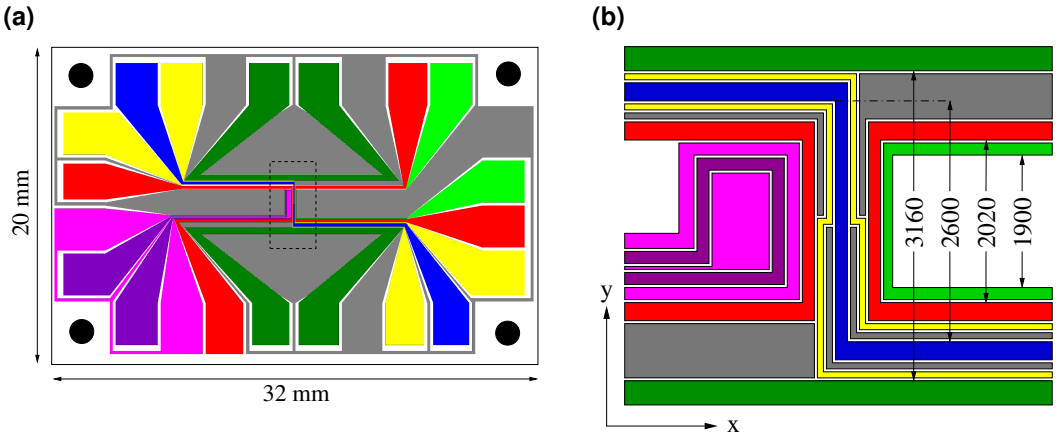

Fig. 4.20: (a) Top view of the Toronto chip. Grey shading indicates the interconnected grounded filler plating. Black circles at the corners indicate through holes in the AlN substrate, used to secure the chip during initial mounting. **(b)** A zoomed view of the central portion of the chip (dashed region in **(a)**) detailing the Z-wire (blue), U-wires (red), dimple wires (yellow), bar wires (dark green), RF antenna (light green) and HF antenna (purples). The y-direction wire lengths are indicated in micrometres; wire widths are listed in Tab. 4.7. All gaps (white) are 10 µm wide. Diagram not to scale.

	y-dir'n segment width (µm)	x-dir'n segment width (µm)	DC resistance (Ω)
Z-wire (blue)	50	200	1.3
U-wires (red)	50	200	1.3, 1.8
dimples (yellow)	10	50	4.5, 4.6
bars (dk. green)	-	400	0.6, 0.7
RF (lt. green)	20	50	3.5
HF "signal" (dk. purple)	50	50	3.0
HF "ground" (lt. purple)	50	50	0.3

Tab. 4.7: Toronto chip wire widths (see Fig. 4.20) and electrical resistances at DC (including contact resistance).

provide a more controllable adjustment of the longitudinal magnetic curvature in the Z-trap.

Finally, two types of AC magnetic field antennae are built into the chip design. The first is a thin U-wire (light green in Fig. 4.20a), meant to roughly match the thin Z-wire antenna of the Orsay chip. The second is an attempt at better impedence matching for better RF and high-frequency (HF) power transmission to the chip. Shown in light and dark purple in Fig. 4.20a, the idea is a based on a stripline coaxial conductor; the dark purple looped wire is the "signal" conductor, and the light purple the "shield" or ground conductor. The chip conductor widths are listed in Tab. 4.7.

Stack and electrical connections All electrical connections are made to the backside of the Toronto chip, which maximizes the optical access to atoms trapped in a chip microtrap. Connecting the backside gold chip pads to current-bearing wires, however, proved to be very challeng-

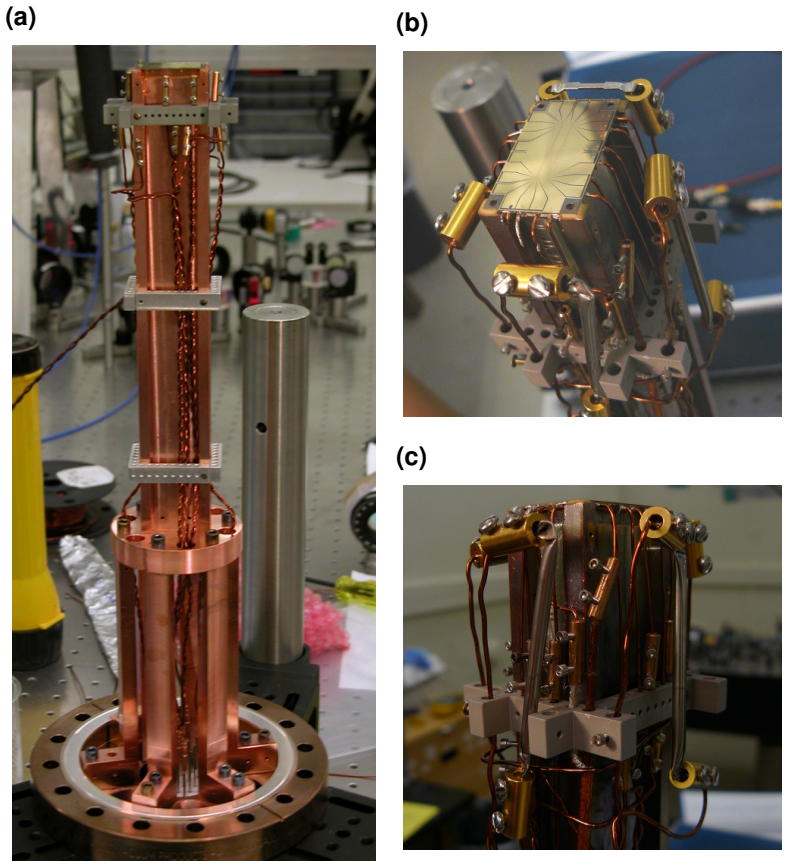

Fig. 4.21: (a) The copper Toronto bolted to a 6" steel Conflat multi-port flange during assembly. The stack measures 365 mm from flange to chip. Kapton-coated copper wires bear DC current to the chip and to dispensers. **(b)** Chip glued onto the stack; backside electrical connections. **(c)** Stack side-view at chip, electrical connections and Alvatec dispensers (vertical silvery tubes) connected with BeCu barrel connectors.

ing. The simplest solution seemed to be to solder copper wires directly onto the gold pads. Conventional tin-based solder worked well, but these solders are unsuitable for UHV applications due to their high outgassing rates [96]. Vacuum-compatible solders are available, but generally require much hotter soldering temperatures (e.g. Allectra UHV-solder, 350°C). The main impediment to high-temperature soldering is the large thermal conductivity of the AlN substrate. The gold pads are so well heat-sunk by the substrate that applying heat locally to a single pad invariably heats the entire chip. Soldering on the first wire was relatively easy, but applying heat to solder on a second adjacent wire would completely melt the first solder joint. After many frustrating attempts at soldering to the AlN chips, we settled on gluing copper lead wires to the gold contact pads with an electrically conductive UHV-compatible epoxy (Epotek H21ND, containing silver flakes in suspension). Although the wire-epoxy-pad bonds are quite weak mechanically[14] the contacts are ohmic with DC resistances on the order of 1 - 4 Ω (see Tab. 4.7).

The electrical connections are shown in Fig. 4.21: 0.6 mm diameter Kapton-insulated copper

[14]The fragility of these bonds led to many broken-off wires, re-glueings, and general stress and anxiety during the process of attaching the chip and making the necessary electrical connections.

wires are glued to the chip's contact pads at one end, and connected by BeCu barrel connectors to similar 1 mm diameter wires at the other. The dispensers are also supported by the stack, and are electrically connected using BeCu barrels and 1.7 mm diameter Kapton-insulated copper wire. RF and HF signals are carried from the air side sources through UHV-compatible SMA connectors on the stack multi-port flange, down through Kapton-insulted UHV-compatible coaxial cables, and onto the chip via barrel connectors.

4.7 Computer control and automation

The experiment is controlled using an ADwin-Pro real-time sequencer[15] from Keithley, Inc. Experimental sequence programs are loaded into the ADwin using control software written in LabWindows and C, and run from a Windows PC. We use digital buffer circuits between the ADwin-Pro and the experimental hardware to protect the ADwin's I/O boards from current overloads. In the case of a large current sink or source, low-cost, easily replaceable components on the buffer boards fail, rather than the ADwin boards.

[15]CPU-T10 80 MHz processor; 8 analog inputs with 12-bit analog-to-digital converter (ADC); 40 analog output channels with 12-bit DAC, 0-10V, 10 µs step time, 5 mA per channel; 32 digital input-output channels, -5V - 5.5V, 6 mA per channel max.

Avoid scattering your energies.

Wing's fortune cookie

5

Making DFG and BEC on an atom chip

This chapter describes the realization of a $^{87}\mathrm{Rb}$ BEC and a $^{40}\mathrm{K}$ DFG in a single chamber, atom-chip-based apparatus. Our approach combines traditional free-space laser cooling with forced evaporative cooling in a tightly confining magnetic chip trap to reach quantum degeneracy. A key element of the experiment is the use of light-induced atom desorption (LIAD), which generates the initial atomic vapour. As discussed in Ch. 4, LIAD allows the $^{87}\mathrm{Rb}$ and $^{40}\mathrm{K}$ vapour pressure to be rapidly increased while loading the magneto-optical trap, then just as rapidly decreased to maximize the lifetime of the atom chip magnetic trap during each experimental cycle. Another important element is the atom chip, which generates the micromagnetic trap and supports radio-frequency (RF) antennae for evaporative cooling. The strong confinement and large collision rate provided by the chip trap allow RF evaporation to quantum degeneracy in just a few seconds.

We first achieved BEC in 2005, which was just the third realization of BEC in Canada. We then modified the experimental sequence to incorporate $^{40}\mathrm{K}$, with the goal of producing a DFG. Since identical fermions do not undergo elastic collisions at low temperatures, spin-polarized gas of $^{40}\mathrm{K}$ cannot be directly evaporatively cooled to quantum degeneracy. Instead, we use ultracold $^{87}\mathrm{Rb}$ as a refrigerant for $^{40}\mathrm{K}$ in a $^{40}\mathrm{K}$–$^{87}\mathrm{Rb}$ mixture. We produce a DFG using sympathetic cooling, in which $^{87}\mathrm{Rb}$ is evaporated and cooled directly, and $^{40}\mathrm{K}$ is "sympathetically" cooled by thermal contact with the $^{87}\mathrm{Rb}$ [26, 22, 122]. Ours was the first demonstration of a DFG and of dual-species DFG-BEC quantum degeneracy in a single-chamber apparatus [27].

The chapter begins with descriptions of the laser cooling, magnetic trapping, magnetic transport, chip loading, and evaporative cooling steps used to make BEC and DFG [45, 33]. We discuss the roles of trap depth and trap volume in microtrap experiments, with particular emphasis on chip loading of $^{87}\mathrm{Rb}$ and $^{40}\mathrm{K}$ in our setup. Next, we discuss the signatures of quantum degeneracy in BEC and DFG, which we observe using time-of-flight absorption imaging. By studying $^{87}\mathrm{Rb}$–$^{40}\mathrm{K}$ thermalization, we observed a dramatic decrease in the $^{87}\mathrm{Rb}$–$^{40}\mathrm{K}$ scattering cross-section at high temperatures, which we attribute to the Ramsauer-Townsend effect. This result has important consequences for sympathetic cooling of $^{40}\mathrm{K}$ with $^{87}\mathrm{Rb}$, which are widely used in the field in the field [11, 19, 22, 24, 25, 26].

5.1 Laser cooling, magnetic trapping and transport

Our experimental approach to creating ^{40}K and ^{87}Rb quantum gases an atom chip is motivated in large part by the scarcity of ^{40}K, which is by far the rarer of the two species: ^{40}K has a natural isotopic abundance only 0.012%, whereas ^{87}Rb has 28% [95]. Even when using a potassium source with ^{40}K enriched to 5%, we find that large MOT beams are essential to capture enough ^{40}K in a background UHV pressure compatible with magnetic trapping. Rather than using a reflected surface MOT [88], which would require a mirror-coated chip of length $\sim$ cm to accommodate our 4-cm-diameter MOT beams, we first load a large conventional MOT – ^{87}Rb only for making BEC, or dual-species ^{40}K–^{87}Rb for making DFG – several centimetres beneath the atom chip, then magnetically trap and transport the atoms to the chip. Once loaded into the Z-trap we evaporate ^{87}Rb directly to BEC with forced RF evaporation, and sympathetically cool ^{40}K to quantum degeneracy with a ^{87}Rb reservoir to minimize ^{40}K atom number loss. This approach also circumvents the need for a mirror-coated atom chip [88, 115]. The experimental sequences for creating a ^{87}Rb BEC, a ^{40}K DFG and a BEC-DFG mixture in both the Orsay chip and Toronto chip setups are all qualitatively similar. We use the dual-species example to illustrate the procedures here, and point out any important differences from the BEC-only setup, or between the Orsay and Toronto chip configurations where appropriate.

Both ^{40}K and ^{87}Rb are initially trapped and cooled in a dual-species MOT formed by six counterpropagating 4-cm-diameter beams centred 5 cm below the atom chip [44, 45]. We use a single-chamber vacuum system, and load the MOT directly from atomic vapour created using a combination of dispensers and light-induced atom desorption (LIAD). During each MOT loading cycle, commercial high-power 405 nm LEDs irradiate the Pyrex vacuum cell for several seconds to generate the atomic vapour (see Sec. 4.1.3). We use commercial Rb and home-made K dispensers to replenish the ^{40}K and ^{87}Rb coatings on the interior walls of the UHV chamber as needed – typically every few days or weeks [45]. A schematic diagram of the cell, MOT beams and magnetic coils is shown in Fig. 4.9.

Fig. 5.1 demonstrates the effect of LEDs on the ^{87}Rb MOT, and the rapid changes in vapour pressure when the LEDs are switched on and off. Once the LEDs are off, the MOT loading rate undergoes a sharp initial decrease from the LED-on value of 3×10^8 s^{-1}, followed by a slower decay to the LED-off value of $\sim 10^6$ s^{-1} in approximately 300 s. The LED-on ^{87}Rb MOT number is roughly 100 times greater than the LED-off value.

The effect of the LEDs is even more crucial for ^{40}K, for which we do not observe a ^{40}K MOT with the LEDs off.[1] The ^{40}K MOT loading rate is roughly 3×10^5 s^{-1} whereas the ^{87}Rb MOT loading rate is 10^8 s^{-1} (see Fig. 5.2). We measure the MOT loading time τ and loading rate γ by fitting N_{MOT} vs. time data to an exponential of the form

$$N_{\mathrm{MOT}}(t) = a\left(1 - e^{-(t-t_0)/\tau}\right) \quad \text{where} \quad \gamma \equiv \left.\frac{\mathrm{d}N_{\mathrm{MOT}}}{\mathrm{d}t}\right|_{t\to t_0} = \frac{a}{\tau}; \tag{5.1}$$

[1] A ^{40}K MOT is always observable if a ^{40}K dispenser is running.

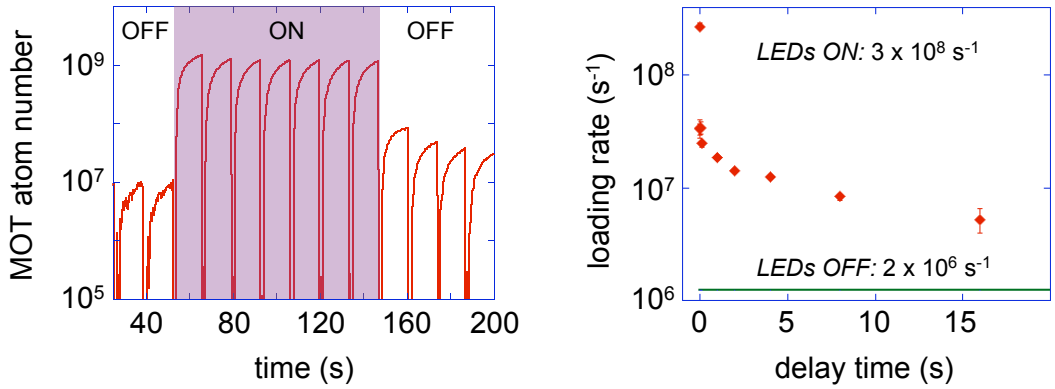

Fig. 5.1: Left: Repeated $^{87}\mathrm{Rb}$ MOT loading with the 405 nm LEDs switched on and off. Right: $^{87}\mathrm{Rb}$ MOT loading rate as a function of time after the LEDs are switched off. The initial sharp decrease is followed by a slower decay to the steady-state LED-off value.

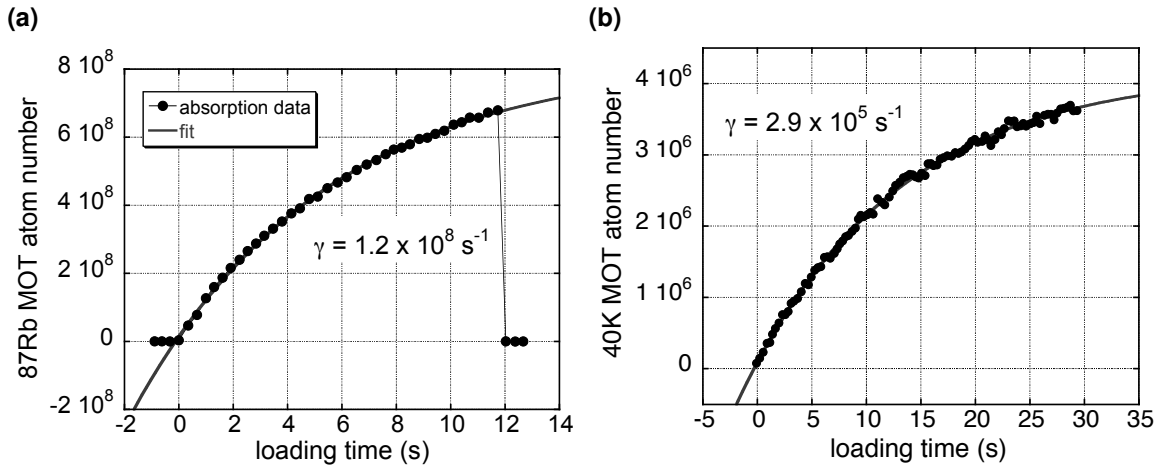

Fig. 5.2: $^{87}\mathrm{Rb}$ and $^{40}\mathrm{K}$ MOT atom number as a function of time with 405 nm LEDs on. Exponential fits using Eq. 5.1 yield **(a)** $a \simeq 8 \times 10^8$, $\tau \simeq 7$ s and loading rate $\gamma \simeq 1 \times 10^8$ s^{-1}; and **(b)** $a \simeq 4 \times 10^6$, $\tau \simeq 14$ s and loading rate $\gamma \simeq 3 \times 10^5$ s^{-1}

a, t_0 and τ are free parameters in the fits [123].

To collect a sufficient number of atoms in the dual-species MOT, we first load the ^{40}K MOT at an optical detuning of -30 MHz ($\sim 5\Gamma$) for 25 - 30 s, then add ^{87}Rb MOT beams detuned by -26 MHz ($\sim 4.3\Gamma$) for 2 - 10 s. MOT detunings are quoted with respect to the $F = 2 \leftrightarrow F' = 3$ and $F = 9/2 \leftrightarrow F' = 11/2$ cycling transitions in ^{87}Rb and ^{40}K, respectively (see Sec. 4.2). The ^{40}K beams remain on during ^{87}Rb MOT loading to maintain the ^{40}K population. This two-step MOT loading sequence is designed to minimize losses due to light-assisted collisions between ground state ^{87}Rb and ^{40}K atoms [124, 123] and between excited-ground collisions [123]. We mitigate against excessive loss in our setup by keeping the ^{87}Rb and ^{40}K as spatially and temporally separated as possible: we capitalize on the rapid ^{87}Rb loading rate to minimize the ^{87}Rb–^{40}K interaction time in the MOT, loading ^{87}Rb for the final 10 - 20% of the ^{40}K load cycle; we also spatially separate the ^{87}Rb and ^{40}K MOT centres by $\simeq 2$ mm. The spatial separation is partially natural, due to the differential gravitational sag of the two species, but is optimized empirically for ^{40}K atom number loaded onto the atom chip by adjusting the MOT beam powers and alignment. We achieve ^{40}K and ^{87}Rb atom numbers of up to 3×10^6 and 4×10^8 after a 20 s ^{40}K followed by a 5 s ^{87}Rb load.

In the final 100 ms of dual-species MOT loading the ^{40}K MOT beam detuning is jumped to -16 MHz to compress and cool the MOT in advance of magnetic trap loading. This step takes the place of optical molasses (which we use on the ^{87}Rb) since molasses cooling for ^{40}K is relatively ineffective [125]. With the ^{40}K MOT beams extinguished, the external magnetic fields are trimmed to zero and the ^{87}Rb MOT beams are detuned to -8.2Γ for 2.2 ms to form optical molasses. After that, both species are optically pumped for 600 µs into the stretched internal magnetic hyperfine states ($|F = 2, m_F = 2\rangle$ for ^{87}Rb and $|F = 9/2, m_F = 9/2\rangle$ for ^{40}K) using dedicated fibre-coupled optical-pumping beams from the laser system tuned to the ^{87}Rb $F = 2 \leftrightarrow F' = 2$ and ^{40}K $F = 9/2 \leftrightarrow F' = 9/2$ transitions (see Sec. 4.2).

With all beams extinguished, the optically pumped atoms are loaded into a quadrupole magnetic trap (QMT) formed by the MOT and transfer coils. The MOT and transfer coils are switched on in $\sim$ 350 µs using the Mag-O-Matic switch (see Sec. 4.3.2) to produce an initial $\sim$37 G/cm QMT gradient along the coil axis – just strong enough to cancel gravity in the vertical direction (radial coil direction). The QMT is then compressed prior to magnetic transport and chip loading by simultaneously ramping up the MOT coil (transfer coil) currents in 400 ms from 24 A to 65 A (21 A to 42 A). The QMT zero point is kept at a fixed position 2.5 cm below the MOT coil centre during QMT loading and compression.

The next step is to transport the atoms vertically by $\sim$5 cm to just below the surface of the atom chip. The transport sequence involves a 500 ms "S"-ramp (min-jerk) of the transfer coil current from 48 A to 0 A to -48 A; the direction of current flow is reversed at the half-way point using a relay. The QMT gradients are maintained during the transfer by the fixed MOT coil current. Atoms are smoothly transferred from the quadrupole magnetic trap into the Z-trap, located roughly 200 µm from the surface with a trap depth of roughly $k_B \times 1$ mK. This is accomplished by ramping down the MOT and transfer currents while simultaneously ramping up the Z-wire

	N_{Rb}	T_{Rb} (µK)	N_K	T_K (µK)
MOT	6e8	130	3e6†	80†
Rb molasses	6e8	40	n/a	n/a
QMT ‡	2e8	90	9e5	280
transfer	2e8	90	9e5	280
Z-trap load	2.5e7	300	2e5	~ 300

† Following 100 ms compressed MOT.
‡ Following compressed QMT.

Tab. 5.1: Summary of typical pre-evaporation atom numbers and temperature.

current and bias fields in 200 ms. Further detail on loading the Z-trap, and on loading chip traps from external traps in general, is presented in the following subsection.

Table 5.1 summarizes approximate atom numbers and temperatures measured after each cooling step. These measurements are based on Gaussian fits to optical density time-of-flight data acquired using absorption imaging (see Sec. 5.4).

5.2 Loading bosons and fermions onto the atom chip

Along with the advantages of large compression and fast collision rate characteristic of atom chip microtraps comes a disadvantage: small trap volume. The volume occupied by a trapped gas depends on its temperature, unlike in the uniform "box" potential to which we are accustomed from thermodynamics. Trap volume is not typically discussed when creating "macroscopic" magnetic traps with large coils, since these trap depths can be orders of magnitude larger than is required to confine laser-cooled atoms. For microtraps, however, the trap volume may limit the number of atoms that can "fit" into the trap in a way that we will quantify in the following subsections. Fig. 5.3 demonstrates saturation of the number of ^{87}Rb atoms loaded into a Z-trap as a function of the MOT atom number as a result of the limited chip trap depth. Our discussion points a clear route to larger atom number, when it would be desirable.

An atom is trapped when its energy is less than the trap depth U_{td}. A good model of a thermalized gas in a trap-depth-limited trap is a truncated Boltzmann distribution [126], where truncation occurs at η times the temperature, i.e. $U_{td} = \eta k_B T$. For typical collision rates in atom chip traps, free evaporation occurs when $\eta \lesssim 3$, while *efficient* evaporation occurs when $\eta \gtrsim 5$.

Laser cooling allows atoms to be delivered to the chip at temperatures less than U_{td} (see Sec. 5.1). However, our loading efficiency is typically 10% or less, while phase-space density is roughly preserved: we load roughly 2×10^7 ^{87}Rb atoms and 2×10^5 ^{40}K into the Z-trap at a phase space density of roughly 10^{-6}. We describe the factors limiting the Z-trap loading efficiency in the following subsections.

The number of fermions initially loaded places an upper bound on the number of ultra-cold fermions we can produce. Furthermore, though we load many more bosons than fermions,

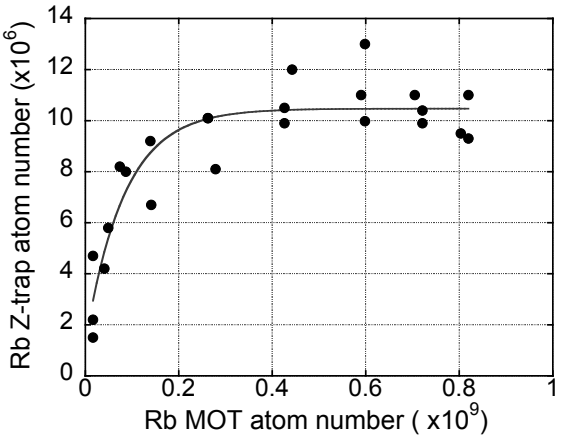

Fig. 5.3: Larger MOTs do not generally produce more atoms on the chip beyond a certain loaded atom number. The limiting chip atom number is set by the effective trap volume. The data shown is $^{87}\mathrm{Rb}$ in a Z-trap with trap depth $h \times 123$ mK, $\Omega_0 \simeq 2\pi \times 2.4$ MHz, $\omega_\perp \simeq 2\pi \times 560$ Hz, $\omega_\| \simeq 2\pi \times 32$ Hz. The data is empirically fit with an exponential as a guide to the eye.

bosons are continually lost during the evaporative cooling process, as described in Sec. 5.3. The decreasing "refrigerant" limits the number and final temperature of fermions that can be cooled. It is therefore important to understand our loading process and ways in which it can be improved.

5.2.1 Effective trap volume

Our discussion here concerns the number, temperature, and density of a gas at the start of evaporative cooling after loading into the microtrap. We will assume an initial phase-space density ρ_0, which is typically $\lesssim 10^{-5}$ for laser cooled atoms. The density distribution of the gas is approximately equal to that of an ideal thermal gas at this point in the experimental cycle.

From Eq. 2.38, the density distribution of an ideal Fermi gas in three dimensions is $n(\mathbf{r}) = \Lambda_T^{-3} f_{3/2}(\mathcal{Z}e^{-\beta U(\mathbf{r})})$, where $U(0) \equiv 0$. The corresponding expression for ideal bosons is obtained by replacing the thermodynamic Fermi function $f_{3/2}(\cdots)$ with the Bose function $g_{3/2}(\cdots)$. In either case, at low fugacity

$$n(\mathbf{r}) \overset{\mathcal{Z}\ll 1}{\longrightarrow} \Lambda_T^{-3} \mathcal{Z} e^{-\beta U(\mathbf{r})}. \tag{5.2}$$

Integrating both sides of the equation, we recover the total atom number

$$N = n_0 \int e^{-\beta U(\mathbf{r})} d\mathbf{r}, \tag{5.3}$$

where $n_0 = n(0)$ is the central (peak) density, and the volume of integration is defined by $U < U_{td}$.

In analogy with a uniform gas, we define the effective volume

$$V_{\text{eff}} = \int e^{-\beta U(\mathbf{r})} d\mathbf{r}. \tag{5.4}$$

where $n_0 \equiv N/V_{\text{eff}}$ [126].

In the limit of $\eta \gg 1$, we can integrate the full Boltzmann distribution to find the trap volume in several typical cases. For a three-dimensional simple harmonic oscillator potential,

$$V_{\text{eff}}^{\text{SHO}} = \left(\frac{2\pi}{M\overline{\omega}^2}\right)^{3/2} (k_B T)^{3/2}, \tag{5.5}$$

where $\overline{\omega}$ is the geometric mean oscillation frequency. For the three-dimensional quadrupole (linear) trap,

$$V_{\text{eff}}^{\text{QT}} = 8\pi \overline{F}^{-3} (k_B T)^3, \tag{5.6}$$

where $U \equiv |\mathbf{F} \cdot \mathbf{r}|$ and $\overline{F}$ is the geometric mean gradient. For a simple three-dimensional box of side L, $V_{\text{eff}} = V = L^3$. Finally, a hybrid two-dimensional quadrupole and one-dimensional box model gives

$$V_{\text{eff}}^{\text{2QB}} = 2\pi L \overline{F}^{-2} (k_B T)^2. \tag{5.7}$$

In all of the above cases, the effective volume has a power-law dependence $V_{\text{eff}} = C_\delta T^\delta$ [58].

5.2.2 A full tank of atoms: maximum trapped atom number

Using the effective volume, we can now relate the trapped atom number to the initial phase-space density ρ_0, which is equivalent to the degeneracy parameter $n_0 \Lambda_T^3$ for $\mathcal{Z} \ll 1$:

$$N = \rho_0 \Lambda_T^{-3} V_{\text{eff}}(T). \tag{5.8}$$

Since $k_B T = U_{td}/\eta$ by definition, we can write out the explicit temperature dependence in Eq. 5.8 to find

$$N_{\text{max}} = \rho_0 \left(\frac{M}{2\pi\hbar^2}\right)^{3/2} C_\delta (U_{td}/\eta)^{\delta+3/2}, \tag{5.9}$$

for a trap with a δ power law effective volume.

This equation shows us why the loaded atom number is typically smaller in microtraps than macrotraps. First, the trap depth U_{td} is typically smaller, which reduces atom number with a power law as fast as $U_{td}^{9/2}$ for a three-dimensional quadrupole trap. Second, even for comparable trap depths, the stronger trapping strength of a microtrap reduces C_δ: $C_3 \propto \overline{\omega}^{-3}$ in the case of a three-dimensional harmonic oscillator, for instance.

Eq. 5.9 also demonstrates the importance of large currents in trapping wires. Consider the

case in which a three-dimensional harmonic microtrap is formed above a single long wire, for which $\omega_\perp \propto B_{0\perp}/I$ where $B_{0\perp}$ is the perpendicular bias field and I is the wire current (see Eq. 3.22). Since the trap depth increases linearly with $B_{0\perp}$, Eq. 5.9 suggests that the maximum atom number at a fixed η and phase-space density is $N_{\max} \propto I^2 B_{0\perp}/\omega_z$. Assuming that the distance from the trapped atoms to the chip surface is fixed, and that $\omega_z \propto \sqrt{I}$, (see Eq. 3.23), $N_{\max} \propto I^{5/2}$. Thus, we see that larger wire currents allow an increase in the number of trapped atoms. (This scaling motivated the high-thermal-conductivity AlN substrate for the Toronto atom chip, which we hoped would permit the use of larger DC currents in the Z-wire (see Sec. 4.6.2.)

5.2.3 Effect of geometry on loaded atom number

We now evaluate the trap volume and the expected maximum atom number loaded into several well-studied chip trap geometries. We start with the earliest proposed traps, described in [28] by Libbrecht, and assume they are loaded with ^{87}Rb in the $|2,2\rangle$ state. For a single-loop quadrupole trap of radius 10 µm and 1 A current, the gradient is 5.4×10^5 G/cm and the trap depth $k_B \times 21$ mK. Assuming the trap can be loaded with $\eta \geq 4$ (corresponding to an initial temperature of ≤ 5 mK), the trap volume would be $V_{\text{eff}} \leq 310$ µm^3. At an initial phase-space density of 10^{-6}, 2×10^4 atoms could be loaded into the trap. However, losses at the central magnetic field zero of the quadrupole trap render it unsuitable for trapping ultra-cold atoms.

The Ioffe "(c)" configuration of [28] consists of concentric half-loops with a 10 µm minimum diameter. Using a 1 A current, the trap has a depth of $k_B \times 1.3$ mK and a curvature that gives $\overline{\omega}/2\pi \approx 94$ kHz. Although the trap is impressively strong, its effective volume is only 0.4 µm^3; less than one atom would be trapped at a phase-space density of 10^{-6}. Larger trap volumes than those of Libbrecht's pioneering geometries were required to achieve quantum degeneracy in atom chip microtraps [16, 17].

Finally, let us consider the Z-trap [88]. The potential at the centre of the trap is harmonic, with a typical geometric mean frequency of $\overline{\omega}/2\pi \approx 300$ Hz in our setup. The applied transverse magnetic bias field (typically value of 20 G) limits the trap depth to $U_{td} \approx k_B \times 1.3$ mK. Assuming the trap is loaded at $\eta = 4$, we find that the effective volume is 1.3×10^7 µm^3, and the maximum trapped atom number 1.2×10^7 at an initial phase-space density of 10^{-6}. Although approximate, our calculation shows that the Z-trap geometry is capable of loading six to seven orders of magnitude more atoms than the Libbrecht geometry for the same initial phase-space density.

Furthermore, the calculation suggests that the loaded atom number in our experiment is limited by trap depth and volume. For our field curvature of 3×10^4 G/cm^2 (geometric mean) and initial temperature of 300 µK, the effective trap volume is 3×10^7 µm^3. One would expect 3×10^7 ^{87}Rb atoms at $\rho_0 \approx 10^{-6}$, and 3×10^5 ^{40}K atoms at $\rho_0 \approx 4 \times 10^{-8}$. This is consistent with our observations to within an order-of-magnitude (2×10^7 for ^{87}Rb and 2×10^5 for ^{40}K), and demonstrates that we are close to, if not at, the maximum possible number of loaded atoms, given the phase-space density and temperature after magnetic transport to the chip.

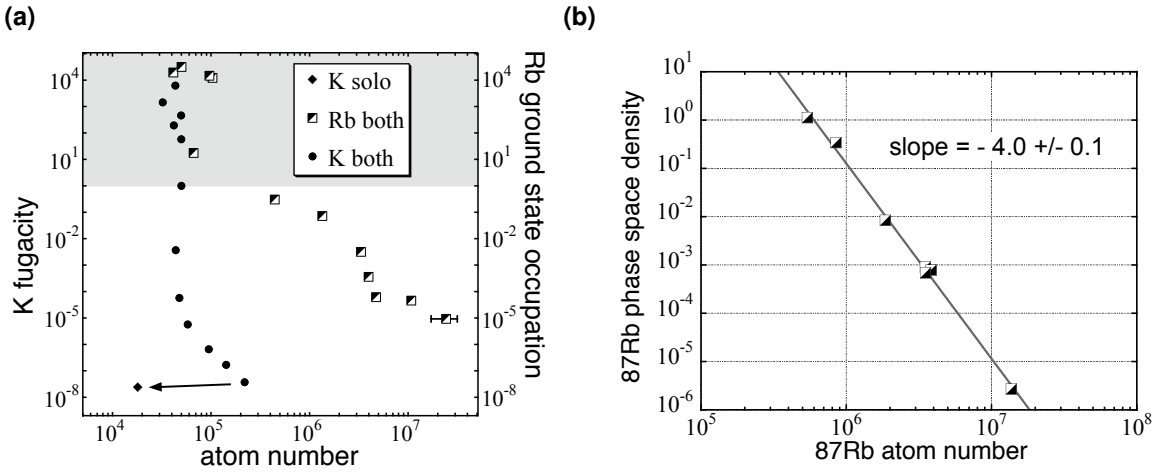

Fig. 5.4: (a) Sympathetic cooling to dual ^{40}K–^{87}Rb quantum degeneracy. Spin-polarized fermions without a bosonic bath cannot be successfully evaporatively cooled (diamond). However, if bosonic ^{87}Rb (squares) is evaporatively cooled, the fermionic ^{40}K is sympathetically cooled (circles) by thermalizing elastic collisions with ^{87}Rb. The vertical axes indicate the evolution of phase-space-density en route to dual quantum degeneracy ($\mathcal{Z} \geq 1$) during evaporation: ^{40}K fugacity $\mathcal{Z}$ on the left, and ^{87}Rb ground state occupation on the right. A typical run-to-run spread in atom number is indicated on the right-most point; all vertical error bars are smaller than the marker size. **(b)** Evaporation to BEC in ^{87}Rb alone is more efficient than sympathetic evaporation. The log-slope efficiency, deduced by a linear fit, is twice that of the sympathetic cooling case (see text).

5.3 Rapid RF evaporative cooling

We reach dual quantum degeneracy in ^{40}K and ^{87}Rb [22, 122, 127, 26] via sympathetic RF evaporative cooling of ^{87}Rb in a Z-trap with $\Omega_0^{(Rb)} = 3.60$ MHz ($B_0 \simeq 2.6$ G), ^{40}K harmonic oscillation frequencies $\omega_{x,z} = 2\pi\times$ 823±7 Hz and $\omega_y = 2\pi\times$ 46±1 Hz, and a trap depth of $k_B\times$1.05 mK [27]. In our case, ^{40}K is cooled indirectly by thermalizing elastic collisions with ^{87}Rb. By sweeping the RF evaporation frequency from 28.6 MHz to 3.65 MHz in as little as 6 s, we reach $T/T_F \simeq 0.1 - 0.2$ with $\epsilon_F \simeq k_B \times 1.1$ μK and as many as 4×10^4 ^{40}K atoms, faster than has been possible in conventional magnetic traps [27, 45]. (However, a ^{6}Li DFG has been produced in an all-optical setup in as little as 3.5 s [128].) This rapid evaporation to degeneracy is made possible by the strong atom chip confinement.

As is evident in Fig. 5.4, the ^{40}K is cooled to quantum degeneracy ($\mathcal{Z} \geq 1$) with only a five-fold loss in atom number, while the ^{87}Rb is evaporated with log-slope efficiency $-\partial[\log(\rho_0)]/\partial[\log(N)] = 2.9 \pm 0.4$, where ρ_0 is the peak phase-space density. When evaporating ^{87}Rb alone to BEC, the evaporation efficiency can be as high as 4.0 ± 0.1; a more rapid evaporation can produce a BEC in just 2 s, sacrificing some evaporation efficiency. For ^{40}K–^{87}Rb mixtures we observe that RF sweep times faster than 6 s are not successful in achieving dual degeneracy; ^{87}Rb and ^{40}K rethermalize more slowly than ^{87}Rb alone, particularly during the initial high-temperature stages of evaporation. Direct measurements of the ^{40}K and ^{87}Rb temperatures indicate that ^{40}K thermalization lags that of ^{87}Rb despite an experimentally optimized RF frequency sweep that is slower at higher temperatures and accelerates at lower temperatures

[27].

Density-dependent loss The large and negative inter-species scattering length $a_{KRb} \simeq -205\ a_0$ [129] (see Sec. 5.5) results in a strong ^{40}K-^{87}Rb attractive interaction. At low temperatures and high atomic densities, this interaction creates an additional mean-field confinement that can lead to massive and sudden losses during sympathetic cooling at a critical ^{87}Rb and ^{40}K atom number [26, 22, 122]. These studies of density-dependent interaction-driven losses point to boson-boson-fermion[2] 3-body decay as the underlying mechanism for the collapse of the mixture [124, 130]. This effect ultimately limits the atom numbers in ^{40}K–^{87}Rb mixtures, and is manifest in our experiment as ^{40}K and ^{87}Rb number losses near the end of evaporation. We are able to produce BECs of as many as 3×10^5 atoms working ^{87}Rb alone, but the simultaneous ^{87}Rb and ^{40}K atom numbers are restricted to at most $\sim 10^5$ and 4×10^4 respectively.

5.4 Thermometry and signatures of degeneracy

We analyze time-of-flight absorption images of expanding ^{87}Rb and ^{40}K clouds to measure in-situ atom number and temperature, and to determine the degree of quantum degeneracy. In bosonic ^{87}Rb the appearance of the sharp condensate peak at the centre of the time-of-flight density distribution is a clear signature of the phase transition from thermal Bose gas to BEC. The bimodal structure of the density profile is easily distinguished from the Gaussian shape of classical, Boltzmann particles. In fermionic ^{40}K, for which there is no phase transition into the quantum degenerate regime, we rely on (a) subtle changes in the density profile and (b) measurements of the expansion energy to identity DFG behaviour.

5.4.1 Analyzing absorption images

In each absorption measurement the Z-trap magnetic fields are abruptly switched off and the atom cloud is allowed to fall and expand for a time-of-flight (TOF) t, after which time the cloud is destructively imaged using absorption imaging on the σ^+ cycling transition [56]. The quantization axis for imaging is defined by a weak ($\sim$ 3.5 G) magnetic bias field applied along the imaging axis during imaging. We use the example of "axial", x-axis imaging throughout[3] this subsection, in which the probe beam and imaging system are aligned along x (see Sec. 4.5). The transmitted probe intensity is registered on a CCD camera as a pixelated function of y and z. The transmission is then converted into an optical density (OD) profile $OD(y, z)$ and fit with the corresponding theoretical expression for an expanding gas of bosonic or fermionic atoms released from a harmonic trap [56, 50] to extract the atom number N and temperature T. In this subsection we describe how optical density is related to the expanded column density $\tilde{n}(y, z)$ (see Sec. 2.2.3 and 2.1.3) and the absorption cross section $\sigma_\lambda(\delta)$ in absorption imaging, and motivate the importance of calibration for accurate atom number measurements.

[2] Fermion-fermion-boson 3-body decay is precluded by the Pauli exclusion principle.
[3] We also routinely collect "radial" time-of-flight images by imaging along y.

Two-level Rabi frequency We describe absorption imaging using a semi-classical description of a plane wave exciting transitions between the ground $|g\rangle$ and excited $|e\rangle$ states of a two-level atom, as in the "Rabi two-level problem" [82, 131]. This extreme simplification of the general photon-multilevel-atom interaction is a reasonable description of an **idealized** measurement in which

(a) all atoms are initially in a stretched hyperfine ground state state $|F, F\rangle$, and

(b) the probe beam is perfectly polarized σ^+ with respect to each atomic spin, and thus excites transitions only between the two levels $|F, F\rangle$ and $|F', F'\rangle$, where $F' = F + 1$.

In ^{87}Rb we use the $5^2S_{1/2}\,|F = 2, m_F = 2\rangle \leftrightarrow 5^2P_{3/2}\,|3, 3\rangle$ transition; in ^{40}K we use $4^2S_{1/2}\,|9/2, 9/2\rangle \leftrightarrow 4^2P_{3/2}\,|11/2, 11/2\rangle$. We also note that the semi-classical description of absorption is appropriate for time-of-flight absorption imaging, in which the expanding atom cloud is dilute and essentially non-interacting.

The probe laser beam is described as a plane wave $\mathbf{E}(\mathbf{r}, t) = E_0\hat{\mathbf{e}}\cos(kx - \omega_L t)$, where $\hat{\mathbf{e}}$ is a unit vector denoting the polarization of the light, $k = 2\pi/\lambda$ and $\omega_L = c/k$, where λ is the optical wavelength and c the speed of light. Assuming the probe beam intensity is weak enough that non-linear effects may be ignored, the electric dipole interaction Hamiltonian between the light and an atomic electron with charge q may be written

$$H_{eg}(\mathbf{r}, t) = -q\mathbf{E}(\mathbf{r}, t) \cdot \mathbf{R} \tag{5.10}$$

using the dipole approximation, where $\mathbf{R}$ is the position operator for the atomic electron [82]. For a two-level atom the matrix element relevant to the ground-excited coupling $\langle e|H_{eg}(\mathbf{r}, t)|g\rangle$ can be be parametrized by a single Rabi frequency Ω_{eg} [94]

$$\hbar\Omega_{eg} \equiv -\mu_{eg}E_0 \quad \text{where} \quad \mu_{eg} = q\langle e|\hat{\mathbf{e}} \cdot \mathbf{R}|g\rangle \tag{5.11}$$

is the electric dipole moment. The idealized measurement scenario ((a) and (b) above) maximizes the light-atom coupling for a given laser frequency ω_L. In principle μ_{eg} can be calculated using the wavefunctions of the ground and excited states of the ^{87}Rb and/or ^{40}K cycling transitions, and using the appropriate Clebsch-Gordan coefficients [103].

Non-ideal measurements and calibration factor Real absorption measurements are are subject to several systematic effects which reduce the light-atom coupling with respect to its maximal, ideal value:

- imperfect σ^+ polarization of the probe beam, leading to weak π or σ^- transitions to adjacent excited Zeeman states;
- some initial atomic population in adjacent trappable Zeeman ground states $|F, F-1\rangle$, $|F, F-2\rangle$ etc., whose Clebsch-Gordan coefficients are not explicitly accounted for in the idealized μ_{eg};

- stray magnetic fields during imaging, which may add spatial or temporal variation to μ_{eg}.

We can describe the effective, reduced coupling matrix element $\tilde{\mu}_{eg}$ in terms of the maximal, ideal value μ_{eg} using

$$\tilde{\mu}_{eg} \equiv \mu_{eg}/C \tag{5.12}$$

where $C \geq 1$. $C = 1$ in the idealized absorption measurement. The systematics mentioned above can result in a slightly different coupling strength (Clebsch-Gordan coefficient) for each atom. C can be thought of as the appropriate correction factor averaged over all atoms in the cloud.

Absorption cross-section and optical density We describe the absorption measurement in terms of a total absorption cross-section and the optical density, incorporating the calibration factor C. From the semi-classical optical Bloch equation treatment of the Rabi two-level problem [132], the photon scattering rate γ_p of light from the laser field is given by

$$\gamma_p = \frac{s_0\Gamma/2}{1 + s_0 + (2\delta/\Gamma)^2}, \tag{5.13}$$

where Γ is the spontaneous population decay rate of the excited state, $\delta \equiv \omega_L - \omega_{eg}$ is the optical detuning from the atomic resonant frequency $\omega_{eg} \equiv (E_e - E_g)/\hbar$ where E_g and E_e are the ground and excited state energies. The "saturation parameter"

$$s_0 \equiv \frac{2|\Omega_{eg}|^2}{\Gamma^2} = \frac{I}{I_{\text{sat}}C^2} \tag{5.14}$$

parametrizes the probe beam intensity I, where $I_{\text{sat}} \equiv \pi hc\Gamma/3\lambda^3$ is the saturation intensity for the cycling transition, and Ω_{eg} the optical Rabi frequency [131]. The intensity I is a function of y, z due to the spatial beam profile, and of x due to absorption. Assuming that light enters and exits the cloud at the same position (y, z) (the "thin lens" approximation applied to the atom cloud) [56], and assuming only incoherent scattering by the atom cloud, the amount of scattered power per unit volume is $\hbar\omega_L\gamma_p n$, where n is the atomic density [131]. For a weak probe beam travelling along x with $I \ll I_{\text{sat}}$ ($s_0 \ll 1$)

$$\frac{\mathrm{d}I}{\mathrm{d}x} = -\hbar\omega_L\gamma_p n \approx -\frac{3\lambda^2/2\pi}{1 + (2\delta/\Gamma)^2} nI(x). \tag{5.15}$$

$\sigma_0 = 3\lambda^2/2\pi$ is the ideal resonant absorption cross-section [133]. The solution of Eq. 5.15 is

$$I(x) = I_0 \exp\left[-\frac{3\lambda^2/2\pi}{1 + (2\delta/\Gamma)^2} nx\right] \tag{5.16}$$

where I_0 is the incident probe beam intensity. In experiments, we measure the total incident and transmitted probe intensity as a function of y and z and construct the transmission $I_{\text{out}}(y, z)/I_0(y, z)$.

In classical scattering and absorption theory the optical intensity of a beam passing through a

medium of non-interacting absorbers, with uniform density n, each with absorption cross-section σ, decreases exponentially [133]

$$I(x) = I_0 e^{-\sigma n x} \equiv I_0 e^{-OD}. \tag{5.17}$$

Eq. 5.17 defines the optical density OD and, assumes a probe intensity weak enough that multiple-scattering, optical pumping and saturation effects can be ignored [133].[4] From Eq. 5.17 the total transmitted intensity through an absorber with x-direction thickness ℓ is

$$\frac{I_{\text{out}}}{I_0} = \frac{I(\ell)}{I_0} = -\sigma n \ell. \tag{5.18}$$

We can relate Eq. 5.18 to our measurements of a non-uniform cloud of atoms using the column density $\tilde{n} \equiv \int dx\ n$, which is equal to $n\ell$ in the case of a uniform gas of finite thickness ℓ. The transmission $I_{\text{out}}(y,z)/I_0(y,z)$ measured on the CCD camera, optical density $OD(y,z)$, atomic column density and absorption cross-section can be be related using Eqs. 5.16, 5.17 and 5.18:

$$OD(y,z) \equiv -\ln\left[\frac{I_{\text{out}}(y,z)}{I_0(y,z)}\right] = \tilde{\sigma}_\lambda(\delta)\ \tilde{n}(y,z) \tag{5.19}$$

where

$$\tilde{\sigma}_\lambda(\delta) = \frac{\sigma_0}{C^2(1+(2\delta/\Gamma)^2)} \equiv \sigma_\lambda(\delta)/C^2 \tag{5.20}$$

is the absorption cross-section written in terms of the ideal value

$$\sigma_\lambda(\delta) = \frac{\sigma_0}{1+(2\delta/\Gamma)^2} \tag{5.21}$$

and the calibration factor C.

The total atom number is obtained by integrating the measured column density

$$N = \int dy\, dz\, \tilde{n}(y,z) = \frac{1}{\tilde{\sigma}_\lambda(\delta)} \int dy\, dz\, OD(y,z) \tag{5.22}$$

using Eq. 5.19, which is larger than the naive estimate by a factor of C^2. Proper atom number calibration consists of estimating C^2 by a method which does not depend on light-atom interaction models of the type presented here (see Sec. 5.4.3.1).

Constructing the optical density image The optical density (OD) image is found by combining three raw images: the "signal" image, which contains the transmitted probe light and the atomic absorption spot; the "reference" image, which contains the transmitted probe light with the atoms removed from the field of view; and the "background" image, collected without the probe beam or atoms present, containing only background scattered light and any other CCD

[4] Eq. 5.17 can also written in terms of an "extinction coefficient due to absorption" $\alpha = -\sigma n$: $I(x) = I_0 e^{-\alpha x}$ [133].

noise (e.g. read noise, digitization noise). The OD image is constructed pixel-by-pixel according to

$$OD(i,j) = -\ln\left(\frac{\text{sig}(i,j) - \text{bg}(i,j)}{\text{ref}(i,j) - \text{bg}(i,j)}\right) \tag{5.23}$$

where $\text{sig}(i,j)$, $\text{ref}(i,j)$ and $\text{bg}(i,j)$ are the signal, reference, and background images; i and j index the two-dimensional CCD pixel array. In an ideal measurement, the OD is zero in everywhere where there is no atomic scattering, and finite where atoms do scatter. The total atom number is proportional to the total OD, obtained by summing the individual pixel contributions.

The three raw images are extracted from the CCD camera as two-dimensional arrays of "ADC counts" (analog-to-digital counts) N_{ADC}, which is related to the number of photons incident on the CCD $\mathcal{N}$ by the quantum efficiency η_{qe} and internal camera gain G (the number of ADC counts per CCD photoelectron): $N_{\text{ADC}} = \eta_{\text{qe}} G \mathcal{N}$. With the MicroPix M640 CCD camera, signal and reference images were taken 35 - 45 ms apart, and combined with a single representative background image that was collected "offline" (i.e. at some other time) to construct the OD image. With the Pixis 1024BR camera, signal, reference and background images taken 400 - 800 µs apart are collected for each OD image.

5.4.2 Non-degenerate clouds

The time-of-flight optical densities of non-degenerate Bose and Fermi clouds at temperatures well above T_c or T_F are well described by a Gaussian profile; multiply the expanded column density of Eq. 2.45 by and multiplying by $\tilde{\sigma}_\lambda(\delta)$. This is equivalent to treating the atoms like Boltzmann particles. Measured optical density profiles are fit to

$$OD(y,z) = A \exp\left[-\frac{(y-y_c)^2}{2\sigma_y^2} - \frac{(z-z_c)^2}{2\sigma_z^2}\right] + m_y y + m_z z + b \tag{5.24}$$

where the optical density amplitude A, cloud centre positions y_c, z_c, Gaussian widths σ_y, σ_z and background offset b and slopes m_y, m_z are free parameters in the fit. The background plane $m_y y + m_z z + b$ accounts for systematic errors in the image. For atoms released from a harmonic potential, the Gaussian widths are related to the temperature T, time-of-flight t and trap harmonic oscillation frequencies ω_i by

$$\sigma_i^2 = \frac{k_B T(1 + \omega_i^2 t^2)}{M\omega_i^2} \tag{5.25}$$

where M is atomic mass. This relationship is used to measure N and T of thermal atoms released from the Z-trap.

To estimate T in the MOT, magnetic trapping and transfer stages, in which the trapping potentials are *not* harmonic, we instead measure the Gaussian cloud size as a function of TOF t and fit the resulting data to the expectation of ballistic expansion in a non-interacting ideal gas in

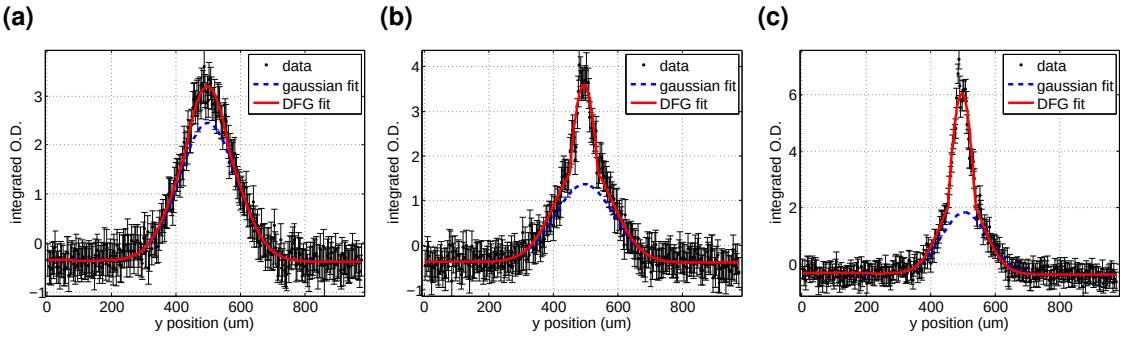

Fig. 5.5: Bimodal fits of ^{87}Rb clouds at and below T_c. We measure temperature using two-dimensional fits to the thermal cloud only. These data show $T/T_c \simeq 1$, 0.7, 0.5 from left to right; $T_c \simeq 240$ μK.

three-dimensions

$$\sigma_i(t) = \sqrt{\sigma_0^2 + \overline{v}^2 t^2} \tag{5.26}$$

where $i \in x, y, z$, $\sigma_0 = \sigma(0)$ is the in-situ cloud size, and $\overline{v}_i$ is the one-dimensional mean thermal velocity along the i^{th} direction [131, 56]. The thermal velocity $\overline{v}_i$ extracted from the fit is then used to estimate the temperature T_i

$$\langle E \rangle_i = \frac{1}{2} M \overline{v}_i^2 = \frac{1}{2} k_B T_i \quad \Rightarrow \quad T_i = M \overline{v}_i^2 / k_B, \tag{5.27}$$

where $\langle E \rangle_i$ is the one-dimensional mean kinetic energy of the gas in the i^{th} direction.

The atom number is extracted from the Gaussian fits according to

$$N = 2\pi A \sigma_y \sigma_z / \tilde{\sigma}_\lambda(\delta) \tag{5.28}$$

where $\tilde{\sigma}_\lambda(\delta)$ is the absorption cross-section for optical detuning δ from the cycling transition. We note that in addition to absorption imaging for accurate N and T measurements, we also use the collected atomic fluorescence stimulated by the MOT beams for quick checks and monitoring of the MOT during each experimental cycle.

5.4.3 BEC

We observe the expected bimodal structure for temperatures below T_c in ^{87}Rb by imaging along x ("axial imaging"). Fig. 5.5 shows fits of ideal BEC theory to raw 2D optical density data which have been summed along z at temperatures corresponding to $T/T_c \sim 1$, 0.7, and 0.4. The data shows $N \sim 10^4$ ^{87}Rb atoms imaged on resonance after a 6 ms time-of-flight from a Z-trap with trap bottom $\Omega_0 \simeq 2\pi \times 415$ kHz, $z_0 \simeq 190$ μm and ^{87}Rb oscillation frequencies $\omega_\perp \simeq 2\pi \times 1.8$ kHz and $\omega_\parallel \simeq 2\pi \times 13.7$ Hz.

We note that we can only distinguish the thermal cloud from the BEC in axial images along x, not in radial images along y. In our anisotropic traps with aspect ratios as large as 130:1 the

radial Thomas-Fermi width of the condensate in time of flight $R_{\mathrm{TF},\perp}$ exceeds that of the thermal cloud $R_{\mathrm{th},\perp}$ when $k_B T < \mu$ (see Secs.2.1.2)

$$R_{\mathrm{TF},\perp} = \sqrt{\frac{2\mu}{M_{\mathrm{Rb}}\omega_\perp^2}}\sqrt{1+\omega_\perp^2 t^2} \quad \text{and} \quad R_{\mathrm{th},\perp} = \sqrt{\frac{2k_B T}{M_{\mathrm{Rb}}\omega_\perp^2}}\sqrt{1+\omega_\perp^2 t^2}. \tag{5.29}$$

Thus, the condensate obscures the thermal cloud, making bimodal fits to extract temperature impractical with radial images.

5.4.3.1 Atom number calibration

$^{87}\mathrm{Rb}$ atom numbers measured using the axial Orsay imaging system were calibrated by observing the temperature dependence of the BEC size. From Eq. 2.22, the Thomas-Fermi BEC radius and atom number are related by

$$R_i = (15N_0 a)^{1/5}\left(\frac{\hbar}{M\omega_i}\right)^{2/5}, \tag{5.30}$$

where M is the $^{87}\mathrm{Rb}$ mass, ω_i the i^{th} trap frequency, and a the s-wave scattering length. Since the only remaining unknowns are the cloud half-width R_i and the condensate atom number N_0, we use this relationship can be used to to determine the calibration factor C^2 (see Sec. 5.4.1) [53]. Eq. 5.30 can be rewritten

$$R_z \equiv B(C^2 N_0^{\mathrm{naive}})^{1/5}, \tag{5.31}$$

where N_0^{naive} is the naive pixel sum atom number (calculated from the measured optical density using the ideal absorption cross-section $\sigma_0 = 3\lambda^2/2\pi$), and $B = (15a)^{1/5}\,(\hbar/M\omega_i)^{2/5}$.

We prepared $^{87}\mathrm{Rb}$ BECs in the Z-trap by evaporating down to a range of final RF frequencies to adjust the condensate fraction over as wide a range as possible. Two-dimensional bimodal fits to time-of-flight data were used to extract the condensate fraction N_0/N and Thomas-Fermi width R_z along the vertical (transverse) axis of the condensate. The naive total atom number N^{naive} was calculated using the pixel-sum optical density and the ideal absorption cross-section $\sigma_\lambda(\delta)$ (see Eq. B.61) and combined with the condensate fraction to establish the naive condensate number N_0^{naive} for each image. Fig.5.6 shows a plot of R_z as a function of N_0^{naive}. A one-parameter fit to a $1/5$ power law yields $C^2 = 1.9 \pm 0.1$ (5%). This calibration was applied to the results from 2005, 2006 which are reported in this chapter.

A less careful, but more recent calibration of the current imaging system is based on a slightly different method [53]. Rather than relying on a fit to a $1/5$ power law, we (a) empirically locate the BEC phase transition by noting the presence or absence of a condensate peak in the thermal background near T_c, (b) compute the value of T_c at this point using accurate temperature measurements from fits to the thermal component of the cloud, (c) compute the true atom number from T_c using Eq. 2.12, which accounts for finite-size and interaction shifts of the critical temperature, and (d) compare N to N^{naive}, calculated from the optical density using σ_0, to determine C^2.

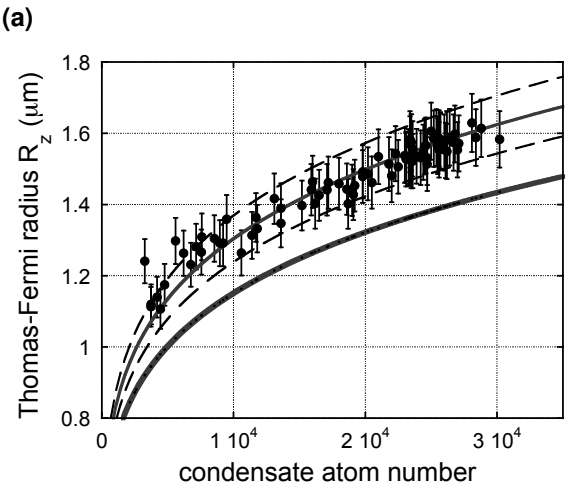

Fig. 5.6: Radial Thomas-Fermi radius R_z of a $^{87}\mathrm{Rb}$ BEC as a function of atom number, for calibration. The thick line shows R_z calculated from the Thomas-Fermi expression Eq. 5.30. The line of best fit (thin solid) yields a calibration factor $C^2 = 1.9 \pm 0.1$. The uncertainty is derived from the C^2 values extracted from the dashed curves, which deviate from the best fit result by $\pm 5\%$. Error bars are uncertainties in R_z from a bimodal fit.

We estimate $C^2 = 1.7 \pm 0.3$, and use this result as a rough calibration of number data from 2007 to the present, including relative BEC number data in presented in Ch. 7. A more careful analysis is needed to confirm this value and to reduce the $\sim 20\%$ systematic uncertainty. This calibration method is expected to be more accurate than the first: it relies on an accurate determination of T_c, which varies as $N^{1/3}$ in general and as N very near T_c, rather than the cloud size, which varies as as $N^{1/5}$ and is therefore less sensitive to N.

5.4.4 DFG

We deduce the in-situ temperature of $^{40}\mathrm{K}$ by fitting time-of-flight optical density images to ideal, non-interacting Fermi gas theory. Unlike with bosons, for which the time-of-flight density profile exhibits a strongly non-Gaussian bimodal structure for $T < T_c$, Fermi gas density profiles deviate much more subtly at low temperatures. As T is reduced below $T/T_F \lesssim 0.5$, Fermi gases appear to stop getting colder, i.e. the Gaussian-estimated width of the time-of-flight density profile is nearly unchanged between $T/T_F \sim 0.3$ and 0. We rely on careful fitting to reliably measure atom number and T/T_F below $T/T_F \sim 0.5$ in our experiments.

We fit two-dimensional optical density data to the Fermi-Dirac column density (see Eqs. 2.44 and 5.24)

$$OD(y,z) = A f_2\left(\mathcal{Z}\exp\left[-\frac{(y-y_c)^2}{2\sigma_y^2} - \frac{(z-z_c)^2}{2\sigma_z^2}\right]\right) + m_y y + m_z z + b \tag{5.32}$$

where the amplitude A, fugacity $\mathcal{Z}$, cloud centre positions y_c, z_c, Gaussian widths σ_y, σ_x and

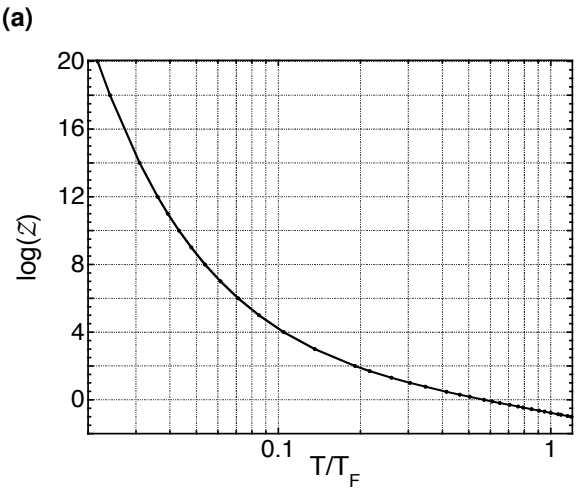

Fig. 5.7: The large variation of $\mathcal{Z}$ in our coldest temperature range $0.1 \lesssim T/T_F \lesssim 0.3$ presents a challenge for least-squares fitting.

background offset b and slopes m_y, m_z are free parameters in the fit.[5] We use the fugacity $\mathcal{Z}$ from fits to obtain the atom number and T/T_F using Eqs. 2.44 and 2.35:

$$N = 2\pi A \sigma_y \sigma_z f_3(\mathcal{Z})/\tilde{\sigma}_\lambda(\delta), \tag{5.33}$$

and

$$T/T_F = (6 f_3(\mathcal{Z}))^{1/3}. \tag{5.34}$$

We use four fit parameters $\mathcal{Z}$, A, σ_y and σ_z, even though only there are only two physically independent parameters (e.g. atom number N and temperature T). Under-constraining the fit by leaving these four parameters free allows us to calculate T/T_F in two ways, as an independent check of our analysis: from N and T according to from Eq. 2.35, or directly from $\mathcal{Z}$ using Eq. 5.34. This consistency check is important because accurate least-squares fitting to extract $\mathcal{Z}$ is technically challenging; in real units, $\mathcal{Z}$ spans a huge dynamic range for a relatively small range of T/T_F values (see Fig. 5.7). To compensate for the under-constrained fit, we check that final fit results yield N, T and T/T_F values which are consistent within statistical error. The statistical uncertainty in T/T_F obtained from fits is 0.05. Using Eq. 5.34, this uncertainty is calculated from the difference in $\mathcal{Z}$ values extracted from fits with $\Delta\chi^2 = \pm 1$ with respect to the best fit (i.e the fit with minimum χ^2). The independent fits results for σ_y and σ_z typically differ by 10%, which corresponds to a systematic temerature uncertainty of ± 20 nK for typical parameters (possibly due to a z-direction magnetic field kick during Z-trap turn-off).

Fig. 5.8 shows an example fit to time-of-flight DFG data of $N \sim 4 \times 10^4$ ^{40}K imaged along y (radial imaging) after a 9 ms time-of-flight. The 2D raw optical density image was radially averaged about the cloud centre to increase the signal-to-noise; the resulting data was fit to a

[5] Note that here the peak optical density is $A f_2(\mathcal{Z}) + b$.

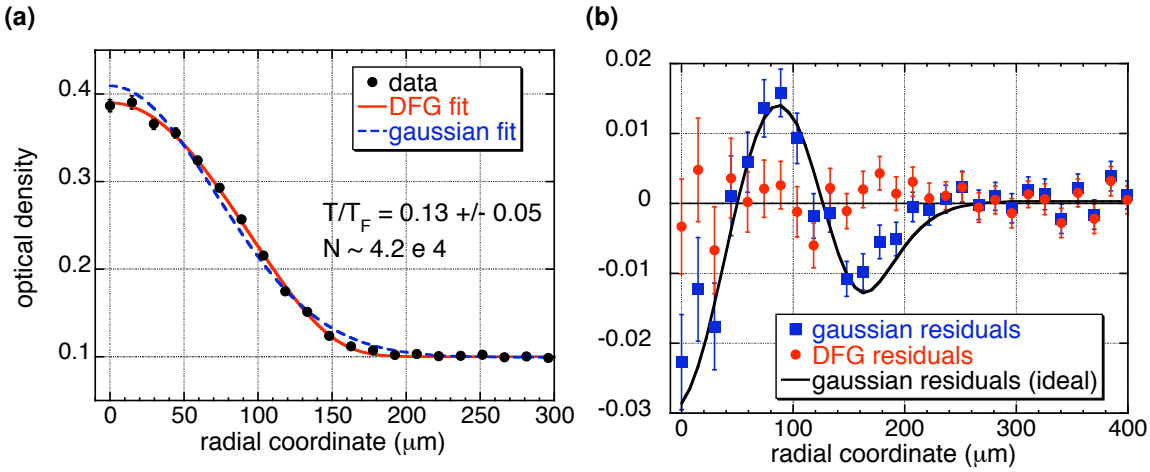

Fig. 5.8: (a) Gaussian (dashed) and Fermi-Dirac (solid) to radially averaged 9 ms time-of-flight data of $N \sim 4.2 \times 10^4$ ^{40}K atoms at $T/T_F = 0.13 \pm 0.05$ imaged after 9 ms of time-of-flight reveal the subtle deviation of the DFG profile from the classical expectation. **(b)** Raw residuals from the Fermi and Gaussian fits. The solid line shows the Gaussian residuals from fits to fictitious DFG data with the same N and T/T_F as the actual data set. Radial averaging was performed about an ellipse defined by the vertical and horizontal cloud widths in the raw 2D optical density image. Error bars are statistical – standard deviations in optical density from radial averaging.

1D version of Eq. 5.32, yielding $T/T_F = 0.13 \pm 0.05$. A Gaussian fit (Eq. 5.32 with $\mathcal{Z} = 1$) is also shown to emphasize that the deviation of ideal DFG from ideal Boltzmann gas theory is very slight even at $T/T_F = 0.13$; the Gaussian fit overestimates the density at cloud centre and edge, and underestimates in between. The reduced-χ^2 of the Fermi and Gaussian fits 0.8 and 2.1 respectively. Fig. 5.8b shows raw residuals of the two fits, emphasizing that the Gaussian fails to capture the shape of DFG data. The Gaussian residuals oscillate about zero, closely following the residuals calculated from Gaussian fits to noise-free simulated DFG test data with the same physical parameters as the actual data set. Above $T/T_F \simeq 0.5$, the Gaussian and Fermi fits are nearly indistinguishable. Fig. 5.9 compares Gaussian and Fermi residuals from fits to ^{40}K clouds at T/T_F values between 0.8 and 0.35 to illustrate this point.

Fermi pressure An additional, more qualitative signature of Fermi degeneracy is Fermi pressure. Unlike the Boltzmann gas, whose spatial width tends toward zero as $T \to 0$, Pauli exclusion results in a finite-sized Fermi gas with a finite average momentum, even at $T = 0$. This Fermi pressure (see Sec. 2.2.3) is evident in Fig. 5.10a, in which the in-trap cloud width deviates from the Boltzmann prediction for $T/T_F \lesssim 0.5$. Absorption images taken at $T/T_F = 0.95$ and $T/T_F = 0.35$ are overlayed with a circle indicating E_F in Figs. 5.10b and 5.10c, demonstrating that the average momentum of the Fermi gas plateaus at low temperature.

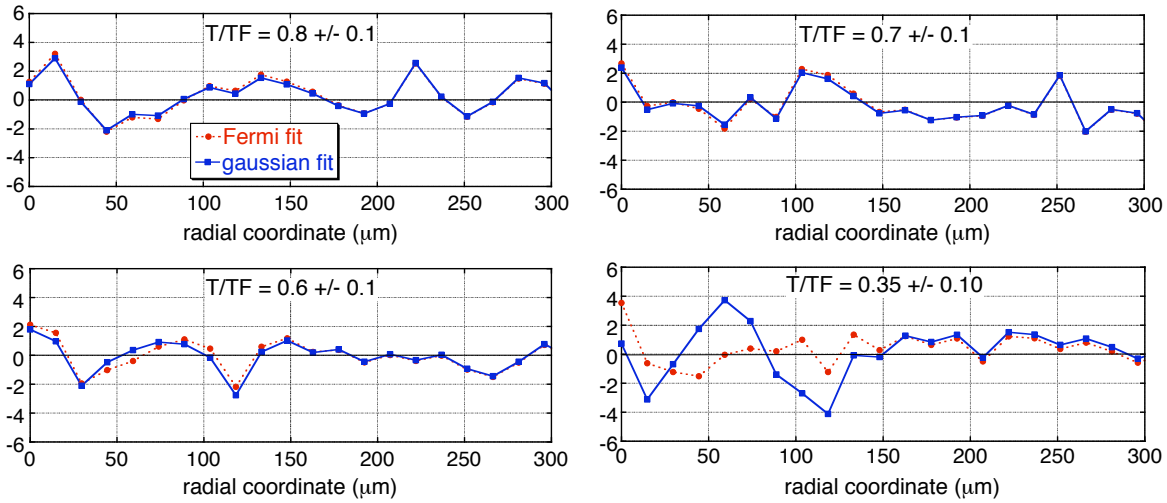

Fig. 5.9: Comparison of normalized fit residuals from Fermi and Gaussian fits to radial ^{40}K DFG data at different values of T/T_F.

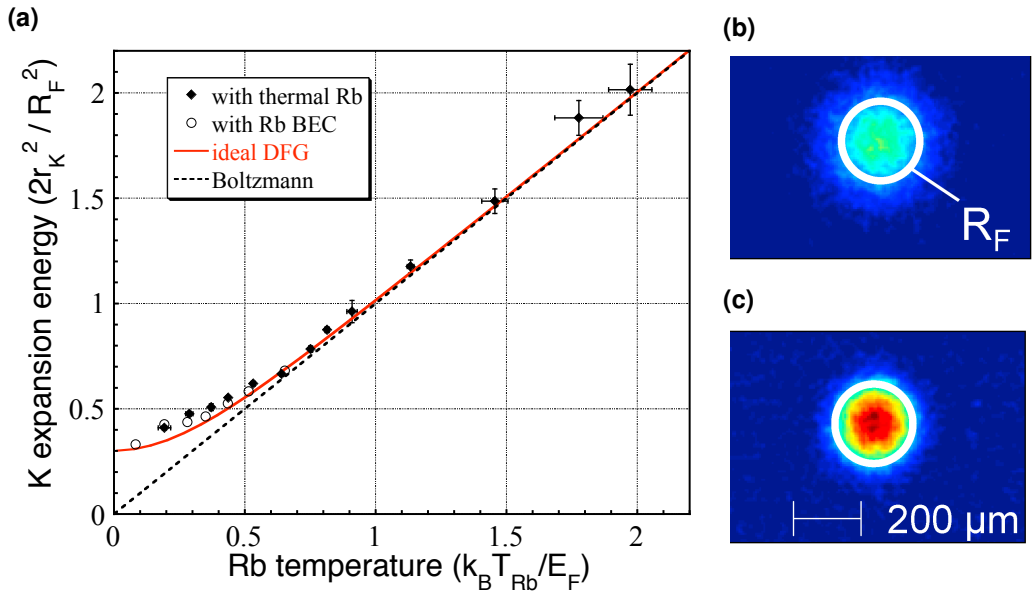

Fig. 5.10: A DFG appears to stop getting colder as the temperature is reduced, even as the reservoir temperature approaches zero. **(a)** The apparent *in situ* fermion temperature measured by Gaussian fits to ^{40}K time-of-flight absorption data, plotted versus ^{87}Rb temperature for both thermal (diamonds) and Bose-condensed (circles) ^{87}Rb. The data follows a curve derived from Gaussian fits to artificial, perfect Fermi distributions (solid line), deviating from the corresponding Boltzmann prediction (dashed) at temperatures below $T/T_F \approx 0.5$. Quantum degeneracy of ^{87}Rb has little effect on the ^{40}K expansion energy in this data (circles vs. diamonds). **(b,c)** Absorption images for $T/T_F = 0.9$ and $T/T_F = 0.35$ respectively, overlayed with white circles of radius R_F rescaled after time-of-flight (see Sec. 2.2.2). By comparison, a Boltzmann gas with T corresponding to "$T/T_F = 0.35$" would have a radius $2\sigma \approx 0.8R_F$.

5.5 Rb–K cross-thermalization

When empirically optimizing the sympathetic cooling trajectory, we find that RF sweep times faster than 6 s are not successful, whereas ^{87}Rb alone can be evaporated to BEC in just 2 s. This indicates that the ^{40}K and ^{87}Rb rethermalize more slowly than ^{87}Rb alone. Measurements of the ^{40}K-^{87}Rb temperature ratio during sympathetic cooling (see Fig. 5.11a) reveals that ^{40}K lags behind ^{87}Rb at high temperatures, despite the fact that our optimal RF frequency ramp is slower at its start, when atoms are hottest, and accelerates near the end, when atoms are coldest.

In the low-temperature limit, we did not expect cross-species thermalization to lag ^{87}Rb-^{87}Rb thermalization, since the ^{40}K-^{87}Rb elastic scattering cross section exceeds the ^{87}Rb-^{87}Rb cross section by roughly a factor of two: $\sigma_{KRb} = 4\pi a_t^2 = 1480 \pm 70$ nm^2 [129] whereas $\sigma_{RbRb} = 8\pi a_t^2 = 689.6 \pm 0.3$ nm^2, using the fermion-boson and boson-boson scattering $T \to 0$ expressions for the cross-section with the triplet scattering length a_t quoted in [129] and [55], respectively. However, in early 2006 when our measurements were published [27] several conflicting values of σ_{KRb} had been previously reported [22, 26, 129, 127, 134, 122, 135].

5.5.1 Measuring the K–Rb scattering cross-section

To investigate σ_{KRb} further, we measured the cross-species thermalization rate at temperatures between 10 µK and 200 µK in a mixture with relatively small ^{40}K atom number: ($N_K \leq 0.04 N_{Rb}$) [27]. We start with a ^{87}Rb-^{40}K mixture in thermal equilibrium in the presence of a fixed RF frequency ν_{RF}. We then abruptly reduce the ^{87}Rb temperature to T_{Rb} by reducing ν_{RF}, wait for a variable hold time, and measure the ^{40}K temperature T_K [136]. Fig. 5.11b shows an example ^{40}K temperature as function of the hold time. The decay of $\Delta T \equiv T_K - T_{Rb}$ can be described generically by the differential equation [137]

$$\frac{\mathrm{d}(\Delta T)}{\mathrm{d}t} = -\frac{\Delta T}{\tau}. \tag{5.35}$$

Adapting the two-species rethermalization model of [137] to our experiment, in which $N_{Rb} \gg N_K$, $\mathrm{d}T_{Rb}/\mathrm{d}t \approx 0$ during the ^{87}Rb measurement time, and T_K approaches T_{Rb} asymptotically, the decay time τ can be written

$$\frac{1}{\tau} = \frac{\sqrt{2}}{3\pi^2} \frac{\sigma_{KRb}}{k_B T_{Rb}} \frac{\sqrt{M_K} M_{Rb}^2 \omega_\perp^2 \omega_\parallel}{(M_K + M_{Rb})^{3/2}} N_{Rb} \tag{5.36}$$

where the harmonic oscillation frequencies ω_i are for ^{87}Rb. We use an exponential fit of the T_K decay data to find τ, and use τ to compute σ_{KRb} using Eq. 5.36.

5.5.2 Ramsauer-Townsend effect at high temperatures

The results of σ_{KRb} measurements show a clear reduction in the scattering cross section at high temperatures. We compare the results to the σ_{KRb}-vs.-temperature behaviour predicted by two scattering models. The simpler "naive" model assumes s-wave scattering from a delta-function

potential, for which the s-wave phase shift δ_0 is given by $k \cot \delta_0 \approx -1/a$ in the low-energy limit, where a is the ^{40}K-^{87}Rb s-wave scattering length and k the relative wavevector in the centre-of-mass frame [82, Ch.8]. k is determined from the measured temperature of the gas T using a velocity-weighted average over the distribution of velocities that corresponds to T. The naive s-wave scattering cross section is then

$$\sigma_{KRb}(k) = \frac{4\pi}{k^2} \sin^2 \delta_0 = \frac{4\pi a^2}{1 + a^2 k^2}, \tag{5.37}$$

which predicts $\sigma_{KRb} > \sigma_{RbRb}$ throughout our temperature range, in stark contrast to the experimental data. Better agreement is given by an effective-range model, which includes the next-order correction to the s-wave scattering phase shift $k \cot \delta_0 \approx -1/a + r_e k^2/2$, where r_e is the effective range of the scattering potential [138]. This reduction of the phase shift results in a reduced scattering cross section [136]

$$\sigma_{KRb}(k) = \frac{4\pi a^2}{\left(1 - \frac{1}{2}|a| r_e k^2\right)^2 + a^2 k^2}, \tag{5.38}$$

which is in good agreement with the experimental data.

The data in Fig. 5.12 was first analyzed assuming a temperature-independent cross-section within the range of initial and final ^{40}K temperatures for each data point. We then re-analyzed the data using a self-consistent method that assumes the effective-range temperature dependence, and found a small upward shift of the best-fit cross-section values. Using this shift as an estimate of the systematic error, we fit the four lowest-temperature data points to the effective-range model of Eq. 5.38 using $r_e = 20.2 \pm 0.3$ nm (calculated according to [138] with $C_6^{KRb} = 4274 \pm 13$ a.u. [139]) and find a ^{40}K–^{87}Rb scattering length $a_{KRb} = -9.9 \pm 1.4 \pm 2.2$ nm, in agreement with [129]. The second uncertainty is systematic, and includes the uncertainty in ^{87}Rb atom number calibration (see Sec. 5.4.3.1).

We attribute the observed reduction in scattering cross-section to the onset of the Ramsauer-Townsend effect, in which the s-wave scattering phase and cross-section approach zero for a particular value of relative energies between particles [140, 27].

We compare the sympathetic cooling of ^{40}K to similar efforts in ^{6}Li, which is the other fermionic alkali species in heavy use in the experimental DFG community (see [50] and references therein). ^{6}Li–^{87}Rb sympathetic cooling and Feshbach resonance measurements [25, 141] demonstrate a zero-temperature cross section approximately 100 times smaller than σ_{KRb}; in other words, a maximum ^{6}Li–^{87}Rb cross-section roughly equal to the lowest ^{40}K–^{87}Rb value we measure. Thus, despite the high-temperature reduction in cross-section ^{40}K and ^{87}Rb are relatively good sympathetic cooling partners.

5.5.3 Required temperature

The reduction in the K–Rb elastic scattering cross-section discussed in Sec. 5.5.2 suggests that we should start the evaporation at a lower temperature. Unfortunately, ^{87}Rb–^{87}Rb elastic collision

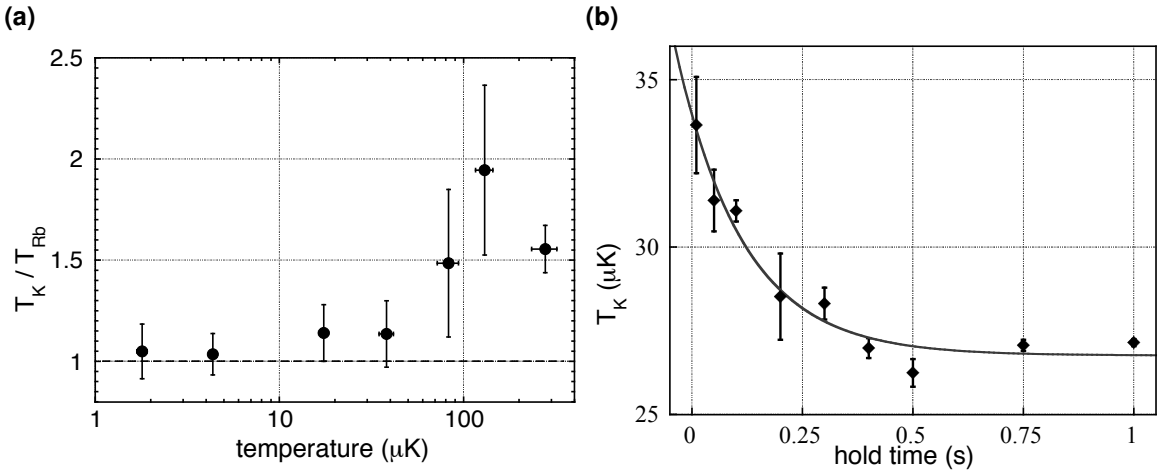

Fig. 5.11: $^{40}\mathrm{K}$ and $^{87}\mathrm{Rb}$ temperatures during evaporation. **(a)** The ratio of $^{40}\mathrm{K}$ to $^{87}\mathrm{Rb}$ temperature approaches 1 at the $^{40}\mathrm{K}$ temperature is lowered during sympathetic cooling. **(b)** We measure the cross-thermalization by abruptly reducing the temperature of $^{87}\mathrm{Rb}$ and watching the temperature of $^{40}\mathrm{K}$ relax with time. The data shown has an asymptotic $^{40}\mathrm{K}$ temperature of 27 μK. The exponential decay constant ($\tau = 6.5\ \mathrm{s}^{-1}$ in this data) is used to extract the $^{40}\mathrm{K}$–$^{87}\mathrm{Rb}$ scattering cross section (see text).

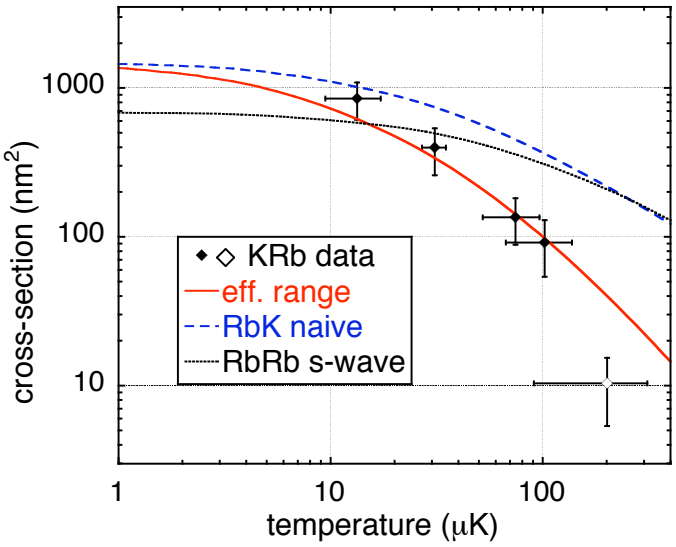

Fig. 5.12: K–Rb cross-species thermalization. Measurements of σ_{KRb} (diamonds) are compared with the s-wave-only (dashed) and effective-range (solid) scattering models (see text). For reference, the s-wave σ_{RbRb} is also shown (dotted). The highest temperature point (open diamond) did not completely thermalize and lies off of the effective range prediction. A more sophisticated analysis may be required for this point, owing to severe trap anharmonicity at this high temperature (see Sec. 3.2.3). The vertical error bars are statistical (one standard deviation); the horizontal error bars show the spread in initial and final $^{40}\mathrm{K}$ temperature during rethermalization.

rate required for efficient evaporative cooling within our magnetic trap lifetime imposes a minimum initial temperature. In this section we will shift our focus to *single-species* collision rates in order to understand this constraint.

Evaporative cooling requires a trap lifetime τ_T that is some multiple of the mean collision time $\gamma_{\rm coll}^{-1}$, since roughly three rethermalizing collisions are typically required before a hot atom exits the trap [126, 91] . This multiple is typically 10^3 and the collision rate $\gamma_{\rm coll}^{-1}$, where $\gamma_{\rm coll} = n_0 \sigma_{el} v_{\rm r}$, is the collision rate at the centre of the trap [91]; n_0 is the central density, σ_{el} is the elastic scattering cross-section, and $v_{\rm r} = \sqrt{8 k_B T/\pi M}$ is the relative average velocity of collision partners [91].

Since $\rho_0 \approx n_0 \Lambda_T^3$ at the start of evaporation (see Sec. 5.2.2), we can express the central density in terms of the phase-space density and find

$$\gamma_{\rm coll} = \frac{\sigma_{el} \rho_0 M}{\pi^2 \hbar^3} (k_B T)^2, \tag{5.39}$$

which is independent of atom number. This relation can be used for a broad range of traps to estimate the minimum temperature for efficient evaporation. Defining $\gamma_{\rm coll}^{min}$ as the minimum scattering rate,

$$(k_B T)^2 \geq \gamma_{\rm coll}^{min} \frac{\pi^2 \hbar^3}{\sigma_{el} \rho_0 M}. \tag{5.40}$$

In the case of ^{87}Rb, approximating σ by its low temperature limit $8\pi a_s^2$, where a_s is the s-wave scattering length, we find that the minimum temperature at the beginning of evaporative cooling is

$$T_0^{min} = 300\ \mu{\rm K} \times \left(\frac{10^{-6}}{\rho_0} \right)^{1/2} \left(\frac{\gamma_{\rm coll}^{min}}{150\ {\rm s}^{-1}} \right)^{1/2}, \tag{5.41}$$

for *any* loaded atom number or trap geometry. In our case, the Rb–Rb elastic collision rate at the start of RF evaporation is roughly 150 s^{-1}, and the phase-space density 10^{-6} or slightly higher. Eq. 5.41 predicts $T_0^{min} = 300$ µK, which exactly coincides with the temperature we measure at the start of evaporation. (The excellent agreement should be taken with a grain of salt, since the model is only approximate.) Can we gain anything be decompressing or compressing the trap? Our trap lifetime $\tau_T \sim 5$ s is only 750 times larger than the collision time $\gamma_{\rm coll}^{-1} = 1/150 \simeq 6.7$ ms – less than optimal, assuming that we require $\tau_t \gtrsim 1000 \gamma_{\rm coll}^{-1}$ for efficient evaporation. Any adiabatic decompression would decrease our collision rate below $\gamma_{\rm coll}^{min}$ and result in significant loss of evaporation efficiency. If the trap lifetime were longer, decompression *would* reduce the temperature without sacrificing evaporation efficiency; $\tau_T > 1000 \gamma_{\rm coll}^{-1}$ would be much easier to satisfy even as $\gamma_{\rm coll}^{-1}$ decreased in the decompression. Compressing the trap near the end of evaporation would increase in K–Rb 3-body loss, which would exacerbate the losses we already observe due to attractive ^{40}K-^{87}Rb interactions near the end of evaporation (see Sec. 5.5.2). Compressing near the beginning of evaporation should not induce much loss since densities are relatively small at that point, but compression causes dramatic loss in our case due to the limited trap depth.

For these reasons, we have little choice but to start our evaporation in the regime where the Ramsauer-Townsend effect is significant.

5.6 Summary

This chapter describes the experimental realization of a $^{87}\mathrm{Rb}$ BEC and a $^{40}\mathrm{K}$ DFG in a single chamber, atom-chip-based apparatus. We describe the laser cooling, magnetic trapping and transport, chip loading, and evaporative cooling steps used to make BEC and DFG [45, 33]. This work represents the first demonstration of DFG in a simple, single chamber apparatus.

We discuss the roles of trap depth and trap volume in microtrap experiments, with particular emphasis on chip loading of $^{87}\mathrm{Rb}$ and $^{40}\mathrm{K}$ in our setup. We also discuss the signatures of quantum degeneracy in BEC and DFG using time-of-flight absorption imaging, including Fermi pressure in the DFG at $T \simeq 0.1T_F$. By studying $^{87}\mathrm{Rb}$–$^{40}\mathrm{K}$ thermalization, we observed a dramatic decrease in the $^{87}\mathrm{Rb}$–$^{40}\mathrm{K}$ scattering cross-section at $T \sim 300\mu\mathrm{K}$, which we attribute to the Ramsauer-Townsend effect. The methods used to achieve DFG and BEC presented here are used in the RF-dressed potential experiments presented in Ch. 6 and Ch. 7.

Explore an unpaved road with a new friend.

Wing's Fortune Cookie

6

Radio-frequency-dressed double-well potentials

Soon after establishing DFG and BEC, we began to experiment with radio-frequency manipulation of cold atoms beyond simple evaporative cooling. After a crash course in the art by the visiting Dr. Thorsten Schumm, we began to work on creating radio-frequency dressed double-well potentials for ultra-cold $^{87}\mathrm{Rb}$ and $^{40}\mathrm{K}$ atoms.

For atoms confined to a magnetic trap, an applied magnetic field oscillating at radio frequencies (RF) can resonantly couple adjacent m_F states. The atomic system in the combined static and time-varying magnetic fields can be described by a Hamiltonian with new, uncoupled eigenstates – the so-called "adiabatic" or "RF-dressed" states [94, 142]. The spatial dependence of these states, and thus the spatial character of the trapping potential, can be manipulated by varying the RF amplitude B_{rf}, and RF frequency ω. If B_{rf} is large enough that the usual adiabatic condition is satisfied so that Landau-Zener tunnelling between dressed states is suppressed [91], then atoms adiabatically follow the RF-dressed magnetic eigenstates and remain trapped in a double-well potential [143, 121, 144]. This effect was first demonstrated on both thermal [145, 142] and quantum degenerate Bose gases [29, 146], and is now a well-established method for dynamically "splitting" an ultra-cold Bose gas [29, 30, 121, 144, 31, 32].

The RF double wells described in this chapter are applied to the measurements of fluctuations in the relative atom number and relative phase of a dynamically split $^{87}\mathrm{Rb}$ BEC in Ch. 7. RF-dressed potentials are particularly useful for creating double-well potentials for neutral atoms because of their technical simplicity, stability, and broad tunability. The RF potential barrier height and double well separation can be adjusted – from zero, i.e. a single well, to nearly arbitrarily large values – simply by tuning the B_{rf} and/or ω. This allows nearly complete control of the inter-well tunnelling strength. These characteristics are the key advantages of RF double-well potentials over other types of double-well potentials, such as the static magnetic, and magnetic-plus-optical-barrier varieties. In the former, fabrication imperfections and current noise in atom chip wires can lead to instability and uncontrolled asymmetry in the double well [147, 148]. In the latter, the well spacing is determined by the waist of a focussed laser beam, which is typically too large (tens of micrometres) to support inter-well tunnelling in the double-well potential [10].

The chapter begins with theory of atom-RF interactions and RF-dressed states applied to double-well potentials on atom chips. We describe the characterization of these potentials using analytic calculations, which we use as a guide to fine-tune RF potentials used in experiments.

Next we demonstrate the species-selectivity of RF potentials. In a ^{87}Rb-^{40}K mixture, this effect permits the simultaneous formation of a double-well potential for ^{87}Rb and single-well potential for ^{40}K, owing to the unequal g_F values for ^{87}Rb and ^{40}K. Finally, we present weak-field spectroscopic measurements of ^{87}Rb in a dressed adiabatic potential, the main result of which is a precise determination of the RF field magnitude at the site of the trapped atoms. These measurements are essential for a qualitative understanding of our RF-dressed potentials, and to calibrate analytic calculations.

6.1 RF-dressed states

In this section, we consider the effect of a radio-frequency (RF) magnetic field on the Zeeman substates of a atom confined to a static magnetic trap of the type described in Ch. 3. In experiments, we apply linearly polarized RF fields to trapped ^{87}Rb and ^{40}K trapped initially in internal states $|F = 2, m_F = 2\rangle$ and $|F = 9/2, m_F = 9/2\rangle$, respectively. The RF field is applied by one or more chip wires running parallel to the y axis, so that the RF field typically lies in the xz plane (see Figs. 6.5a, 6.5b). The method presented here is based on the geometric spin-1/2 representation of optical absorption and emission in a two-level atom in the rotating wave approximation [94, Section V.A.4]. It follows closely with [143, 148], and applies generally to any atom in internal state $|F, m_F\rangle$.

6.1.1 Atomic spin in a time-varying magnetic field

We imagine an atom at point $\mathbf{r}$ in the lab frame subject to a static magnetic trapping field $\mathbf{B}_0(\mathbf{r})$, and a rapidly oscillating linearly polarized RF field $\mathbf{B}_{\rm rf}(\mathbf{r}, t) \equiv \mathbf{B}_{\rm rf}(\mathbf{r})\cos(\omega t)$. The semi-classical interaction Hamiltonian for an atom with total angular momentum $\mathbf{F}$ in the combined (classical) static and RF magnetic field $\mathbf{B}(\mathbf{r}, t) = \mathbf{B}_0(\mathbf{r}) + \mathbf{B}_{\rm rf}(\mathbf{r}, t)$ is [94]

$$H(\mathbf{r}, \mathbf{t}) = -\boldsymbol{\mu} \cdot \mathbf{B}(\mathbf{r}, t) \tag{6.1}$$

$$= \frac{g_F \mu_B}{\hbar} \mathbf{F} \cdot [\mathbf{B}_0(\mathbf{r}) + \mathbf{B}_{\rm rf}(\mathbf{r})\cos(\omega t)]. \tag{6.2}$$

We introduce local spatial coordinates X, Y, Z, in which the Z direction is determined by the local orientation of $\mathbf{B}_0(\mathbf{r})$, and decompose the linearly polarized RF field into components parallel and transverse to $\mathbf{B}_0(\mathbf{r})$:

$$\mathbf{B}_{\rm rf}(\mathbf{r})\cos(\omega t) \equiv \left[B_{{\rm rf},X}(\mathbf{r})\hat{\mathbf{X}} + B_{{\rm rf},Z}(\mathbf{r})\hat{\mathbf{Z}}\right]\cos(\omega t) \tag{6.3}$$

where

$$B_{{\rm rf},Z}(\mathbf{r}) = \frac{|\mathbf{B}_0(\mathbf{r}) \cdot \mathbf{B}_{\rm rf}(\mathbf{r})|}{|\mathbf{B}_0(\mathbf{r})|}, \quad \text{and} \quad B_{{\rm rf},X}(\mathbf{r}) = \frac{|\mathbf{B}_0(\mathbf{r}) \times \mathbf{B}_{\rm rf}(\mathbf{r})|}{|\mathbf{B}_0(\mathbf{r})|}. \tag{6.4}$$

The classical response of an atomic spin to a fixed magnetic field is precession about the direction of the magnetic field [82]. We use Ω_0 to denote the angular frequency of Larmor precession

about $\mathbf{B}_0(\mathbf{r})$, and Ω_{rf} to denote the angular frequency of Larmor precession about $\mathbf{B}_{\text{rf}}(\mathbf{r})$ [94, Section V.A.3]:

$$\hbar\Omega_0 \equiv g_F\mu_B B_0(\mathbf{r}) \quad \text{and} \tag{6.5}$$

$$\hbar\Omega_{\text{rf}} \equiv \frac{1}{2}g_F\mu_B B_{\text{rf}}(\mathbf{r})\cos(\omega t) = \hbar\sqrt{\Omega_X^2+\Omega_Z^2}\cos(\omega t), \quad \text{introducing} \tag{6.6}$$

$$\hbar\Omega_X \equiv \frac{1}{2}g_F\mu_B B_{\text{rf,X}}(\mathbf{r}), \quad \text{and} \quad \hbar\Omega_Z \equiv \frac{1}{2}g_F\mu_B B_{\text{rf,Z}}(\mathbf{r}). \tag{6.7}$$

Note that, although the static trap field $\mathbf{B}_0(\mathbf{r})$ is not spatially uniform, we are free to re-define the XYZ coordinate system at every point $\mathbf{r}$ so that Z always points along $\mathbf{B}_0(\mathbf{r})$. Note also that $\Omega_0, \Omega_{\text{rf}}, \Omega_X, \Omega_Z$ are $\mathbf{r}$-dependent. For convenience of notation, the $\mathbf{r}$ is omitted in these quantities for the remainder of this section. Their spatial dependence is explored further in Sec. 6.2, and ultimately permits the formation of double-well potentials.

6.1.2 Classical picture: rotating wave approximation and rotating frame

With just the static field $\mathbf{B}_0(\mathbf{r})$ pointing along Z, the spin precesses about Z at Larmor frequency Ω_0. To understand the effect of the RF field on the evolution of the spin, we consider the X and Z components of the resulting total field $\mathbf{B}(\mathbf{r},t)$ separately.

The X component $B_{\text{rf,X}}(\mathbf{r})\cos(\omega t)$ can be decomposed into two fields of equal amplitude $B_{\text{rf,X}}(\mathbf{r})/2$, rotating in the XY plane at the frequency ω in the clockwise and counterclockwise directions. The response of the atomic spin to these two rotating components of $B_{\text{rf,X}}(\mathbf{r})$ is most readily understood by conceptually shifting into a reference frame which also rotates about Z at frequency ω [149]. On resonance ($\omega = \Omega_0$), the counterclockwise component of $B_{\text{rf,X}}(\mathbf{r})\cos(\omega t)$ is stationary in the rotating frame, and can thus couple efficiently to the spin, which is also stationary in the rotating frame on resonance. The other component rotates clockwise at frequency 2ω, too quickly to couple to the spin. Ignoring this 2ω component of the RF field on or near resonance is known as the *rotating wave approximation* (RWA) [94]. In this approximation, the total X component field is

$$B_{\text{eff},X} \approx \frac{1}{2}B_{\text{rf,X}}(\mathbf{r}) \tag{6.8}$$

in the rotating frame, with an associated Larmor precession frequency Ω_X. The factor of $1/2$ and time-independence of $B_{\text{eff},X}$ motivates the "1/2" convention and time-independence in the definition of Ω_X, and for symmetry, in the definition of Ω_Z (see Eq. 6.7).

Next we consider the Z component of $\mathbf{B}_{\text{rf}}(\mathbf{r})$. Classically, the effect of $B_{\text{rf,Z}}(\mathbf{r})\cos(\omega t)$ on the atom is to modulate its precession frequency about Z in time at the RF frequency ω. The total Z-direction field amplitude is $B_0(\mathbf{r}) + B_{\text{rf,Z}}(\mathbf{r})\cos(\omega t)$ in the original (non-rotating) frame, and the Larmor precession frequency becomes $\Omega_0 + 2\Omega_Z\cos(\omega t)$. In the rotating frame, the effective Larmor precession frequency is decreased to $\Omega_0 + 2\Omega_Z\cos(\omega t) - \omega$, which implies an effective

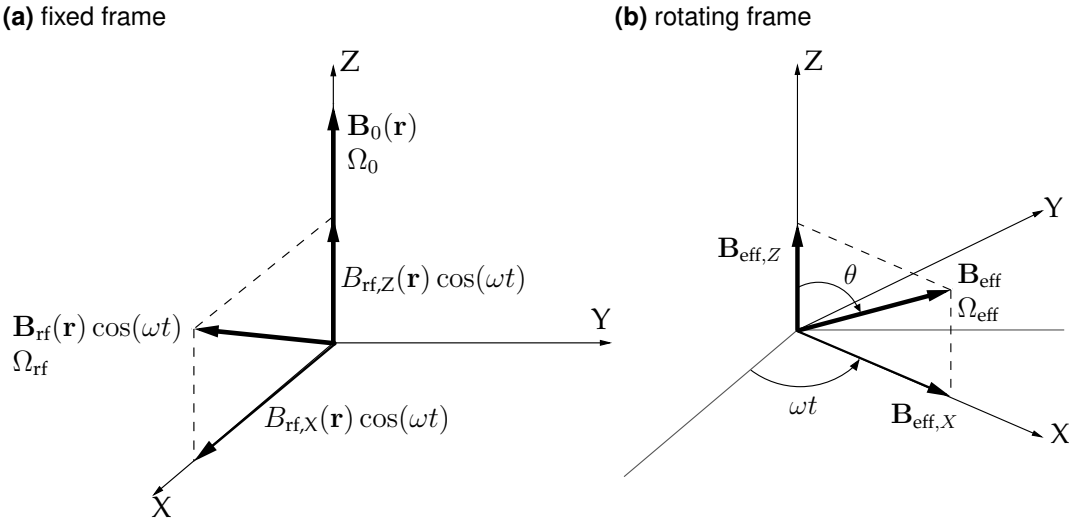

Fig. 6.1: (a) The static field $\mathbf{B}_0(\mathbf{r})$ and RF fields $\mathbf{B}_{\text{rf}}(\mathbf{r})\cos(\omega t)$ in the static XYZ coordinate system, with their respective Larmor precession frequencies Ω_0 and Ω_{rf}. **(b)** Effective static magnetic fields in the rotating frame on resonance. Classically, the spin precesses about the effective static magnetic field $\mathbf{B}_{\text{eff}}$ at Larmor frequency Ω_{eff} (see text).

total Z component magnetic field

$$B_{\text{eff},Z} = B_0(\mathbf{r}) + B_{\text{rf,Z}}(\mathbf{r})\cos(\omega t) - \hbar\omega/g_F\mu_B. \tag{6.9}$$

The total effective magnetic field in the rotating frame is then

$$\mathbf{B}_{\text{eff}}(\mathbf{r},t) = B_{\text{eff},X}(\mathbf{r})\hat{\mathbf{X}} + B_{\text{eff},Z}(\mathbf{r},t)\hat{\mathbf{Z}}, \tag{6.10}$$

with magnitude

$$\begin{aligned} B_{\text{eff}}(\mathbf{r},t) &= \left[\left(B_0(\mathbf{r}) + B_{\text{rf,Z}}(\mathbf{r})\cos(\omega t) - \frac{\hbar\omega}{g_F\mu_B}\right)^2 + \frac{1}{4}B_{\text{rf,X}}(\mathbf{r})^2\right]^{1/2} \\ &= \frac{\hbar}{g_F\mu_B}\sqrt{(2\Omega_Z\cos(\omega t) - \delta)^2 + \Omega_X^2} \end{aligned} \tag{6.11}$$

and associated Larmor precession frequency about $\mathbf{B}_{\text{eff}}(\mathbf{r},t)$

$$\Omega_{\text{eff}} = \sqrt{(2\Omega_Z\cos(\omega t) - \delta)^2 + \Omega_X^2}, \tag{6.12}$$

where the "RF detuning" δ is defined as

$$\delta \equiv \omega - \Omega_0. \tag{6.13}$$

6.1.3 Interaction Hamiltonian

We now use the rotating frame and RWA to compute the interaction Hamiltonian between the atom and the total magnetic field. Using Eqs. 6.3 and 6.4, the Hamiltonian of Eq. 6.1 may be written

$$H(\mathbf{r},t) = \frac{g_F\mu_B}{\hbar}F_Z[B_0(\mathbf{r}) + B_{\text{rf,Z}}(\mathbf{r})\cos(\omega t)] + \frac{g_F\mu_B}{\hbar}F_X B_{\text{rf,X}}(\mathbf{r})\cos(\omega t) \tag{6.14}$$

$$= \Omega_0 F_Z + 2\Omega_Z F_Z\cos(\omega t) + 2\Omega_X F_X\cos(\omega t) \tag{6.15}$$

where F_X and F_Z are the X and Z vector components of the $\mathbf{F}$ operator.

We can understand the time evolution of the hyperfine states $|F, m_F\rangle$ of the trapped atom by considering the time evolution of the spinor $\Psi(\mathbf{r},t)$, whose components $\psi_m(\mathbf{r},t)$ (where $-F \leq m \leq F$) correspond to the wavefunctions of the Zeeman hyperfine states. Rather than solving the Schrodinger equation

$$i\hbar\dot{\Psi}(\mathbf{r},t) = H(\mathbf{r},t)\Psi(\mathbf{r},t) \tag{6.16}$$

in the lab frame, we move into a frame rotating about Z at frequency ω, as described in Sec. 6.1.2. This can be accomplished using the rotation operator

$$R_Z(-\omega t) = \exp(i\omega t F_Z/\hbar), \tag{6.17}$$

which transforms $\Phi(\mathbf{r},t)$ and $H(\mathbf{r},t)$ in the usual way [82, Section B_{VI}]:

$$\Psi(\mathbf{r},t) \to \Phi(\mathbf{r},t) \equiv R_Z(-\omega t)\Psi(\mathbf{r},t) \quad (\text{i.e.} \quad \Psi(\mathbf{r},t) \equiv R_Z^\dagger(-\omega t)\Phi(\mathbf{r},t)\ ) \tag{6.18}$$

$$H(\mathbf{r},t) \to R_Z(-\omega t)H(\mathbf{r},t)R_Z^\dagger(-\omega t). \tag{6.19}$$

Substituting Eq. 6.18 into Eq 6.16, and acting on the result with $R_Z(\omega t)$ from the left yields

$$i\hbar\dot{\Phi}(\mathbf{r},t) = \left[-\omega F_Z + R_Z(-\omega t)H(\mathbf{r},t)R_Z^\dagger(-\omega t)\right]\ \Phi(\mathbf{r},t) \tag{6.20}$$

$$\equiv H_{\text{rot}}(\mathbf{r},t)\Phi(\mathbf{r},t), \tag{6.21}$$

where the rotated-frame Hamiltonian $H_{\text{rot}}(\mathbf{r},t)$ may be re-written using Eq. 6.15 as

$$H_{\text{rot}}(\mathbf{r},t) = -\omega F_Z + R_Z(-\omega t)H(\mathbf{r},t)R_Z^\dagger(-\omega t) \tag{6.22}$$

$$= -\omega F_Z + \Omega_0 F_Z + 2\Omega_Z F_Z\cos(\omega t) + 2\Omega_X\cos(\omega t)R_Z(-\omega t)F_X R_Z^\dagger(-\omega t) \tag{6.23}$$

$$= -\delta F_Z + 2\Omega_Z F_Z\cos(\omega t) + 2\Omega_X\cos(\omega t)\left[F_X\cos(\omega t) - F_Y\sin(\omega t)\right] \tag{6.24}$$

$$= -\delta F_Z + \Omega_X F_X + 2\Omega_Z F_Z\cos(\omega t) + \Omega_X F_X\cos(2\omega t) - \Omega_X F_Y\sin(2\omega t). \tag{6.25}$$

Following Sec. 6.1.2, we apply the rotating wave approximation here by ignoring the terms in Eq. 6.25 oscillating at frequencies ω and 2ω; they cannot effectively couple to the spin, and may be ignored to a good approximation. Doing so leaves behind a *time-independent* effective

Hamiltonian in the rotating frame:

$$H_{\text{eff}} = -\delta F_Z + \Omega_X F_X. \tag{6.26}$$

The stationary effective Hamiltonian may be written in terms of the total effective magnetic field in the rotating frame. To do this we introduce the unit vector $\hat{\mathbf{n}}_\theta = \cos\theta\hat{\mathbf{X}} + \sin\theta\hat{\mathbf{Z}}$ along the direction of $\mathbf{B}_{\text{eff}}$, which makes an angle θ with the Z axis in the rotating frame (see Fig. 6.1). The Hamiltonian may then be written

$$H_{\text{eff}} = F_\theta\sqrt{\delta^2 + \Omega_X^2}, \quad \text{where} \tag{6.27}$$

$$F_\theta = \mathbf{F}\cdot\hat{\mathbf{n}} = F_Z\cos\theta + F_X\sin\theta \tag{6.28}$$

$$\tan\theta \equiv \frac{B_{\text{eff},X}}{B_{\text{eff},Z}} = -\frac{\Omega_X}{\delta}; \quad \sin\theta = \frac{\Omega_X}{\sqrt{\delta^2+\Omega_X^2}} \quad \text{and} \quad \cos\theta = \frac{-\delta}{\sqrt{\delta^2+\Omega_X^2}} \tag{6.29}$$

$$\text{for} \quad 0 \le \theta \le \pi. \tag{6.30}$$

Eq. 6.27 is the Hamiltonian describing the precession of a classical spin in a magnetic field

$$\mathbf{B}_{\text{eff}}(\mathbf{r}) = \frac{\hbar}{g_F\mu_B}\sqrt{\delta^2+\Omega_X^2}\left[\sin\theta\hat{\mathbf{X}} + \cos\theta\hat{\mathbf{Z}}\right] \tag{6.31}$$

at the frequency $\Omega_{\text{eff}} = \sqrt{\delta^2+\Omega_X^2}$.

The dressed states The eigenstates of H_{eff} are the so-called "dressed states" [94]. The effective Hamiltonian contains Zeeman energy terms Ω_0 and Ω_X, as well as the an energy term due to the "dressing" RF photon at frequency ω. We denote the dressed spin states by $|F, m'_F\rangle \equiv |m'_F\rangle$ for simplicity. m'_F is the effective dressed state magnetic quantum number. The dressed states are superpositions of the bare, undressed Zeeman states $|F, m_F\rangle \equiv |m_F\rangle$. They may be thought of as rotations of the bare states about the Y axis by the angle θ

$$|m'_F\rangle = R_Y(\theta)|m_F\rangle, \tag{6.32}$$

and have energies[1]

$$U_{\text{eff}}(\mathbf{r}) \equiv \langle m'_F|H_{\text{eff}}(\mathbf{r})|m'_F\rangle = \hbar m'_F\sqrt{\delta^2+\Omega_X^2}. \tag{6.33}$$

On resonance, $\delta = 0$, $\theta = \pi/2$, and $\mathbf{B}_{\text{eff}}$ points along the X axis. Far below resonance, $\delta \ll 0$, $\theta \to 0$, $\mathbf{B}_{\text{eff}}$ points along Z, and the dressed states coincide with the bare states $|m_F\rangle$. Far above resonance, $\delta \gg 0$, $\theta \to \pi$, $\mathbf{B}_{\text{eff}}$ points along $-Z$, and the dressed states coincide with the inverted bare states $|-m\rangle$.

[1]The matrix elements of H_{eff} are easily evaluated in the basis of dressed states using Eq. 6.27 since $F_\theta|m'_F\rangle = \hbar m'_F|m'_F\rangle$. m'_F is the θ-direction projection of the angular momentum, just as m_F is typically the z axis projection, and $F_Z|F, m_F\rangle = \hbar m_F|F, m_F\rangle$ [82].

6.2 Realizing RF-dressed double-well potentials

This section describes the formation of spatial double-well potentials using RF-dressed states. The first theoretical proposals [142, 150] and experimental demonstrations of RF-dressed potentials focussed on confinement on two-dimensional surfaces [145]. The Schmiedmayer group [29, 121] later showed that the spatial dependence of the effective Hamiltonian could be exploited to create double-well potentials with variable well separation and barrier height by combining a static three-dimensional harmonic chip trap of the type described in Ch. 3 with a linearly polarized RF field.

The spatial dependence of the dressed states of Sec. 6.1 is key to understanding the formation of double wells. To emphasize this point, we re-write Eq. 6.33 with the explicit $\mathbf{r}$ dependence, and using slightly modified notation:

$$U_{\text{eff}}(\mathbf{r}) = \hbar m'_F \sqrt{\delta(\mathbf{r})^2 + \Omega(\mathbf{r})^2} \tag{6.34}$$

$$= m'_F \sqrt{\left[\hbar\omega - g_F \mu_B B_0(\mathbf{r})\right]^2 + \left[g_F \mu_B B_{\text{rf},\perp}(\mathbf{r})/2\right]^2}, \tag{6.35}$$

where $\Omega(\mathbf{r}) \equiv \Omega_X(\mathbf{r}) \equiv g_F \mu_B B_{\text{rf},\perp}/2$ is the RF Rabi frequency, $\delta(\mathbf{r})$ is the RF detuning, $B_0(\mathbf{r}) = |\mathbf{B}_0(\mathbf{r})|$ is the static magnetic field amplitude. We introduce the notation $B_{\text{rf},\perp}(\mathbf{r}) \equiv B_{\text{rf},X}(\mathbf{r})$, which is the component of the RF field that is perpendicular to the static trapping field at the point $\mathbf{r}$. $B_{\text{rf},X}(\mathbf{r})$ is defined by

$$B_{\text{rf},\perp}(\mathbf{r}) = \frac{|\mathbf{B}_0(\mathbf{r}) \times \mathbf{B}_{\text{rf}}(\mathbf{r})|}{|\mathbf{B}_0(\mathbf{r})|} = |\hat{\mathbf{B}}_0(\mathbf{r}) \times \mathbf{B}_{\text{rf}}(\mathbf{r})| \tag{6.36}$$

where $\hat{\mathbf{B}}_0(\mathbf{r})$ is a unit vector in the direction of $\mathbf{B}_0(\mathbf{r})$.

6.2.1 Double well formation

We imagine starting with a 3D harmonic magnetic trap. In our experiments, this is always a Ioffe-Pritchard-type Z-trap. For simplicity, we consider first the effect of RF radiation polarized along x on a spin-1/2 system – an atom with $F = 1/2$ and $m_F = \pm 1/2$. This system is easily generalized to higher spins, in particular to $F = 2$ and $F = 9/2$ for ^{87}Rb and ^{40}K in our experiments.

An RF field at frequency ω resonantly couples the adjacent spin states at positions $\mathbf{r_1}$ satisfying

$$g_F \mu_B B_0(\mathbf{r}_1) = \hbar\omega. \tag{6.37}$$

Fig. 6.2 shows the magnetic spin-1/2 potentials calculated as a function of the radial coordinate of the static trap. (The needle-shaped Z-trap is radially symmetric in the xz plane, and elongated along y. See Ch. 3) The finite RF Rabi frequency $\Omega_{\text{rf}}(\mathbf{r}_1)$ leads to an avoided crossing between the dressed states $|m'_F = \pm 1/2\rangle$ at $\mathbf{r}_1$. The dressed state level separation at the avoided crossing is $\hbar\Omega$, and is thus proportional to $B_{\text{rf},\perp}(\mathbf{r})$.

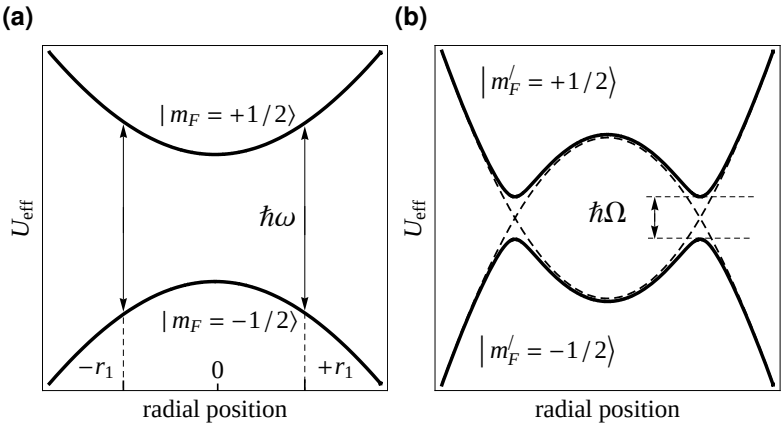

Fig. 6.2: Effective potential of the two RF-coupled spin-1/2 magnetic Zeeman states in a radially symmetric harmonic magnetic field. **(a)** The RF is resonant with the bare states at radial positions $\pm r_1$. **(b)** The coupled dressed states (solid) show avoided crossings of the uncoupled states (dashed) at $\pm r_1$, whose separation is proportional to the RF Rabi frequency. The effective dressed potential calculations in the figure are based on the finite-wire-width model described in Ch. 3, and are described in more detail in Sec. 6.3.

Though the upper dressed state $|m'_F = 1/2\rangle$ of Fig. 6.2b appears to be a double-well potential, the radial symmetry of the resonance condition in the static magnetic field means that we have so far only described an ellipsoidal shell of minimum effective potential, rather than two localized minima. The resonance condition of 6.37 defines this 3D surface, which was explored theoretically and experimentally with a uniform RF field in [142, 150, 145]. The symmetry in the full effective potentials is lifted, however, by the spatial dependence of $B_{\text{rf},\perp}(\mathbf{r})$, which we have ignored so far in these paragraphs. This leads to two local minima on the shell and the desired double-well potential.

A cross-section of the "resonance shell" ellipsoid defined by Eq. 6.37 is drawn in Fig. 6.3a (red circle), superimposed on a unit vector field of the static magnetic trap in the radial xz plane (in the Orsay RF configuration). Though $\hbar\omega = g_F \mu_B B_0(\mathbf{r})$ at every point on this ring, U_{eff} varies around the ring due to the spatial dependence of $B_{\text{rf},\perp}(\mathbf{r})$. The total RF field is polarized primarily along x in this example. By definition (Eq. 6.36), $B_{\text{rf},\perp}(\mathbf{r})$ reaches is minimum value when it is parallel to the local static magnetic field, or more generally, when $|\mathbf{B}_0(\mathbf{r}) \times \mathbf{B}_{\text{rf}}(\mathbf{r})|$ is minimized. In the static Z-trap, whose x and z magnetic field components form a quadrupole pattern, $B_{\text{rf},\perp}(\mathbf{r})$ and $U_{\text{eff}}(\mathbf{r})$ are minimized at two points in the xz plane (black spots in Fig. 6.3a). In 3D, $U_{\text{eff}}(\mathbf{r})$ is minimized along two lines running roughly parallel y on the surface of the resonance shell. These lines of minimum $U_{\text{eff}}(\mathbf{r})$ are the double-well potential minima for $m'_F > 0$ and can be used to trap and manipulate ultra-cold atoms.

Figs. 6.3c and 6.3d show the calculated effective potential for $m'_F = 2$ in ^{87}Rb in the xz and xy planes, and demonstrate the full 3D double-well potential minima (darkest purple). The calculations were carried out using typical experimental parameters for RF manipulation in the Orsay chip setup (see Sec. 6.2.2).

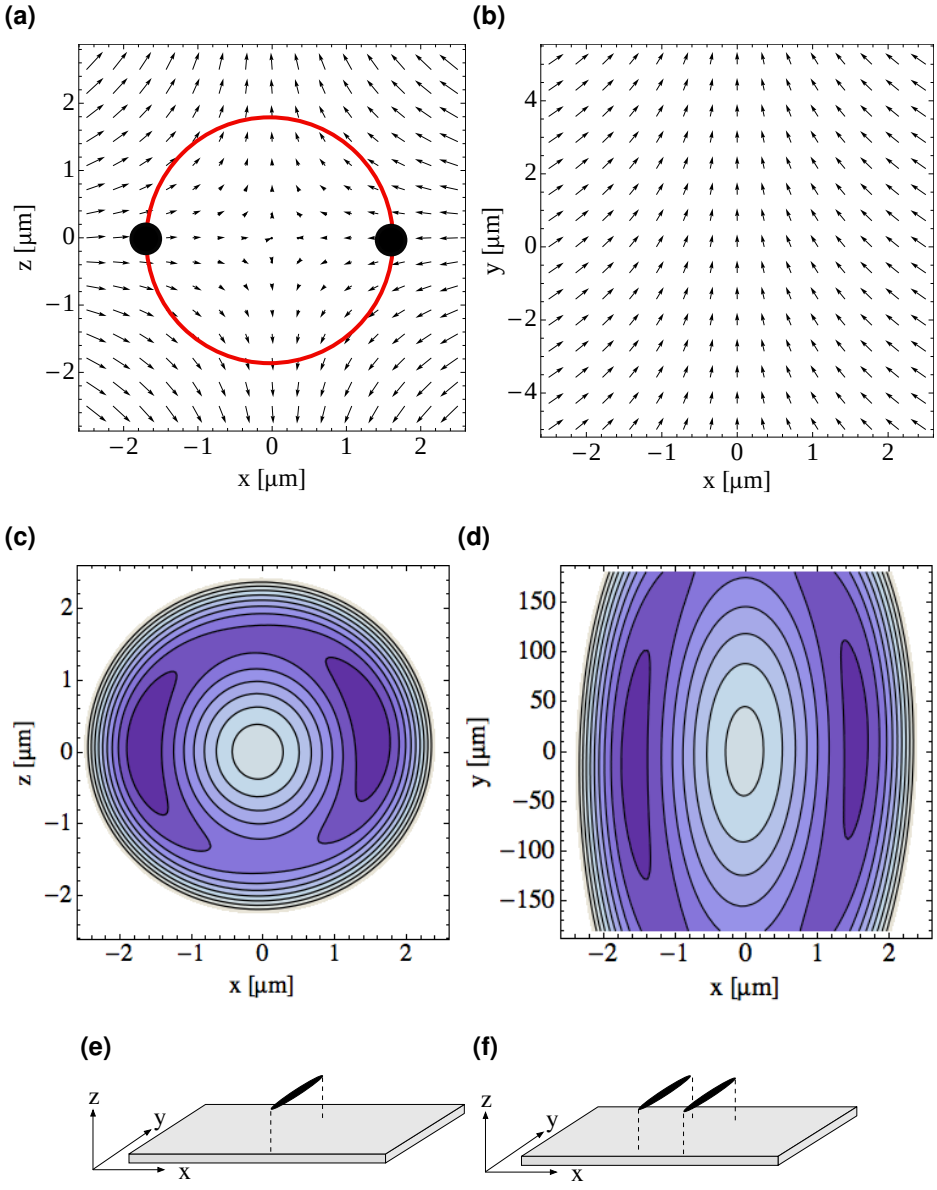

Fig. 6.3: Formation of an RF double well (see text) **(a)** Radial plane unit vector field of static trap in the Orsay configuration, and the resonance ring. **The RF field is polarized horizontally in the xz plane in this configuration.** The double well forms at those points on the ring (black circles) where $B_{\mathrm{rf}}(\mathbf{r})$ is most parallel to $\mathbf{B}_0(\mathbf{r})$. **(b)** The static field of the Z-trap actually points mainly along y at its centre, though the x and z components form a quadrupole pattern in the xz plane. **(c,d)** Contour plots of $U_{\mathrm{eff}}(\mathbf{r})$ for $m'_F = 2$ in $^{87}\mathrm{Rb}$, showing the full 3D character of the double well. Darker, inner colours represent smaller values of the potential. All figures based on analytic calculations in an Orsay chip setup (see text). **(e,f)** Cartoons showing the orientation of atoms trapped in a static single well, as well as a dressed double well with respect to the atom chip.

6.2.2 Atom chip implementations

Since 2006, we have used both the Orsay and Toronto chips (see Ch. 3) to create RF-dressed double-well potentials. The magnetic field polarizations are slightly different in the two setups, as depicted schematically in Fig. 6.5. The z axis points "up" in the diagram, but points "down" in the lab frame (same direction as gravity).

Horizontal splitting In both configurations, we are interested in producing as symmetric a double-well potential as possible. To this end, we work exclusively with "horizontal" double wells, i.e. potentials having the axis of separation of the two clouds lying x. The motivation for horizontal splitting is two-fold. First, it ensures that atoms in both wells are balanced with respect to the gravitational potential. In coherent BEC splitting experiments (see Ch. 7), imbalance leads to to dephasing between the two halves of the split BEC [37]. Second, the horizontal geometry allows large double-well separations without danger of one cloud crashing into the nearby chip, which could be a problem if the clouds were vertically split, for instance. Large separations (10's of µm , up to ~ 150 µm) are necessary to optically resolve the two split clouds, which is a key requirement for accurate atom number counting (see Ch. 7).

Orsay chip configuration The Orsay configuration uses a single chip wire to apply RF to atoms confined to a static Z-trap. The RF wire (the same one used in forced RF evaporative cooling) is located 80 µm from the centre of the Z-wire, is 10 µm thick, and supplies an RF field which is roughly horizontal at $x \approx 80$ µm in the xz plane, in a coordinate system centred on the Z-wire. Horizontal splitting with static Z-traps is possible at any point on the circular arc depicted in Fig. 6.5a [31]. This is a consequence of the fact that the effective potential minima occur at positions on the xz-plane resonance ring at which $B_{\mathrm{rf},\perp}(\mathbf{r}) \parallel B_{0,xz}$, as described in Sec. 6.2.1. Since the chip wire geometry fixes the radius of this ring at 80 µm , we use a shifted Z-trap centred at $x_0 \approx 80$ µm , $z_0 \approx 80$ µm), to *maximize the atom-chip distance*, and hence the quality of the magnetic trap. In general, atom chip magnetic trap lifetimes decrease with decreasing distance from the chip due to the $1/r$ dependence of static and RF magnetic field noise from stray or noisy chip wire currents [118, 15]. Fig. 6.4 shows this effect as measured with the Orsay chip.

The main disadvantages of the Orsay RF configuration are:

1. Inflexibility of the trap position: moving away from ($x = 80$ µm , $z = 80$ µm) results in either non-horizontal splitting, increased double-well asymmetry, decreased magnetic trap lifetime, or some combination of all three.

2. Inherent asymmetry: the usual Z-trap is naturally asymmetric along z, but using a shifted trap below the RF wire introduces an additional x axis asymmetry. This results in an asymmetry in the RF dressed double potential, which becomes severe at large well separations (see Fig. 6.10).

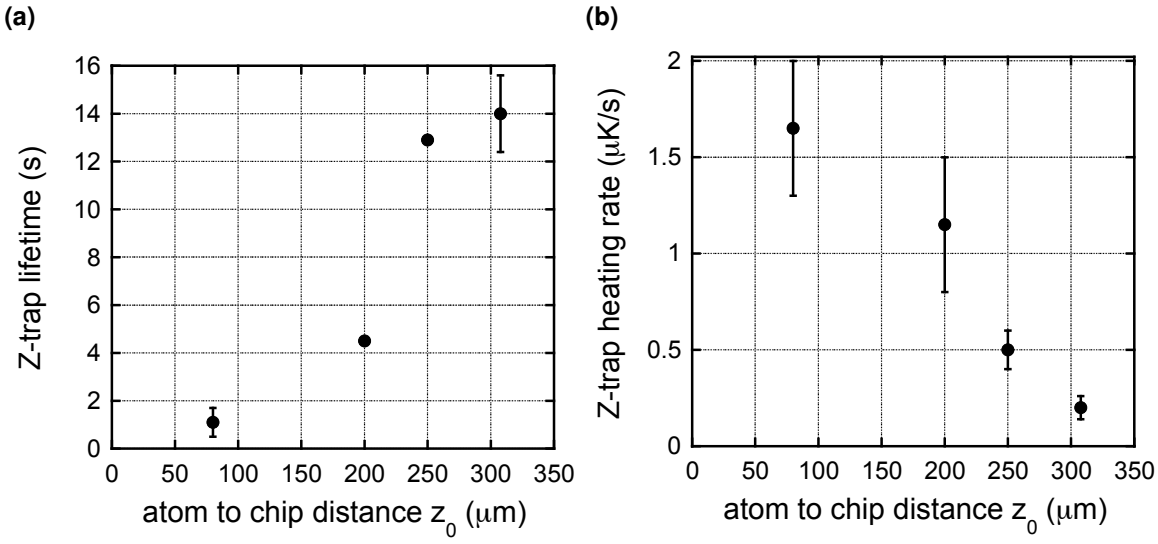

Fig. 6.4: Heating rate and lifetime of a thermal cloud of $N \sim 10^4$ ^{87}Rb atoms at an initial temperature $T \gtrsim T_c$ as a function of the atom-to-surface distance z_0. Heating and loss are caused by magnetic field noise arising from AC current noise in the chip wires [15]. Each lifetime / heating rate measurement involved preparing a cold cloud at a variable distance z_0 with a trap minimum corresponding to $\Omega_0(0) = 2\pi\times$ 405 kHz, and measuring N and T in time of flight after a variable in-trap hold time of 0 to 15 s. Error bars indicate the absolute spread over repeated measurements.

3. Non-uniformity of the RF field: the RF wire creates gradients in $B_{\text{rf}}(\mathbf{r})$ along x and z which distort the dressed potential. Though the gradients scale as $1/r^2$, we cannot reduce them by moving further from the chip without introducing other systematics, as explained in 1.

Toronto chip configuration The Toronto chip's RF configuration addresses each of the Orsay chip's drawbacks. Rather than using a single RF antenna wire, the RF field is supplied by two independent wires [30] (the "U-wires", see Sec. 4.6.2), which are independently powered by the PhaseOMatic RF source described in Sec. 4.4.3. The two RF amplitudes $B_{\text{rf,1}}$ and $B_{\text{rf,2}}$ and their relative phase are tunable and computer controlled. This RF setup results in the following improvements on the Orsay configuration:

1. Horizontal splitting can be achieved using an un-shifted Z-trap at any distance from the chip. The quadrupole xz-plane orientation of the Z-trap necessitates a vertical, linearly polarized RF field to achieve horizontal splitting. This RF field can be produced along the line (x=0, y=0, z=z_0) for any z_0 with $B_{\text{rf,1}} = B_{\text{rf,2}}$ and $\phi = \pi$ (see Fig. 6.5b).

2. Independent amplitude and phase control of the two RF sources permits the creation of RF fields of arbitrary polarization in xz [30, 121, 144]. With $\phi = \pi$, the linear polarization in xz may be adjusted by tuning the relative amplitudes $B_{\text{rf,1}}$ and $B_{\text{rf,2}}$, which can be used to fine-tune horizontal splitting.

3. The static trap and RF field are inherently symmetric in the xz plane at $x = 0$. This allows

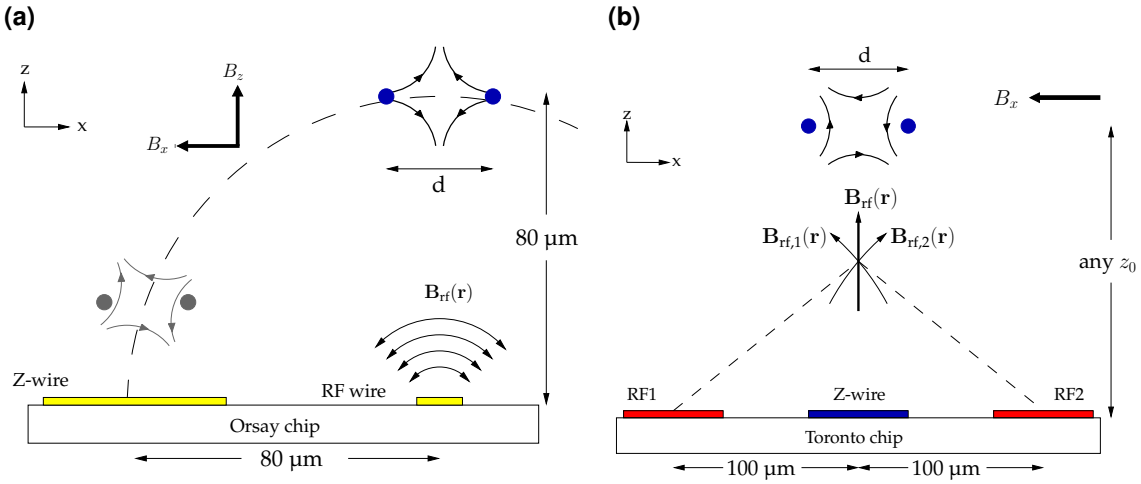

Fig. 6.5: (a) Orsay chip RF splitting geometry. Horizontal splitting is possible anywhere along the dashed arc; we use the position furthest from the chip, directly below the single RF wire, which is naturally asymmetric about the RF wire. **(b)** Toronto RF splitting geometry. RF fields from the two U-shaped RF wires add to produce RF with arbitrary polarization in the xz plane. Symmetric, horizontal splitting is achieved in a Z-trap at any distance z_0 from the chip surface using equal RF1 and RF2 amplitudes and a relative phase of π, which produces a net RF field polarized vertically in the plane. In both figures blue dots indicate the positions of double well minima, and thick black arrows the external bias fields in the plane. (External "Ioffe" fields not shown.)

symmetric double-well potentials even at double well separations of 150 μm or more.

4. The RF antenna wires are electrically isolated from one another, and from the Z-wire. From a technical standpoint, this makes it much easier to prevent RF leakage from the RF sources into the Z-wire or other "DC" chip wires. In the Orsay setup, by contrast, the RF and Z-wires shared a ground connection.

6.2.3 Splitting: from static single-well to dressed double-well

Here we build upon the ideas of the previous section to describe the loading of a double-well dressed potential. The starting point is always a degenerate or near-degenerate atomic sample in $|F = 2, m_F = 2\rangle$ for ^{87}Rb and/or $|F = 9/2, m_F = 9/2\rangle$ for ^{40}K, prepared in a Z-trap as described in Ch. 5 with the RF dressing field off. The RF field is then gradually turned on so that the atoms adiabatically follow the dressed states and remain trapped in $|m'_F = 2\rangle$ and/or $|m'_F = 9/2\rangle$ as the state deforms from a single harmonic trap into a double-well potential. This process is referred to as "splitting" since the original, single cloud is divided in two by the potential barrier which forms at the centre of the dressed state.

As RF is applied to the static trap, the harmonic dressed potential flattens out, becoming less and less quadratic until the curvature at trap centre eventually changes sign and a non-zero potential barrier forms (see Fig. 6.6). We describe two experimental splitting methods, which we refer to as "frequency splitting" and "amplitude splitting". These names derive from the fact that

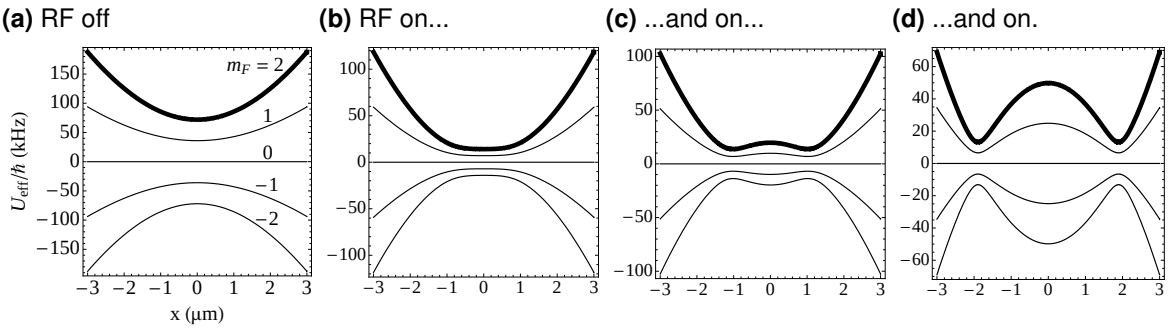

Fig. 6.6: RF splitting demonstrated with ^{87}Rb effective dressed potentials. Atoms initially in $|F = 2, m_F = 2\rangle$ (thick, upper curve) adiabatically follow the dressed potential as it flattens, and eventually deforms into a double well as the RF amplitude and/or frequency are increased from **(a)** to **(d)**.

each relies on a time sweep of the RF frequency (at a fixed amplitude), or the RF amplitude (at a fixed RF frequency) to raise the barrier. Both yield qualitatively similar results and double-well potentials, but are based on different interactions between the static and RF magnetic fields.

6.2.3.1 Frequency splitting

In frequency splitting, the double well separation and barrier height are controlled dynamically using ω sweeps at a fixed RF amplitude. The locations of the double well minima are determined by the resonance condition of Eq. 6.37. A typical time sequence of ω and $B_{\rm rf}(\mathbf{r})$ is depicted schematically in Fig. 6.7. The first step is to ramp on the RF amplitude from zero to some finite value, with the ω tuned below resonance: $\omega < \Omega_0(0)$ and $\delta(0) < 0$. The goal of this "dressing" step is to reach the situation depicted in Fig. 6.6b, in which the potential is deformed, but a central potential barrier does not yet exist. We typically use $\delta(0) \sim -2\pi \times 50$ kHz to $-2\pi \times 10$ kHz and ramp $B_{\rm rf}(\mathbf{r})$ from 0 to on the order of 300 mG [2] in 10 to 100 ms. The RF amplitude is such that $B_{\rm rf}/B_0 \sim 0.1$ to 0.4.

In the "splitting", the RF frequency is swept from below to above resonance at a constant amplitude to raise the potential barrier. Fig. 6.8 shows the evolution of barrier height and double well separation as ω and/or $B_{\rm rf}$ is increased during frequency and amplitude splitting splitting. The data in Fig. 6.8 are the results of analytic calculation of a splitting scenario in the Toronto chip setup (see Sec. 6.2.2). In this example, the undressed static trap is centred 193 μm directly below the Z-wire, has harmonic oscillation frequencies $\omega_{x,z} \simeq 2\pi \times 1.7$ kHz and $\omega_y \simeq 2\pi \times 13.7$ Hz, and a minimum bottom corresponding to $\Omega_0(0) = 2\pi \times 416.5$ kHz.

Fig. 6.10 shows absorption images of split ^{87}Rb and ^{40}K clouds. The upper row shows averaged images of $N \sim 1.5 \times 10^4$ ^{87}Rb atoms initially in a quasi-pure BEC (no discernible thermal cloud) split and separated by 70 μm using frequency splitting. In these data, a static trap with $\Omega_0 = 2\pi \times 3.095$ MHz is split with a 40 ms sweep of the RF frequency from $\omega = 2\pi \times 1.55$ MHz

[2] The smaller the RF amplitude, the more reliable the results of RWA calculations based on Eq. 6.35. However, $B_{\rm rf}(\mathbf{r})$ must be large enough to suppress Landau-Zener tunnelling between dressed states.

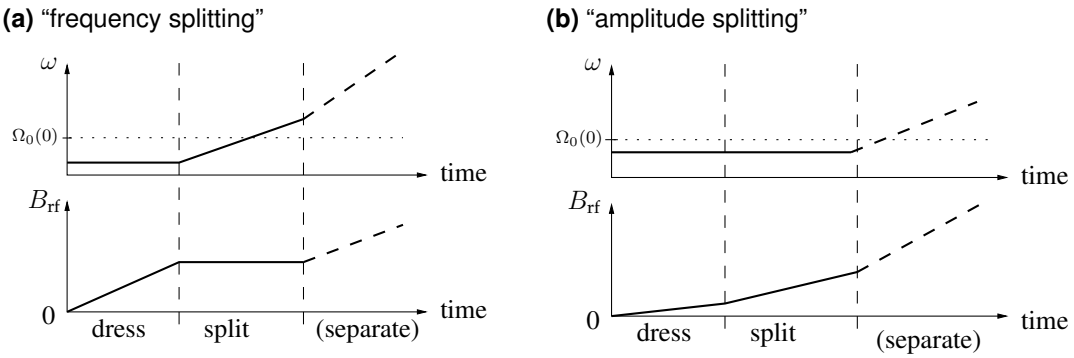

Fig. 6.7: $B_{\rm rf}(\mathbf{r})$ and ω timing diagrams for "frequency splitting" and "amplitude splitting". The dashed lines indicate the optional "separation" step, which is used when counting left and right atom numbers, but not in matter wave interference experiments. See Ch. 7.

to $\omega_{\rm final}$ at a fixed amplitude $B_{\rm rf} = 2000$ mG. The two split clouds are imaged after switching off the traps and a 1.5 ms time-of-flight expansion.

The lower row shows raw (single-shot) images of $N \sim 2 \times 10^4$ ^{40}K atoms at $T/T_F \simeq 1$, split and separated by 100 µm using frequency splitting. The static Z-trap with ^{40}K parameters $\Omega_0 = 2\pi \times 724$ kHz and $\omega_{x,z} \simeq 2\pi \times 800$ kHz is split with a similar 40 ms frequency sweep from $\omega = 2\pi \times 500$ kHz to $\omega_{\rm final}$ at $B_{\rm rf} = 2000$ mG. The split clouds are imaged on resonance after 1 ms time-of-flight. The imaging geometry for both examples is depicted in Fig. 6.9

Since the resonance condition of Eq. 6.37 determines the double well locations, arbitrarily large double well separations are achievable in principle for a static trap of infinite spatial extent. In practice, the maximum double-well separation and barrier height are limited by (a) atom loss due to Landau-Zener tunnelling between dressed states, and (b) the finite extent of the Z-trap. We have achieved double well separations of up to 280 µm using a ω sweeps up to $\delta(0) \sim 10\Omega_0(0)$, accompanied by increases in $B_{\rm rf}$ to maintain a dressed level repulsion sufficient to suppress Landau-Zener tunnelling at the double-well positions (The dressed state level repulsion $\hbar\Omega(\mathbf{r}) \propto B_{{\rm rf},\perp}(\mathbf{r})$ decreasing with increasing distance from the trap centre for RF dressing in a Z-trap, as explained in the next section.)

6.2.3.2 Amplitude splitting

In amplitude splitting, the RF amplitude is ramped up at a fixed, near-resonant RF frequency (see Fig. 6.7). The dressed states deform as $B_{\rm rf}$ is increased, raising a barrier in the centre of the trap to form the double well, as depicted in Fig. 6.6. Unlike frequency splitting, in which the resonance condition (Eq. 6.37) determines the double well separation and barrier height, here the spatial dependence of $B_{{\rm rf},\perp}(\mathbf{r})$ is responsible for deforming the dressed potential as $B_{\rm rf}$ increases.

Even for a completely uniform RF field, $B_{{\rm rf},\perp}(\mathbf{r})$ is non-uniform along x due to the non-uniformity of that static trapping field $\mathbf{B}_0(\mathbf{r})$. The RF fields used in our experiments also have their own spatial non-uniformities, but in both the Orsay and Toronto chip configurations, the net $B_{{\rm rf},\perp}(\mathbf{r})$ non-uniformity is nevertheless dominated by the non-uniformity of $\mathbf{B}_0(\mathbf{r})$ from the

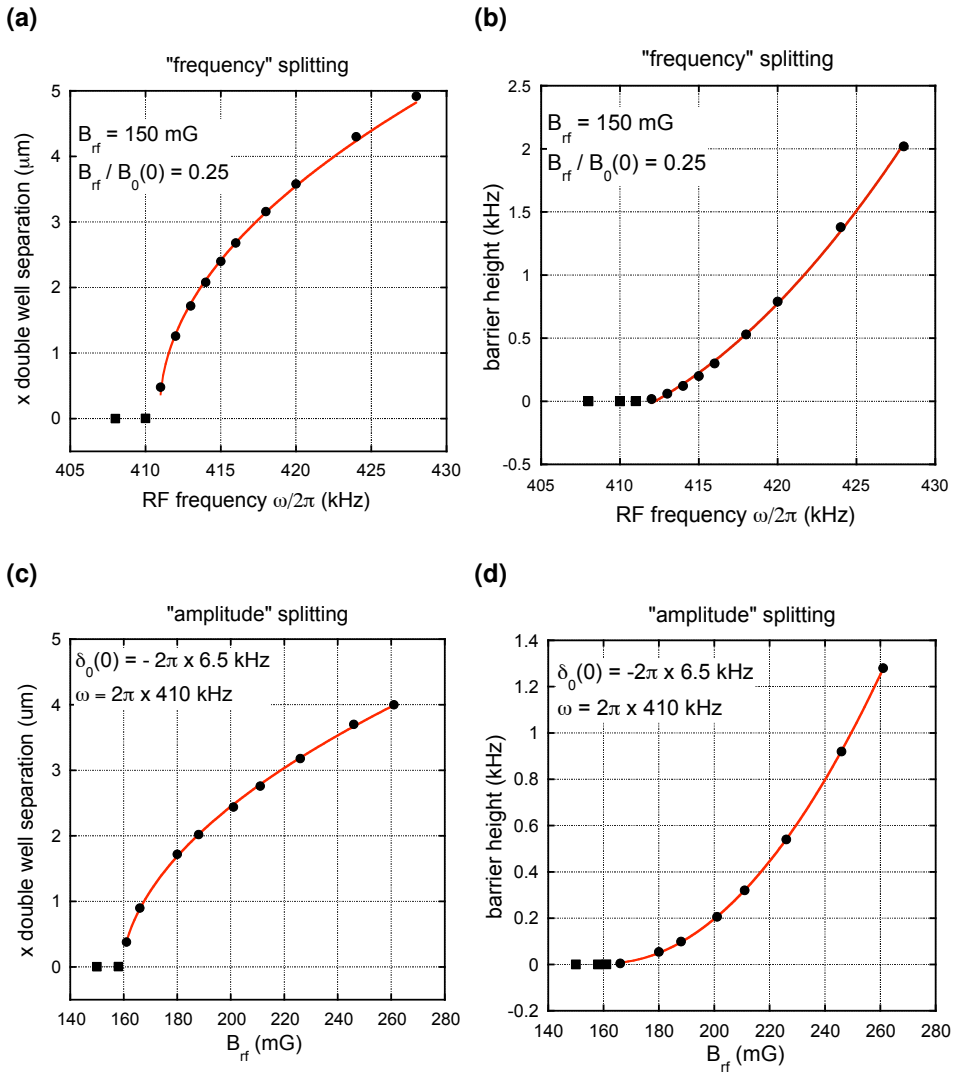

Fig. 6.8: Calculated barrier height and double well separation in "amplitude" and "frequency" splitting for $^{87}\mathrm{Rb}$ in $|m'_F = 2\rangle$, based on Eq. 6.35. Solid lines are empirical fits to $\Delta x \propto (\omega/2\pi)^{1/2}$ and $B_{\mathrm{rf}}^{1/2}$ in **(a)** and **(c)**, and $\Delta x \propto (\omega/2\pi)^2$ and B_{rf}^2 in **(b)** and **(b)**.

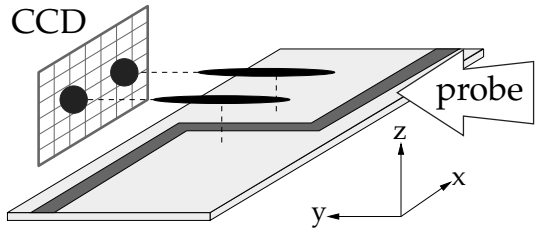

Fig. 6.9: Time-of-flight absorption imaging geometry for observing split clouds and matter wave interference patterns.

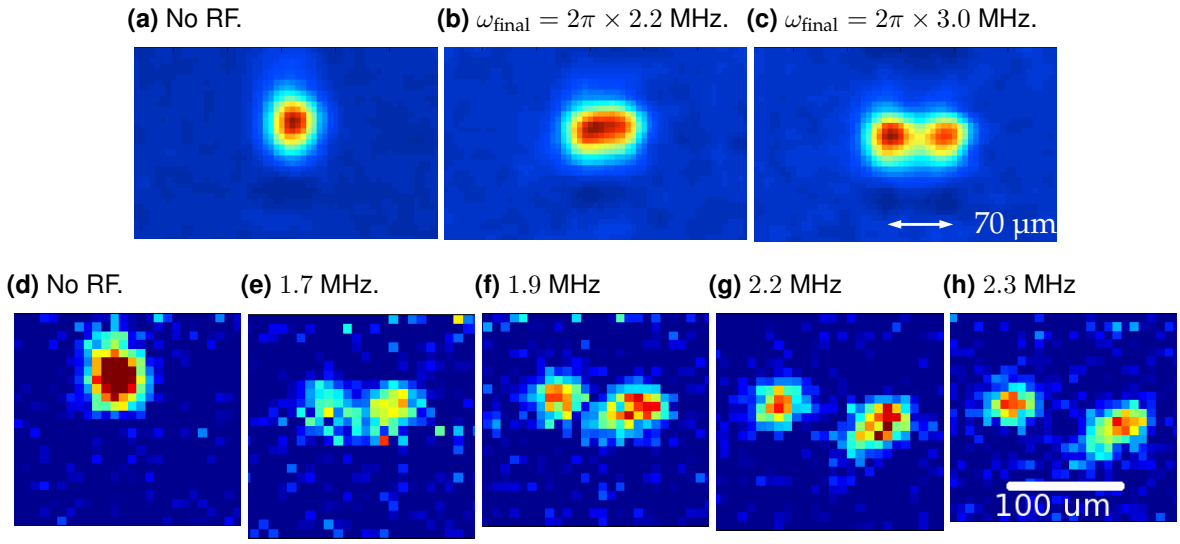

Fig. 6.10: **(a-c)** Averaged absorption images of 1.5×10^4 ^{87}Rb atoms imaged in the xz plane after 1.5 ms time-of-flight (see text). **(d-h)** Raw absorption images of $N \sim 2 \times 10^4$ ^{40}K atoms at $T/T_F \sim 1$ imaged after 1 ms time of flight, labelled by $\omega_{\text{final}}/2\pi$ in frequency splitting. The tilted splitting at large separations is due to inherent asymmetry in the Orsay RF configuration (see Sec. 6.2.2). The atom chip surface is located at the top edge of each image.

Z-trap. Fig. 6.11 shows calculated static, instantaneous RF fields, as well as a plot of $B_{\text{rf},\perp}(\mathbf{r})$ along x for varying $B_{\text{rf}}(\mathbf{r})$ field strengths. In particular, Fig. 6.11a shows the $B_{\text{rf},\perp}(\mathbf{r})$ is peaked at the static trap centre $x = 0$, and drops off sharply with increasing x. As $B_{\text{rf}}(\mathbf{r})$ is ramped up at a fixed frequency ω, this peak in $B_{\text{rf},\perp}(\mathbf{r})$ grows and becomes sharper, which ultimately leads to the barrier in the centre of the dressed potential.

One technical advantage of amplitude splitting over frequency splitting is that, with our DDS-based RF sources, arbitrary RF amplitude sweep functions are possible, whereas ω sweeps are linear or piecewise linear. Amplitude splitting has been effective in performing coherent splitting with small double-well separations for matter wave interferometry (see Sec. 7.1.1). For large well separations – used in relative atom number counting (see Sec. 7.2.1), frequency separation is the only option, for technical reasons. The RF powers required to maintain the level separation between adjacent dressed states for well separations beyond a few µm exceed the capability of our electronics at a fixed ω.[3] Maintaining dressed state level repulsion is critical for maitaining the trap lifetime of atoms in the double-well potential.

6.2.4 Beyond RWA analysis

Since Eq. 6.35 depends on the RWA, it is only valid for RF fields that are weak with respect to the static field. In a 3D harmonic static trap with $\min|\mathbf{B}_0(\mathbf{r})| = B_0(\mathbf{r} = 0) \equiv B_0$, Eq. 6.35 is an excellent approximation when $B_{\text{rf}} \ll B_0$. Lesanovsky et al. [121, 144] have calculated effective dressed potentials without this approximation by diagonalizing the full interaction Hamiltonian

[3] The corresponding RF currents also exceed the current capacity of the Orsay RF antenna wire.

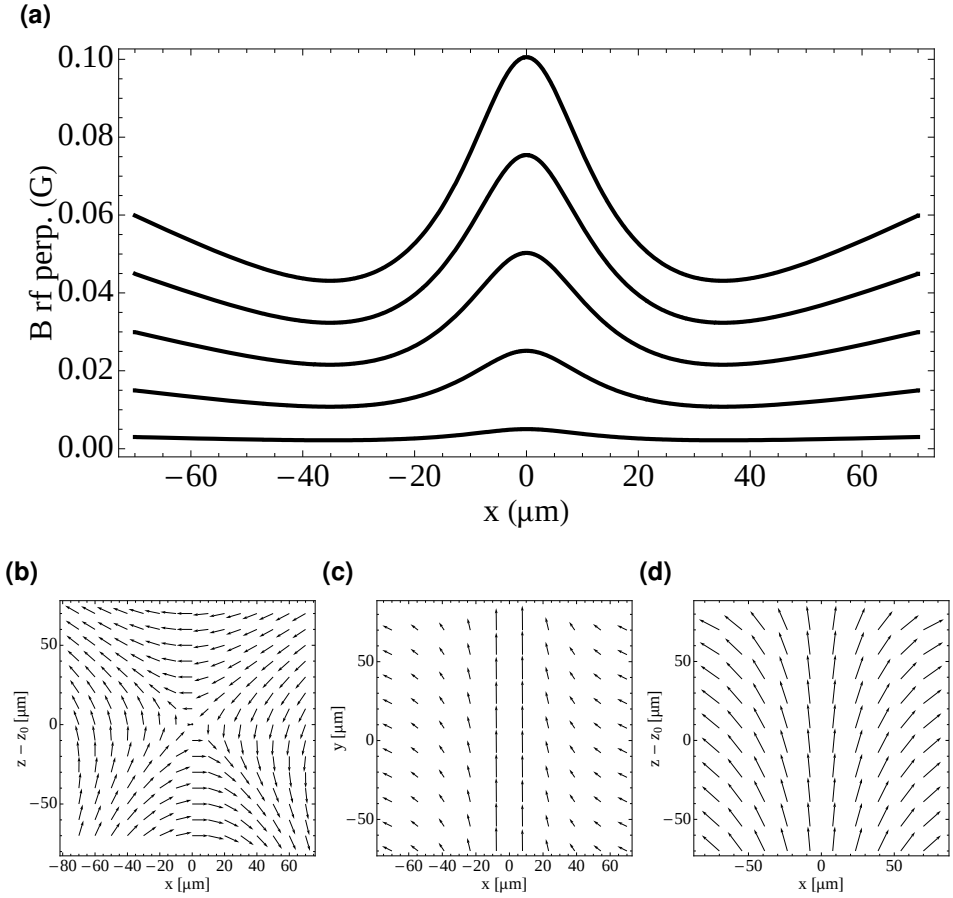

Fig. 6.11: (a) Spatial non-uniformity of $B_{\mathrm{rf},\perp}(\mathbf{r})$, calculated in the Toronto configuration with RF currents of 1, 5, 10, 15 and 20 mA peak (bottom to top curve) in each RF antenna wire, and plotted against x at the static trap position $y = y_0 = 0$ and $z = z_0 = 192$ μm . **(b,c)** Vector plots of the static magnetic field through the trap centre. **(d)** Instantaneous vector field of $B_{\mathrm{rf}}(\mathbf{r})$, which lies almost entirely in the xz plane near the trap centre $y = y_0$ in the Toronto chip configuration.

of Eq. 6.25, and have applied this work to experiments [151] involving relatively large RF field magnitudes $B_{\rm rf} \approx B_0$. Unlike the early work with dressed potentials, which used a traditional macroscopic magnetic trap and an external coil as RF antenna [145], RF field amplitudes generated by atom chip wires tens of micrometres from the atoms can easily equal or exceed $B_0(0)$. However, in the experiments presented in this thesis we were careful to maintain $B_{\rm rf} \lesssim 0.2 B_0(0)$, for which we expect the RWA-based calculations to still be applicable [151]. As the sensitivity of our measurements improves, however, fuller characterization of double-well potentials will likely demand calculations and analysis which include beyond-RWA effects.

6.3 Analytic dressed potential calculations

After RF splitting, two separated clouds can be detected using absorption imaging after times of flight short enough that the clouds have not yet overlapped. Because we cannot resolve the split atomic populations in-situ – or for any well separation less than our imaging resolution of $\sim$ 20 µm – we rely on other means to characterize the double-well potentials at small well separations. In particular, we are most interested in the shape of the potential for barrier heights on the order of the BEC chemical potential μ or DFG Fermi energy E_F, for which inter-well tunnelling and coherence effects are strongest. Barrier heights on these energy scales occur at well separations on the order of 1 to 5 µm , well below our imaging resolution. Therefore we use a combination of analytic calculations and dressed state RF spectroscopy to characterize RF-dressed double-well potentials, which are the focus of this and the next two sections.

The effective dressed potential calculations are based on the finite-width-wire equations derived for static magnetic traps in Ch. 3. Dressed potentials are calculated according to Eq. 6.35, with $\mathbf{B}_0(\mathbf{r})$ and $\mathbf{B}_{\rm rf}(\mathbf{r})$ calculated directly from chip wire magnetic fields according to the "thick-fin." formulae of Ch. 3. Because they rely on the RWA, these calculations are only approximate (albeit very good approximations for $B_0(\mathbf{r}) \gg B_{\rm rf}$), and are not sufficient on their own to fully characterize our dressed potentials. Nevertheless, they have been an extremely useful for our qualitative understanding of the three-dimensional shape of the potentials, and their susceptibility to magnetic gradients at length scales below the optical resolution of our imaging systems. Calculations have also provided insight into the behaviour at large well separations, particularly the susceptibility to Landau-Zener tunnelling loss, which motivated the increase of $B_{\rm rf}$ to achieve the lossless frequency splitting and separation described in Ch. 7.

6.3.1 Effect of spatial gradients in $B_{\rm rf}$: the "banana"

The RF fields produced by atom chip RF antenna wires are spatially non-uniform in both their direction and amplitude. This fact was ignored in our initial experiments with RF double wells since $B_{\rm rf}(\mathbf{r})$ is *nearly* uniform over the few micrometres near the static trap centre where the double well ultimately forms.

When using frequency splitting to create large well separations in the Orsay setup, absorption images of split ^{87}Rb clouds at 2 ms time-of-flight revealed a surprise: two dense regions (the two

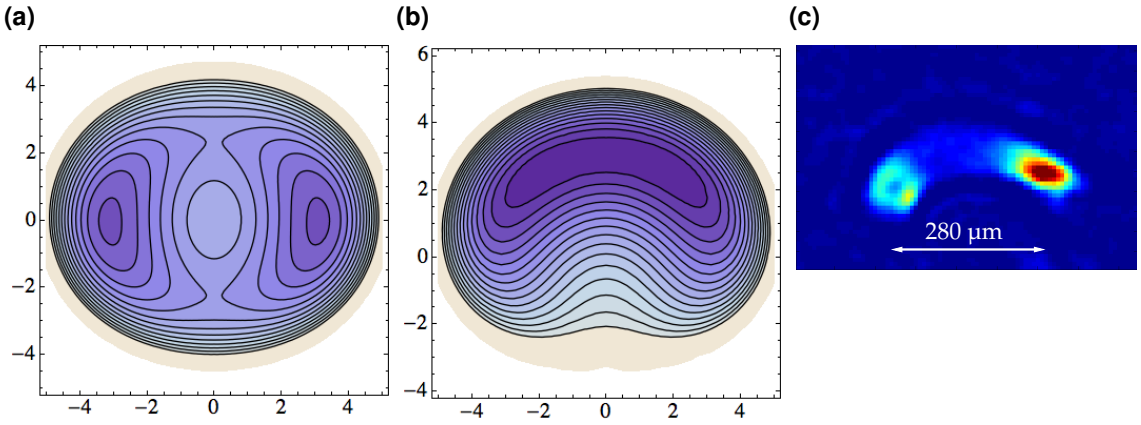

Fig. 6.12: Two double-well potential calculations in a static trap having $\Omega_0(0) = 1034$ kHz, centre position ($x_0 = 0, y_0 = 0, z_0 = 193$ um) and oscillations frequencies $\omega_\perp/2\pi = 1.1$ kHz, $\omega_\parallel/2\pi = 13.7$Hz. **(a)** Splitting with a uniform $B_{\rm rf}(\mathbf{r})$ produces the expected symmetric double-well potential, whereas **(b)** splitting with a more realistic chip wire RF field shows the dreaded banana. **(c)** Optical density resonant absorption image of two widely-split Rb clouds imaged after 0.3 ms time-of-flight (TOF). The hottest atoms fill in the dressed potential, revealing the banana shape. The apparent "hole" and relative brightness of the two clouds is due to poor imaging focus at this short TOF.

clouds after splitting) connected by a lower-density arched "banana" shape (see Fig. 6.12c). A closer examination of the dressed potential using analytic calculations revealed the source of this unexpected signal: an asymmetry in the double well resulting from spatial gradients in $B_{\rm rf}(\mathbf{r})$, even at micrometre-scale well separations.

Fig. 6.12 compares the results of two double well potential calculations: the first using chip wire fields to simulate $B_{\rm rf}(\mathbf{r})$ in the Orsay chip setup, the second using an idealized uniform $B_{\rm rf}(\mathbf{r})$. The uniform-$B_{\rm rf}(\mathbf{r})$ example shows a symmetric double well potential in the xz plane, while the "real" $B_{\rm rf}(\mathbf{r})$ example shows the banana.

The RF splitting configuration of the Toronto design was chosen in part to address the $B_{\rm rf}(\mathbf{r})$ issues with the Orsay configuration. The RF gradients could be reduced by moving the splitting setup further away from the RF wire ($dB_{\rm rf}/dr \sim 1/r^2$), but not without compromising the potential as explained in Sec. 6.2.2. By contrast, the combined RF field from two independent antenna wires in the Toronto configuration has lower spatial gradients along x and z, as demonstrated in Fig. 6.13. This investigation led to an understanding of how control and eliminate the "banana effect" in the Toronto configuration.

Dressed potential calculations also show that the banana effect can be mitigated by reducing the applied y-direction Ioffe bias field in both the Orsay and Toronto configurations. Fig. 6.14 shows four ^{87}Rb $|m'_F = 2\rangle$ dressed potentials calculated in the Orsay configuration for for $B_{\rm rf} = 320$ mG (RF current of 13 mA in the RF wire), and a static trap in which the Z-wire current and bias fields B_x and B_z are adjusted to maintain the harmonic oscillations frequencies at $\omega_{x,z} = 2\pi \times 1.4$ kHz as the Ioffe field B_y is adjusted. Dressed potentials with Ioffe fields corresponding to $\Omega_0(0) \sim 2\pi \times 1600$ kHz – typical of our early splitting attempts – show a strong

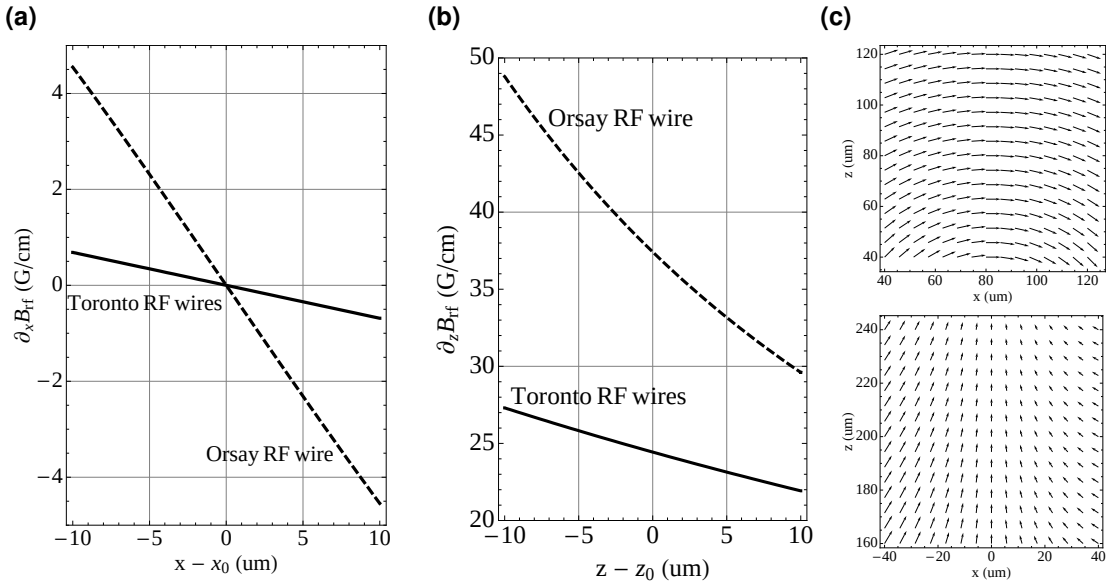

Fig. 6.13: Gradients in $B_{\rm rf}$ generated by the single Orsay RF wire (dashed) and the twin Toronto RF wires (solid). **(a,b)** x and z direction gradients are plotted along x and z in the vicinity of the static trap centres of the Orsay and Toronto configurations. For the Orsay curves, $x_0 \approx 80$ µm and $z_0 \approx 80$ µm . For the Toronto curves, $x_0 \approx 0$ µm and $z_0 \approx 193$ µm . The Toronto configuration shows smaller gradients in both cases. **(c)** Diagrams of $B_{\rm rf}(\mathbf{r})$ vector field in the xz plane in the vicinity of the static trap for comparison.

banana character. Those with $\Omega_0(0) \sim 2\pi \times 400$ kHz or $2\pi \times 200$ kHz produce much more symmetric double wells, which prompted an experimental switch to lower-Ioffe field static traps for splitting.

6.3.2 Well separation and barrier height

In double well experiments involving BECs, the well-to-well tunnelling rate depends exponentially on the potential barrier height [152]. Tunnelling is generally strong for barrier heights V on the order of the chemical potential of the condensate μ, which is in range of $h \times 1$ to $h \times 2$ kHz for ^{87}Rb condensates of 1000 atoms in our experiments. This barrier height corresponds to well separations $d \lesssim 5$ µm .

Fig. 6.8 shows the calculated barrier height and x-direction double well separation as a function of applied $B_{\rm rf}(\mathbf{r})$. These calculations provide a useful guide to the qualitative scaling of double-well parameters during splitting, but must be used in tandem with direct measurements to accurately characterize the potential.

6.3.3 Axial trap frequencies

So far we have not mentioned the axial curvature of the potential during splitting. While is it clear that radial curvatures are most perturbed during splitting, analytic calculations also reveal that the axial curvature is slightly decreased during splitting. Fig. 6.15 compares calculated

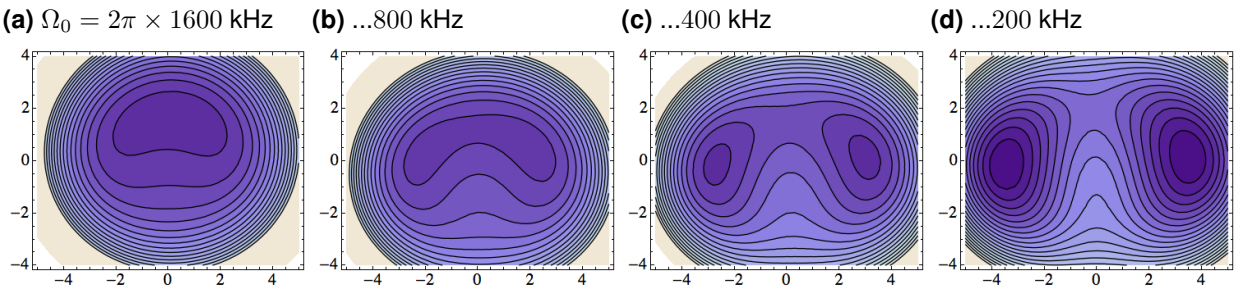

Fig. 6.14: Calculated dressed potentials for ^{87}Rb in $|F = 2, m_F = 2\rangle$ (see text). The banana effect is mitigated by reducing B_0 – in this case, by reducing the applied Ioffe bias field while keeping $B_{\rm rf}$ and the static trap parameters (position, oscillation frequencies) fixed.

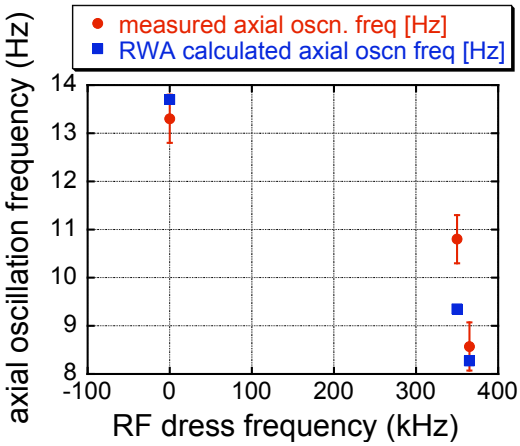

Fig. 6.15: Comparison of calculated and measured axial oscillation frequencies in an RF-dressed trap. $\omega = 0$ denotes a completely undressed trap (i.e. RF off).

and measured axial harmonic oscillation frequencies during RF dressing of a static Z-trap in the Toronto configuration with $z_0 \approx 193$ µm , undressed trap frequencies $\omega_{x,z} \simeq 2\pi \times 1.7$ kHz and $\omega_y \simeq 2\pi \times 13.7$ Hz, and a trap bottom $\Omega_0(0) = 2\pi \times 416.5$ kHz. The RF is fixed at at $B_{\rm rf} \approx 286$ mG. "$\omega = 0$" in the plot corresponds to a completely undressed static trap.

6.4 Species selective RF splitting

In this section, we explore the species-selective nature of RF-dressed double wells. In a two-species mixture, this effect permits the simultaneous formation of a double-well potential for ^{87}Rb and single-well potential for ^{40}K [45, 33], and vice versa. This result demonstrates that the adiabatic potentials experienced by each species can be dramatically different in an applied RF field, owing to the unequal values of g_F for ^{87}Rb and ^{40}K: $g_F = 1/2$ for ^{87}Rb in $|F = 2, m_F = 2\rangle$, and $g_F = 2/9$ for ^{40}K in $|F = 9/2, m_F = 9/2\rangle$.

Fig. 6.16 shows absorption images of the ^{40}K-^{87}Rb mixture 0.3 ms after being released from the RF-dressed trap. The ^{87}Rb cloud is split using frequency splitting. (A strong "banana" effect

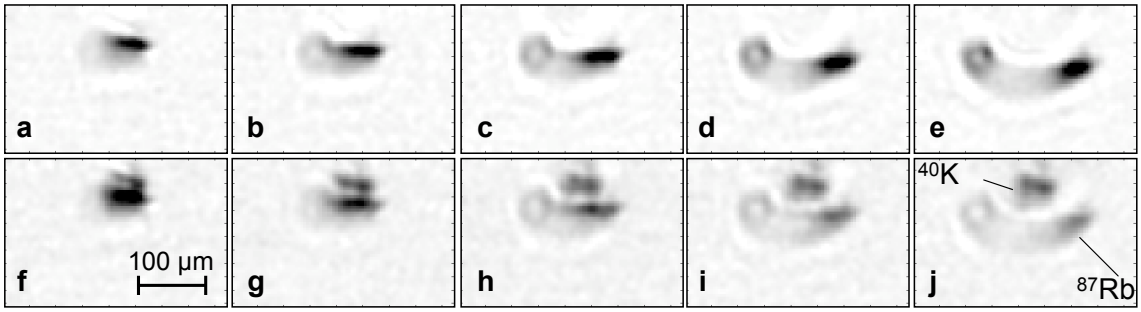

Fig. 6.16: A static chip trap loaded with a ^{40}K-^{87}Rb mixture is dressed with RF radiation. A sweep of the RF frequency ω creates a double well for ^{87}Rb, but leaves ^{40}K in a single well. Absorption images of the mixture with probe light resonant to ^{87}Rb only (**top row**) reveal the split ^{87}Rb cloud, while those taken with two-colour probe light resonant to both species (**bottom row**). The bottom row demonstrates that the shape of the ^{40}K potential is nearly unaffected by the RF dressing. The arc visible in the split ^{87}Rb data is the "banana" effect described in Sec. 6.3.1

is also visible – see Sec. 6.3.1). At the same time, the ^{40}K dressed potential is a single well nearly identical to the original undressed potential. ^{40}K is visible as the upper single "blob" in the bottom row of Fig. 6.16.

We use Eq. 6.35 to calculate effective adiabatic potentials for ^{87}Rb and ^{40}K, and use them to explain the simultaneous creation of single- and double-well potentials in a ^{40}K–^{87}Rb mixture. For clarity, we consider the formation of the ^{87}Rb double well and ^{40}K single well separately. Our starting point is a $|9/2, 9/2\rangle$–$|2, 2\rangle$ ^{40}K–^{87}Rb mixture confined to a static, anisotropic harmonic Z-trap directly with $B_0(0) = 1.214$ G, $\omega_{x,z} = 2\pi\times$ 1.23 kHz and $\omega_y = 2\pi\times$ 13.7 Hz.

Rb double well An RF field with initial frequency $\omega = 2\pi \times 800$ kHz and detuning $\delta^{(Rb)} = -2\pi\times 50$ kHz is applied by ramping up its amplitude from zero to the final value $B_{RF} = 200$ mG. A potential barrier is formed at $\mathbf{r} = 0$ by sweeping the RF frequency through the resonant point $\delta^{(Rb)}(0) = 0$. As the RF field is applied, each undressed state is adiabatically connected to one dressed state; here $m_F^{(Rb)} = 2$ is connected to $m_F'^{(Rb)} = 2$, shown as the upper-most black curve in Fig. 6.17a. After sweeping to a final RF frequency $\omega = 2\pi \times 860$ kHz, the barrier height is $h\times$2.4 kHz and the x-direction double well separation is 4 μm (see Fig. 6.17c). The $m_F'^{(Rb)}$ level repulsion at the double well minima is 70 kHz, sufficient to prevent Landau-Zener spin flips at our working temperatures $T \lesssim 1$ μK. The ^{87}Rb population thus remains trapped in the $m_F'^{(Rb)} = 2$ dressed level.

K single well The trapping potential for the ^{40}K atoms is affected in a very different way for the same magnetic field configuration. In our current example (Figs. 6.17a, 6.17b), the detuning for ^{40}K is positive; $\delta^{(K)}(0) = 2\pi \times 482$ kHz at the trap minimum. Near $\mathbf{r} = 0$, the RF dressing adiabatically connects $m_F^{(K)} = 9/2$ to $m_F'^{(K)} = -9/2$. Since $[\delta^{(K)}(0)]^2 \gg [\Omega^{(K)}(0)]^2$, the potential curvature near $\mathbf{r} = 0$ is largely unaffected by the RF coupling (see Eq. 6.35). The dressed states are most deformed where $\delta^{(K)}(\mathbf{r}) \approx 0$, which corresponds to an x-direction double-well separation

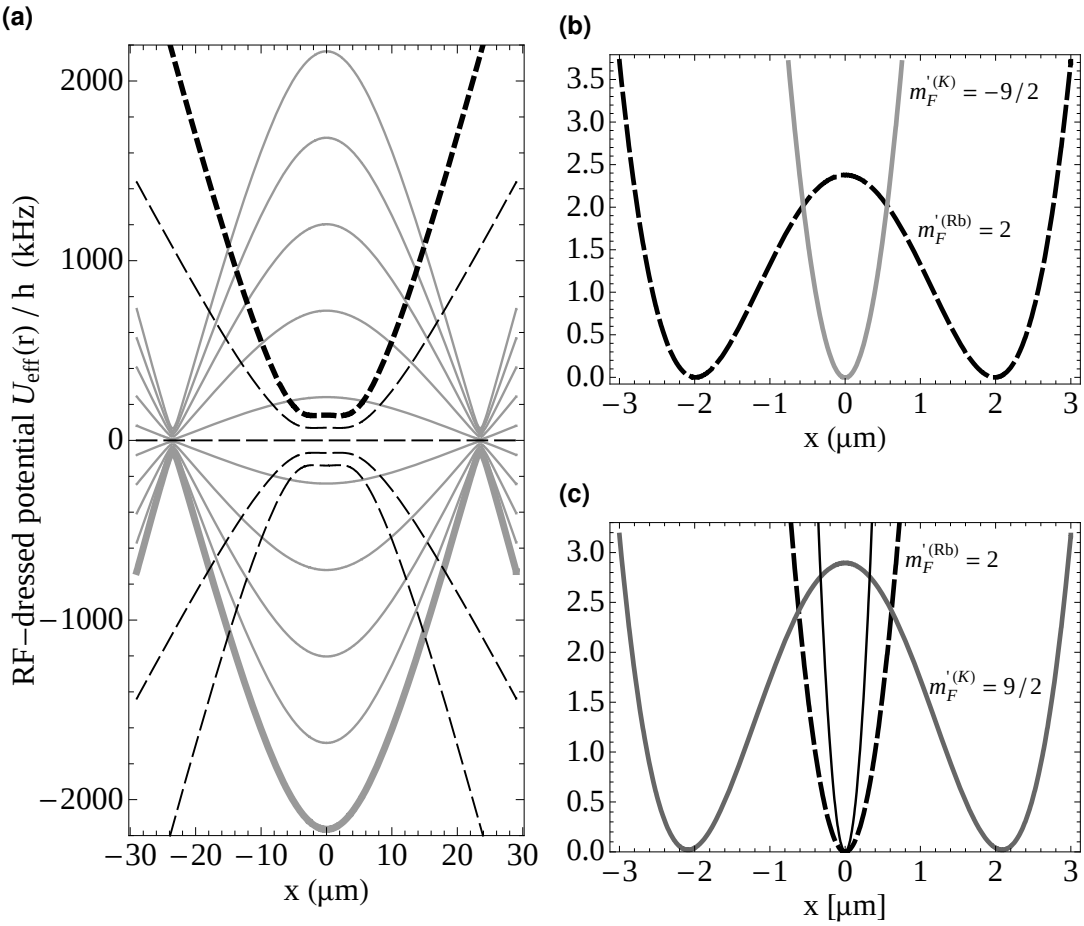

Fig. 6.17: Simultaneous adiabatic RF-dressed potentials for $^{87}\mathrm{Rb}$ and $^{40}\mathrm{K}$. **(a)**: The $^{87}\mathrm{Rb}$-double-well case. $^{87}\mathrm{Rb}$ (black) and $^{40}\mathrm{K}$ (grey) effective dressed potentials are plotted as a function of the spatial coordinate x (see Fig. 6.5). Each curve corresponds to a single value of m'_F for $^{87}\mathrm{Rb}$ and $^{40}\mathrm{K}$, with the upper-most curves corresponding to $m'_F = 2$ and $m'_F = 9/2$ respectively. $^{87}\mathrm{Rb}$ atoms populate their upper-most $m'_F = 2$ dressed state (thick, dashed), while $^{40}\mathrm{K}$ atoms populate their lower-most $m'_F = -9/2$ single well dressed state (thick, grey). **(b)**: A closer view of the $^{87}\mathrm{Rb}$ double well and $^{40}\mathrm{K}$ single well, plotted together on a single vertical $U_{\rm eff}/h$ axis in units of kHz. Both curves have been shifted vertically to align their potential minima at zero kHz. **(c)**: A closer view of the $^{40}\mathrm{K}$ double well and $^{87}\mathrm{Rb}$ single well, with vertical axis similar to **(b)**. The dressed $^{87}\mathrm{Rb}$ single well (black, dashed) deviates slightly from the undressed single well (solid, thin black), illustrating the slight loss of radial trap curvature.

$d \simeq 2 \times 23$ µm, and a potential energy of roughly 110 µK above the local minimum at $\mathbf{r} = 0$. Since our experiments are typically conducted with $T \lesssim 1$ µK, we can be satisfied that the ^{40}K potential retains its original form near $\mathbf{r} = 0$ without inducing any ^{40}K loss.

One important feature of this single- and double well arrangement is that the ^{87}Rb double well separation and barrier height may be tuned over a wide range by adjusting ω and B_{RF} without affecting the shape of the ^{40}K potential.

An obvious extension of the work described here and in [45] would be to reverse the roles of boson and fermion, creating a double well for fermions overlapped with a single well for bosons. The magnetic hyperfine structure of ^{40}K and ^{87}Rb makes this possible in a ^{40}K–^{87}Rb mixture, but with slightly different results than in the ^{87}Rb-double-well case.

Here we sweep the RF frequency from $\omega = 2\pi \times 338$ kHz to $\omega = 2\pi \times 383$ kHz. In the same static trap with $B_0 = 1.214$ G, $\delta^{(K)}$ changes sign from $-2\pi \times 50$ kHz to $+2\pi \times 5$ kHz, while $\delta^{(Rb)}$ remains negative throughout. This creates a ^{40}K double well in the $m_F'^{(K)} = 9/2$ state with x-direction well separation $d \sim 4$ µm, barrier height $h\times$2.9 kHz at $\mathbf{r} = 0$, and $m_F'^{(K)}$ level repulsion ~ 70 kHz at coordinates $x = \pm 2.1$ µm. In contrast to the ^{87}Rb-double-well scenario, here *both* ^{40}K and ^{87}Rb adiabatically follow their respective upper-most dressed levels, which exhibit their strongest spatial deformation near the trap centre. While ^{40}K experiences a double well potential, the ^{87}Rb $m_F'^{(Rb)} = 2$ potential is a single well with slightly reduced radial curvature from the initial, undressed $m_F = 2$ potential, as shown in Fig. 6.17c.

In addition to the species-selectivity of this process, it should be emphasized that atom chips are particularly well-suited to creating adiabatic dressed state potentials due to the proximity of the atoms to chip wire RF antennae. The double-wells described in this section were created using RF Rabi frequencies $\Omega \sim 100$ - 200 kHz, though we can achieve values as large as 1 MHz with tens of milliamperes rms in the chip wire antenna. By comparison, achieving $\Omega \approx 1$ MHz with an air-side RF antenna would require a circular coil of radius 3 cm and 3 turns bearing 10 A rms of AC current.

6.5 Dressed state RF spectroscopy

Analytic calculations of RF-dressed potentials rely on careful calibration of the static and RF magnetic field magnitudes and polarizations. To calibrate B_{rf} and to experimentally characterize our RF-dressed potentials, we perform spectroscopy on the dressed potentials, following [151]. The idea is that a weak "tickling" RF magnetic field – $B_{\text{tkl}} \simeq 6 \times 10^{-4} B_{\text{rf}}$ in our case – applied to ^{87}Rb BEC trapped in a dressed potential can induce transitions to untrapped dressed states without significantly deforming the potential. The frequencies of the resulting loss features in trapped atom number are measured as a function of the RF dressing field amplitude B_{rf} at RF dressing frequency ω, and can be used to directly measure the RF amplitude experienced by atoms in the dressed trap.

Fig. 6.18 shows a schematic energy level diagram showing undressed and dressed Zeeman states of ^{87}Rb. On the left are the bare Zeeman states of ^{87}Rb in a static Z-trap whose magnetic field minimum $B_0(0) \equiv B_0$ defines the frequency $\Omega_0 \equiv g_F \mu_B B_0/\hbar$. The atoms are ini-

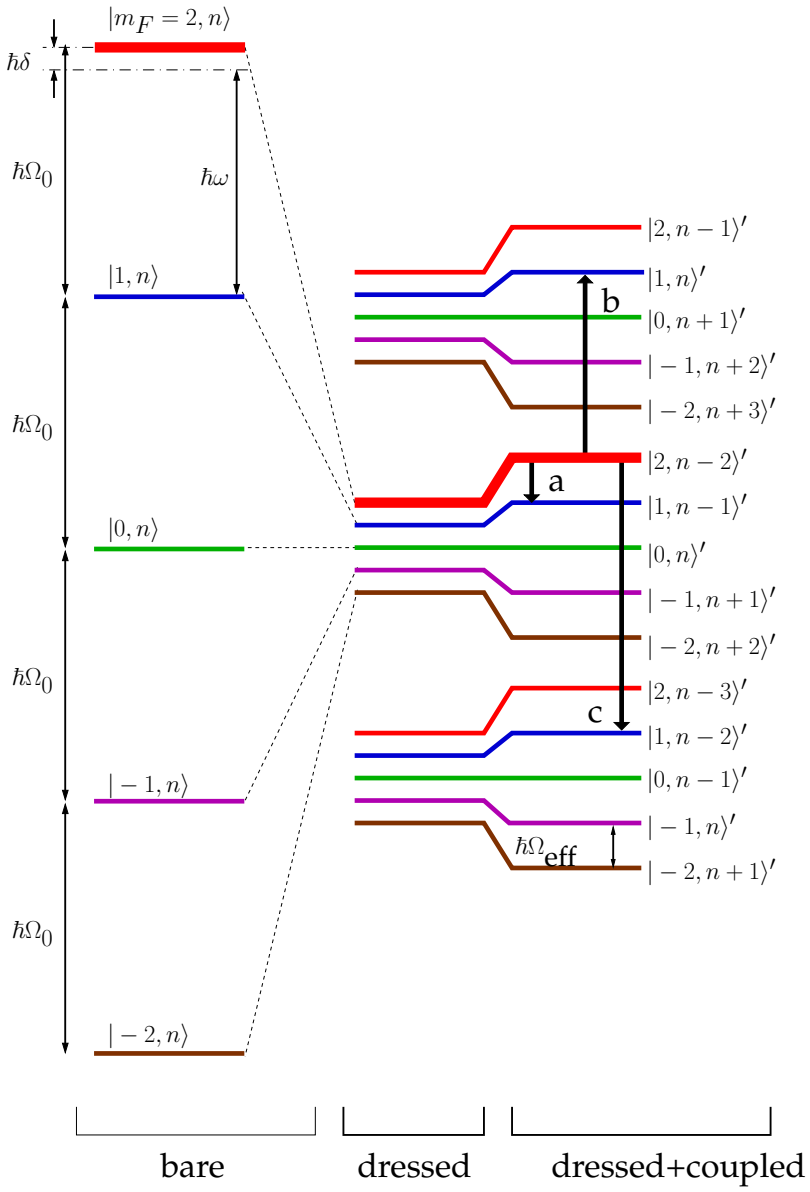

Fig. 6.18: Energy level diagram of bare and dressed Zeeman states for $^{87}\mathrm{Rb}$. The notation $|m_F, n\rangle$ is used throughout, where n is the number of RF "photons", and m_F the usual magnetic quantum number. The dressed states (centre) are correspond to the bare states (left) shifted in energy by 0, 1, 2, ... RF photons. Adjacent dressed states are separated by the RF detuning δ within each manifold. Atom-photon coupling of the dressed states leads to level separations of $\hbar\Omega_{\text{eff}} = \hbar\sqrt{\delta^2 + \Omega^2}$ between the full "dressed+coupled" states $|m_F, n\rangle'$, where δ is the RF detuning and Ω the RF Rabi frequency. The only allowed dressed state transitions within the RWA are $a \equiv \hbar\Omega_a$, $b \equiv \hbar\Omega_b$ and $c \equiv \hbar\Omega_c$ (see text).

tially in the state $|F = 2, m_F = 2\rangle$, shown in thick red. The centre of the diagram shows the bare states shifted by $\kappa\hbar\omega$ where the RF "photon" number $\kappa = 0, 1, 2....$ These shifts correspond to zero, one, two-photon etc. excitations of the Zeeman states. The RF frequency is red-detuned with respect to Ω_0 so that $\delta \equiv \omega - \Omega_0 < 0$, as in our experiments. On the right of the figure are the "dressed and coupled" states, which account for the $n\hbar\omega$ energy shifts as well as the dressed state coupling induced by the RF Rabi frequency $\Omega = 2g_F\mu_B B_{\rm rf}/\hbar$. The diagram shows the energy levels in the RWA, in which $|\delta| \ll \Omega_0$ and $\Omega \ll \Omega_0$. In this case, the dressed states can be grouped into "manifolds" [94, 151], of which three are shown. In describing dressed states so far we have only considered a the central manifold of dressed states, labelled $|m'_F = 2, n-2\rangle', |1, n-1\rangle', |0, n\rangle', |-1, n+1\rangle', |-2, n+2\rangle'$ where m'_F is the dressed state magnetic quantum number and n is the number of RF "photons" in the dressed state. As demonstrated in [151], the manifolds are no longer separable in this way at large values of $B_{\rm rf}$ ($B_{\rm rf} \gtrsim B_0$). In this case, the off-resonant terms ignored in the RWA become important (see Eq. 6.25), and each dressed state becomes a superposition of bare states from many manifolds. In our experiments, we generally use $B_{\rm rf}$ and δ small enough that the RWA is approximately valid: $B_{\rm rf}/B_0 \sim 0.1-0.3$ and $\delta/\Omega_0 \sim 0.05 - 0.01$. See also [151].

We wish to probe the dressed state energy ladder by applying the tickling field to a ^{87}Rb BEC trapped in the dressed state $|m'_F = 2, n-2\rangle'$. In the RWA, the only allowed transitions involving this state are between adjacent manifolds satisfying $\Delta m'_F = 0, 1$. These are labelled a, b and c in Fig. 6.18. Thus, when applying $B_{\rm tkl}$ to dressed atoms, we expect resonant loss features at only these three tickle frequencies. Using Fig. 6.18, they may be written

$$\hbar\Omega_a \equiv \hbar\omega \tag{6.38}$$

$$\hbar\Omega_b \equiv \hbar\omega - \hbar\Omega_{\rm eff} \tag{6.39}$$

$$\hbar\Omega_c \equiv \hbar\omega + \hbar\Omega_{\rm eff} \tag{6.40}$$

where $\hbar\Omega_{\rm eff} = \hbar\sqrt{\delta^2 + \Omega^2}$; δ is the RF detuning and Ω the RF Rabi frequency. Fig. 6.19 shows raw data of dressed state resonances b and c at a fixed RF dressing amplitude $B_{\rm rf}(\mathbf{r})$, measured in the Orsay configuration. The experimental procedure detailed here is specific to this data, though we use this general method to measure $B_{\rm rf}$ in all atom chip RF splitting experiments.

The ^{87}Rb BEC is initially trapped in Zeeman state $|F = 2, m_F = 2\rangle$ in a static Z-trap directly below the Orsay RF wire (see Fig. 6.5a) at $x_0 \approx 80$ µm , $y_0 = 0$, $z_0 \approx 80$ µm with $\Omega_0 = 2\pi\times$1550$\pm$1 kHz (B_0 =2214$\pm$2 mG). The trap is dressed by ramping $B_{\rm rf}$ from 0 to 323 mG in 100 ms at a fixed RF frequency $\omega = 2\pi\times$1532 kHz, or $\delta = -2\pi \times 18$ kHz. During this step the atoms adiabatically follow and remain in the dressed state $|m'_F = 2\rangle$, which is deformed to the point shown in Fig. 6.6b (i.e. no potential barrier). **N.B.** The value of $B_{\rm rf}$ is not precisely known before performing tickle spectroscopy. The value quoted above was calculated after the fact based on the calibration explained here.

Next, the weak tickling field with $B_{\rm tkl} \simeq 0.2\,{\rm mG} \approx 6 \times 10^{-4} B_{\rm rf}$ is applied[4] for 100 ms at a

[4]In our Orsay chip setup, $B_{\rm tkl}$ is supplied directly from the output of a Stanford Research systems SRS D345 signal

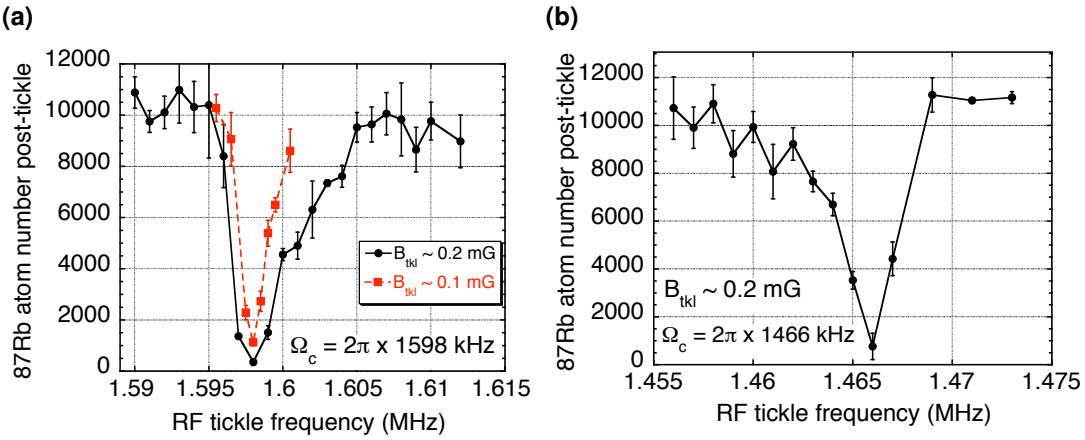

Fig. 6.19: RF tickle spectroscopy resonance features, measured as a dip in the number of atoms detected after applying the tickle RF field. Error bars are standard deviations over repeated measurements. **(a)** The upper resonance Ω_c, measured at two different tickle field amplitudes. Some power broadening is visible, but no frequency shift, verifying that the $B_{\rm tkl}$ is small enough that the dressed potentials are not significantly perturbed. **(b)** The lower frequency resonance Ω_b.

fixed frequency $\omega_{\rm tkl}$. All fields are then switched off and the remaining trapped atom number is measured with a resonant absorption image after a 0.3 ms time-of-flight. The tickle resonances shown in Fig. 6.19 are measured by repeating this process at various tickle frequencies $\omega_{\rm tkl}$. To verify that the measured frequencies were not dependent on $B_{\rm tkl}$ (i.e. to verify that the tickling field did not significantly perturb the dressed potentials), we repeated the measurements after reducing the tickle field amplitude by a factor of two. This resulted in a narrowed resonance feature, but no overall frequency shift. The asymmetry in the resonance features is due to the finite temperature and spatial extent of the trapped BEC. Each resonant frequency is taken to be the frequency corresponding to maximum atom number loss (i.e. at the tip of each resonance dip in Fig. 6.19).

Measuring the tickle resonances as a function of $B_{\rm rf}$ at a fixed ω provides a direct measurement of $B_{\rm rf}$ experienced by the trapped atoms. Fig. 6.20 shows data of the resonances Ω_b (lower curve) and Ω_c (upper curve) as a function of the RF current in the chip antenna wire. The Ω_c data is fit to a function of the form $y = (\omega/2\pi) + \sqrt{(\delta/2\pi)^2 + Dx^2}$, and Ω_b to $y = (\omega/2\pi) - \sqrt{(\delta/2\pi)^2 + Dx^2}$; x is the dependent variable proportional to RF amplitude, and δ (RF detuning) and D are free parameters. Extracting δ from the fit also gives a measurement of the Larmor frequency Ω_0, since the applied RF frequency ω is well known. The desired calibration of the RF amplitude – RF field amplitude per control unit – is $B_{\rm rf}/x = 4\sqrt{D}h/\mu_B \simeq 2\sqrt{D}/(700\,{\rm kHz/G})$ for ^{87}Rb in an $F = 2$ state ($g_F = 1/2$). $B_{\rm rf}/x$ has units of mG/mA if x is RF current, or mG/V if x is a raw control voltage.[5]

generator connected to the RF antenna wire. In the Toronto setup, $B_{\rm tkl}$ is supplied by the RF evaporation source and RF evaporation antenna wire, which are not otherwise used for RF dressing.

[5]In the lab we calibrate $B_{\rm rf}$ against the raw RF amplitude control voltage of a voltage-controlled RF attenuator. This method is most precise since the error associated with the RF current measurement is much smaller than that of a control voltage measurement.

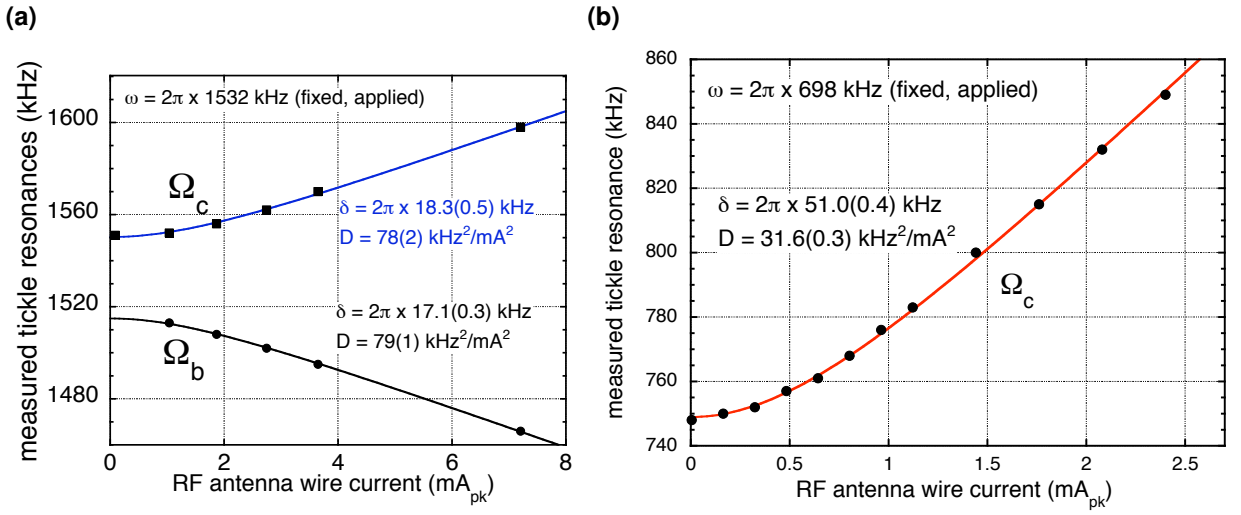

Fig. 6.20: (a) Dressed state resonance frequencies Ω_b and Ω_c as functions of the RF amplitude (RF wire current). **(b)** A more routine measurement of Ω_c only, which is used to calibrate the RF amplitude $B_{\rm rf}$. The RF frequency ω is set by the RF source, while δ and the calibration parameter D are determined from fits (see text).

Comparing to geometric estimates of $B_{\rm rf}$ based on RF wire currents The data in Fig. 6.20a yield a $B_{\rm rf}$ calibration of 25.3±0.5 mG/mA$_{pk}$, expressed in terms of RF current in the antenna wire. Combining this calibration result with the 2% uncertainty on RF current measurements[6] results in a total uncertainty of 3% in $B_{\rm rf}$ deduced from spectroscopy. We can also estimate the $B_{\rm rf}$ calibration using the thin-wire formula for the magnetic field generated by current in a wire (Eq. 3.16). This approach gives 24.7 mG/mA using direct measurement of RF currents and the calculated distance between the RF wire and the atoms. The uncertainty on this value is at least 5%, however, due mainly to the uncertainty in the Z-trap position. Therefore, we take the tickle spectroscopy calibration of $B_{\rm rf}$ to be *the* calibration.

We routinely use RF tickle spectroscopy to precisely measure $B_{\rm rf}$ in all our atom chip RF splitting experiments, focusing on the upper Ω_c resonance. Example data of Ω_c vs. RF current is shown in Fig. 6.20b for a Z-trap configuration with $x_0 \approx 80$ µm , $y_0 = 0$, $z_0 \approx 80$ µm and $\Omega_0 = 2\pi \times 746$ kHz.

6.6 Summary

This chapter describes the formation of RF-dressed adiabatic double-well potentials for ^{87}Rb and ^{40}K. We describe how a single-well potential can be dynamically deformed into a double-well potential, by ramping the RF frequency or the RF amplitude. This method provides tremendous experimental control over the potential barrier height and double well separation, which control inter-well tunnelling in these systems. We perform weak-field spectroscopy on RF-dressed states,

[6]The RF current is deduced from the voltage drop across the 1% tolerance impedence matching resistor in the RF circuit (see Fig.4.12) measured using high-impedence voltage probes.

and use the resulting resonant atom number loss features to determine the RF dressing amplitude to a precision of 3%. This calibration is critical in characterizing the RF double-well potentials. We also discuss the species-selectivity of RF potentials, and demonstrate the simultaneous trapping of $^{87}\mathrm{Rb}$ in a double well and $^{40}\mathrm{K}$ in a single well, starting from an ultra-cold $^{87}\mathrm{Rb}$-$^{40}\mathrm{K}$ mixture in a single well harmonic trap. The RF double well techniques discussed in this chapter are applied to the measurement of fluctuations in the relative atom number and relative phase of a split BEC in Ch. 7.

A routine will turn into an enchanting escapade.

Wing's fortune cookie

7

Measuring the relative atom number and relative phase of a split BEC

The first observation of matter wave interference between two BECs, which were initially separated and dropped on top of one another [10], stimulated great interest in BECs in double-well potentials. Research directions based on these quantum systems have ranged from fundamental questions regarding the definition of relative phase between two BECs (for example, [36, 37]), to more practical efforts to create squeezed states and entanglement in macroscopic quantum systems for atom interferometry and precision measurement [43, 39, 79, 153, 6].

In this chapter, we describe the experimental realization of a BEC in an RF double-well potential. Using the methods described in Ch. 6, a single-well potential is smoothly deformed into a double well to "split" the BEC. In a single realization of the experiment, we measure either the relative atom number N_r, by spatially separating the two halves of the split BEC and imaging after short times of flight, or the relative phase ϕ, using the interference pattern formed as the BECs overlap and interfere after long times of flight. We then repeat the preparation and measurement steps to measure fluctuations in N_r and ϕ over successive experimental realizations.

For a gas of distinguishable, non-interacting particles, the splitting process can be described using binomial statistics.[1] In this case, for "balanced" splitting (i.e. equal mean populations of the left and right wells), we expect binomial ("shot noise") relative atom number fluctuations: $\Delta N_r = \sqrt{N}$, where N is the total atom number among the two wells (see Sec. 7.2.3 and Appendix B). The binomial distribution of the discrete atom number N_r approaches the Poisson distribution in the limit of a large N [156]. In the case of a BEC in a double-well, if the condensate is described by a coherent state with a definite relative phase ϕ, then the fluctuations in N_r are also Poissonian [37]. If the BEC is split quickly and non-adiabatically, we expect to observe the same Poissonian relative atom number variance $\mathrm{Var}(N_r) \equiv (\Delta N_r)^2 = N$. If the BEC is split slowly and adiabatically, however, nonlinear repulsive atom-atom interactions favour narrower number distributions, making it possible to observe sub-Poissonian relative number fluctuations [63, 31, 43, 157, 153].

Our main result is the observation of relative atom number fluctuations at the shot-noise

[1] This applies, for instance, to classical particles or $T = 0$ bosons. Non-condensed bosons exhibit super-Poissonian statistics [154], while identical Fermions exhibit sub-Poissonian statistics [155].

level using time-of-flight resonant absorption imaging. We estimate that our number counting technique is sensitive enough to observe -14 dB of number squeezing, i.e. a variance in N_r 14 dB below the shot-noise level. This sensitivity sets the stage for the creation and observation of number squeezed clouds in future work. The bulk of the chapter is devoted to the phase and atom number counting measurement and analysis methods which support this result. The chapter closes with a discussion of the prospects for observing sub-Poissonian relative number fluctuations in future work in our experiment, as well as the types of measurements which become accessible using the number and phase measurement tools described here.

7.1 Measuring relative phase

Matter wave interference is a direct method for determining the relative phase between two BECs. If the two BECs are prepared completely independently, a well-defined relative phase ϕ can be measured in any single realization of an interference experiment, but the value of ϕ is completely random and unpredictable from experiment to experiment [36, 48]. The opposite is true if the two BECs are created "coherently" out of the same initial BEC. In the ideal case, repeated ϕ measurements are peaked around zero, with an rms width determined by the number-phase uncertainty relation $\Delta\phi = 1/\Delta N_r$, where ΔN_r is the spread in relative atom numbers [67]. In practice, we expect to observe a distribution of phases about a mean value $\langle\phi\rangle \approx 0$ with a width broadened by technical fluctuations [29].

This section describes measurements of the relative phase between the left and right sides of a BEC split using an RF double-well potential. We focus on the analysis of time-of-flight matter wave interference patterns, from which we measure the "shot-to-shot" (i.e. experiment-to-experiment) phase variance. We demonstrate evidence for coherent splitting of the BEC, and characterize the phase sensitivity. We show that the phase measurement tool developed here can be used to characterize double well dynamics predicted by the BJJ model described in Ch. 2.

7.1.1 Phase measurement procedure

We start with a $^{87}\mathrm{Rb}$ BEC prepared in a static Z-trap with an RF trap bottom $\Omega_0 = 2\pi \times 420$ kHz ($B_0 \simeq 0.6$ G) and oscillation frequencies $\omega_{x,z} = 2\pi \times 1.75 \pm 0.05$ kHz and $\omega_y = 2\pi \times 13 \pm 1$ Hz. The BEC is split by dynamically deforming the single well into an RF dressed adiabatic double well (see Ch. 6). The RF is applied in two stages: "dressing" and "splitting", described schematically in Fig. 6.7a. The applied RF field is generated by RF currents in two RF antenna wires on the Toronto chip (see Secs. 4.4.3 and 4.6.2).

Dressing The RF amplitude B_{rf} is ramped on from 0 to 320 mG at a constant RF detuning $\delta = \omega - \Omega_0 = -2\pi \times 20$ kHz in 100 ms. This decreases the potential curvature along x, but does not yet introduce a potential barrier (see Fig. 6.6b).

Splitting The potential barrier height b is increased in the centre of the trap until $b \sim \mu$, where μ is the chemical potential of the condensate. This is accomplished using either frequency splitting (a ramp of ω) or "amplitude splitting" (a ramp of $B_{\rm rf}$, see Sec. 6.2.2). For $N = 10^4$ ^{87}Rb atoms, typical double-well parameters are a well separation $\Delta x \sim 2-3$ µm , barrier height $b \sim 2-3$ kHz, and $\mu \sim 1-2$ kHz.

> **Aside** The 10 ms timescale is long compared to the initial and final transverse oscillation period of the unsplit and split wells $2\pi/\omega_\perp \sim 1$ ms, but short compared to the longitudinal period $2\pi/\omega_\parallel \sim 100$ ms. Though this introduces the possibility of longitudinal excitations during splitting, we find that for split times longer than 10 ms the interference contrast becomes too small to accurately measure the fringe spacing and phase. The decrease in contrast may be caused by asymmetric longitudinal displacement of the clouds during splitting. A transverse optical dipole trap was added to the experiment in 2009 to further investigate and mitigate this effect.

Matter wave interference After splitting, the double-well potential is abruptly switched off and the two separated BECs expand, overlap and interfere during times of flight on the order of 20 ms. The interference pattern in the expanding density profile is detected using resonant absorption imaging along the longitudinal y-axis (see Fig. 6.9).

An unsplit cloud released from the anisotropic, needle-shaped Z-trap expands most rapidly in the radial x and z directions, reaching a flat "pancake" shape in the xz plane for $t \gg \omega_{x,z}^{-1}$, i.e. $t \gtrsim 10$ ms in our traps. When the trap is dressed, but not yet split, as depicted in Fig. 6.6b, the reduced radial curvature of the potential results in broader in-trap density distribution along the splitting direction x, and therefore a narrower density distribution at long times of flight [46]. The smallest x-direction cloud width roughly corresponds to the minimum potential curvature along x. Increasing $B_{\rm rf}$ or ω from this point leads to interference fringes of decreasing fringe spacing as the barrier height and double well separation increase.

Single-shot phase measurement We analyze the fringe spacing, visibility and phase of a single-shot interference pattern by summing the two-dimensional optical density (OD) image along the direction parallel to the fringes to increase signal to noise, and fitting the resulting one-dimensional interference pattern to

$$f(x) = G(x)\left[1 + \mathcal{V}\cos\left(\frac{2\pi(x - x_0)}{\Delta x} + \phi\right)\right], \tag{7.1}$$

where $G(x)$ is a Gaussian envelope centred at $x = x_0$, Δx is the fringe spacing, $\mathcal{V}$ is the visibility, and ϕ is the phase. As discussed in Sec. 2.3.2, ϕ is the relative phase of the two BECs. Fig. 7.1 shows examples of OD interferograms, and a fit to two-dimensional summed data.

The time-of-flight (TOF) must be large enough that the fringe spacing is discernible in the interferogram, given our ∼20 µm optical resolution. Fig. 7.2b shows the trade-off between measurements taken at shorter and longer times of flight. Working at larger TOF increases Δx and

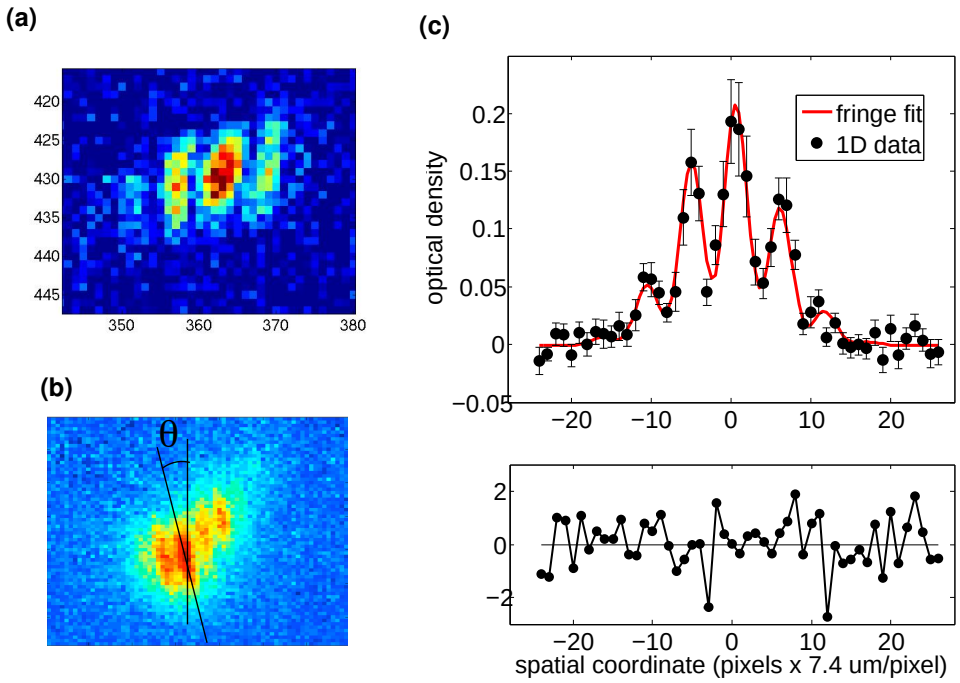

Fig. 7.1: (a) Raw OD data in the xz plane of $^{87}\mathrm{Rb}$ interference fringes imaged on resonance after 19.5 ms TOF (see text). Axes are in units of 7.4 µm pixels. **(b)** A 10-image average demonstrates the fringe tilt angle α, which can result from potential asymmetry and/or stray magnetic field gradients during trap turn-off. **(c)** The raw two-dimensional OD profile from **(a)** is averaged long the direction (θ) which optimizes fringe visibility, then fit to a gaussian-times-cosine function to extract the fringe spacing, phase and visibility (see text). Error bars in the figure are statistical from the 1D average. A fit to these data gives $\mathcal{V} = 0.6 \pm 0.1$, $\phi = -40^\circ \pm 18^\circ$, and $\Delta x = 5.8 \pm 0.1$ pixels, where uncertainties are statistical from the fit. The lower panel shows normalized residuals.

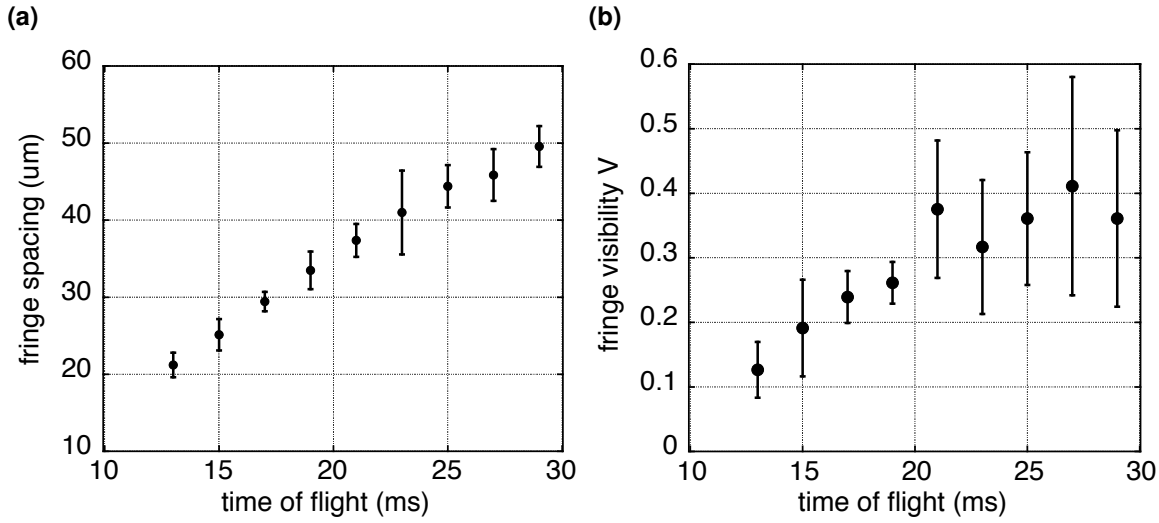

Fig. 7.2: Detecting BEC interference fringe spacing and visibility as a function of time-of-flight (TOF). Fringes are not discernible at TOF < 13 ms, at which point the fringe spacing coincides with the 20 µm resolution of the imaging system ("1st generation", see Ch. 4). Fitting interferograms to a gaussian-plus-cosine function (see text) also becomes challenging for $\mathcal{V} < 0.1$.

$\mathcal{V}$, but decreases the overall optical density and signal to noise in the absorption image. This results in the larger error bars (standard deviations) at TOF $\gtrsim$ 20 ms in the figure. Conversely, working at smaller TOF increases the signal to noise, but decreases the fringe spacing, making an accurate fit more difficult. At TOF = 25 ms we estimate the following statistical uncertainties for the fringe spacing, visibility and phase:[2] $\delta(\Delta x) \approx 0.1$ pixels $\approx 1\mu$m , $\delta(\mathcal{V}) \approx 0.1$ and $\delta\phi \approx 20°$. In principle, we expect maximum fringe visibility ($\mathcal{V} = 1$) from the single-shot interference pattern of two interfering BECs at $T = 0$, whether the splitting process was coherent or not (see Sec. 2.3.2). In practice, $\mathcal{V} = 0.4$ to 0.6 is typical of our measurements. We attribute the reduced visibility to technical effects, including slight misalignment of the probe beam with respect to the interference pattern, and the incoherent contribution of the small background thermal cloud. The data in Fig. 7.2 were collected using a quasi-pure BEC of $N \sim 10^4$ ^{87}Rb atoms released from a dressed static trap in the Orsay setup with $\Omega_0 = 2\pi \times 1023$ kHz and oscillation frequencies $\omega_{x,z} \simeq 2\pi \times 1.7$ kHz.

Shot-to-shot phase fluctuations The variance in the relative phase $\mathrm{Var}(\phi) \equiv (\Delta\phi)^2$ is measured using successive repetitions of the BEC preparation, splitting and measurement steps, and compared to the expected values for coherent and number-squeezed BEC states.

[2]These estimates are for the "1st generation" imaging system (MicroPix CCD, see Sec. 4.5.1). The current "2nd generation" imaging system (Pixis CCD and 4x objective, see Sec. 4.5.2) has $\delta(\Delta x) \approx 0.3$ µm .

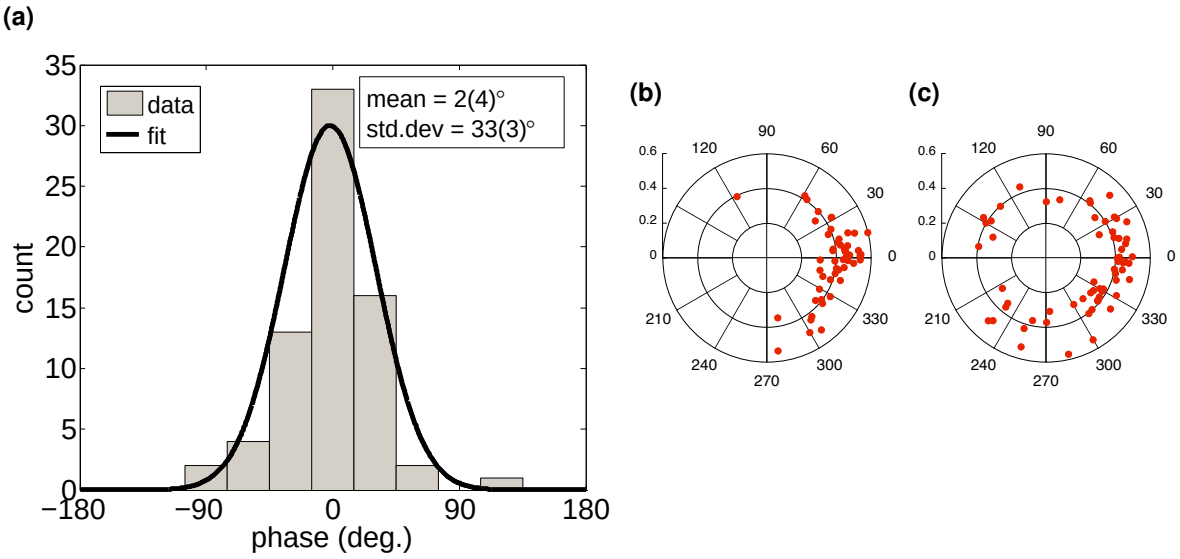

Fig. 7.3: (a) The shot-to-shot fluctuation in the relative phase is $\Delta\phi = 33° \pm 3°$, measured with atoms released from the trap immediately after splitting. Typical values of $\Delta\phi$ measured immediately after splitting range from $20°$ to $40°$ in our experiment. **(b)** A polar plot of single-shot phase and visibility for the data in **(a)** shows evidence of coherent splitting. **(c)** Phase coherence between the split BECs is significantly decreased after an in-trap hold time of 1.0 ms, evidenced by the broadened phase distribution. $\Delta\phi = 86° \pm 5°$ and $\alpha = 0.4 \pm 0.3$ for this data.

7.1.2 Results

Example data of the shot-to-shot relative phase fluctuations are depicted in Fig. 7.3. The histogram of relative phases was built up by preparing quasi-pure BECs (no discernible thermal cloud) of $N = 2 \times 10^4$ atoms in a Z-trap with $\Omega_0 = 2\pi \times 770$ kHz, $\omega_\perp = 2\pi \times 1.7$ kHz and $\omega_\parallel \simeq 2\pi \times 14$ Hz. The potential was dressed in 100 ms and split using a 40 ms ramp of $B_{\rm rf}$, after which the trap was immediately switched off. The interference pattern was detected on resonance after 19 ms of time-of-flight.

Evidence for coherence The data clearly show that the distribution of relative phases is not random, which suggests that the splitting process is coherent. The measured mean and variance of the phase distribution are $\langle\phi\rangle \simeq 2°$ and $(\Delta\phi)^2 \simeq (33°)^2$, whereas the corresponding values for a random distribution of phases between $-180°$ and $180°$ are $0°$ and roughly $(105°)^2$, respectively [31]. Typical values of $\Delta\phi$ measured immediately after splitting range from $20°$ to $40°$ in our experiment, comparable to values measured in similar experiments in the Ketterle [31] and Oberthaler [76] groups. Following [42] we also compute the coherence $\alpha = \langle\cos\phi\rangle$ directly from the single-shot phases, which is a better measure of coherence ("non-randomness") for the circular variable ϕ [31, 74]. As discussed in Sec. 2.3, $\alpha \approx 1$ implies coherent splitting with $\Delta\phi \approx 0$, while $\alpha \approx 0$ implies incoherent splitting and random phases. The data in Fig. 7.3a give $\alpha = 0.9 \pm 0.3$; the uncertainty is based on the single-shot uncertainty in ϕ. Fig. 7.3b shows a polar plot of the phase and visibility for the same data presented in Fig. 7.3a. Fig. 7.3c shows the results

of a similar experiment in which the split BECs were held in the trap for 1.0 ms before release, leading to dephasing and broadening of the phase distribution; we measure $\Delta\phi = 86° \pm 5°$ and $\alpha = 0.4 \pm 0.3$ after the hold time.

Quantum and thermal phase fluctuations As discussed in Sec. 2.3.4, we expect $\Delta\phi$ to reflect quantum and thermal fluctuations in ϕ from the equilibrium value [42, 76, 74], as well as technical fluctuation introduced by the measurement (e.g. statistical error from the fits, and stray magnetic fields during time-of-flight) and by technical fluctuations in the double-well potential itself.

The $T = 0$ quantum phase fluctuations can be estimated using the number-phase uncertainly relation $\Delta N_r \Delta\phi \geq 1$ (see Sec. 2.3.3). For N atoms in a number squeezed state characterized by squeezing parameter $s \equiv \sqrt{N}/\Delta N_r$ [31], the phase width due to quantum fluctuations is

$$\Delta\phi_q = \frac{1}{\Delta N_r} = \frac{s}{\sqrt{N}}. \tag{7.2}$$

Using Eq. 7.2 we can see that our measured $\Delta\phi$ is much larger than the predicted value from quantum fluctuations. For example, with $N = 10^4$ atoms in a shot-noise-limited $s = 1$ coherent state, $\Delta\phi_q \approx 0.6°$. Even for a -10dB number squeezed state with $N = 10^4$, for which $s = \sqrt{10}$ and $\Delta N_r = 10$, $\Delta\phi_q \approx 2°$. This is far less than our the $20°$ – $40°$ typical of our measurements, but we note that our $20°$ single-shot phase measurement uncertainty makes this comparison difficult.

Using the two-mode model of a split BEC in a double well (see Sec. 2.3), we can estimate the effects of thermal fluctuations on $\Delta\phi$. Assuming the Boltzmann distribution of temperatures drives thermal phase fluctuations, we associate an energy $k_B T/2$ to each one-dimensional classical degree of freedom in the Josephson Hamiltonian (see Eq. 2.63)

$$\frac{1}{2}k_B T = \frac{1}{2}E_j\langle\phi_{th}^2\rangle \Rightarrow (\Delta\phi)^2 \approx \langle\phi_{th}^2\rangle = \frac{k_B T}{E_j}. \tag{7.3}$$

where E_j is the Josephson energy describing inter-well tunnelling and assuming that phase fluctuations are small (see Sec. 2.3.4). To obtain the Josephson energy E_j, we numerically solve the 3D Gross-Pitaevskii equation in our potential using a standard split-step iteration algorithm and propagation in imaginary time. For $N = 2 \times 10^4$, we estimate $E_j \sim h \times 5$ kHz. Using a rough estimate of temperature for this data $T \sim 100$ nK, we obtain $\Delta\phi_{th} \sim 40°$, which is in rough agreement with the measured values of $20°$ to $40°$. According to this estimate, our observed shot-to-shot relative phase fluctuations are dominated by thermal fluctuations. The estimate is only approximate, however, since E_j is strongly dependent on the exact shape of the potential.

7.2 Measuring relative atom number

The relative atom number N_r is the complementary observable to the relative phase ϕ, as discussed in Sec. 2.3. One might imagine using phase measurements alone to infer the magnitude of ΔN_r: using the number-phase uncertainty relations predicted by the two-mode BJJ model (Eqs. 2.61 and 2.64), or using the rate of phase diffusion in the time after splitting to infer ΔN_r, as

in [31]. We opt instead to measure the relative atom number directly, by measuring the left-hand and right-hand double well populations after splitting using time-of-flight absorption imaging. This allows ΔN_r to be determined independently of any model of the double-well system.

In this section, we describe the N_r measurement procedure and discuss in detail the correction for systematic measurement errors, which are dominated by fluctuations in the total atom number, and by OSN in absorption images. The main result is the demonstration of N_r fluctuations at the shot-noise level, which is presented in Sec. 7.2.5. We show that our atom number counting methods are limited by OSN, but estimate that they are sufficiently sensitive to observe number squeezing of as much as -14 dB.

7.2.1 Number measurement procedure

The procedure for creating and splitting the BEC is similar to that used to measure the relative phase. The major differences are (a) that the double well separation is dramatically increased after splitting to permit optical resolution of the left-hand and right-hand clouds, and (b) that the two BECs are imaged at small times of flight to prevent any overlap of the expanding clouds.

Dressing and splitting The initial dressing step is identical to that of Sec. 7.1.1. To damp out collective modes excited by the RF dressing (which would lead to increased left-right population fluctuations), we hold the BEC in the dressed trap for up to 800 ms. Splitting is then carried out by ramping the RF frequency ω from below to above resonance in roughly 100 ms at a rate of 200 Hz/ms.

Separation Since we cannot optically resolve the two split clouds after splitting (when their separation is on the order of 2 to 5 µm), we apply a separation step in which the double well separation is further increased to ~ 160 µm using an 2.5 MHz/ms sweep of ω in 30 ms. The RF amplitude is also increased linearly during the separation stage to prevent loss due to Landau-Zener tunnelling between adjacent dressed states; in a dressed atom chip Z-trap, the dressed Zeeman level spacing decreases with increasing well-separation at a fixed B_{rf}, as described in Sec. 6.2.3.

We verify that the atom number is maintained constant during splitting and separation. As discussed in the next section the predicted shot-noise level in relative atom number, to which we compare measured N_r fluctuations, depends on the total atom number N. Since we only measure N after splitting and separation, preserving N during these two steps allows us to infer the initial atom number using the measured left and right atom numbers $N \equiv N_R + N_L$.

7.2.2 Imaging, background OD subtraction, and atom number calculation

After separating the two clouds, the static and RF magnetic fields are switched off[3] and the two clouds are imaged with a resonant absorption probe after a 2 ms time-of-flight. The signal (probe + atoms), reference (probe only) and background (background light and noise only, no probe)

[3]The slowest of the bias coils has a $1/e$ time constant of 400 µs.

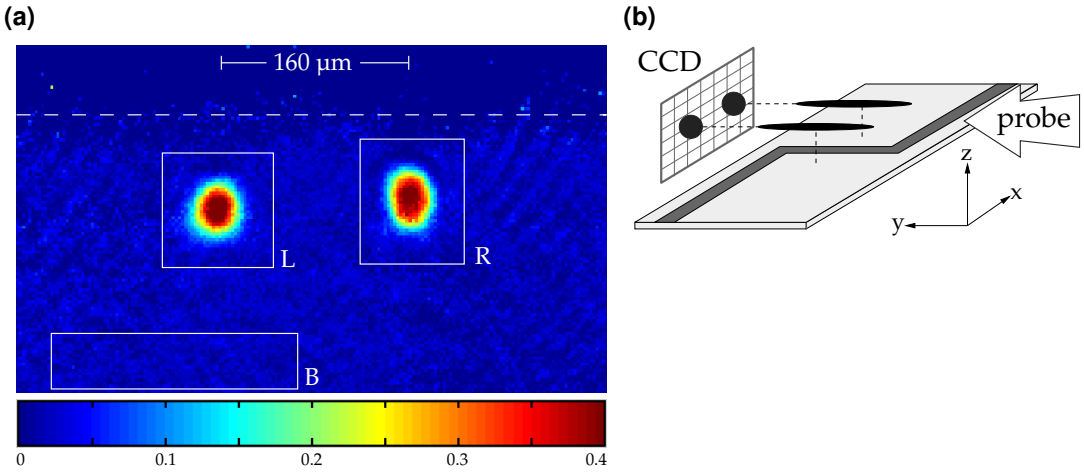

Fig. 7.4: (a) A false-colour OD image in the xz plane showing the demarcation of regions ("boxes") used for atom number analysis. The two bright spots correspond to two atom clouds, imaged here after a 2 ms time-of-flight, and separated by 160 μm . Region B ("background") is chosen so as to contain none of the atomic signal, and is used to define the mean background level $\overline{OD}_{bg}$ (see text). Pixel-by-pixel sums of the OD in regions L and R ("left" and "right") are used to compute the atom numbers N_L and N_R. The dashed horizontal line indicates the position of the atom chip surface. The colour bar at bottom shows the OD colour scaling for the image. **(b)** Imaging geometry for split clouds.

images used to construct the OD image (see Sec. 5.4.1) are collected 410 μs apart using "Kinetics mode" on a Pixis 1024BR CCD camera and the "2nd generation" imaging system (see Sec. 4.5). Each exposure lasts 100 μs. The probe intensity is tuned to $I \approx 0.2$ mW/cm^2 ($I/I_{\text{sat}} \simeq 1/10$) which corresponds to roughly 190 scattered photons per atom in 100 μs.

The divided OD image is constructed according to Eq. 5.23. The left and right atom numbers N_L and N_R are computed using a pixel-by-pixel sum of the OD [56] in the "L" and "R" image regions (see Fig. 7.4a)

$$N_{L,R} = \frac{1}{\tilde{\sigma}_\lambda(\delta)} \sum_{\langle i,j \rangle} \left[OD(i,j) - \overline{OD}_{bg} \right] A_{\text{pix}}(i,j) = \frac{A_{\text{pix}}}{\tilde{\sigma}_\lambda(\delta)} \sum_{\langle i,j \rangle} \left[OD(i,j) - \overline{OD}_{bg} \right] \tag{7.4}$$

where the sums run over all pixels within the image region L or R, $\tilde{\sigma}_\lambda(\delta)$ is the calibrated atomic absorption cross-section as a function of the probe detuning δ (see Sec. 5.4.1), A_{pix} is the area of a single image pixel, and $\overline{OD}_{bg}$ is the mean background OD in the divided image.

Background OD subtraction Any mismatch in probe beam intensities between the signal and reference images will lead to a systematic offset in the background OD, and thus in the measured atom number. To correct for this effect we construct a mean OD for the image using a background group of pixels far from the atomic signal. The mean OD in this background region $\overline{OD}_{bg}$ is then subtracted on a per-pixel basis from each $OD(i,j)$ value, as noted Eq. 7.4. $|\overline{OD}_{bg}| \lesssim 0.03$ is typical of our data. A full account of systematic errors in OD is given in Sec. 7.2.4

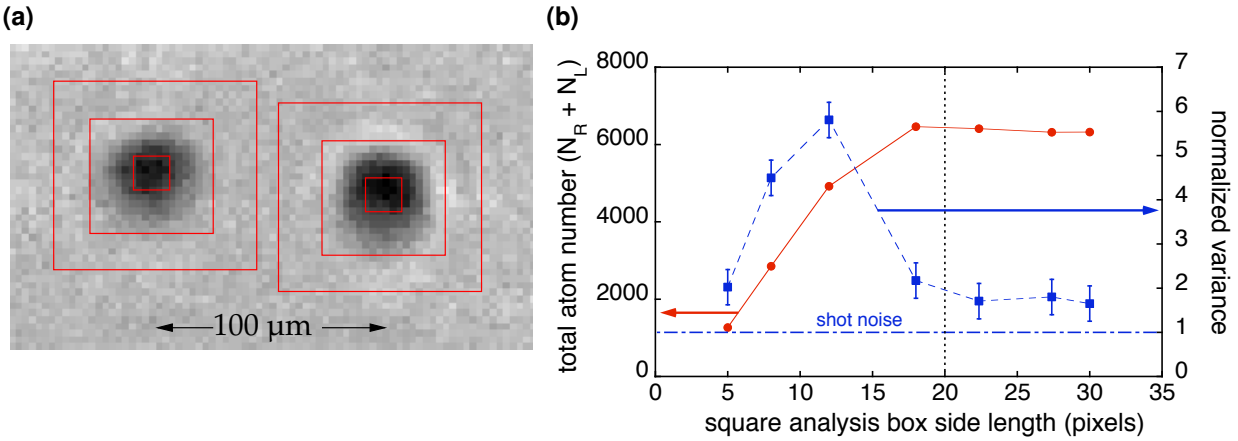

Fig. 7.5: (a) An OD image of $N \sim 7000$ ^{87}Rb atoms imaged after a 2 ms time-of-flight showing square analysis boxes of side lengths 30, 18 and 5 pixels. The peak OD is 0.25 and the Gaussian cloud widths are roughly 4 pixels (13 μm). **(b)** We work in a regime in which atom number counting and variance of the relative atom number are insensitive to the box size. A typical working box size is indicated by the vertical dashed line. Too-small boxes lead to an underestimate of N and overestimate of $\mathrm{Var}(N_r)$ (see text).

Choosing analysis box sizes The analysis regions ("boxes") in a data set are chosen independently for "L" and "R" (see Fig. 7.4a); the same box definitions are used for all images in a given data set. Boxes must be large enough to capture all of the atomic absorption signal without overlapping, which would lead to double-counting atoms in the left and right clouds. Smaller analysis boxes reduce the systematic error due to OSN, as discussed in Sec. B.2. If boxes are chosen too small, however, then we underestimate N_R and N_L, and hence N_r and $\mathrm{Var}(N_r)$ by ignoring the atomic signal at the edges of the clouds. Another danger of "too-small" boxes is the conversion of shot-to-shot time-of-flight cloud position jitter into apparent relative number fluctuations; this "noise" leads to an overestimate of $\mathrm{Var}(N_r)$. The effects of box size on N and $\mathrm{Var}(N_r)$ are demonstrated in Fig. 7.5b, which also shows a range of box sizes for which atom number counting and $\mathrm{Var}(N_r)$ are insensitive to the box size. To minimize OSN, we use the smallest boxes in the size-insensitive regime, denoted by the vertical dashed line in the figure for this data set. We find in general that box side lengths of roughly 5σ, where σ is the Gaussian width of one cloud, safely capture all the atoms without spuriously increasing $\mathrm{Var}(N_r)$.

7.2.3 Quantifying relative number fluctuations

We repeatedly create and split a cold cloud and calculate the total and relative atom numbers

$$N \equiv N_R + N_L \tag{7.5}$$

$$N_r \equiv N_R - N_L. \tag{7.6}$$

in each repetition. The variance $\mathrm{Var}(N_r)$ over n repetitions of this process is computed directly from the N_r ensemble data, and is compared to the variance predicted by binomial statistics.

The statistical prediction defines the shot-noise level for ideal, non-interacting particles. The measured fluctuations in N_r are compared to the shot-noise level using the **normalized variance** $\widetilde{V}$:

$$\widetilde{V} \equiv \frac{\mathrm{Var}(N_r)^{\mathrm{meas'd}}}{\mathrm{Var}(N_r)^{\mathrm{binom}}} \tag{7.7}$$

where

$$\mathrm{Var}(N_r)^{\mathrm{binom}} = 4\overline{N}\overline{p}_R(1-\overline{p}_R) + (2\overline{p}_R - 1)^2\sigma_N^2. \tag{7.8}$$

Fluctuations in N_r at the shot-noise level correspond to $\widetilde{V} = 1$, those larger than shot noise to $\widetilde{V} > 1$, and those smaller than shot noise to $\widetilde{V} < 1$.

Shot noise from binomial statistics Eq. 7.8 is the variance in N_r from a binomial splitting process in which each atom is imagined to have probabilities $\overline{p}_R$ and $1-\overline{p}_R$ of populating the right-hand and left-hand clouds, respectively, after splitting (see Appendix B for the derivation).[4] The mean values of the left and right atom numbers are $\overline{N}_L = \overline{p}_L\overline{N}$ and$\overline{N}_R = \overline{p}_R\overline{N}$, respectively. Eq. 7.8 reduces to the more recognizable binomial shot noise expression $\mathrm{Var}(N_r) = \overline{N}$ in the case of perfectly "balanced splitting", i.e when $\overline{p}_R = 1/2$ and $\overline{N}_R = \overline{N}_L$.

The total atom number N is allowed to fluctuate over the n repetitions of the experiment with a variance $\mathrm{Var}(N) = \sigma_N^2$ in the derivation of Eq. 7.8; in each of the n repetitions, N is chosen from a Gaussian probability distribution of mean $\overline{N}$ and width σ_N. Eq. 7.8 demonstrates that for imbalanced splitting ($p_R \neq \frac{1}{2}$), fluctuations in N add to the observed variance in N_r. Thus, it is important to include N fluctuations in the statistical derivation of the shot-noise level. This allows us to identify actual fluctuations in N_r independent of fluctuations in N, and ensures that $\widetilde{V} = 1$ corresponds to true shot noise in N_r.

The quantities in Eq. 7.7 are all calculated directly from the N_R, N_L data according to the

[4] Eq. 7.8 is the "N-analysis" (as it is known in the lab) corrected to account for non-zero N fluctuations. Appendix B also describes and evaluates two alternate analysis methods: the "p-analysis", and the "Heidelberg analysis", which is described in the supplementary material of [43]. All three methods produce identical results for $\overline{p}_R = 1/2$. The three methods agree to well within statistical uncertainties for our data, which has $\overline{p}_R$ typically between 0.47 and 0.53. The "N-analysis" is used here since it is the simplest conceptually, and easily applied to "blanks" analysis.

following formulae (the index $i = 1..n$ denotes data from the i^{th} splitting repetition):

$$\text{Var}(N_r)^{\text{meas'd}} = \frac{1}{n}\sum_{i=1}^{n}(N_r^{(i)} - \overline{N}_r)^2, \text{ where} \tag{7.9}$$

$$\overline{N}_r = \frac{1}{n}\sum_{i=1}^{n}(N_R^{(i)} - N_L^{(i)}); \tag{7.10}$$

$$\overline{N} = \frac{1}{n}\sum_{i=1}^{n}(N_R^{(i)} + N_L^{(i)}); \tag{7.11}$$

$$\overline{p}_R \equiv \left\langle \frac{N_R}{N} \right\rangle = \frac{1}{n}\sum_{i=1}^{n}\frac{N_R^{(i)}}{N_R^{(i)} + N_L^{(i)}}; \tag{7.12}$$

$$\sigma_N^2 = \text{Var}(N) = \frac{1}{n}\sum_{i=1}^{n}(N^{(i)} - \overline{N})^2. \tag{7.13}$$

7.2.4 Correcting for systematic errors in OD – "blanks" analysis

Systematic errors in the measurement of absorption images and the creation of OD images can result in spurious contributions to the measured atom number and variance $\text{Var}(N_r)$. We divide the dominant systematic imaging effects in our experiment into three categories:

1. **OSN** in the measured probe beam intensity
2. **a non-zero background OD** resulting from mismatched probe beam intensity between the signal and reference images
3. **residual fringes in the OD image** due to mechanical vibrations in the imaging system or vacuum chamber during imaging, diffraction lines in the probe beam scattered from the atom chip surface, aberrations introduced by the imaging optics, or dust and other debris on optical surfaces.

Of these, only OSN cannot be eliminated; it is a fundamental noise which would exist in any apparatus or measurement procedure, assuming classical states of light are used [40]. Even with perfectly stabilized probe beam intensities and mechanically rigid imaging optics, shot noise in the photodetection process sets a finite lower bound on the measured value of $\text{Var}(N_r)$. A number of probe photons N_{ph} incident on a CCD camera generates a certain number of photoelectrons $\mathcal{N}_{pe} = \eta_{qe}N_{ph}$, where η_{qe} is the camera's quantum efficiency. Since the absorption of a photon and the creation of a photoelectron is a quantized and probabilistic process, we expect Poissonian image-to-image shot noise fluctuations $\sqrt{\mathcal{N}_{pe}}$ in the photoelectron number [40]. CCD read noise and dark counts contribute to the technical noise at the level of $\sim 1\%$ of OSN (see Sec. B.2).

We correct for these statistical OD effects as follows. The effect of unequal signal and reference probe intensities is compensated by subtracting a background OD offset from the OD in each pixel, for each image, as described in Sec. 7.2.2. Fringes in the OD are suppressed taking advantage of the rapid multiple exposures possible with our Pixis 1024BR CCD camera (see

Sec 4.5.2), which was purchased specifically for its low read noise and rapid imaging capabilities. The remaining spurious contribution to $\mathrm{Var}(N_r)$ – which is now dominated by OSN, after hard work at suppressing other technical fluctuations in our images – is quantified by analyzing images collected without atoms, and subtracted from the measured relative number variance as described in the following paragraph.

Blanks correction We identify two contributions to the measured normalized variance $\mathrm{Var}(N_r)^{\mathrm{meas'd}}$ described in Secs. 7.2.2 and 7.2.3: the first is our target signal from actual relative atomic population fluctuations during splitting, which we denote $\mathrm{Var}(N_r)^*$; the second is the spurious contribution of the systematic OD effects described in the previous paragraph, which we denote $\mathrm{Var}(N_r)^{\mathrm{blanks}}$ [158]. We assume that the two effects are uncorrelated. Since OSN, OD offsets and OD fringes are a function of the probe beam, imaging optics and CCD camera, they are present in images taken with or without atoms present. Therefore, we quantify these effects by examining OD images constructed according to Eq. 5.23 *without* atoms present – "blanks" images. We calculate the spurious contribution to the normalized variance $\mathrm{Var}(N_r)^{\mathrm{blanks}}$ by analyzing a data set of "blanks" images using the same analysis regions and procedure used for with-atoms images (see Sec. 7.2.2 and 7.4).

Because these two contributions to $\mathrm{Var}(N_r)^{\mathrm{meas'd}}$ are uncorrelated, their variances can be added and subtracted directly. We use this property to isolate the target signal $\mathrm{Var}(N_r)^*$ from measured signal $\mathrm{Var}(N_r)^{\mathrm{meas'd}}$

$$\mathrm{Var}(N_r)^* = \mathrm{Var}(N_r)^{\mathrm{meas'd}} - \mathrm{Var}(N_r)^{\mathrm{blanks}} \tag{7.14}$$

and use it to define the **corrected normalized variance**

$$\widetilde{V}^* \equiv \frac{\mathrm{Var}(N_r)^*}{4\overline{N}\overline{p}_R(1-\overline{p}_R) + (2\overline{p}_R - 1)^2\sigma_N^2} \equiv \widetilde{V}^{\mathrm{meas'd}} - \widetilde{V}^{\mathrm{blanks}}. \tag{7.15}$$

$\mathrm{Var}(N_r)^{\mathrm{meas'd}}$, $\overline{N}$, $\overline{p}_R$ and $\sigma_N^2 = \mathrm{Var}(N)$ are all computed directly from "with-atoms" images using Eqs. 7.9 to 7.13; $\mathrm{Var}(N_r)^{\mathrm{blanks}}$ is constructed according to Eq. 7.9 directly from "blanks" images. All corrected normalized atom number variances are computed according to Eq. 7.15. This method allows the spurious systematic contributions to the measured atom number variance – due to technical measurement noise and/or any noise introduced by the imaging processing and analysis software – to be subtracted in a single step.

Rapid imaging for OD fringe suppression We minimize technical noise from fringes in the OD image by minimizing the time between the signal and reference images Δt_{img}. In principle, any fringes in a single-shot image of the probe beam (due to partial reflections from surfaces of imaging optics, aberrations or other sources) should be common to both signal and references images, and thus be "divided out" in the OD construction. In practice, mechanical vibrations of imaging optics and other elements in the probe beam path on timescales faster than Δt_{img} can result in imperfect cancellation of these effects in the OD, leading to residual fringes in OD

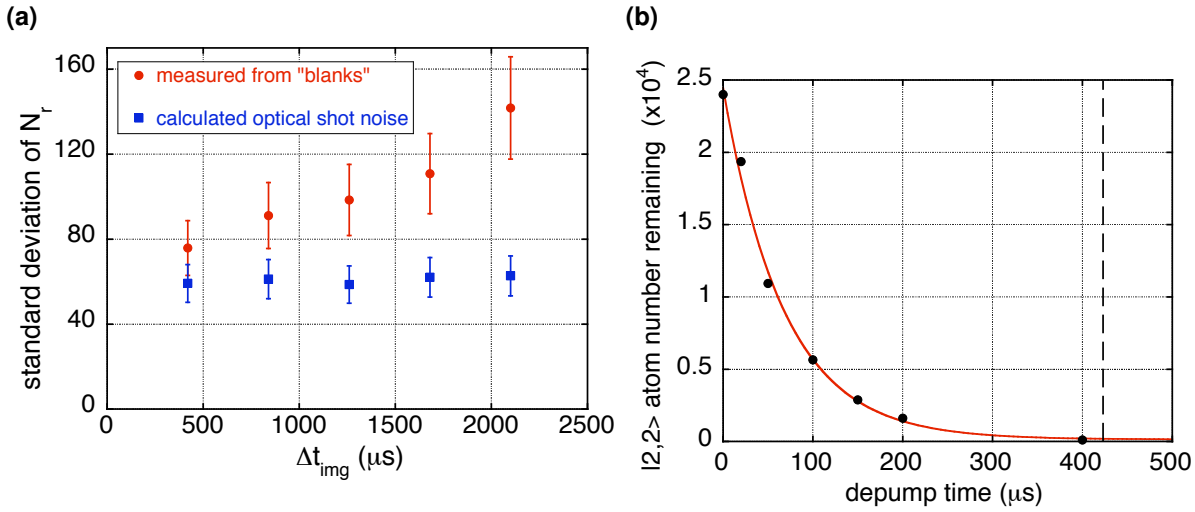

Fig. 7.6: (a) The standard deviation of the spurious relative atom number due to blanks noise (circles) approaches that calculated for OSN (squares) as the time $\Delta t_{\rm img}$ between signal and reference absorption images is decreased. We work at $\Delta t_{\rm img} = 420$ µs, at which the contribution of OSN to the blanks variance is roughly 60% (see text). Error bars are based on uncertainties in OD due to OSN from Eq. B.54. These data assume a $C^2 = 1.7$ atom number calibration factor (see Sec. 5.4.3.1). **(b)** After the 100 µs signal image exposure, ^{87}Rb atoms in $|F = 2, m_F = 2\rangle$ are depumped into the dark state $|1, 1\rangle$, then re-imaged with the σ^+, $|2, 2\rangle \leftrightarrow |3, 3\rangle$ imaging probe (see text). The number of atoms remaining in $|2, 2\rangle$ is shown as a function of the depump pulse duration at a fixed intensity. There is no discernible atomic signal after 420 µs (dashed line) when the reference image is collected. An exponential fit (solid line) gives a $1/e$ lifetime of 68 µs.

images.

The benefits of rapid imaging are demonstrated in Fig.7.6a, which shows the spurious contribution to the standard deviation of N_r measured in blanks data as a function of $\Delta t_{\rm img}$.[5] The figure also shows the calculated standard deviation of N_r due to OSN (OSN) for each data set, demonstrating that the standard deviation of N_r from blanks images approaches that calculated from OSN as $\Delta t_{\rm img}$ is reduced. At our working $\Delta t_{\rm img} = 420$ µs for these data, $\mathrm{Var}(N_r)^{\rm blanks} = (77 \pm 14)^2$ and $\mathrm{Var}(N_r)^{\rm OSN} \simeq (59 \pm 9)^2$, which roughly corresponds to an 60% contribution of OSN to the total atom number variance. Error bars are statistical. Each $\Delta t_{\rm img}$ data point was computed from a data set of 66 to 70 blank images collected with a probe intensity $I \approx I_{\rm sat}/10$. The contribution of OSN to the measured atom number variance is discussed in further detail in Sec. B.2.

Depumping to facilitate rapid imaging The rate of free-fall of the atomic cloud limits the minimum time between signal and reference images $\Delta t_{\rm img}$ in regular absorption imaging; a proper "no-atoms" reference image requires waiting for the falling cloud to completely exit the imaging field of view before exposing the reference image. With our imaging field of view of 416 µm × 3328 µm the free-fall wait time after 2 ms time-of-flight is 9 ms. Mechanical vibrations of imaging optics, the CCD camera and the atom chip on timescales faster than 9 ms result in fringes in the

[5] To be clear, $\Delta t_{\rm img}$ is the time elapsed between the end of the 100 µs signal image exposure and the beginning of the 100 µs reference image exposure.

divided OD image.

We eliminate the free-fall wait-time requirement by optically depumping the atoms into a dark state immediately after the signal image is collected. A weak depumping beam tuned to $|F = 2, m_F = 2\rangle \leftrightarrow |F' = 2, m'_F = 2\rangle$ in $^{87}\mathrm{Rb}$ is applied along x in the time after the signal image exposure ends and before the reference image exposure begins. Atoms populate the $|F = 1, m_F = 1\rangle$ dark ground state – dark with respect to the imaging probe beam polarized σ^+ on the $^{87}\mathrm{Rb}$ cycling transition – by spontaneous decay from the $|F' = 2, m'_F = 2\rangle$ excited state. The depumping beam is actually polarized σ^+ with respect to the x direction, but the π component of this beam with respect to the imaging quantization axis (defined by a weak magnetic bias field along y during this time – see Sec. 5.4.1) provides sufficient coupling to transfer the population into the $|1, 1\rangle$ dark state. Fig. 7.6b shows the effect of the depumping beam on the $|2, 2\rangle$ population as function of time.

With the atoms having been made to "disappear" in this way, Δt_{img} can be reduced to a few hundred microseconds, dramatically reducing the amplitude of fringes in the OD images. After implementing the depumping technique the practical lower bound on Δt_{img} becomes the CCD shift rate. Following the 100 µs exposure of the signal image (with atoms), the Pixis camera should take 128×3.2 µs $= 409.6$ µs CCD shift time before exposing the subsequent image. We find that $\Delta t_{\mathrm{img}} = 420$ µs is the smallest useable value, and use it for all imaging. The atoms are depumped during this shift time.

7.2.5 Results: shot-noise level number fluctuations

Using the measurement and analysis methods described in Secs. 7.2.3 and 7.2.4, we observe relative atom number fluctuations at the shot-noise level over successive repetitions of $^{87}\mathrm{Rb}$ BEC splitting. Fig. 7.7 shows an example shot noise data set of left and right atom numbers N_L and N_R, and the resulting total and relative atom numbers $N = N_R + N_L$ and $N_r = N_R - N_L$.

Table 7.1 summarizes the "measured", "blanks" and ultimate "blanks-corrected" fluctuations for this data set. The first two rows of Table 7.1 show the measured variance and standard deviation of N_r; the third row shows the calculated OSN contribution in "blanks" data; the last three rows show the normalized variance, and the statistical and systematic uncertainties in the blanks-corrected normalized variance. The most important values in the table are the blanks-corrected normalized variance $\widetilde{V}^*$ and its associated statistical and systematic uncertainties, which are shown in the lower-right hand corner.

The sensitivity of our $\mathrm{Var}(N_r)$ measurements is limited by technical optical noise, which itself is dominated by OSN, as described in Sec. 7.2.4. Since we subtract the blanks variance $\mathrm{Var}(N_r)^{\mathrm{blanks}}$ from the measured variance $\mathrm{Var}(N_r)^{\mathrm{meas'd}}$, the uncertainty in the blanks-corrected variance $\mathrm{Var}(N_r)^*$, and ultimately the normalized, blanks-corrected variance $\widetilde{V}^*$, depends on the uncertainties $\delta\mathrm{Var}(N_r)^{\mathrm{blanks}}$ and $\delta\mathrm{Var}(N_r)^{\mathrm{meas'd}}$. We summarize these uncertainties here, noting that further detail is available in Appendix B.

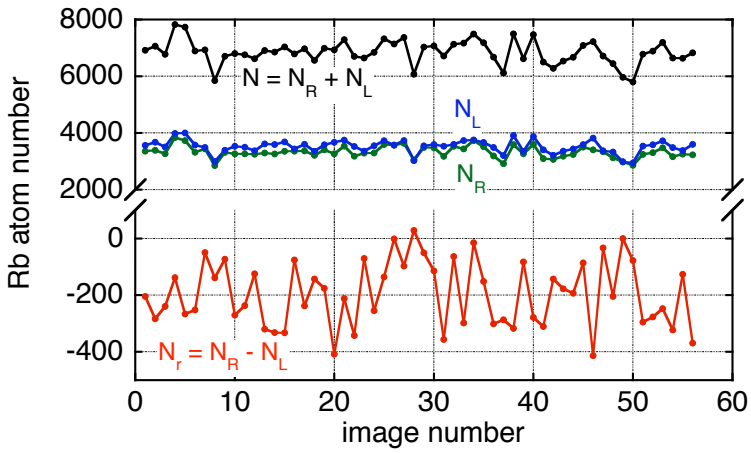

Fig. 7.7: Example raw data showing atom number fluctuations at the shot noise level. This data set has $\overline{N} \simeq 6851$, $\mathrm{Var}(N) \simeq (421)^2$, $\overline{p}_R = 0.486$, calculated from $n_a = 56$ "with-atoms" images. All 56 images were collected consecutively, each using an experimental cycle lasting roughly 30 s. Thus, the entire data set was collected in roughly 28 minutes.

	measured (with atoms)	blanks (no atoms)	blanks-corrected
measured N_r variance	$\mathrm{Var}(N_r)^{\mathrm{meas'd}} = 13230$	$\mathrm{Var}(N_r)^{\mathrm{blanks}} = 4811$	$\mathrm{Var}(N_r)^* = 8419$
measured N_r std. dev.	$\sigma_{N_r}^{\mathrm{meas'd}} = 115.0$	$\sigma_{N_r}^{\mathrm{blanks}} = 69.4$	$\sigma_{N_r}^* = 91.8$
calculated OSN N_r variance		$\mathrm{Var}(N_r)_{\mathrm{OSN}} = (53.9)^2$	
normalized variance	$\widetilde{V}^{\mathrm{meas'd}} = 1.92$	$\widetilde{V}^{\mathrm{blanks}} = 0.69$	$\widetilde{V}^* = 1.22$
statistical uncertainty			$\delta\widetilde{V}^* = 0.37$
systematic uncertainty			$\delta\widetilde{V}^* = 0.2$

Tab. 7.1: N_r error analysis summary of typical shot-noise-level data set, for which $\widetilde{V} \sim 1$ would be expected. This data set has $\overline{p}_R = 0.486$, $\overline{N} \simeq 6851$, $\sigma_N \simeq 421$, $n_a = 56$ "with-atoms" images, $n_b = 141$ blanks images. The statistical error is dominated by n_a, and can be decreased by increasing n_a (see Eq. B.1.4). The systematic uncertainty $\delta\widetilde{V}^*$ reflects the 20% uncertainties in the the total atom number calibration factor $C^2 = 1.7 \pm 0.3$ (see Sec. 5.4.3.1).

Systematic error The systematic error in $\widetilde{V}^*$ reflects the uncertainty in the atom number calibration factor $C^2 = 1.7 \pm 0.3$, and adds a $\sim 20\%$ systematic uncertainty to $\widetilde{V}^*$. The C^2 measurement is based on a comparison of T_c measured with a $^{87}\mathrm{Rb}$ BEC to the value predicted for N atoms (see Sec. 5.4.3.1).

Statistical error The net statistical uncertainty $\delta\widetilde{V}^*$ is typically between 0.3 to 0.5 for our data, roughly twice the systematic uncertainty. Statistical uncertainties are computed using standard error propagation techniques (see Eq. B.38 and Sec. B.1.4). For roughly balanced splitting data ($\overline{p}_R \approx 1/2$), the uncertainty in the blanks-corrected variance $\delta\mathrm{Var}(N_r)^*$ is dominated by (a) the standard error in the variances $\mathrm{Var}(N_r)^{\mathrm{meas'd}}$ and $\mathrm{Var}(N_r)^{\mathrm{blanks}}$

$$\delta\mathrm{Var}(N_r)^{\mathrm{meas'd}} = \mathrm{Var}(N_r)^{\mathrm{meas'd}}\sqrt{\frac{2}{n_a-1}} \quad \text{and} \quad \delta\mathrm{Var}(N_r)^{\mathrm{blanks}} = \mathrm{Var}(N_r)^{\mathrm{blanks}},\sqrt{\frac{2}{n_b-1}} \tag{7.16}$$

and (b) the standard error on in the mean total atom number

$$\delta\overline{N} = \frac{\sigma_N}{\sqrt{n_a-1}} \tag{7.17}$$

[159, 156]. n_a is the number of "with-atoms" images; n_b is the number of "blanks" images. We typically observe atom number fluctuations about a stable mean value ($\overline{N}_r \approx 0$) over 40 – 80 **consecutive** experimental repetitions (roughly 15 – 30 minutes in real time) within a larger data set. Fig. 7.7 shows raw data from a single 56-repetition data set. Longer contiguous data sets are susceptible to slow experimental drifts in both N and $\mathrm{Var}(N_r)$. Blanks data are collected using shortened experimental cycle times[6], and are thus much less susceptible to long-term drift. We typically use $n_b = 100$ – 150 images, which is enough to reduce their statistical contribution $\delta\widetilde{V}^*$ below 1%. Statistical uncertainties in the atom number data can be reduced by using larger with-atoms data sets – either by improving experimental stability on the 0.5 hr to 2 hr timescale or by amalgamating data sets as in [43].

Sensitivity and detection limits We assume that the measured variance is always larger than blanks variance: $\mathrm{Var}(N_r)^{\mathrm{meas'd}} \geq \mathrm{Var}(N_r)^{\mathrm{blanks}}$ (see Sec. 7.2.4). The smallest detectable relative atom number variance is

$$\mathrm{Var}(N_r)^*_{\mathrm{min}} = 0 \pm \delta\mathrm{Var}(N_r)_{\mathrm{min}} \tag{7.18}$$

where the uncertainty $\delta\mathrm{Var}(N_r)_{\mathrm{min}}$ represents the detection limit of atom number variance in our experiment. Using the data from Tab. 7.1 and setting $\mathrm{Var}(N_r)^{\mathrm{meas'd}} \equiv \mathrm{Var}(N_r)^{\mathrm{blanks}}$ we obtain $\delta\mathrm{Var}(N_r)_{\mathrm{min}} = 375$. This corresponds to a relative atom number fluctuation (standard deviation) of $\sqrt{375} \simeq 20$ atoms. Thus, the minimum detectable number squeezing factor s, assuming balanced splitting with a variance of 375 and a total atom number of $\overline{N} = 10^4$, is

[6] Blanks data require only the imaging portion of the experimental apparatus. Eliminating the trapping and cooling stages of the experimental cycle to collect blanks images greatly reduces the cycle time.

$s = \sqrt{\overline{N}/\mathrm{Var}(N_r)} \simeq 5$. This corresponds to roughly -14 dB of number variance squeezing. Assuming that technical optical noise is completely dominated by OSN, $\mathrm{Var}(N_r)^{\mathrm{meas'd}} \equiv \mathrm{Var}(N_r)^{\mathrm{blanks}} \equiv \mathrm{Var}(N_r)_{\mathrm{OSN}} = 31.7$ from Tab. 7.1 gives $\delta\mathrm{Var}(N_r)_{\mathrm{min}} = 225$ and $s \simeq 7$, roughly -16.5 dB of squeezing. As noted in Sec. B.2.2.1, the OSN contribution can always be reduced by reducing the analysis box size to increase the atom number sensitivity.

To summarize, although we so far have not observed repeatable, robust sub-shot-noise fluctuations in N_r, these estimates show that sub-shot-noise fluctuations are well within the sensitivity of our measurement and analysis methods.

7.3 Outlook: prospects for observing number squeezing

In Sec. 7.2.1, we demonstrate relative atom number fluctuations at the shot-noise level in a split BEC, and show that our number counting method is sensitive to N_r fluctuations well below the shot-noise level. Though we expect shot noise fluctuations in N_r in a rapidly split BEC, the two-mode BJJ model of the system (discussed in Sec. 2.3) predicts sub-shot-noise N_r fluctuations for adiabatic splitting. This prediction has recently been verified experimentally with the observation of number squeezing in split BECs in the Ketterle [31] and Oberthaler [43] groups. In this section we explore the prospects for observing number squeezing in future work in our experiment.

Number squeezing by adiabatic splitting Number squeezing arises from nonlinear repulsive atom-atom interactions during the splitting process, which favour states with smaller relative atom number fluctuations [63, 157, 79]. At the beginning of splitting, we imagine the system to be in the strong tunnelling Josephson regime of the two-mode BJJ model, which is characterized by $E_j/E_c \gg N$, where E_j is the "Josephson tunnelling" energy, and E_c is the "on-site interaction" or "charging" energy (see Sec. 2.3). During splitting, inter-well tunnelling and E_j are reduced by increasing the potential barrier and double-well separation. In particular, if the wells are separated linearly in time, the two-mode model predicts an exponential decrease of E_j and a roughly constant E_c and chemical potential μ during splitting [79]. Since the relative number variance is given by $(\Delta n)^2 = (\Delta N_r)^2/4 = \sqrt{E_j/E_c}$ in the Josephson regime, we expect decreasing relative number fluctuations as the BEC is split [157, 153].

Experimental realizations Jo et al. [31] report -20 dB of relative number squeezing[7] from an indirect measurement based on the rate of phase diffusion of a split BEC. Their experimental geometry is very similar to ours, involving the splitting of an anisotropic BEC using RF potentials. It remains unclear whether or how this result can be reconciled with the two-mode BJJ model, since their temperature range (they quote $T_c \sim 1$ μK and $\mu \sim k_B \times 300$ μK) would suggest thermal atom number fluctuations well above their measurements (see below). Estève et al. [43] report

[7] We report the amount of squeezing in variance terms: "dB of squeezing" $\equiv -10 \log[N/\mathrm{Var}(N_r)]$. -20 dB of squeezing corresponds to a "squeezing factor" $s \equiv \sqrt{N/\mathrm{Var}(N_r)} = 10$ [31].

a more modest -3 dB of squeezing in a more isotropic, all-optical splitting experiment, and use direct atom number counting similar to the methods we described in Sec. 7.2.1.

Estimates for our system We estimate the expected amount of number squeezing in our experiment using recent two-mode treatments the splitting process [79, 153]. For slowly varying E_j, the system can adiabatically evolve into a final state with sub-shot-noise fluctuations in N_r [63, 157, 79, 153]. However, as tunnelling and E_j decrease with increasing well separation, the splitting process will eventually become non-adiabatic; the two-mode level-separation vanishes as $E_j \to 0$. Following Leggett and Sols [36, 71], Burkov et al. [153] estimate a final relative number rms fluctuation in the fully split system of

$$\Delta N_r = \sqrt{\frac{5N}{4\mu\tau_{\text{split}}}} \tag{7.19}$$

in the Thomas-Fermi regime for a BEC initially in a harmonic trap, where τ_{split} is the splitting time. Eq. 7.19 predicts -20 dB of squeezing from our most recent experimental parameters ($N = 5000$ and $\tau_{\text{split}} = 20$ ms), which is well below our shot-noise-level observations. However, the prediction of Eq. 7.19 is supported by the results of Jo et al. [31], as noted in [153].

The role of finite temperatures – a continuing investigation One possible explanation for this discrepancy is the effect of thermal fluctuations on the observed variance of N_r at finite temperatures. Assigning an energy $k_B T/2$ to each degree of freedom of the harmonic oscillator BJJ Hamiltonian of Eq. 2.62 results in

$$\widetilde{V}_{\text{th}} = \frac{5k_B T}{2\mu}, \tag{7.20}$$

which expresses the expected normalized variance of relative atom number fluctuations due to thermal excitations of the BJJ in terms of the temperature T and the chemical potential μ (in the Thomas-Fermi regime, for a BEC initially in a harmonic trap). Using parameters typical of our experiment ($N = 5000$, $\mu = h \times 1$ kHz, and $T_c \approx 250$ nK), Eq. 7.20 implies that temperatures $T \lesssim 20$ nK are required to observe sub-shot-noise fluctuations with $\widetilde{V} \lesssim 1$. We measure initial BEC temperatures in the single harmonic trap *before* splitting of $T \sim 80$ nK – 120 nK, which, if taken as the BEC temperatures *during* splitting, would imply normalized variances of $\widetilde{V}_{\text{th}} \sim 4$ – 6. By contrast, we observe $\widetilde{V} \sim 1$. Our data might be explained by the presence of adiabatic cooling as the single well is deformed into the double well during splitting, as suggested in [43]. This effect could result in temperatures much below the initial 80 nK – 120 nK values during splitting, and might thus reduce thermal fluctuations enough to allow shot-noise or sub-shot-noise fluctuations in N_r .

Looking ahead The role of finite temperature fluctuations in BEC splitting experiments continues to be a topic of interest in the field, particularly in light of the results of [31] and [43]. Because

of the contrasting geometries of these two experiments – strongly anisotropic vs. isotropic double wells – they also raise questions about the role of dimensionality in adiabatic BEC splitting, and about the validity of the two-mode model in strongly anisotropic potentials. Our experiment combines the geometry and splitting methods of [31] with the direct atom number detection methods of [43]. These aspects of our experiment, combined with the relative number and relative phase measurement tool developed in this thesis, make our experiment well suited to contributing to this ongoing discussion.

7.4 Summary

This chapter describes the dynamic splitting of a $^{87}\mathrm{Rb}$ BEC confined to an RF double-well potential. The RF splitting technique allows the inter-well tunnelling strength to be tuned over a wide range by changing the potential barrier height and well separation. The focus of the work is the measurement of fluctuations in the relative atom number and relative phase over successive experimental repetitions of the splitting process. The relative atom number N_r is the difference in the right-hand and left-hand well populations, which are measured using resonant absorption imaging at short times of flight. The relative phase ϕ is measured from the interference pattern formed by the two overlapping clouds in long times of flight. The main results of the chapter are (a) the demonstration of a non-random distribution of relative phases, which suggests coherent splitting, and (b) direct measurements of atom number fluctuations at the shot-noise level. We show that our atom number counting methods are limited by OSN, but estimate that they are nevertheless sensitive enough to observe number squeezing of as much as -14 dB. The number and phase measurement tools described in this chapter lay the foundation for future investigations of number squeezing in BEC splitting experiments, particularly the role of temperature and trap geometry on number and phase fluctuations in the double well system.

Be prepared to modify your plan.

Wing's fortune cookie

8 Conclusions and outlook

This thesis describes experiments with quantum degenerate Fermi and Bose gases confined to static and dynamic micromagnetic atom chip traps. The experimental apparatus was designed and built with the specific goal of achieving a DFG of ^{40}K on an atom chip via sympathetic cooling with ^{87}Rb. With this relatively simple, single-chamber apparatus we first achieved BEC and DFG in 2005. These were the first DFG on an atom chip in the ultra-cold atoms research community, and the third BEC in Canada. Having established dual-species quantum degeneracy, we implemented radio-frequency dressed magnetic double-well potentials for ^{87}Rb and ^{40}K. We established techniques for measuring the relative atom number and relative phase of a BEC in a dynamically split double-well potential. Here we summarize and comment on the main results of this thesis, and close with outlines of new research directions stemming from this work.

DFG on an atom chip The union of Fermi gases and atom chip technology is an important step forward in degenerate quantum gas research. We demonstrate for the first time that a DFG can be produced via sympathetic cooling with a BEC using a single-chamber apparatus. The strong confinement and large inter-species collision rate afforded by the micromagnetic atom chip trap permits a more rapid sympathetic radio-frequency evaporation to quantum degeneracy than has so far been possible in magnetic traps [27]. Our approach represents a significant technical achievement in that it obviates the need for the minutes-long vacuum lifetimes, multi-chamber vacuum systems and Zeeman slowers required in conventional DFG experiments [50]. We also demonstrate dramatically shortened experimental cycle times from atomic vapour to DFG, which is a point of practical value in day-to-day laboratory research.

Using a DFG/BEC mixture we studied ^{87}Rb-^{40}K cross-thermalization during our evaporation. We observed a sharp reduction in the cross-section at the high-temperature start of our sympathetic evaporation, which we attribute to the Ramsauer-Townsend effect [27, 45, 33]. We demonstrate that the high-temperature Ramsauer-Townsend reduction in the ^{40}K-^{87}Rb elastic scattering cross-section is an important aspect of sympathetic cooling in ^{40}K-^{87}Rb mixtures. Despite the reduced evaporation efficiency at high temperatures, we demonstrate sympathetic evaporation to ^{40}K DFG at temperatures as low as $T \approx 0.1T_F$ in as little as six seconds, and observe Fermi pressure in the time-of-flight expansion of the gas upon its release from the chip trap.

RF double-well potentials for BEC and DFG We have implemented radio-frequency dressed double-well potentials for fermionic ^{40}K, bosonic ^{87}Rb and ^{40}K-^{87}Rb mixtures. We demonstrate for the first time that the RF-dressed potentials are species-selective, permitting the formation of simultaneous ^{87}Rb double-well and ^{40}K single-well potentials in a ^{40}K-^{87}Rb mixture, and vise versa. Using a dynamically split BEC, we develop measurement and analysis techniques to measure fluctuations in the relative atom number and relative phase over many experimental realizations, based on direct atom number counting and matter wave interference. These measurements can be used to characterize the dynamics of the split BEC system. We observe shot-noise level fluctuations in the relative atom number using time-of-flight absorption imaging. These measurement tools lay the foundation for future investigations of thermal and quantum fluctuations in this system, and of and matter wave coherence in BEC and DFG systems.

Looking ahead, the combination of Bose and Fermi degeneracy, double-well atom chip potentials, and number and phase measurement tools suggest several new research directions.

Number squeezing by dynamic splitting of a BEC Two recent experiments have reported relative number squeezing in a dynamically split BEC [43, 31]. The first [31] uses a chip-based anisotropic RF double well very similar to the ones described in this thesis, but their measurement procedure is based on phase measurements alone. By measuring the rate of phase diffusion in the split BEC, they infer a number squeezing factor much larger than that predicted by the two-mode BJJ model. The second experiment [43] uses nearly isotropic optical double-well potentials, and reports much more modest number squeezing. These two contrasting results raise questions about the validity of the two-mode Bose Josephson junction model in strongly anisotropic systems, and the precise roles of trap geometry and finite temperature fluctuations in producing number squeezed states in this system. The RF double well and measurement tools described in this thesis combine elements of both experiments, and are thus an excellent fit for this problem. We measure both number and phase directly as in [43], but work with strongly anisotropic BECs which are split along their narrow, transverse axis as in [31].

Bose-Fermi mixtures and double-well potentials The species selectivity of RF-dressed double-well potentials may be useful in studying boson-fermion interactions in ultra-cold atomic mixtures. The strong attractive interaction between ^{40}K and ^{87}Rb, known to impede sympathetic cooling in ^{40}K–^{87}Rb mixtures, depends on the inter-species collision rate, and hence the ^{40}K and ^{87}Rb number densities [22, 122, 26, 27]. Adiabatic RF manipulation could be used to reduce the ^{87}Rb peak density by decompressing the $m_F'^{(Rb)} = 2$ effective potential at the centre of the trap during sympathetic RF evaporation. Ideally, the RF-dressed collision rate would be small enough to avoid a density-driven collapse, but still large enough to maintain good inter-species rethermalization for sympathetic cooling.

These potentials are also amenable to the study of phase coherence in the ^{40}K–^{87}Rb mixture as the potential barrier is raised. Recent studies of phase-coherent RF splitting of ^{87}Rb

BECs on atom chips [30, 31, 29] and in optical traps [77, 43] have focused on interactions and tunnelling. An interesting extension of this work would be to assess the effects of a background, unsplit fermion "bath" on the tunnelling dynamics and coherence properties of this system.

Fermion splitting statistics To our knowledge, we are the first group to apply double-well potentials to an ideal Fermi gas. In a BEC, sub-Poissonian relative atom number fluctuations are made possible by repulsive atom-atom interactions. The non-interacting ideal Fermi gas may also exhibit sub-Poissonian relative number statistics during splitting as result of spatial antibunching [155]. Spatial bunching in bosons has been observed in an anisotropic Bose gas above T_c using in-situ density correlation measurements [160]. Double well potentials and dynamic splitting are alternative methods which may be used to explore number fluctuations in Fermi systems [161, 162, 155], and coherence effects in multi-component Fermi gases [163, 164].

A

Magnetic field of finite-width and finite-length wire segments

This appendix presents derivations of the expressions used to calculate magnetic fields generated by atom chip wires. Sec. A.1 presents the expression for an infinitesimally thin wire segment of finite length. Sec. A.2 builds on this to arrive at the full expression for the finite-width, finite-length wire segment. The magnetic field models of Ch. 3 build up a total Z-wire magnetic field by summing the contributions of individual straight wire segments according to the expressions derived here.

A.1 Finite length, infinitesimal width

Consider a wire segment of zero width and height, but of finite length $2L$ as shown in, Fig. A.1. The wire segment bears a DC current I in the $+x$ direction. The vector $\mathbf{r}$ connects a given point on the wire segment to the observation point $\mathbf{P}$. According to the Biot-Savart formula (see Eq. 3.10) the magnitude of the differential magnetic field $\mathrm{d}B$ at $\mathbf{P}$ is

$$\mathrm{d}B = \frac{\mu_0 I}{4\pi}\frac{d\ell\, r\sin\phi}{r^3} = \frac{\mu_0 I}{4\pi}\frac{dx\,\cos\alpha}{r^2}, \tag{A.1}$$

evaluating the cross product and using a change of variables. From the diagram, $\alpha = \phi - \pi/2$, $x = r\sin\alpha$ and $\mathrm{d}x = r\cos\alpha \mathrm{d}\alpha$. Also $z = r\,\cos\alpha$ and so $\mathrm{d}x = z\,\mathrm{d}\alpha$. The magnitude of the total field $B = |\mathbf{B}|$ in the yz plane may now be evaluated by integrating $\mathrm{d}B$ with respect to α between α_1 and α_2:

$$\begin{aligned} B &= \int_{\alpha_1}^{\alpha_2} dB \;= \frac{\mu_0 I z}{4\pi r^2}\left(\int_0^{\alpha_2} d\alpha\,\cos\alpha \;+\; \int_{\alpha_1}^{0} d\alpha\,\cos\alpha\right) \\ &= \frac{\mu_0 I z}{4\pi r^2}\big(\sin\alpha_1 - \sin\alpha_2\big). \end{aligned} \tag{A.2}$$

Generalizing to a wire segment parallel to the x axis, but along the line $y = R$ in the xy plane, as shown in Fig. A.2, we can now re-write Eq. A.2 in terms of the perpendicular distance

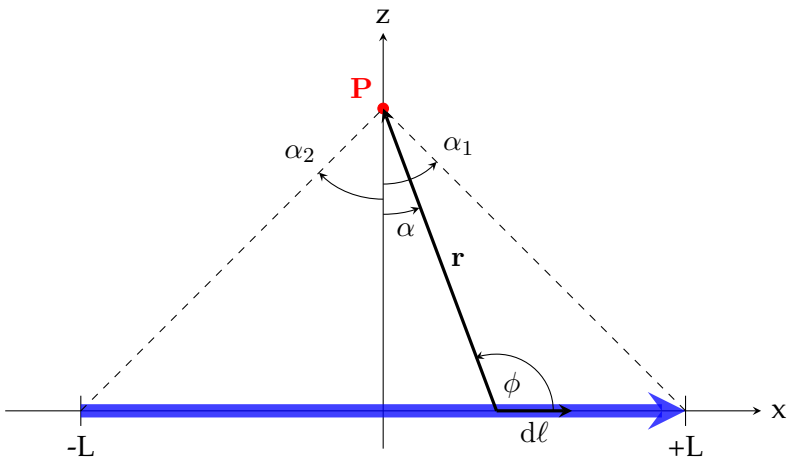

Fig. A.1: Calculation of the magnetic field at point P due to current in wire segment of length $2L$ can be carried out by integrating the Biot-Savart formula over the limits $\alpha \in [\alpha_1, \alpha_2]$.

$d = \sqrt{(y-R)^2 + z^2}$ from the line $y = R$ to the point $\mathbf{P}$:

$$B = \frac{\mu_0 I}{4\pi d}\big(\sin\alpha_2 - \sin\alpha_1\big). \tag{A.3}$$

Using Eq. A.3, and recognizing that

$$\sin\alpha_2 = \frac{x+L}{\sqrt{(x+L)^2+d^2}} \quad \text{and} \quad \sin\alpha_1 = \frac{x-L}{\sqrt{(x-L)^2+d^2}} \tag{A.4}$$

from Fig. A.2, the full expressions for the magnetic field and field amplitude at $\mathbf{P} = (x, y, z)$ may be written as [165]

$$\mathbf{B}(x,y,z) = \frac{\mu_0 I}{4\pi d}\left(\frac{x+L}{\sqrt{d^2+(x+L)^2}} - \frac{x-L}{\sqrt{d^2+(x-L)^2}}\right)\left(-\frac{z}{d}\mathbf{y} + \frac{y-R}{d}\mathbf{z}\right) \tag{A.5}$$

$$B(x,y,z) = \frac{\mu_0 I}{4\pi d}\left(\frac{x+L}{\sqrt{d^2+(x+L)^2}} - \frac{x-L}{\sqrt{d^2+(x-L)^2}}\right). \tag{A.6}$$

A.2 Finite length, finite width

The magnetic field due to a wire segment of finite length and width is obtained by summing the contributions of many parallel, infinitesimally thin wire segments spread across the segment width w, and normalizing the total current to be nominal value I. To build up an expression for the total field of a wire of thickness w, we integrate Eq. A.5 with respect to R from $R_1 = R - w/2$ to $R_2 = R + w/2$, and normalize the integration by the factor $\int_{R1}^{R2} \mathrm{d}R = w$. The x component of

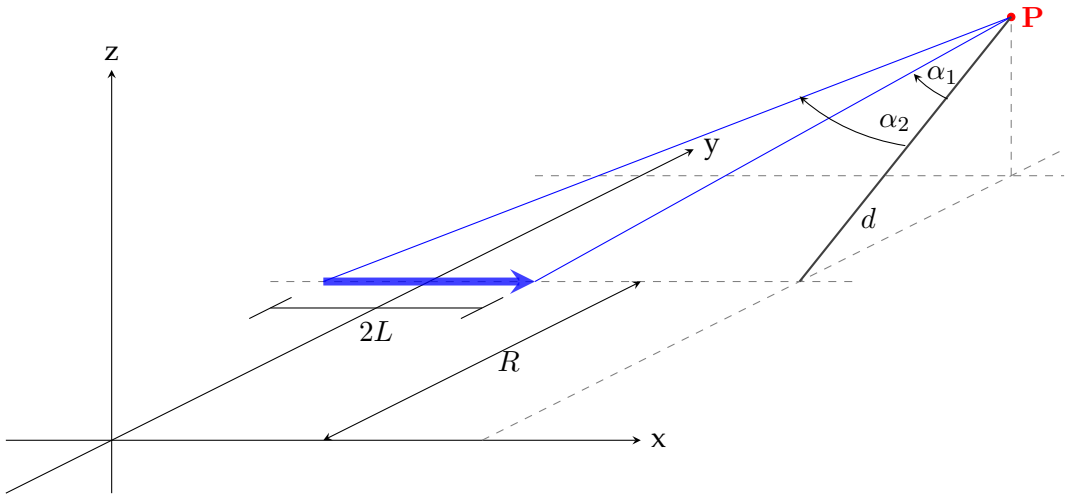

Fig. A.2: Magnetic field at point $\mathbf{P}$ due to current in a wire segment of length $2L$ running parallel to the x axis at $y = R$.

the field $B_x = 0$. The y-component of the field is:

$$\begin{aligned}
B_y &= \frac{1}{w}\int_{R1}^{R2} \mathrm{d}R\,\frac{\mu_0 I}{4\pi}\left(\frac{L+x}{\sqrt{d^2+(x+L)^2}}+\frac{L-x}{\sqrt{d^2+(L-x)^2}}\right)\left(-\frac{z}{(y-R)^2+z^2}\right)\\
&= -\frac{\mu_0 I}{4\pi}\frac{1}{w}\left\{-\tan^{-1}\left(\frac{(L-x)(R-\frac{w}{2}-y)}{z\sqrt{(L-x)^2+(R-y)^2+z^2}}\right)\right.\\
&\quad -\tan^{-1}\left(\frac{(L+x)(R-\frac{w}{2}-y)}{z\sqrt{(L+x)^2+(R-y)^2+z^2}}\right)\\
&\quad +\tan^{-1}\left(\frac{(L-x)(R+\frac{w}{2}-y)}{z\sqrt{(L-x)^2+(R-y)^2+z^2}}\right)\\
&\quad \left.+\tan^{-1}\left(\frac{(L+x)(R+\frac{w}{2}-y)}{z\sqrt{(L+x)^2+(R-y)^2+z^2}}\right)\right\}.
\end{aligned} \tag{A.7}$$

The z-component of the field is:

$$\begin{aligned}
B_z &= \frac{1}{w}\int_{R1}^{R2} \mathrm{d}R\,\frac{\mu_0 I}{4\pi}\left(\frac{L+x}{\sqrt{d^2+(x+L)^2}}+\frac{L-x}{\sqrt{d^2+(L-x)^2}}\right)\left(\frac{y-R}{(y-R)^2+z^2}\right)\\
&= \frac{\mu_0 I}{4\pi}\frac{1}{w}\left\{-\tanh^{-1}\left(\frac{\sqrt{(L-x)^2+(R-\frac{w}{2}-y)^2+z^2}}{L-x}\right)\right.\\
&\quad -\tanh^{-1}\left(\frac{\sqrt{(L+x)^2+(R-\frac{w}{2}-y)^2+z^2}}{L+x}\right)\\
&\quad +\tanh^{-1}\left(\frac{\sqrt{(L-x)^2+(R+\frac{w}{2}-y)^2+z^2}}{L-x}\right)\\
&\quad \left.+\tanh^{-1}\left(\frac{\sqrt{(L+x)^2+(R+\frac{w}{2}-y)^2+z^2}}{L+x}\right)\right\}.
\end{aligned} \tag{A.8}$$

Using these expressions, the total magnetic field and the and field magnitude at point $\mathbf{P} = (x, y, z)$ can be calculated according to

$$\mathbf{B}_{\text{thick-fin.}}(x, y, z) = (0, B_y, B_z), \quad \text{and} \tag{A.9}$$

$$B_{\text{thick-fin.}}(x, y, z) = \sqrt{\mathbf{B}_{\text{thick-fin.}}(x, y, z) \cdot \mathbf{B}_{\text{thick-fin.}}(x, y, z)}. \tag{A.10}$$

These full expressions are quite cumbersome and have been omitted here. Analytic calculations are implemented using Eqs. A.7 and A.8 directly.

A.3 A simplified expression along z

A expression for the magnetic field amplitude as a function of z of an infinitely long wire of width w is given in [14, 166]:

$$B(z) = \frac{\mu_0}{\pi}\frac{I}{w}\cot^{-1}\left(\frac{2z}{w}\right). \tag{A.11}$$

Eq. A.11 corresponds to a special case of the general expressions derived in this appendix. Setting $x = 0$, $y = 0$ and $R = 0$ in Eq. A.7 yields

$$B_y = -\frac{\mu_0 I}{\pi w}\tan^{-1}\left(\frac{Lw/2}{z\sqrt{L^2 + z^2}}\right) \quad \text{and} \quad B_z = 0. \tag{A.12}$$

Taking the limit $L \to \infty$ for an infinitely long wire,

$$B(0, 0, z) = B_y \to \frac{\mu_0}{\pi}\frac{I}{w}\tan^{-1}\left(\frac{w}{2z}\right) = \frac{\mu_0}{\pi}\frac{I}{w}\cot^{-1}\left(\frac{2z}{w}\right), \tag{A.13}$$

in agreement with Eq. A.11. This leads to an w-dependent expression for the trap position z_0, analogous to Eq. 3.15:

$$z_0 = \frac{w}{2}\left[\tan\left(\frac{w\pi B_{\text{bias}}}{\mu_0 I}\right)\right]^{-1}. \tag{A.14}$$

B

Analysis of relative atom number fluctuations

This appendix describes in detail the analysis of relative atom number fluctuations in the RF double well splitting experiments of Ch. 7. The main results are (a) the development of a binomial model of splitting for distinguishable, non-interacting particles, which defines the "shot-noise" level, and (b) an analysis of optical shot noise (OSN) in our imaging, and its role in limiting the sensitivity of atom number counting in these experiments.

B.1 Atom shot noise and binomial splitting statistics

In this section we calculate the relative number fluctuations in an idealized splitting experiment assuming non-interacting classical particles and binomial splitting statistics. In particular, we focus on accounting for shot-to-shot fluctuations in the total atom number N so that fluctuations in N_r can be accurately estimated with respect to shot noise. The results of the calculations presented here are implemented in data analysis described in Sec. 7.2.

We assume a lossless splitting process in which the total atom number N and relative atom number N_r are defined by

$$N \equiv N_R + N_L \tag{B.1}$$

$$N_r \equiv N_R - N_L \tag{B.2}$$

in each repetition. The variance $\mathrm{Var}(N_r)$ over n repetitions of this process is computed directly from the N_r ensemble data, and compared to the variance predicted by binomial statistics. The statistical prediction defines the shot-noise level for ideal, non-interacting particles. The measured fluctuations in N_r are compared to the shot-noise level by introducing a the **normalized variance** $\widetilde{V}$:

$$\widetilde{V} \equiv \frac{\mathrm{Var}(N_r)^{\mathrm{meas'd}}}{\mathrm{Var}(N_r)^{\mathrm{binom}}}. \tag{B.3}$$

Fluctuations exceeding the shot-noise level correspond to $\widetilde{V} > 1$, while those smaller than shot noise correspond to $\widetilde{V} < 1$.

B.1.1 Binomial splitting with fixed N

We first consider N atoms at the input of an idealized atomic "beam-splitter", and assume that each atom is "beam-split" independently of the others. We imagine that each atom exits the beam-splitter in one of two output ports, "left" (L) and "right" (R). After all N atoms have passed through the beam-splitter, the left and right populations are N_L and N_R, respectively.

The beam-splitter is assumed to have the following properties:

- the fixed, a priori probabilities that a single atom exits through the left and right outputs are p_L and p_R, respectively;
- p_L and p_R are independent of N;
- the beam-splitting process is lossless and conserves the total atom number, so that

$$p_L + p_R = 1 \tag{B.4}$$
$$N_L + N_R = N. \tag{B.5}$$

In the language of statistics, the N atoms represent N "independent trials" of the statistical splitting process. The act of sending N atoms through the beam-splitter constitutes a single "experiment". If we define a "success" event as a single atom exiting from output port k ($k = L, R$ for left and right), then the probability that N_k atoms exit from the k output port is given by binomial distribution [156, 159]:

$$P(N_k \text{ successes in } N \text{ trials}) = B_{N,p_k}(N_k) = \binom{N}{N_k} p_k^{N_k}(1-p_k)^{N-N_k}. \tag{B.6}$$

If the splitting experiment is repeated n times, with exactly N atoms in each repetition, we expect a binomial distribution of N_L, N_R and N_r.

The binomial splitting model presented above is a useful starting point, but suffers from three conceptual flaws:

1. In reality, the total atom number N is not constant from experiment to experiment ("shot-to-shot"), but rather fluctuates randomly with a standard deviation of roughly $0.15\overline{N}$ as each cloud is freshly prepared for splitting.
2. The a priori probabilities p_k are not known. We can only approximate p_k with the ensemble mean value $\overline{p}_k = \langle N_k/N \rangle$ computed directly from the raw atom number data. The symbol $\langle X \rangle \equiv \overline{X}$ represents the ensemble mean of the random variable X from n independent experiments.
3. Systematic errors (such an asymmetry in the double well splitting potential) can lead to a correlation between $\overline{p}_k$ and N, counter to the assumption that these two quantities are independent.

In the following subsections we present and compare more realistic statistical models which account for shot-so-shot variation in N. We also consider the a priori probabilities p_k and show that the approximation $\overline{p}_k \approx p_k$ is valid.

The naive model: fixed total atom number The simplest model of splitting assumes that a sample of exactly N atoms is prepared for splitting in each of the n repetitions of the experiment, and is a useful for demonstrating how the shot-noise level is calculated from binomial statistics.

Using Eq. B.6, the mean and variance of N_k ($k = L, R$) are given by [156, 159]:

$$\overline{N}_k \equiv \langle N_k \rangle = N p_k \tag{B.7}$$

$$\mathrm{Var}(N_k) = \sigma^2_{N_k} = N p_k (1 - p_k) \tag{B.8}$$

using the symbols $\overline{X} \equiv \langle X \rangle$, $\mathrm{Var}(X)$ and σ_X to represent the ensemble mean ("expected value"), variance and standard deviation of a random variable X. The variance may be expressed in terms of expected values in the usual way [159]:

$$\mathrm{Var}(X) = \langle X^2 \rangle - \langle X \rangle^2. \tag{B.9}$$

The mean and variance of the relative atom number N_r are

$$\overline{N}_r = \langle N_R - N_L \rangle = \overline{N}_R - \overline{N}_L \tag{B.10}$$

$$\mathrm{Var}(N_r) = \mathrm{Var}(2N_R - N) = 4\mathrm{Var}(N_R) = 4N p_R (1 - p_R) \tag{B.11}$$

using Eq. B.8 and the fact that $\mathrm{Var}(N) = 0$ by assumption. The normalized variance in the naive model is thus defined as

$$\widetilde{V}_{\text{naive}} \equiv \frac{(\sigma^{\text{meas'd}}_{N_r})^2}{4\overline{N}\overline{p}_R(1 - \overline{p}_R)} \tag{B.12}$$

where $(\sigma^{\text{meas'd}}_{N_r})^2 = \mathrm{Var}(N_r)^{\text{meas'd}}$ is the measured variance in N_r, and $\overline{p}_R$ is the ensemble mean "probability". Both quantities are computed directly from experimental data according to

$$\mathrm{Var}(N_r)^{\text{meas'd}} = \frac{1}{n}\sum_{i=1}^{n}(N_r^{(i)} - \overline{N}_r)^2, \text{ where} \tag{B.13}$$

$$\overline{N}_r = \frac{1}{n}\sum_{i=1}^{n}(N_R^{(i)} - N_L^{(i)}) \quad \text{and} \tag{B.14}$$

$$\overline{p}_R \equiv \left\langle \frac{N_R}{N} \right\rangle = \frac{1}{n}\sum_{i=1}^{n}\frac{N_R^{(i)}}{N_R^{(i)} + N_L^{(i)}}. \tag{B.15}$$

The superscripts denote data measured in the i^{th} repetition of the splitting experiment.

B.1.2 Binomial splitting with fluctuating N

Over the course of n repetitions of the splitting experiment, fluctuations in the total atom number N will invariably add noise to the raw N_L, N_R and N_r data. This is apparent in the fact that naive expressions for $\mathrm{Var}(N_k)$ and $\mathrm{Var}(N_r)$ in Eqs. B.8 and B.11 depend explicitly on N. The measured variance in N_r will therefore contain two broad contributions: the first from statistical fluctuations in N_L and N_R, which is the "signal" we wish to measure; the second from random fluctuations in N_r due to a randomly fluctuating total atom number N. This subsection describes a method of accommodating a fluctuating total atom number in binomial models of splitting.

B.1.2.1 Joint probability distribution functions

In the language of repeated trials, we are interested in the mean value and variance of a random variable X (e.g. N_r) over n repetitions of an experiment, given that the number of independent trials N in each experiment is not constant from one experiment to the next. The expected value of X over n experiments is then given by a sum involving the joint probabilities $P(N \cap X)$ – the probability of X successes **and** exactly N independent trials in a given experiment:

$$\overline{X} \equiv \langle X \rangle = \sum_{N=0}^{\infty} \sum_{X=0}^{N} X\, P(N \cap X) = \sum_{N=0}^{\infty} \sum_{X=0}^{N} X\, P(N) P(X|N). \tag{B.16}$$

$P(X|N)$ is the conditional probability – the probability of obtaining X successes in N trials, given that the number of independent identical trials is exactly N.[1] $P(N)$ is the a priori probability that the number of identical trials in a given experiment is exactly N. Note that the sum over N runs over all possible numbers of repeated trials (from 0 to ∞), while the sum over X runs over all possible numbers of successes (from 0 to N), so that

$$\sum_{N=0}^{\infty} P(N) = \sum_{X=0}^{N} P(X|N) = 1 \tag{B.17}$$

The conditional probability distribution function (PDF) is just the binomial distribution function of Eq. B.6, and is well approximated by a normalized Gaussian PDF of the same mean and standard deviation for a fixed value of the probability p when N is large [156, 159]:

$$P(X|N) = B_{N,p}(X) \approx G_{\overline{X},\sigma_X}(X) \tag{B.18}$$

$$\text{with} \quad \overline{X} = pN \quad \text{and} \quad \sigma_X^2 = Np(1-p) \tag{B.19}$$

as in Eqs. B.7 and B.8, and

$$G_{\overline{X},\sigma_X}(X) = \frac{1}{\sigma_X \sqrt{2\pi}} \exp\left[-\frac{(X-\overline{X})^2}{2\sigma_X^2} \right]. \tag{B.20}$$

[1] That $P(A \cap B) = P(A)P(B|A)$ for two dependent events A and B is an expression of the "conditional probability theorem" (cite). It may seem obvious. It is important to remember that $P(B|A)$ is the probability of event B given that event A has occurred or will occur. If B is not conditional on A, then $P(B|A) = P(B)$.

Since we are interested in means and variances of roughly continuous atom number variables, we can approximate the sums as integrals. Eq. B.16 then becomes

$$\overline{X} \approx \int_0^\infty dN \int_0^N dX\, X\, P(N)\, G_{\overline{X},\sigma_X}(X) \tag{B.21}$$

To compute the mean values and variances of a random variable X (e.g. N_r), we require a PDF describing the fluctuating total atom number. In what follows we use a Gaussian distribution of total atom numbers. In other words, we assume that for each experiment consisting of N independent splitting events (i.e. N atoms passing through the beam-splitter and being split independently), N is chosen from a Gaussian probability distribution $P(N) \equiv G_{\overline{X},\sigma_X}(X)$ centred at $N = \overline{N}$, and with standard deviation σ_N.

As an example calculation using joint probabilities, consider the mean and variance of N_k in the presence of a fluctuating total atom number N. The mean is given by

$$\begin{aligned}
\overline{N}_k \equiv \langle N_k \rangle &\approx \frac{1}{2\pi\sigma_{N_k}\sigma_N} \int_0^\infty dN \int_0^N dN_k\, N_k\, e^{-(N-\overline{N})^2/2\sigma_N^2}\, e^{-(N_k-\overline{N}_k)^2/2\sigma_{N_k}^2} \\
&\approx \frac{1}{2\pi\sigma_{N_k}\sigma_N} \int_{-\infty}^\infty dx \int_{-\infty}^\infty du\, (u+\overline{N}_k) e^{-x^2/2\sigma_N^2}\, e^{-u^2/2\sigma_{N_k}^2} \\
&\qquad \text{defining } x \equiv N - \overline{N} \text{ and } u \equiv N_k - \overline{N}_k = N_k - p_k N, \\
&\qquad \text{and assuming that } N \gg N - \overline{N} \text{ and } N \gg N_k - \overline{N}_k \\
&= \frac{1}{2\pi\sigma_{N_k}\sigma_N} \int_{-\infty}^\infty dx \int_{-\infty}^\infty du\, (u + p_k(x+\overline{N})) e^{-x^2/2\sigma_N^2}\, e^{-u^2/2\sigma_{N_k}^2} \\
&= p_k \overline{N}.
\end{aligned} \tag{B.22}$$

B.1.2.2 A priori splitting probabilities p_k

Using the joint-probability approach, we can also address the conceptual difficulty presented by the a priori probabilities p_k. As in Sec. B.1.1, we continue to assume here that the a priori probabilities p_k are constant from experiment to experiment. Since our data consists purely of atom number populations after splitting, we have no way to measure the p_k in a given N-atom splitting experiment. Instead, we approximate p_k as an average quantity over the entire n-experiment data set in our analysis (see Eq. B.15).

It should be emphasized that $\overline{p}_k$ is an approximation to an idealized, fixed a priori probability p_k. The validity of this approximation can be tested by computing the expected value of N_k/N

from n repetitions of the N-atom splitting experiment. Using the approximation of Eq. B.21,

$$\begin{aligned}\overline{p}_k \equiv \left\langle \frac{N_k}{N} \right\rangle &\approx \int_0^\infty dN \int_0^N dN_k \, \frac{N_k}{N} \, P(N) \, G_{\overline{N}_k, \sigma_{N_k}}(N_k) \\ &\approx \int_0^\infty dN \, \frac{P(N)}{N} \int_{-\infty}^\infty dx \, (x + p_k N) G_{0,\sigma_{N_k}}(x) \qquad \text{(B.23)} \\ &\quad \text{defining } x \equiv N_k - \overline{N}_k = N_k - p_k N \\ &\quad \text{and assuming that } N \gg N - \overline{N} \text{ and } N \gg N_k - \overline{N}_k \\ &= p_k \int_0^\infty dN \, P(N) \\ &= p_k \qquad \text{(B.24)}\end{aligned}$$

Thus, the expected value of the ratio N_k/N is just the a priori probability p_k. Despite the fact that we cannot measure p_k directly, Eq. B.23 justifies the approximation $p_k \approx \overline{p_k} = \langle N_k/N \rangle$, which is obtained directly from data.

B.1.3 Three methods of accounting for fluctuations in N

In this subsection we present three data analysis methods, each of which attempts to extract the true statistical N_r variance from the raw N_r data. Each analysis method is presented along with the corresponding shot-noise level predicted by binomial statistics. The performance of each model in the face of large fluctuations in N are compared using simulated data. The three models are referred to as "N-analysis", "p-analysis" and "Heidelberg analysis" in lab slang. **N.B.** The "N" and "p" analysis presented here are corrected updates from the original 2007/2008 implementations, and now properly account for non-zero N fluctuations. All three methods produce nearly identical results for $\overline{p}_R = 1/2$. In real data $\overline{p}_R$ is roughly bounded by 0.47 and 0.53, for which the three methods agree to well within statistical uncertainties. We present "N-analysis" results in Ch. 7 since it is the simplest conceptually, and easily applied to "blanks" analysis.

B.1.3.1 N-analysis

In the "N-analysis" method, the fluctuations in N_r are examined directly. The variance in N_r is computed from the experimental data using Eqs. B.13 and B.14. Following Eq. B.3, a normalized variance in N_r is constructed by comparing the measured variance $\mathrm{Var}(N_r)^{\mathrm{meas'd}}$ to the binomial expectation $\mathrm{Var}(N_r)^{\mathrm{binom}}$. Assuming Gaussian shot-to-shot fluctuations in N with a mean value $\overline{N}$ and variance $\mathrm{Var}(N) = \sigma_N^2 = \overline{N}$, $\mathrm{Var}(N_r)^{\mathrm{binom}}$ can be calculated using the joint probability approach of Sec. B.1.2:

$$\mathrm{Var}(N_r)^{\mathrm{binom}} = 4\overline{N} p_R (1 - p_R) + (2p_R - 1)^2 \sigma_N^2. \qquad \text{(B.25)}$$

Note that the for perfectly balanced splitting (i.e. $\overline{p}_R = 1/2$) all common mode fluctuations in N_R and N_L due to fluctuations in N exactly cancel in the measured relative number N_r, rendering

the measured variance in N_r completely independent of fluctuations in N. In the more realistic case of slightly imbalanced splitting the second term in Eq. B.25 becomes appreciable, scaling as σ_N^2.

The normalized variance in the N-analysis is defined as

$$\widetilde{V}_N \equiv \frac{\mathrm{Var}(N_r)^{\mathrm{meas'd}}}{4\overline{N}\overline{p}_R(1-\overline{p}_R)+(2\overline{p}_R-1)^2\sigma_N^2}. \tag{B.26}$$

Eq. B.26 reduces to the "naive" expression given in Eq. B.12 when N is fixed ($\sigma_N = 0$), which we intuitively expect. **This method is used in the analysis of data presented in this thesis (see Ch. 7).**

B.1.3.2 p-analysis

In the "p-analysis" method, the raw N_L and N_R data are divided by the total atom number N for each repetition of the splitting experiment as a way of eliminating the effects of fluctuations in N. This transforms the raw data from sets of atom numbers into sets of left-hand, right-hand and relative *splitting fractions*

$$f_L \equiv \frac{N_L}{N}, \quad f_R \equiv \frac{N_R}{N} \quad \text{and} \quad f_r \equiv \frac{N_r}{N} \tag{B.27}$$

The variance in f_r is computed from the experimental data using

$$\mathrm{Var}(f_r)^{\mathrm{meas'd}} = \frac{1}{n}\sum_{i=1}^{n}(f_r^{(i)}-\overline{f}_r)^2 \quad \text{and} \tag{B.28}$$

$$\overline{f}_r = \frac{1}{n}\sum_{i=1}^{n}\left(\frac{N_R^{(i)}-N_L^{(i)}}{N_R^{(i)}+N_L^{(i)}}\right) \tag{B.29}$$

where the superscripts denote data measured in the i^{th} repetition of the splitting experiment.

The expected variance in the relative splitting fraction $\mathrm{Var}(f_r)^{\mathrm{binom}}$ can be calculated using the joint probability approach of Sec. B.1.2:

$$\mathrm{Var}(f_r)^{\mathrm{binom}} \simeq \frac{4p_R(1-p_R)}{\overline{N}}\left[1+\left(\frac{\sigma_N}{\overline{N}}\right)^2\right] \tag{B.30}$$

up to second order in $\sigma_N/\overline{N}$. The calculation of Eq. B.30 is valid for fluctuations in N small enough that $N-\overline{N} \ll \overline{N}$. $N-\overline{N}$ has a standard deviation of at most $0.15N$ in our experiment.

The normalized variance in the p-analysis is defined as

$$\widetilde{V}_p \equiv \frac{\overline{N}\,\mathrm{Var}(f_r)^{\mathrm{meas'd}}}{4\overline{p}_R(1-\overline{p}_R)\left[1+\left(\sigma_N/\overline{N}\right)^2\right]}. \tag{B.31}$$

B.1.3.3 Heidelberg analysis

The Heidelberg analysis method [43, and its supplementary material] has similarities to the both N-analysis and the p-analysis. Like the p-analysis, it counteracts fluctuations in N with a shot-by-shot correction to the measured N_r. The correction is a subtraction of a quantity reminiscent of $\overline{N}_r$, unlike in the p-analysis in which the correction is a division by N. The Heidelberg analysis consists of computing the variance-like quantity

$$\Delta M^2 \equiv \frac{1}{n}\sum_{i=1}^{n}\left[\frac{N_R^{(i)} - N_L^{(i)}}{2} - (\overline{p}_R - \tfrac{1}{2})(N_R^{(i)} + N_L^{(i)})\right]^2, \tag{B.32}$$

where $M \equiv N_r/2$; the superscripts denote the i^{th} repetition of the splitting experiment, and $\overline{p}_R$ has the same definition as in Eq. B.15 [43]. We use the symbol ΔM^2 to distinguish the quantity in Eq. B.32 from the conventional variance in M, $\text{Var}(M)$. In particular, we note that $\text{Var}(M) = \text{Var}(N_r)/4 \neq \Delta M^2$. This can be verified by writing out $\text{Var}(M)$ following Eq. B.13:

$$\begin{aligned}
\text{Var}(M)^{\text{meas'd}} &= \frac{1}{n}\sum_{i=1}^{n}\left[\frac{N_r^{(i)}}{2} - \frac{\overline{N}_r}{2}\right]^2 \\
&= \frac{1}{n}\sum_{i=1}^{n}\left[\frac{N_r^{(i)}}{2} - \frac{1}{n}\sum_{j=1}^{n}\frac{f_r^{(j)}N^{(j)}}{2}\right]^2 \\
&= \frac{1}{n}\sum_{i=1}^{n}\left[\frac{N_R^{(i)} - N_L^{(i)}}{2} - \frac{1}{n}\sum_{j=1}^{n}(f_R^{(j)} - \tfrac{1}{2})(N_R^{(j)} + N_L^{(j)})\right]^2 \\
&\neq \Delta M^2.
\end{aligned} \tag{B.33}$$

In the Heidelberg analysis, the total atom number $N_R^{(j)} + N_L^{(j)}$ is not averaged in the sum over j as in the N-analysis, but is left to vary from shot to shot. The sum over j then reduces to the ensemble mean value

$$\frac{1}{n}\sum_{j=1}^{n}(f_R^{(j)} - \tfrac{1}{2}) = \overline{f}_R - \tfrac{1}{2} = \overline{p}_R - \tfrac{1}{2}. \tag{B.34}$$

The subtle difference between the Heidelberg analysis and the N- and p-analyses is revealed by the statistically expected variance. Unlike in the N- and p-analyses, the construction ΔM^2 of Eq. B.32 is completely independent of σ_N! Using the joint probability approach of Sec. B.1.2,

$$\text{Var}(M)^{\text{binom}} = \overline{N}\bar{p}_R(1 - \bar{p}_R) \tag{B.35}$$

for any Gaussian distribution of N with width σ_N. The normalized variance in the Heidelberg

analysis is defined as

$$\widetilde{V}_H \equiv \frac{(\Delta M^2)^{\text{meas'd}}}{\overline{N}\overline{p}_R(1-\overline{p}_R)}. \tag{B.36}$$

B.1.3.4 Model performance comparison using simulated data

Here we compare the performance of the four data analysis models using simulated splitting data. The simulated data consists of pairs of N_L and N_R data chosen pseudo-randomly from a Gaussian distribution function, given an initial choice of the target mean atom number $\overline{N}$ and its standard deviation σ_N, the mean splitting probability $\overline{p}_L$, the target normalized variance $\widetilde{V}^{\text{target}}$ in the relative atom number, and the number of experimental repetitions n. The goal of this exercise is to compare the relative success of each model at reproducing the target value $\widetilde{V}^{\text{target}} = 1$ as a function of the amplitude of total number fluctuations.

Fig. B.1 shows plots of normalized variance as a function of the fractional atom number fluctuation $\sigma_N/\overline{N}$ calculated using the naive, N-, p- and H-analysis methods for two values of the mean splitting probability: $\overline{p}_L = 0.55$ and $\overline{p}_L = 0.52$.

As expected, Fig. B.1 shows that the naive model (see Eq. B.12) greatly overestimates $\widetilde{V}^{\text{target}}$ for all but the very smallest values of $\sigma_N/\overline{N}$. The overestimate is less severe when the splitting is closer to balanced (i.e. $\overline{p}_L$ closer to $\frac{1}{2}$). The N- and H-analyses both reproduce $\widetilde{V}^{\text{target}} = 1$ even for large fractional fluctuations in N. The p-analysis also reproduces $\widetilde{V}^{\text{target}} = 1$ for $\sigma_N/\overline{N} \lesssim 0.2$. The p-analysis is not as robust to fluctuations in N as the N- and H-analyses, however, as evidenced by the overestimate of $\widetilde{V}^{\text{target}}$ for $\sigma_N/\overline{N} \gtrsim 0.25$ when $\overline{p}_L = 0.55$.

The simulated data used here would be considered very unstable compared to our best laboratory data: we routinely generate splitting data with $\sigma_N/\overline{N} \sim 0.15$ and splitting fractions $0.48 \lesssim \overline{p}_L \lesssim 0.52$. This exercise is therefore a very demanding test of the analysis methods. From these tests, we conclude that

- The naive analysis is completely inadequate for $\sigma_N \neq 0$,
- the p-analysis overestimates the true normalized variance in cases of $\sigma_N/\overline{N} \gtrsim 0.25$ and $\overline{p}_L \gtrsim 0.55$, but
- the p-analysis, N-analysis and H-analysis all recover the true normalized variance at experimentally realistic levels of splitting imbalance and total number fluctuation.

B.1.4 Statistical uncertainty in $\widetilde{V}^*$

The standard error in a measured variance V is $V\sqrt{2/(n-1)}$, where n is the number of samples [159]. To calculate the statistical error in the corrected normalized variance in the relative atom number $\widetilde{V}^* = \text{Var}(N_r)^{\text{meas'd}} - \text{Var}(N_r)^{\text{blanks}}$ (see Eq. 7.14), we add the contributions of the raw

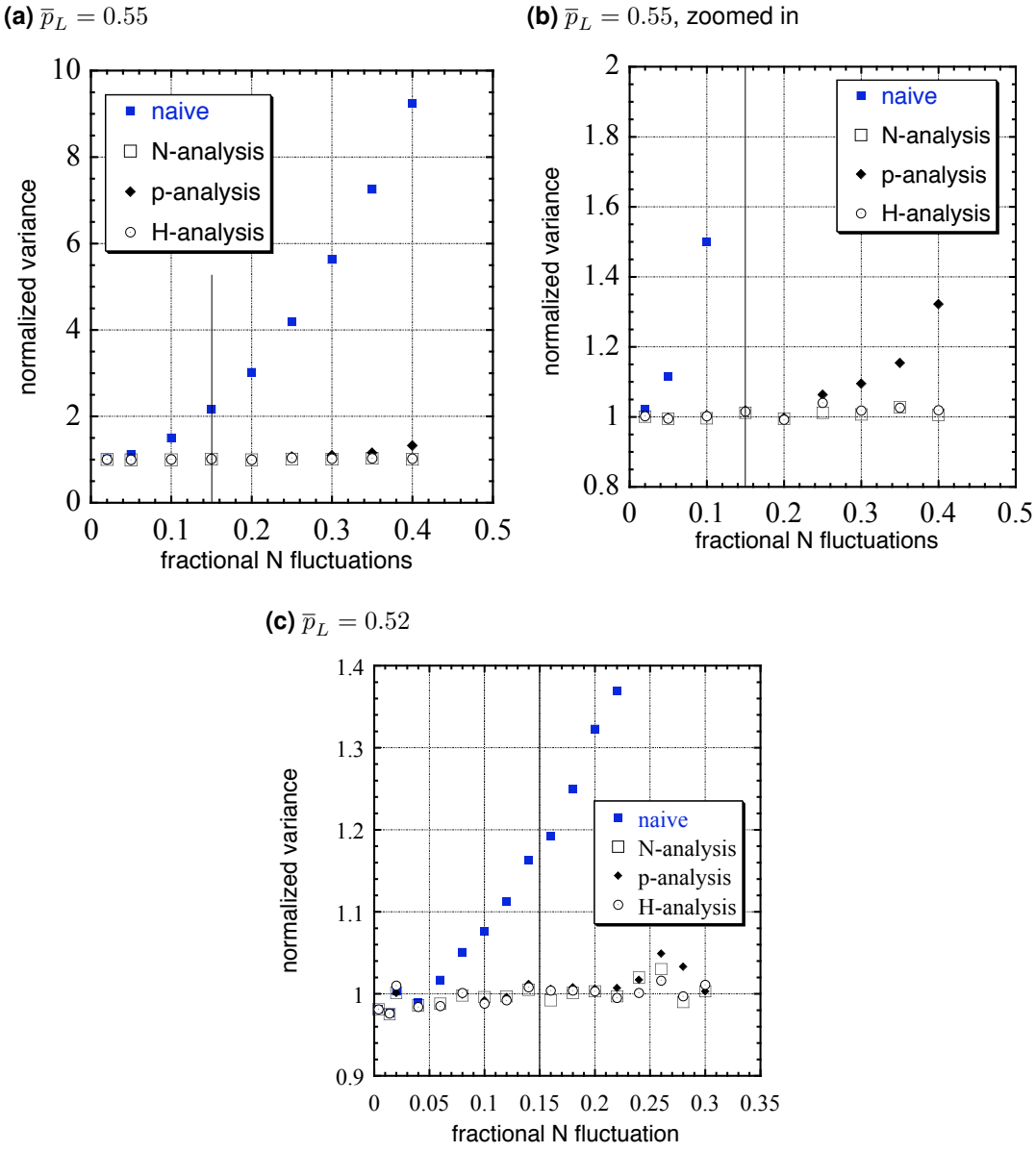

Fig. B.1: A comparison of the normalized variance calculated from the naive, N-analysis, p-analysis and H-analysis methods. The plots demonstrate to what degree each method reproduces the true variance $\widetilde{V}^{\text{target}} = 1$ using simulated splitting data with $\overline{N} = 5000$, $n = 10^4$, and $\overline{p}_L = 0.55$ or 0.52 (see text). The data are normalized variances calculated according to Eqs. B.12, B.26, B.31 and B.36. The horizontal axes are $\sigma_N/\overline{N}$. The black vertical lines indicate the amplitude of typical experimental fluctuations in N of roughly 15% of N, i.e. $\sigma_N/\overline{N} \sim 0.15$.

"measured" variance and "blanks" variance in quadrature

$$\delta\mathrm{Var}(N_r)^* = \sqrt{(\mathrm{Var}(N_r)^{\mathrm{meas'd}})^2\left(\frac{2}{n_a-1}\right) + (\mathrm{Var}(N_r)^{\mathrm{blanks}})^2\left(\frac{2}{n_b-1}\right)} \tag{B.37}$$

where n_a is the number of regular "with-atoms" images, and n_b the number of blanks images used in the analysis. Applying conventional error propagation techniques [156] to the Eq.. B.26 expression for the normalized blanks-corrected variance $\widetilde{V}^*$, the statistical uncertainty in the blanks-corrected normalized variance in the relative atom number $\widetilde{V}^*$ from the "N-analysis" is given by

$$\delta\widetilde{V}^* = \widetilde{V}^*\sqrt{\frac{\alpha}{\beta^2} + \frac{\gamma^2\varepsilon^2 + \delta^2\zeta^2}{(\gamma+\delta)^2}}, \quad \text{where} \tag{B.38}$$

$$\alpha \equiv [\mathrm{Var}(N_r)^{\mathrm{meas'd}}]^2\frac{2}{n_a-1} + [\mathrm{Var}(N_r)^{\mathrm{blanks}}]^2\frac{2}{n_b-1} \tag{B.39}$$

$$\beta \equiv \mathrm{Var}(N_r)^{\mathrm{meas'd}} - \mathrm{Var}(N_r)^{\mathrm{blanks}} \tag{B.40}$$

$$\gamma \equiv 4\overline{N}\overline{p}_R(1-\overline{p}_R) \tag{B.41}$$

$$\delta \equiv (2\overline{p}_R - 1)^2\sigma_N^2 \tag{B.42}$$

$$\varepsilon \equiv \frac{\sigma_N^2}{(n_a-1)\overline{N}^2} + \frac{\sigma_{p_R}^2}{(n_a-1)\overline{p}_R^2} + \frac{\sigma_{p_R}^2}{(n_a-1)(1-\overline{p}_R)^2} \tag{B.43}$$

$$\zeta \equiv \frac{2}{n_a-1} + \frac{16\sigma_{p_R}^2}{(n_a-1)(2\overline{p}_R-1)^2}. \tag{B.44}$$

For $p_R \approx 1/2$ the quick estimate $\widetilde{V}^*\sqrt{2/(n_a-1)}$ only overestimates $\delta\widetilde{V}^*$ by about $\sim 20\%$. Eq. B.38 is used to compute the statistical error bars on all number fluctuation results presented Sec. 7.2.5.

B.2 Quantifying optical shot noise

In this section we calculate and measure the contribution of OSN in our images. After suppressing fringe noise in our optical density (OD) images (see Sec.7.2.4), OSN is the dominant source of technical optical noise in our atom number counting experiments.

Read noise We expect read noise (RN) and CCD dark counts to be almost negligible compared to OSN in absorption imaging. An $I \simeq I_{\mathrm{sat}}/10$ probe intensity registers as roughly 6100 e^- (photoelectrons) per pixel. OSN is therefore on the order of $\sqrt{6100} \approx 78\,\mathrm{e}^-$, versus the 12.2 e^- rms read noise predicted by the CCD camera manufacturer. This RN agrees with our independent estimates of $\sim 13\,\mathrm{e}^-$ from dark image statistics and 12 e^- from analysis of the low-light-intensity pixels in blanks images (see Sec. 7.2.4). Dark counts are negligible – a mean value of less than 1×10^{-5} e^- per pixel in our cooled CCD chip, according to the manufacturer – and in any event are subtracted off each image during the analysis. Adding these three values in quadrature give a total noise 79 e^- per pixel – a 1% increase with respect to OSN alone.

B.2.1 Optical shot noise and optical density

Here we calculate the effect of OSN in the probe beam intensity on the OD and relative atom number fluctuations from blanks images (see Sec. 7.2.4). In CCD detection of probe laser light, an incident number of photons N_{ph} generates a certain number of photoelectrons $\mathcal{N}_{pe} = \eta_{qe} N_{ph}$ in the CCD, where η_{qe} is the camera's quantum efficiency. Since the absorption of a photon and the creation of a photoelectron is a quantized and probabilistic process, we expect Poissonian image-to-image shot noise fluctuations $\sqrt{\mathcal{N}_{pe}}$ in the photoelectron [40].

In absorption imaging a two-dimensional OD profile is computed using the signal (probe beam + atoms), reference (probe beam only) and background (no probe, no atoms) images, as described in Eq. 5.23. To estimate the effects of OSN on a measured atom number, we need to know the total number of photoelectrons detected in the given analysis region ("box") of the CCD image in the 100 µs exposure time for each signal and reference image in the data set. Referring to the total signal and reference photoelectron numbers in a given analysis box as $\mathcal{N}_{\text{sig}}$ and $\mathcal{N}_{\text{ref}}$, we can re-write Eq. 5.23 to express the total analysis box OD as

$$e^{OD} = \frac{\mathcal{N}_{\text{ref}}}{\mathcal{N}_{\text{sig}}}. \tag{B.45}$$

Poissonian OSN is characterized by fluctuations of the measured photoelectron numbers about their mean values $\overline{\mathcal{N}}_{\text{sig}}$ and $\overline{\mathcal{N}}_{\text{ref}}$ over the ensemble data set of n images

$$\delta\mathcal{N}_{\text{sig}} = \sqrt{\overline{\mathcal{N}}_{\text{sig}}} \quad \text{and} \quad \delta\mathcal{N}_{\text{ref}} = \sqrt{\overline{\mathcal{N}}_{\text{ref}}}, \tag{B.46}$$

which lead to fluctuations in the mean value $\overline{e^{OD}}$. Since there are no atoms present in blanks data, $OD \approx 0$ in each pixel. This allows us to make the following approximation:[2]

$$\overline{e^{OD}} \approx e^{\overline{OD}}. \tag{B.47}$$

For photoelectron numbers large enough that $\mathcal{N} \gg \delta\mathcal{N}$, i.e. $\mathcal{N} \gg \sqrt{\mathcal{N}}$, the following approximation is also valid [167]:

$$\overline{\left(\frac{\mathcal{N}_{\text{ref}}}{\mathcal{N}_{\text{sig}}}\right)} \approx \frac{\overline{\mathcal{N}}_{\text{ref}}}{\overline{\mathcal{N}}_{\text{sig}}}. \tag{B.48}$$

For a typical probe intensity $I \approx I_{\text{sat}}/10$, $\mathcal{N}_{pe} \approx 1500$ per pixel (4×10^5 to 6×10^5 per analysis box), which justifies Eq. B.48. Taking Eqs. B.45, B.47 and B.48 together, we can write the following expression relating the mean values of the OD and photoelectron numbers in a given analysis box, computed over the ensemble of images:

$$e^{\overline{OD}} = \frac{\overline{\mathcal{N}}_{\text{ref}}}{\overline{\mathcal{N}}_{\text{sig}}}. \tag{B.49}$$

[2] $\langle e^x \rangle \approx e^{\langle x \rangle}$ for $x \ll 1$.

We can now work out the fluctuation in optical density $\delta\overline{OD}$ due to OSN in the analysis box as follows. From Eq. B.49,

$$\delta(e^{\overline{OD}}) = \delta\left(\frac{\overline{\mathcal{N}}_{\text{ref}}}{\overline{\mathcal{N}}_{\text{sig}}}\right), \quad \text{which implies}$$

$$(\delta\overline{OD})\, e^{\overline{OD}} = \frac{\overline{\mathcal{N}}_{\text{ref}}}{\overline{\mathcal{N}}_{\text{sig}}}\sqrt{\left(\frac{\delta\overline{\mathcal{N}}_{\text{sig}}}{\overline{\mathcal{N}}_{\text{sig}}}\right)^2 + \left(\frac{\delta\overline{\mathcal{N}}_{\text{ref}}}{\overline{\mathcal{N}}_{\text{ref}}}\right)^2} = e^{\overline{OD}}\sqrt{\frac{1}{\overline{\mathcal{N}}_{\text{sig}}} + \frac{1}{\overline{\mathcal{N}}_{\text{ref}}}} \tag{B.50}$$

using Eqs. B.45 and B.46, and the fact that fluctuations in $\mathcal{N}_{\text{sig}}$ and $\mathcal{N}_{\text{ref}}$ are independent (since the signal and reference images are collected separately). Dividing Eq. B.50 by $e^{\overline{OD}}$ and using Eq. B.45, we arrive at the expression for $\delta\overline{OD}$ [158]:

$$\delta\overline{OD} = \sqrt{\frac{\overline{\mathcal{N}}_{\text{sig}} + \overline{\mathcal{N}}_{\text{ref}}}{\overline{\mathcal{N}}_{\text{sig}}\overline{\mathcal{N}}_{\text{ref}}}} = \sqrt{\frac{1 + e^{\overline{OD}}}{\overline{\mathcal{N}}_{\text{ref}}}}. \tag{B.51}$$

The corresponding expression for the fluctuation in the atom number over many repeated images due to OSN is obtained by multiplying Eq.B.51 by the area of the analysis box

$$A_{\text{box}} \equiv n_{\text{pix}} A_{\text{pix}}, \tag{B.52}$$

where n_{pix} is the number of image pixels in the analysis box (typically 300 to 400) and A_{pix} is the area of one image pixel, and dividing by the absorption cross-section $\tilde{\sigma}_\lambda(\delta)$, according to [158]:

$$(\delta N)_{OSN} = \frac{A_{\text{box}}}{\tilde{\sigma}_\lambda(\delta)}\sqrt{\frac{1 + e^{\overline{OD}}}{\overline{\mathcal{N}}_{\text{ref}}}}. \tag{B.53}$$

Equation B.53 can be further simplified using the fact that and $OD \approx 0$ for each image pixel in blanks analysis, and $e^{\overline{OD}} \approx 1 + \overline{OD}$:

$$(\delta N)_{OSN} \approx \frac{A_{\text{box}}}{\tilde{\sigma}_\lambda(\delta)}\sqrt{\frac{2}{\overline{\mathcal{N}}_{\text{ref}}}} \tag{B.54}$$

Assuming that shot noise fluctuations in photoelectron number are completely uncorrelated from one CCD pixel to another, the apparent, spurious N_R and N_L values obtained in blanks images should be completely independent. Their OSN contributions can therefore be added in quadrature:

$$(\delta N_r)^2_{\text{OSN}} = (\delta N_R)^2_{\text{OSN}} + (\delta N_L)^2_{\text{OSN}}. \tag{B.55}$$

We use Eqs. B.54 and B.55 to compute the contribution of OSN to the spurious variance in the relative atom number, and compare it to the total OD systematic noise measured from blanks images (see Sec. 7.2.4. Eq. B.54 is exact only for $OD = 0$, but is an excellent approximation since $OD \approx 0$ across the entire blanks image. Analysis of typical blanks data shows that Eq. B.54

underestimates $(\delta N_r)^2_{OSN}$ by less than 1% compared to the results of Eq. B.53 and

$$(\delta N)_{\text{OSN}} = \sqrt{\sum_i \left(\frac{A_{\text{pix}}}{\tilde{\sigma}_\lambda(\delta)}\delta\overline{OD}^{(i)}\right)^2} = \frac{A_{pix}}{\tilde{\sigma}_\lambda(\delta)}\sqrt{\sum_i \frac{1+e^{\overline{OD}^{(i)}}}{\overline{\mathcal{N}}^{(i)}_{\text{ref}}}} \tag{B.56}$$

which is the result of applying Eq. B.53 pixel-by-pixel, where i denotes the i^{th} pixel in the analysis box.

B.2.2 Optical shot noise analysis of real blanks data

Including read noise in blanks analysis We measure the fluctuations in OD using blanks data and compare the results to the OSN prediction. The spatial non-uniformity of the probe leads to CCD intensities between roughly 0 to 2500 ADC per pixel across each signal and reference blanks image. Thus read noise (RN) can become comparable or even exceed OSN at in the low-intensity regions of the blanks image. Our typical analysis boxes are near the centre of each OD image (see Fig. 7.4a) where the probe intensity is large enough RN is negligible compared to OSN. In the present more careful analysis of the entire blanks image, however, we explicitly account for RN.

Since RN and OSN are independent effects, we add their variances in quadrature to obtain the total OD variance in blanks images

$$\text{Var}(OD)^{\text{blanks}} = \text{Var}(OD)_{\text{OSN}} + \text{Var}(OD)_{\text{RN}}. \tag{B.57}$$

An expression for $\text{Var}(OD)_{\text{RN}}$ can be worked out following the procedure for OSN in Eq. B.50:

$$(\delta\overline{OD})_{\text{RN}} = \sqrt{\left(\frac{\delta\overline{\mathcal{N}}_{\text{sig}}}{\overline{\mathcal{N}}_{\text{sig}}}\right)^2 + \left(\frac{\delta\overline{\mathcal{N}}_{\text{ref}}}{\overline{\mathcal{N}}_{\text{ref}}}\right)^2} \tag{B.58}$$

where the $\overline{\mathcal{N}}$ and $\delta\overline{\mathcal{N}}$ are the mean and rms fluctuations of photoelectron numbers over the blanks data set due to RN alone in the signal and reference images. Assuming that the mean and rms fluctuations are roughly equal in the signal and reference images, we can write

$$\text{Var}(OD)_{\text{RN}} \equiv (\delta\overline{OD})^2_{\text{RN}} = \frac{2\,\sigma^2_{\text{RN}}}{\overline{\mathcal{N}}^2_{\text{ref}}} \tag{B.59}$$

using the notation $\sigma_{\text{RN}} \equiv \delta\overline{\mathcal{N}}_{\text{ref}} \approx \overline{\mathcal{N}}_{\text{sig}}$ to denote the rms fluctuation in photoelectrons due to RN. From Eq. B.57 and Eq. B.51 we can thus write to total expression for the blanks variance in OD due to OSN and RN

$$\text{Var}(OD)^{\text{blanks}} = \frac{2}{\overline{\mathcal{N}}_{\text{ref}}} + \frac{2\,\sigma^2_{\text{RN}}}{\overline{\mathcal{N}}^2_{\text{ref}}}. \tag{B.60}$$

Eq. B.60 is compared with OD variances computed from blanks data in Fig. B.2.

B.2.2.1 OSN and analysis box size

Following-up on Sec. 7.2.4 we explore the role of analysis box size on the measured blanks OD variance. Working with an ensemble of blanks images, each full image area is divided into square analysis boxes of area $A_{\text{box}} \equiv a_{\text{box}}^2$. (We typically use $a_{\text{box}} \sim 20$.) For each analysis box size we calculate the ensemble variance of the OD in each box $\text{Var}(OD)$, as well as the mean raw CCD values $\overline{N}_{\text{ADC}}$ in the reference image, calculated over all blanks images in the data set. "ADC" stands for analog-to-digital counts; the ADC value is related to the number of photoelectrons by the conversion factor α, $N_{\text{ADC}} = \alpha\mathcal{N}$, which is determined by the camera electronics. The resulting per-box $\overline{N}_{\text{ADC}}$ values from the binned images span the full range of intensities contained in the roughly-Gaussian probe envelope – anywhere from roughly 10 to 10000 ADC counts depending on the box size used.

Fig. B.2 shows a scatter plot of $\text{Var}(OD)$ vs. $1/\overline{N}_{\text{ADC}}$ (OD noise vs. inverse probe intensity). Analyses of the single blanks data set using box sizes $a_{\text{box}} = 1$ to 22 are shown on the same axes for comparison, along with best fit curves of representing Eq. B.60. Each data point represents a single analysis box averaged over the blanks data set. Thus there are more single-pixel data points (red) than $a_{\text{box}} = 22$ data points (pink).

Fig. B.2 shows that for a given box size, $\text{Var}(OD)$ due to OSN is smaller for higher probe intensities (smaller $1/N_{\text{ADC}}$) and larger at lower probe intensities (larger $1/N_{\text{ADC}}$. This behaviour agrees with Eq. B.51, and with the qualitative expectation that OSN is a smaller effect (fractionally) at high optical intensities that at low optical intensities. At the smallest box size (single-pixel boxes, red) the blanks data is shot-noise limited; the red points lie along the dashed black line, which is a fit of Eq. B.60.

Fits A fit to this data of the form $y = ax^2 + bx$ with a and b as free parameters gives the ADC-to-e$^-$ conversion factor $\alpha = 3.8$ e$^-$/ADC and an rms RN $\sigma_{\text{RN}} = 12.3$, in good agreement with the manufacturer's specifications of 4.04 e^-/ADC and 12.22 e$^-$. We estimate uncertainties of roughly 5% and 25%, respectively, due to the huge single-pixel OD fluctuations at the smallest probe intensities, which have been manually truncated from this data. The larger-box data lies increasingly above the dashed OSN+RN line with increasing box size (and thus increasing probe intensity $\propto \overline{N}_{\text{ADC}}$ per box). This behaviour agrees with the qualitative expectation that OSN-limited imaging more difficult to achieve at higher probe intensities (lower $1/\overline{N}_{\text{ADC}}$ in this case).

The solid black line that overlaps and obscures the dashed line at large $1/N_{\text{ADC}}$ is the dashed curve forced to a constant $\text{Var}(OD)$ as $N_{\text{ADC}} \to \infty$. In the ideal case, we expect $\text{Var}(OD) \to 0$ as the probe intensity is increased. In real blanks data, shot-to-shot technical fluctuations in the relative signal and reference image probe intensities – even without OSN – contribute a finite $\text{Var}(OD)$. We estimate this effect in our blanks data using a single 500×70 mega-box which captures highest probe intensities in the image. The single data point from this analysis gives $1/\overline{N}_{\text{ADC}} = 2.6 \times 10^{-8}$ and $\text{Var}(OD) = 6.24 \times 10^{-7}$ (orange dot). The solid black line is the OSN+RN fit added to this measured offset. This curve lies much nearer to the high-intensity (large box) data than the pure OSN+RN fit, suggesting that technical probe intensity fluctuations

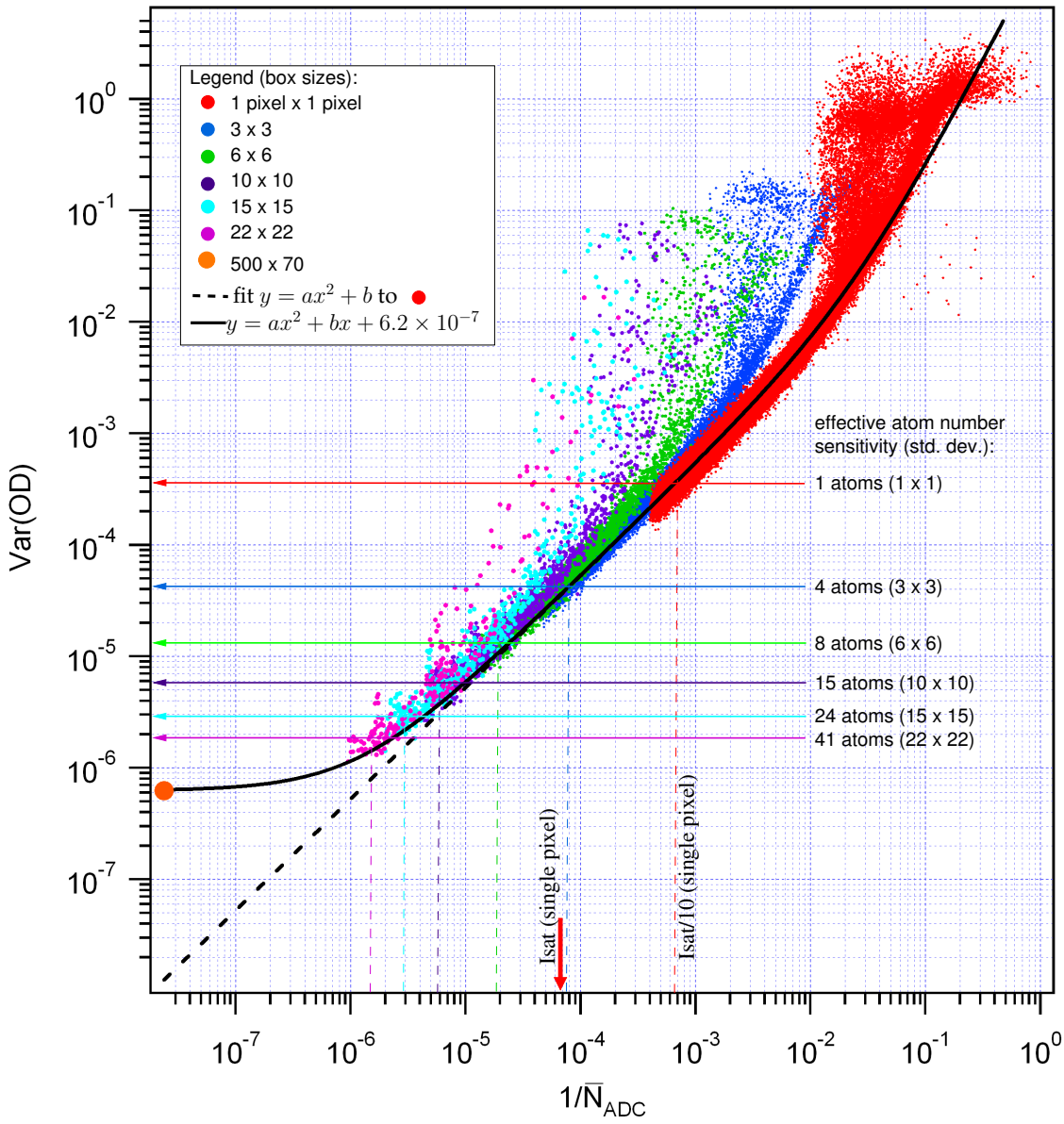

Fig. B.2: Variance in OD versus inverse probe beam intensity (in raw ADC units) calculated over a set of 100 blanks images. Each colour represents analysis of the same blanks data using a different analysis box size (in pixels); each data point corresponds to $\mathrm{Var}(OD)$ and $1/\overline{N}_{\mathrm{ADC}}$ for one box. The black dashed and overlapping solid lines are based on fits to the "optical-shot-noise-plus-read-noise" expression of Eq. B.57. OD noise is closer to the OSN+RN limit for smaller boxes. Smaller boxes also lead to greater atom number detection sensitivity (smaller detectable "effective" atom numbers). Atom numbers are calculated using the $C^2 = 1.7 \pm 0.3$ imaging calibration factor (see text).

are an important effect at large box sizes. Note that we see the effect of probe intensity fluctuations despite subtracting a background OD from each OD image before number counting, as described in Sec. 7.2.2.

Atom number sensitivity The blanks analysis of Fig. B.2 can also be used to estimate the limits on atom number detection imposed by OSN and other technical optical noise. The basic idea is to convert the observed fluctuation in OD into an effective atom number fluctuation for a given box size.

The atom number in a given box measured by absorption imaging is

$$N = A_{\text{box}} OD/\tilde{\sigma}_\lambda(\delta) = A_{\text{pix}} a_{\text{box}}^2 OD/\tilde{\sigma}_\lambda(\delta) \tag{B.61}$$

where $\tilde{\sigma}_\lambda(\delta)$ is the calibrated absorption cross-section [158, 56]. OD noise characterized by $\text{Var}(OD)$ therefore translates into an effective atom number standard deviation of

$$\sigma_{\text{Neff}} \equiv \frac{A_{\text{pix}} a_{\text{box}}^2 \sqrt{\text{Var}(OD)}}{\tilde{\sigma}_\lambda(\delta)} \simeq 1.7 \times 36.36 \times a_{\text{box}}^2 \sqrt{\text{Var}(OD)} \tag{B.62}$$

for resonant imaging ($\delta = 0$) and a $C^2 = 1.7$ calibration factor (see Sec. 5.4.3.1). To estimate $\text{Var}(OD)$ for a given box size from the blanks data, we first calculate $1/N_{\text{ADC}}$ per box by multiplying 1520 ADC per pixel at $I = I_{\text{sat}}/10$ by the number of pixels in the box a_{box}^2. The $1/N_{\text{ADC}}$ per box values are indicated by vertical dashed lines in Fig. B.2. The corresponding $\text{Var}(OD)$ values for each box size are indicated by solid horizontal lines, marked at the positions where the vertical lines cross the centre of the data. The effective atom number fluctuations are indicated to the right of each horizontal line. By this method we estimate our single-pixel sensitivity to be roughly 2 atoms, and our single- 22×22-pixel-box sensitivity to be roughly 41 atoms, each with statistical uncertainties of 2%. The relative atom number sensitivity for a 22×22 box would thus be around $\sqrt{41^2 + 41^2} \simeq 58$. This estimate roughly agrees with the typical blanks variances measured with conventional two-box blanks analysis (see Sec. 7.2.4): $\text{Var}(N_r)^{\text{blanks}} = 60$ in Fig. 7.6a and $\text{Var}(N_r)^{\text{blanks}} = 53$ in Tab. 7.1. More broadly, this result shows that the lower bound on detectable atom number imposed by OSN decrease with decreasing box size. We could increase our detection sensitivity by imaging at smaller times-of-flight or working with colder and/or denser clouds, both of which would reduce the cloud size in the image, permitting smaller analysis boxes for a fixed total atom number and probe intensity.

References

[1] H. M. van Driel and A. D. May, *Boris P. Stoicheff: A tribute on the occasion of his 75th birthday*, Can. J. Phys. **78**, xiii (2000). 1

[2] J. J. Garcia-Rippol, M. A. Martin-Delgado, and J. I. Cirac, *Implementation of Spin Hamiltonians in Optical Lattices*, Phys. Rev. Lett. **93**, 250405 (2004). 1

[3] L. Amico, R. Fazio, A. Osterloh, and V. Vedral, *Entanglement in many-body systems*, Rev. Mod. Phys. **80**, 517 (2008). 1

[4] M. W. Zwierlein, J. R. Abo-Shaeer, A. Schirotzek, C. H. Schunck, and W. Ketterle, *Vortices and superfluidity in a strongly interacting Fermi gas*, Nature **435** (2005). 1

[5] A. L. Fetter and A. A. Svidzinsky, *Vortices in a trapped dilute Bose-Einstein condensate*, J. Phys.: Condens. Matter **13**, R135 (2001). 1

[6] M. A. Kasevich, *Coherence with atoms*, Science **298**, 1363 (2002). 1, 3, 132

[7] M. H. Anderson, J. R. Ensher, M. R. Matthews, C. E. Wieman, and E. A. Cornell, *Observation of Bose-Einstein condensation in a dilute atomic vapor*, Science **269**, 198 (1995). 1

[8] K. B. Davis, M.-O. Mewes, M. R. Andrews, N. van Druten, D. S. Durfee, D. Kurn, and W. Ketterle, *Bose-Einstein Condensation in a Gas of Sodium Atoms*, Phys. Rev. Lett. **75**, 3969 (1995). 1

[9] C. C. Bradley, C. A. Sackett, J. J. Tollet, and R. G. Hulet, *Evidence of Bose-Einstein Condensation in an Atomic Gas with Attractive Interactions*, Phys. Rev. Lett. **75**, 1687 (1995). 1

[10] M. R. Andrews, C. G. Townsend, H.-J. Miesner, D. S. Durfee, D. M. Kurn, and W. Ketterle, *Observation of interference between two Bose condensates*, Science **275**, 637 (1997). 1, 3, 103, 132

[11] B. DeMarco and D. S. Jin, *Onset of Fermi degeneracy in a trapped atomic gas*, Science **285**, 1703 (1999). 2, 78

[12] N. W. Ashcroft and N. W. Mermin, *Solid State Physics*, Thomson Learning Inc., USA (1976). 2

[13] R. K. Pathria, *Statistical Mechanics*, Butterworth Heineman, Woburn, MA, 2nd edn. (1996). 2, 7, 13, 14, 15, 16

[14] J. Reichel, *Microchip traps and Bose-Einstein condensation*, Appl. Phys. B **75**, 469 (2002). 2, 26, 30, 35, 158

[15] J. Fortágh and C. Zimmermann, *Magnetic microtraps for ultracold atoms*, Rev. Mod. Phys. **79**, 235 (2007). 2, 26, 112, 113

[16] H. Ott, J. Fortágh, G. Schlotterbeck, A. Grossmann, and C. Zimmermann, *Bose-Einstein condensation in a surface microtrap*, Phys. Rev. Lett. **87**, 230401 (2001). 2, 24, 26, 85

[17] W. Hänsel, P. Hommelhoff, T. W. Hänsch, and J. Reichel, *Bose-Einstein condensation on a microelectronic chip*, Nature **413**, 498 (2001). 2, 24, 26, 85

[18] A. G. Truscott, K. E. Strecker, W. I. McAlexander, G. B. Partridge, and R. G. Hulet, *Observation of Fermi pressure in a gas of trapped atoms*, Science **291**, 2570 (2001). 2

[19] F. Schreck, L. Khaykovich, K. L. Corwin, G. Ferrari, T. Bourdel, J. Cubizolles, and C. Salomon, *Quasipure Bose-Einstein Condensate Immersed in a Fermi Sea*, Phys. Rev. Lett. **87**, 080403 (2001). 2, 78

[20] S. R. Granade, M. E. Gehm, K. M. O'Hara, and J. E. Thomas, *All-Optical Production of a Degenerate Fermi Gas*, Phys. Rev. Lett. **88**, 120405 (2002). 2

[21] Z. Hadzibabic, C. A. Stan, K. Dieckmann, S. Gupta, M. W. Zwierlein, A. Görlitz, and W. Ketterle, *Two-Species Mixture of Quantum Degenerate Bose and Fermi Gases*, Phys. Rev. Lett. **88**, 160401 (2002). 2

[22] G. Roati, F. Riboli, G. Modugno, and M. Inguscio, *Fermi-Bose Quantum Degenerate ^{40}K-^{87}Rb Mixture with Attractive Interaction*, Phys. Rev. Lett. **89**, 150403 (2002). 2, 78, 86, 87, 98, 153

[23] M. Bartenstein, A. Altmeyer, S. Riedl, S. Jochim, C. Chin, J. H. Denschlag, and R. Grimm, *Crossover from a Molecular Bose-Einstein Condensate to a Degenerate Fermi Gas*, Phys. Rev. Lett. **92**, 120401 (2004). 2

[24] M. Köhl, H. Moritz, T. Stöferle, K. Günter, and T. Esslinger, *Fermionic Atoms in a Three Dimensional Optical Lattice: Observing Fermi Surfaces, Dynamics, and Interactions*, Phys. Rev. Lett. **94**, 080403 (2005). 2, 78

[25] C. Silber, G. Günther, C. Marzok, B. Deh, P. W. Courteille, and C. Zimmermann, *Quantum-degenerate mixture of fermionic lithium and bosonic rubidium gases*, Phys. Rev. Lett. **95**, 170408 (2005). 2, 78, 99

[26] C. Ospelkaus, S. Ospelkaus, K. Sengstock, and K. Bongs, *Interaction-driven dynamics of ^{40}K / ^{87}Rb Fermi-Bose gas Mixtures in the Large-Particle-Number limit*, Phys. Rev. Lett. **96**, 020401 (2006). 2, 78, 86, 87, 98, 153

[27] S. Aubin, S. Myrskog, M. H. T. Extavour, L. J. LeBlanc, D. McKay, A. Stummer, and J. H. Thywissen, *Rapid sympathetic cooling to Fermi degeneracy on a chip*, Nature Physics **2**, 384 (2006). 2, 4, 69, 78, 86, 87, 98, 99, 152, 153

[28] J. D. Weinstein and K. G. Libbrecht, *Microscopic magnetic traps for neutral atoms*, Phys. Rev. A **52**, 4004 (1995). 2, 26, 74, 85

[29] T. Schumm, S. Hofferberth, L. M. Wildermuth, S. Groth, I. Bar-Joseph, J. Schmiedmayer, and P. Krüger, *Matter-wave interferometry in a double well on an atom chip*, Nature Physics **1**, 57 (2005). 2, 3, 103, 109, 133, 154

[30] S. Hofferberth, I. Lesanovsky, B. Fischer, J. Verdu, J. Schmiedmayer, and P. Krüger, *Radio-frequency dressed state potentials for neutral atoms*, Nature Physics **2**, 710 (2006). 2, 103, 113, 154

[31] G. B. Jo, S. Will, T. A. Pasquini, M. Saba, W. Ketterle, and D. E. Pritchard, *Long Phase Coherence Time and Number Squeezing of Two Bose-Einstein Condensates on an Atom Chip*, Phys. Rev. Lett. **98**, 030407 (2007). 2, 3, 63, 103, 112, 132, 137, 138, 139, 149, 150, 151, 153, 154

[32] J. J. P. van Es, S. Whitlock, T. Fernholz, A. H. van Amerongen, and N. J. van Druten, *Longitudinal character of atom-chip-based rf-dressed potentials*, Phys. Rev. A **77**, 063623 (2008). 2, 103

[33] M. H. T. Extavour, L. J. LeBlanc, J. McKeever, A. B. Bardon, S. Aubin, S. Myrskog, T. Schumm, and J. H. Thywissen, *Fermions on atom chips*, In V. Vuletic and J. Reichel (eds.), *Atom Chips*, Wiley-VCH (In press, 2009). 2, 4, 78, 102, 123, 152

[34] Y. J. Wang, D. Z. Anderson, V. M. Bright, E. A. Cornell, Q. Diot, T. Kishimoto, M. Prentiss, R. A. Saravanan, R. Segal, and S. Wu, *Atom Michelson interferometer on a chip using a Bose-Einstein condensate*, Phys. Rev. Lett. **94**, 090405 (2005). 2

[35] Y. Colombe, T. Steinmetz, G. Dubois, F. Linke, D. Hunger, and J. Reichel, *Strong atom-field coupling for Bose-Einstein condensates in an optical cavity on a chip*, Nature **450**, 272 (2007). 2

[36] A. J. Leggett and F. Sols, *On the Concept of Spontaneously Broken Gauge Symmetry in Condensed Matter Physics*, Found. of Phys. **21**, 353 (1990). 3, 20, 21, 132, 133, 150

[37] Y. Castin and J. Dalibard, *Relative phase of two Bose-Einstein condensates*, Phys. Rev. A **55**, 4330 (1997). 3, 17, 20, 21, 112, 132

[38] J. Javanainen and S. M. Yoo, *Quantum Phase of a Bose-Einstein Condensate with an Arbitrary Number of Atoms*, Phys. Rev. Lett. **76**, 161 (1996). 3, 17, 20

[39] W. Li, A. Tuchman, H.-C. Chien, and M. A. Kasevich, *Extended Coherence time with Atom-Number Squeezed States*, Phys. Rev. Lett. **98**, 040402 (2007). 3, 132

[40] R. Loudon, *The Quantum Theory of Light*, Oxford University Press, 3nd edn. (2000). 3, 143, 170

[41] S. Raghavan, A. Smerzi, S. Fantoni, and S. R. Shenoy, *Coherent oscillations between two weakly-coupled Bose-Einstein condensates: Josephson effects, π oscillations, and macroscopic quantum self-trapping*, Phys. Rev. A **59**, 620 (1999). 3, 6

[42] R. Gati and M. K. Oberthaler, *A bosonic Josephson junction*, J. Phys. B: At. Mol. Opt. Phys. **40**, R61 (2007). 3, 6, 17, 18, 19, 20, 21, 22, 137, 138

[43] J. Estève, C. Gross, A. Weller, S. Giovanazzi, and M. K. Oberthaler, *Squeezing and entanglement in a Bose-Einstein condensate*, Nature **455**, 1216 (2008). 3, 19, 132, 142, 148, 149, 150, 151, 153, 154, 166

[44] S. Aubin, M. H. T. Extavour, S. Myrskog, L. J. LeBlanc, J. Estève, S. Singh, P. Scrutton, D. McKay, R. McKenzie, I. D. Leroux, A. Stummer, and J. H. Thywissen, *Trapping fermionic ^{40}K and bosonic ^{87}Rb in a chip trap*, J. Low Temp. Phys. **140**, 377 (2005). 4, 79

[45] M. H. T. Extavour, L. J. LeBlanc, T. Schumm, B. Cieslak, S. Myrskog, A. Stummer, S. Aubin, and J. H. Thywissen, *Dual-species quantum degeneracy of ^{40}K and ^{87}Rb on an atom chip*, In C. Roos, H. Häffner, and R. Blatt (eds.), *Atomic Physics, Proceedings of the 20th International Conference on Atomic Physics*, vol. 20, 241 – 249, American Institute of Physics (2006). 4, 78, 79, 86, 102, 123, 126, 152

[46] C. J. Pethick and H. Smith, *Bose-Einstein Condensation in Dilute Gases*, Cambridge University Press, Cambridge, UK (2002). 6, 8, 9, 10, 20, 134

[47] F. Dalfovo, S. Giorgini, L. P. Pitaevskii, and S. Stringari, *Theory of Bose-Einstein condensation in trapped gases*, Rev. Mod. Phys. **71**, 463 (1999). 6, 8, 9, 10, 11, 12, 20

[48] A. J. Leggett, *Bose-Einstein condensation in the alkali gases: Some fundamental concepts*, Rev. Mod. Phys. **73**, 307 (1990). 6, 10, 19, 20, 21, 22, 133

[49] A. Griffin, D. W. Snoke, and S. Stringari, *Bose-Einstein Condensation*, Cambridge University Press, Cambridge, UK (1996). 6

[50] W. Ketterle and M. Zwierlein, *Making, probing and understanding ultracold Fermi gases*, In M. Inguscio, W. Ketterle, and C. Salomon (eds.), *Ultra-cold Fermi Gases*, Proceedings of the International School of Physics "Enrico Fermi", IOS Press, Amsterdam, Oxford, Washington DC (2008). 6, 87, 99, 152

[51] Y. Castin, *Basic theory tools for degenerate Fermi gases*, In M. Inguscio, W. Ketterle, and C. Salomon (eds.), *Ultra-cold Fermi Gases, Proceedings of the International School of Physics Enrico Fermi*, vol. 164, 289 – 349, IOS Press (2008). 6, 12, 15

[52] S. Giorgini, L. P. Pitaevskii, and S. Stringari, *Condensate fraction and critical temperature of a trapped interacting Bose gas*, Phys. Rev. A **54**, R4633 (1999). 9

[53] F. Gerbier, J. H. Thywissen, S. Richaud, M. Hugbert, P. Bouyer, and A. Aspect, *Critical Temperature of a Trapped, Weakly Interacting Bose Gas*, Phys. Rev. Lett. **92**, 030405 (2004). 9, 93

[54] J. Dalibard, *Collisional dynamics of ultra-cold atomic gases*, In C. E. W. M. Inguscio, S. Stringari (ed.), *Bose-Einstein Condensation in Atomic Gases*, Proceedings of the International School of

Physics "Enrico Fermi", 321–349, IOS Press, Amsterdam, Oxford, Washington DC (1999). 9

[55] E. G. M. van Kempen, S. J. J. M. F. Kokkelmans, D. J. Heinzen, and B. J. Verhaar, *Interisotope Determination of Ultracold Rubidium Interactions from Three High-Precision Experiments*, Phys. Rev. Lett. **88**, 093201 (2002). 10, 98

[56] W. Ketterle, D. S. Durfee, and D. M. Stamper-Kurn, *Making, probing and understanding Bose-Einstein condensates*, In M. Inguscio, S. Stringari, and C. E. Wieman (eds.), *Bose-Einstein Condensation in Atomic Gases*, Proceedings of the International School of Physics "Enrico Fermi", 67–176, IOS Press, Amsterdam, Oxford, Washington DC (1999). 11, 12, 30, 87, 89, 92, 140, 175

[57] G. M. Bruun and C. W. Clark, *Ideal gases in time-dependent traps*, Phys. Rev. A **61**, 061601 (2000). 12, 16

[58] S. Bagnato, D. E. Pritchard, and D. Kleppner, *Bose-Einstein condensation in an external potential*, Phys. Rev. A **35**, 4354 (1987). 13, 84

[59] D. A. Butts and D. S. Rokhsar, *Trapped Fermi gases*, Phys. Rev. A **55**, 4346 (1997). 14, 16

[60] J. Reichel and J. Thywissen, *Using magnetic chip traps to study Tonks-Girardeau quantum gases*, J. Phys. IV France **116**, 265 (2004). 14

[61] K. Huang, *Statistical Mechanics*, John Wiley & Sons, USA, 2nd edn. (1987). 16

[62] D. Ananikian and T. Bergeman, *Gross-Pitaevskii equation for Bose particles in a double-well potential: Two-mode models and beyond*, Phys. Rev. A **73**, 013604 (2006). 17, 18, 19

[63] C. Menotti, J. R. Anglin, J. I. Cirac, and P. Zoller, *Dynamic splitting of a Bose-Einstein condensate*, Phys. Rev. A **63**, 023601 (2001). 17, 19, 132, 149, 150

[64] M. Naraschewski, H. Wallis, A. Schenzle, J. I. Cirac, and P. Zoller, *Interference of Bose condensates*, Phys. Rev. A **54**, 2185 (1996). 17

[65] R. W. Spekkens and J. E. Sipe, *Spatial fragmentation of a Bose-Einstein condensate in a double-well potential*, Phys. Rev. A **59**, 3868 (1999). 17, 18, 19

[66] B. J. Dalton, *Two-mode theory of BEC interferometry*, J. Mod. Opt. **54**, 615 (2007). 17, 19

[67] J. Javanainen and M. Wilkens, *Phase and Phase Diffusion of a Split Bose-Einstein Condensate*, Phys. Rev. Lett. **78**, 4675 (1997). 17, 19, 133

[68] M. Lewenstein and L. You, *Quantum Phase Diffusion of a Bose-Einstein Condensate*, Phys. Rev. Lett. **77**, 3489 (1996). 17

[69] H. Wallis, A. Röhrl, M. Naraschewski, and A. Schenzle, *Phase-space dynamics of Bose condensates: Interference versus interaction*, Phys. Rev. A **55**, 2109 (1997). 17

[70] F. Sols, *Randomization of the phase after suppression of the Josephson coupling*, Physica B **194-196**, 1389 (1994). 17

[71] A. J. Leggett and F. Sols, *Comment on "Phase and Phase Diffusion of a Split Bose-Einstein Condensate"*, Phys. Rev. Lett. **81**, 1344 (1998). 17, 19, 150

[72] J. Javanainen and M. Wilkens, *Javanainen and Wilkens reply*, Phys. Rev. Lett. **81**, 1345 (1998). 17, 19

[73] J. Javanainen and M. Y. Ivanov, *Splitting a trap containing a Bose-Einstein condensate: Atom number fluctuations*, Phys. Rev. A **60**, 2351 (1999). 17, 19

[74] L. Pitaevskii and S. Stringari, *Thermal vs Quantum Decoherence in Double Well Trapped Bose-Einstein Condensates*, Phys. Rev. Lett. **87**, 180402 (2001). 17, 19, 20, 21, 22, 137, 138

[75] S. Levy, E. Lahoud, I. Shomroni, and J. Steinhauer, *The a.c. and d.c. Josephson effects in a Bose-Einstein condensate*, Nature **449**, 579 (2007). 17

[76] R. Gati, J. Estève, B. Hemmerling, T. B. Ottenstein, J. Appmeier, A. Weller, and M. K. Oberthaler, *A Primary Noise Thermometer for Ultracold Bose Gases*, New J. Phys. **8**, 189 (2006). 17, 18, 20, 21, 23, 137, 138

[77] R. Gati, M. Albiez, J. Foelling, B. Hemmerling, and M. K. Oberthaler, *Realization of a single Josephson junction for Bose-Einstin condensates*, Appl. Phys. B **82**, 207 (2006). 17, 154

[78] M. Albiez, R. Gati, J. Fölling, S. Hunsmann, M. Cristiani, and M. K. Oberthaler, *Direct Observation of Tunneling and Nonlinear Self-Trapping in a Single Bosonic Josephson Junction*, Phys. Rev. Lett. **95**, 010402 (2005). 17, 23

[79] L. Pezzé, A. Smerzi, G. P. Berman, A. Bishop, and L. Collins, *Dephasing and breakdown of adiabaticity in the splitting of Bose-Einstein condensates*, New J. Phys. **7** (2005). 19, 21, 132, 149, 150

[80] M. Naraschewski and R. J. Glauber, *Spatial coherence and density correlations of trapped Bose gases*, Phys. Rev. A **59**, 4595 (1999). 20

[81] R. Gati, *Bose-Einstein Condensates in a Single Double Well Potential*, Ph.D. thesis, Combined Faculties for the Natural Sciences and for Mathematics of the Ruperto-Carola University of Heidelberg, Germany (2007). 23

[82] C. Cohen-Tannoudji, B. Diu, and F. Laloë, *Quantum Mechanics*, Hermann and John Wiley & Sons, Inc., France (1977). 24, 25, 88, 99, 104, 107, 108

[83] W. Wing, *On neutral particle trapping in quasistatic electromagnetic fields*, Progress in Quantum Electronics **8**, 181 (1984). 25

[84] K. Diekmann, *Bose-Einstein Condensation with High Atom Number in a Deep Magnetic Trap*, Ph.D. thesis, Van der Waals-Zeeman Institute, University of Amsterdam (2001). 25

[85] G. Breit and I. I. Rabi, *Measurement of nuclear spin*, Physical Review **38** (1932). 25

[86] E. Majorana, *Atomi orientati in campo magnetico variabile*, Nuovo Cimento **9** (1932). 26

[87] S. Gov, S. Shtrikmann, and H. Thomas, *Magnetic trapping of neutral particles: Classical and Quantum-mechanical study of a Ioffe-Pritchard type trap*, J. Appl. Phys. D **87** (2000). 26

[88] J. Reichel, W. Hänsel, and T. W. Hänsch, *Atomic micromanipulation with magnetic surface traps*, Phys. Rev. Lett. **83**, 3398 (1999). 26, 42, 79, 85

[89] J. H. Thywissen, M. Olshanii, G. Zabow, M. Drndić, K. S. Johnson, R. M. Westervelt, and M. Prentiss, *Microfabricated magnetic waveguides for neutral atoms*, Eur. Phys. J. D **7**, 361 (1999). 26

[90] J. D. Jackson, *Classical Electrodynamics*, Wiley, New York, NY, 2nd edn. (1977). 27

[91] W. Ketterle and N. J. van Druten, *Evaporative cooling of trapped atoms*, Adv. in At., Mol. and Opt. Phys. **37**, 181 (1996). 29, 39, 101, 103

[92] L. Della Pietra, S. Aigner, C. vom Hagen, S. Groth, I. Bar-Joseph, H. J. Lezec, and J. Schmiedmayer, *Designing potentials by sculpting wires*, Phys. Rev. A **75**, 063604 (2007). 36

[93] C. Aussibal, *Réalisation d'un condensat de Bose-Einstein sur une microstructure*, Ph.D. thesis, Laboratoire Charles Fabry, L'Université Paris IV Université Paris IV (2003). 36, 69

[94] C. Cohen-Tannoudji, J. Dupont-Roc, and G. Grynberg, *Atom-Photon Interactions: Basic Processes and Applications*, John Wiley & Sons, Inc., New York (1992). 39, 88, 103, 104, 105, 108, 128

[95] D. R. Lide (Ed.), *CRC Handbook of Chemistry and Physics, 82nd ed.*, CRC Press, Inc., Boca Raton, FL USA (2001). 42, 46, 73, 79

[96] J. F. O'Hanlon, *A User's Guide to Vacuum Technology*, Wiley, Hoboken, NJ USA, 3rd edn. (2003). 43, 76

[97] B. DeMarco, H. Rohner, and D. S. Jin, *An enriched ^{40}K source for fermionic atom studies*, Rev. Sci. Instrum. **70**, 1967 (1999). 46

[98] B. DeMarco, *Quantum Behaviour of an Atomic Fermi Gas*, Ph.D. thesis, University of Colorado (2001). 46

[99] L.-S. Ma, L. Hollberg, J. H. Shirley, and J. L. Hall, *Modulation transfer spectroscopy for stabilizing lasers*, Unite States Patent Number 4590597, 20 May 1986. 47

[100] J. H. Shirley, *Modulation transfer processes in optical heterodyne saturation spectroscopy*, Optics Letters **7**, 537 (1982). 47

[101] J. L. Hall, L. Hollberg, T. Baer, and H. G. Robinson, *Optical heterodyne saturation spectroscopy*, Appl. Phys. Lett. **39**, 680 (1981). 47

[102] G. C. Bjorklund and M. D. Levenson, *Sub-Doppler frequency-modulation spectroscopy of $I2$*, Phys. Rev. A **24**, 166, doi:\bibinfo{doi}{10.1103/PhysRevA.24.166} (1981). 47

[103] D. A. Steck, *Rubidium 87 D Line Data*, Available online at http://steck.us.alkalidata (revision 2.1, 1 September 2008). 49, 88

[104] R. S. Williamson, *Magneto-Optical Trapping of Potassium Isotopes*, Ph.D. thesis, University of Wisconsin – Madison (1997). 49

[105] E. Arimondo, M. Inguscio, and P. Violino, *Experimental determinations of the hyperfine structure in the alkali atoms*, Rev. Mod. Phys. **49**, 31 (1977). 49

[106] N. Bendali, H. T. Duong, and J. L. Vialle, *High-resolution laser spectroscopy on the D_1 and D_2 lines of $^{39,40,41}K$ using RF modulated laser light*, J. Phys. B. **14**, 4231 (1981). 49

[107] F. Touchard, P. Guimbal, S. Büttgenbach, R. Klapisch, M. De Saint Simon, J. Serre, C. Thibault, H. T. Duong, P. Juncar, S. Liberman, J. Pinard, and J. L. Vialle, *Isotope shifts and hyperfine structure of $^{38-47}K$ by laser spectroscopy*, Physics Letters B **108**, 169 (1982). 49

[108] R. Nyman, G. Varoquaux, B. Viller, D. Sacchet, F. Moron, Y. L. Coq, A. Aspect, and P. Bouyer, *Tapered-amplified AR-coated laser diodes for Potassium and Rubidium atomic-physics experiments*, ArXiv:cond-mat/0511737v1, 2005. 51

[109] M. H. T. Extavour, *Design and construction of magnetic trapping and transport elements for neutral atoms*, Master's thesis, Department of Physics, University of Toronto (2004). 52, 55, 57

[110] G. Varoquaux, *Agile Computer Control of a Complex Experiment*, Computing in Science and Engineering **10**, 55 (2008). 69

[111] J. Estève, *Du miroir au guide d'onde atomique: effets de rugosité*, Ph.D. thesis, Laboratoire Charles Fabry de Institut d'Optique, Université Paris IV (2004). 69, 70, 74

[112] D. Jervis, *Fabrication of an atom chip*, Master's thesis, Department of Physics, University of Toronto (2007). 69, 74

[113] B. Becker, C. Lee, and Z. Lin, *Thermal conductivity in advanced chips*, Advanced Packaging **14**, 14 (2005). 73

[114] J. F. Shackelford, *CRC Material Science and Engineering Handbook, 2nd ed.*, CRC Press, Inc., Boca Raton, FL USA (1994). 73

[115] J. Reichel, W. Hänsel, P. Hommelhoff, and T. W. Hänsch, *Applications of integrated magnetic microtraps*, Appl. Phys. B **72**, 81 (2001). 74, 79

[116] J. Estève, C. Aussibal, T. Schumm, C. Figl, D. Mailly, I. Bouchoule, C. I. Westbrook, and A. Aspect, *Role of wire imperfections in micromagnetic traps for atoms*, Phys. Rev. A **70**, 043629 (2004). 74

[117] S. Aigner, L. D. Pietra, Y. Japha, O. Entin-Wohlman, T. David, R. Salem, R. Folman, and J. Schmiedmayer, *Long-Range Order in Electronic Transport Through Disordered Metal Films*, Science **319**, 1226 (2008). 74

[118] J. Fortágh, H. Ott, S. Kraft, A. Günter, and C. Zimmermann, *Surface effects in magnetic microtraps*, Phys. Rev. A **66**, 041604 (2002). 74, 112

[119] T. Schumm, J. Estève, C. Figl, J. B. Trebbia, C. Aussibal, H. Nguyen, D. Mailly, I. Bouchoule, C. I. Westbrook, and A. Aspect, *Atom chips in the real world: the effects of wire corrugation*, Eur. Phys. J. D **32**, 171 (2005). 74

[120] D.-W. Wang, M. Lukin, and E. Demler, *Disordered Bose-Einstein Condensates in Quasi-One-Dimensional Magnetic Microtraps*, Phys. Rev. Lett. **72**, 076802 (2004). 74

[121] I. Lesanovsky, T. Schumm, S. Hofferberth, L. M. Andersson, P. Krüger, and J. Schmiedmayer, *Adiabatic radio-frequency potentials for the coherent manipulation of matter waves*, Phys. Rev. A **73**, 033619 (2006). 74, 103, 109, 113, 118

[122] G. Modugno, G. Roati, F. Riboli, F. Ferlaino, R. Brecha, and M. Inguscio, *Collapse of a Degenerate Fermi Gas*, Science **297**, 2240 (2002). 78, 86, 87, 98, 153

[123] M. H. Anderson, W. Petrich, J. R. Ensher, and E. A. Cornell, *Reduction of light-assisted collisional loss rate from a low-pressure vapor-cell trap*, Phys. Rev. A **50**, R3597 (1994). 81

[124] S. Ospelkaus, C. Ospelkaus, R. Dinter, J. Fuchs, M. Nakat, K. Sengstock, and K. Bongs, *Degenerate K–Rb Fermi-Bose gas mixtures with large particle numbers*, J. Mod. Optics **54**, 661 (2007). 81, 87

[125] G. Modugno, C. Benkö, P. Hannaford, G. Roati, and M. Inguscio, *Sub-Doppler cooling of fermionic* ^{40}K *atoms*, Phys. Rev. A **60**, R3373 (1999). 81

[126] O. J. Luiten, M. W. Reynolds, and J. T. M. Walraven, *Kinetic theory of the evaporative cooling of a trapped gas*, Phys. Rev. A **53**, 381 (1996). 82, 84, 101

[127] J. Goldwin, S. Inouye, M. L. Olsen, B. Newman, B. D. DePaola, and D. S. Jin, *Measurement of the interaction strength in a Bose-Fermi mixture with* ^{87}Rb *and* ^{40}K, Phys. Rev. A **70**, 021601 (2004). 86, 98

[128] K. M. O'Hara, S. L. Hemmer, M. E. Gehm, S. R. Granade, and J. E. Thomas, *Observation of a Strongly Interacting Degenerate Fermi Gas of Atoms*, Science **298**, 2179 (2002). 86

[129] F. Ferlaino, C. D'Errico, G. Roati, M. Zaccanti, M. Inguscio, G. Modugno, and A. Simoni, *Precise determination of K-Rb scattering lengths from Feshbach spectroscopy*, Phys. Rev. A **73**, 040702 (2006). 87, 98, 99

[130] C. Ospelkaus, *Fermi-Bose mixtures – From mean-field interactions to ultracold chemistry*, Ph.D. thesis, Department of Physics, University of Hamburg, Germany (2006). 87

[131] H. J. Metcalf and P. van der Straten, *Laser Cooling and Trapping*, Springer-Verlag New York, Inc., New York (1999). 88, 89, 92

[132] L. Allen and J. Eberly, *Optical resonance and two-level atoms*, Dover Publications, Inc., New York (1987). 89

[133] P. Milonni and J. E. Eberly, *Lasers*, Wiley, New York (1988). 89, 90

[134] A. Simoni, F. Ferlaino, G. Roati, G. Modugno, and M. Inguscio, *Magnetic Control of the Interaction in Ultracold K-Rb Mixtures*, Phys. Rev. Lett. **90**, 163202 (2003). 98

[135] S. Inouye, J. Goldwin, M. L. Olsen, C. Ticknor, J. L. Bohn, and D. S. Jin, *Observation of Heteronuclear Feshbach Resonances in a Mixture of Bosons and Fermions*, Phys. Rev. Lett. **93**, 183201 (2004). 98

[136] M. Anderlini, E. Courtade, M. Cristiani, D. Cossart, D. Ciampini, C. Sias, O. Morsch, and E. Arimondo, *Sympathetic cooling and collisional properties of a Rb-Cs mixture*, Phys. Rev. A **71**, 061401 (2005). 98, 99

[137] A. Mosk, S. Kraft, M. Mudrich, K. Singer, W. Wohlleben, R. Grimm, and M. Weidemüller, *Mixture of ultracold lithium and caesium atoms in an optical dipole trap*, Appl. Phys. B **73**, 791 (2001). 98

[138] V. V. Flambaum, G. F. Fribakin, and C. Harabati, *Analytical calculation of cold-atom scattering*, Phys. Rev. A **59**, 1998 (1999). 99

[139] A. Derevianko, J. F. Babb, and A. Dalgarno, *High-precision calculations of van der Waals coefficients for heteronuclear alkali-metal dimers*, Phys. Rev. A **63**, 052704 (2001). 99

[140] J. S. Townsend, *A modern approach to quantum mechanics*, McGrawy-Hill, New York (1992). 99

[141] C. Marzok, B. Deh, C. Zimmermann, Ph. W. Courteille, E. Tiemann, Y. Vanne, and A. Saenz, *Feshbach resonances in an ultracold ^{7}Li and ^{87} Rb mixture*, Phys. Rev. A **79**, 012717 (2009). 99

[142] O. Zobay and B. M. Garraway, *Two-Dimensional Atom Trapping in Field-Induced Adiabatic Potentials*, Phys. Rev. Lett. **86**, 1195 (2001). 103, 109, 110

[143] Y. Colombe, *Condensat de Bose-Einstein, champs évanescents et piégeage bidimensionnel*, Ph.D. thesis, Université Paris 13 (2004). 103, 104

[144] I. Lesanovsky, S. Hofferberth, J. Schmiedmayer, and P. Schmelcher, *Manipulation of ultracold atoms in dressed adiabatic radio-frequency potentials*, Phys. Rev. A **74**, 033619 (2006). 103, 113, 118

[145] Y. Colombe, E. Knyazchyan, O. Morizot, B. Mercier, V. Lorent, and H. Perrin, *Ultracold atoms confined in rf-induced two-dimensional trapping potentials*, Europhys. Lett. **67**, 593 (2004). 103, 109, 110, 120

[146] M. White, H. Gao, M. Pasienski, and B. DeMarco, *Bose-Einstein condensates in RF-dressed adiabatic potentials*, Phys. Rev. A **74**, 023616 (2006). 103

[147] Y. Shin, C. Sanner, G.-B. Jo, T. A. Pasquini, M. Saba, W. Ketterle, and D. Pritchard, *Interference of Bose-Einstein condensates split with an atom chip*, Phys. Rev. A **72**, 021604R (2005). 103

[148] T. Schumm, *Bose-Einstein condensates in magnetic double well potentials*, Ph.D. thesis, Combined Faculties for the Natural Sciences and for Mathematics of the Ruperto-Carola University of Heidelberg, Germany (2006). 103, 104

[149] I. I. Rabi, N. F. Ramsey, and J. Schwinger, *Use of Rotating Coordinates in Magnetic Resonance Problems*, Rev. Mod. Phys **26**, 167 (1954). 105

[150] O. Zobay and B. M. Garraway, *Atom trapping and two-dimensional Bose-Einstein condensates in field-induced adiabatic potentials*, Phys. Rev. A **69**, 023605 (2004). 109, 110

[151] S. Hofferberth, B. Fischer, T. Schumm, J. Schmiedmayer, and I. Lesanovsky, *Ultracold atoms in radio-frequency dressed potentials beyond the rotating-wave approximation*, Phys. Rev. A **76**, 013401 (2007). 120, 126, 128

[152] A. Smerzi, S. Fantoni, S. Giovannazzi, and S. R. Shenoy, *Quantum Coherent Atomic Tunneling between Two Trapped Bose-Einstein Condensates*, Phys. Rev. Lett. **79**, 4950 (1997). 122

[153] A. Burkov, M. Lukin, and E. Demler, *Decoherence Dynamics in Low-Dimensional Cold Atom Interferometers*, Phys. Rev. Lett. **98**, 200404 (2007). 132, 149, 150

[154] J. Estève, J.-B. Trebbia, T. Schumm, A. Aspect, C. Westbrook, and I. Bouchoule, *Observations of density fluctuations in an elongated Bose gas: ideal gas and quasi-condensate regimes*, Phys. Rev. Lett. **96**, 130403 (2006). 132

[155] M. Budde and K. Mølmer, *Number distributions for fermions and fermionized bosons in periodic potentials*, Phys. Rev. A **70**, 053618 (2004). 132, 154

[156] J. R. Taylor, *An Introduction to Error Analysis*, University Science Books, Sausalito, California, 2nd edn. (1997). 132, 148, 160, 161, 162, 169

[157] J. Grond, J. Schmiedmayer, and U. Hohenester, *Optimizing number squeezing when splitting a mesoscopic condensate*, Phys. Rev. A **79** (2009). 132, 149, 150

[158] M. Greiner, C. Regal, J. Stewart, and D.S.Jin, *Probing Pair-Correlated Fermionic Atoms through Correlations in Atom Shot Noise*, Phys. Rev. Lett. **94**, 110401 (2005). 144, 171, 175

[159] C. E. Weatherburn, *A First Course in Mathematical Statistics*, Cambridge University Press, Cambridge, UK, 2nd edn. (1949). 148, 160, 161, 162, 167

[160] T. Jeltes, J. M. McNamara, W. Hogervorost, W. Vassen, V. Krachmalnicoff, M. Schellekens, A. Perrin, H. Chang, D. Boiron, A. Aspect, and C. I. Westbrook, *Comparison of the Hanbury Brown-Twiss effect for bosons and fermions*, Nature **445**, 402 (2007). 154

[161] M. N. Tran, M. V. N. Murthy, and R. K. Bhaduri, *Ground-state fluctuations in finite Fermi systems*, Phys. Rev. E **63**, 031105 (2001). 154

[162] M. N. Tran, *Exact ground-state number fluctuations of trapped ideal and interacting fermions*, J. Phys. A: Math. Gen. **36**, 961 (2003). 154

[163] R. Loudon, *Fermion and boson beam-splitter statistics*, Phys. Rev. A **58**, 4904 (1998). 154

[164] B. Yurke, *Input states for enhancement of fermion interferometer sensitivity*, Phys. Rev. Lett. **56**, 1515 (1986). 154

[165] M. I. Grivich and D. P. Jackson, *The magnetic field of current-carrying polygons: An application of vector field rotations*, Am. J. Phys. **68**, 469 (2000). 156

[166] W. Hänsel, *Magnetische Mikrofallen für Rubidiumatome*, Ph.D. thesis, Max-Planck-Institut für Quantenoptik (2001). 158

[167] P. J. Winzer, *Accuracy of error propagation exemplified with ratios of random variables*, Rev. Scient. Instrum. **71**, 1447 (2000). 170